Low-energy observables and fine-tuning in the MSSM

Schutten, Marrit

DOI:
10.33612/diss.655341930

Low-energy observables and fine-tuning in the MSSM

One convention to rule them all

Marrit Schutten

Low-energy observables and fine-tuning in the MSSM

One convention to rule them all

Marrit Schutten

rijksuniversiteit
groningen

Front cover: Cover design by Lina van Otterdijk
Back cover: Cover design by Lina van Otterdijk
Printed by ProefschriftMaken —— www.proefschriftmaken.nl

Observabelen en finetuning in het MSSM bij lage energie

Eén conventie om allen te regeren

Marrit Schutten

university of groningen

Low-energy observables and fine-tuning in the MSSM

One convention to rule them all

PhD thesis

to obtain the degree of PhD at the
University of Groningen
on the authority of the
Rector Magnificus Prof. C. Wijmenga
and in accordance with
the decision by the College of Deans.

This thesis will be defended in public on

Tuesday 30 May 2023 at 16:15 hours

by

Marrit Tamara Schutten

born on 1 April 1992
in Venlo

Supervisors

Prof. R.G.E. Timmermans
Prof. W.J.P. Beenakker

Assessment Committee

Prof. D. Boer
Prof. S. Hoekstra
Prof. T. Plehn

Abstract

There are several indications that the Standard Model of particle physics is not a complete description. In this thesis we study two supersymmetric extensions of the Standard Model and their phenomenology. In order to determine the viability of these models, we search for regions in parameter space where we can satisfy the experimental constraints, specifically for low energy observables such as the muon anomalous magnetic moment $(g-2)_\mu$ and the electron electric dipole moment d_e^E. We then test how fine-tuned the resulting model points are.

First, we explore the phenomenology of pMSSM spectra that are minimally fine-tuned, result in the right $\Omega_{\rm DM}h^2$ *and* simultaneously offer an explanation for Δa_μ. We identify interesting regimes for future LHC searches on the production of $\widetilde{\chi}_2^0\widetilde{\chi}_1^\pm$ pairs, and a low-mass $\widetilde{\tau}^\pm$ search without an assumed mass degeneracy between $\widetilde{\tau}_1^\pm$ and $\widetilde{\tau}_2^\pm$. Furthermore we find that dark matter direct detection experiments that probe $\sigma_{\rm SD,p}$ will ultimately be sensitive to all of our minimally fine-tuned spectra.

Secondly we extend the pMSSM to include CP violating phases (cpMSSM), which allows us to study the electron electric dipole moment. For this purpose we have adapted several existing software packages and developed our own in-house code to supplement these packages. We also propose a measure of fine-tuning (Δ_ϕ) for this CP violating sector and calculate it with another in-house code. We find that we can satisfy the experimental constraints on d_e^E in the cpMSSM, even for phases of $\mathcal{O}(10^{-2})$ and relatively low sparticle masses of $\mathcal{O}(100)$ GeV. A first study on the fine-tuning shows that lower values of d_e^E correlate to higher values of Δ_ϕ. At the same time we find that this measure does not take all the properties of the model properly into account. We motivate a new fine-tuning measure and propose several interesting areas for future research.

Abstract

Abstract (Nederlands)

Er zijn verschillende aanwijzingen dat het standaardmodel geen volledige beschrijving van de deeltjesfysica biedt. In dit proefschrift bestuderen we twee supersymmetrische uitbreidingen van het standaardmodel en hun fenomenologie. Om te testen of deze modellen levensvatbaar zijn, zoeken we naar regio's in de parameterruimte waar we aan alle experimentele randvoorwaarden kunnen voldoen. Specifiek bekijken we meetbare grootheden bij lage energie, zoals het afwijkend magnetisch moment van het muon (Δa_μ) en het elektrisch dipoolmoment (EDM) van het elektron d_e^E. We bekijken ook hoe finetuned deze modellen zijn.

Eerst onderzoeken we de fenomenologie van specta in het pMSSM die minimaal gefinetuned zijn, de juiste waarde voor $\Omega_{\rm DM}h^2$ hebben *en* tegelijkertijd een verklaring bieden voor Δa_μ. We identificeren interessante massa-intervallen waar naar gezocht kan worden in de LHC voor de productie van $\widetilde{\chi}_2^0\widetilde{\chi}_1^\pm$ paren, en benadrukken het belang van de zoektocht naar $\widetilde{\tau}^\pm$ deeltjes met lage massa, waarbij er geen aannames worden gedaan over de ontaarding tussen $\widetilde{\tau}_1^\pm$ en $\widetilde{\tau}_2^\pm$. Daarnaast vinden we dat de categorie experimenten die donkere materie direct proberen waar te nemen en de observabele $\sigma_{\rm SD,p}$ meten, uiteindelijk gevoelig zullen zijn voor al onze spectra met minimale finetuning.

Ten tweede breiden we het pMSSM uit met fases die CP symmetrie schenden (cpMSSM), waardoor we het elektrisch dipoolmoment van het elektron kunnen bestuderen. Hiervoor hebben we verschillende software pakketten aangepast en een eigen code ontwikkeld ter ondersteuning van de bestaande software. We stellen ook een definitie van de mate van finetuning voor, Δ_ϕ, die de finetuning in deze sector kan vatten, en creëren we nieuwe code om deze maat uit te rekenen. We vinden datapunten in het cpMSSM die voldoen aan de experimentele limiet op het elektrisch dipoolmoment van het elektron, zelfs voor fases in de orde van $\mathcal{O}(10^{-2})$ en relatief lage massa's van de supersymmetrische deeltjes in de orde van $\mathcal{O}(100)$ GeV. Een eerste studie naar Δ_ϕ laat een direct verband zien tussen d_e^E en Δ_ϕ: lagere waarden van d_e^E correleren met hogere waarden van Δ_ϕ. Tegelijkertijd zien we dat deze mate van finetuning niet altijd voldoet om de eigenschappen van het model goed in kaart te brengen. We motiveren daarom het voorstel voor een nieuwe mate van finetuning en stellen verschillende interessante richtingen voor om het onderzoek voort te zetten.

Abstract (Nederlands)

Acronyms

BSM	beyond the standard model	5
C	charge conjugation	6
CMB	cosmic microwave backgrond	7
cpMSSM	pMSSM with explicit CP violation	13
CPV	CP violation	6
DM	dark matter	5
DMDD	DM direct detection	13
EDM	electric dipole moment	5
eEDM	electron EDM	10
EFT	effective field theory	50
EWSB	electroweak symmetry breaking	4
FT	fine-tuning	9
LHC	Large Hadron Collider	3
LSP	lightest supersymmetric particle	64
MSSM	minimal supersymmetric standard model	17
P	parity	6
pMSSM	phenomenological MSSM	13
QFT	quantum field theory	3
RGEs	renormalisation group equations	60
SM	standard model	3
SUSY	supersymmetry	9
T	time reversal	6
WIMP	weakly interacting massive particle	8

Contents

Chapter 1

Introduction

The field of particle physics is based on the concept that there exist fundamental building blocks, fundamental particles, that cannot be divided in smaller parts. We can describe the behaviour of these particles with the laws of physics, using the standard model (SM) of particle physics. With this model we can explain how atoms and molecules are formed from these building blocks, and predict the outcome of experiments. The interplay between theory and experiment is called phenomenology: the study of measurable quantities that depend on the theoretical model in question, which allows for a better understanding of the physics behind those models and experiments. The ultimate goal is to understand the laws of physics under all circumstances, such that we can reliably predict the outcome of any experiment.

In this work we will focus on two models, in which we study several observables to constrain these models and to better understand their phenomenology. To understand the relevance of these models, we will start with an introduction to the SM to see why we would be interested in new models in the first place.

1.1 The Standard Model

The SM of particle physics describes the fundamental particles and their interactions. The free parameters of the theory are the particle properties such as their masses, and the coupling strengths of the interactions. These have to be determined experimentally. Once all the parameters are known, we can predict how particles interact and decay according to this model. So far we have not been able to find significant deviations from the SM predictions on any SM observables, although the SM has been very thoroughly tested at electron-positron colliders (such as LEP and SLC) and different Large Hadron Collider (LHC) experiments.

To study the SM we use the framework of quantum field theory (QFT), in which particles are understood to be excitations of quantum fields. Of the four fundamental interactions, three can be accurately modelled by gauge bosons as force carriers.[1] In Figure 1.1 we show an overview of the matter particles and force carriers.

We can describe the SM by the following gauge groups

$$SU(3)_C \times SU(2)_L \times U(1)_Y, \tag{1.1}$$

and we require that the SM is locally invariant under the corresponding gauge transformations. This results in the three fundamental interactions that are mediated by the gauge bosons.

The $SU(3)_C$ symmetry corresponds to the strong interaction, which is mediated by massless gluons. The combination $SU(2)_L \times U(1)_Y$ gives rise to the electroweak interactions. The corresponding gauge bosons are the $W^{\pm}$- and Z^0-boson for the

[1] Ideally we would also model the fourth interaction, gravity, with a spin-2 force carrier. However, we do not know how to describe the theory of gravity, general relativity, in a QFT framework properly. This is therefore a separate field of study.

weak interaction and the photon for the electromagnetic interaction.[2] Of these, only the photon is massless, which presents a challenge for the underlying theory: the requirement that the SM has to be invariant under local gauge transformations does not allow the gauge bosons to be massive, as we cannot describe their mass terms in a locally gauge invariant way. The experimental observation that the $W^{\pm}$- and Z^0-bosons have a mass of 80.4 and 91.2 GeV respectively, is therefore not straightforwardly compatible with the concept of local gauge invariance.

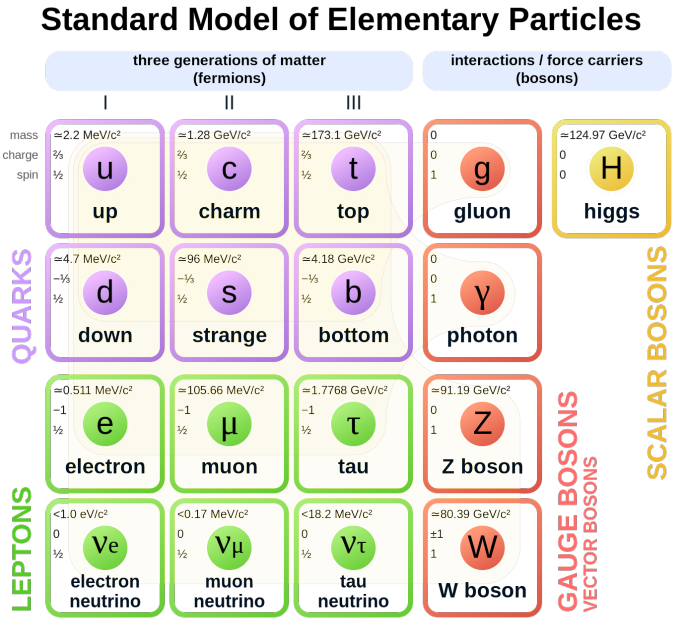

Figure 1.1 Elementary particles in the Standard Model: the quarks and leptons as the matter particles, the gauge bosons and the Higgs boson [1].

However, the masses of the W- and Z-bosons can be generated with the Higgs mechanism. Through the process of electroweak symmetry breaking (EWSB) the $SU(2)_L \times U(1)_Y$ is spontaneously broken to an electromagnetic $U(1)_Q$ symmetry. As a result of EWSB, we obtain the massive $W^{\pm}$- and Z^0-bosons, instead of the massless gauge bosons that would be associated with an unbroken symmetry. The fact that the symmetry is broken is represented by a non-zero vacuum expectation value for the Higgs field. We can interpret the $U(1)_Q$ as a symmetry of the ground state, the vacuum, whereas the $SU(2)_L \times U(1)_Y$ symmetry is not realised in the vacuum.

[2] Note that the electromagnetic interaction corresponds to the electromagnetic $U(1)_Q$ group, not the hypercharge $U(1)_Y$ group. See the part about electroweak symmetry breaking.

The gauge boson corresponding to the resulting $U(1)_Q$ symmetry is the photon, which mediates the electromagnetic interaction. With the Higgs mechanism we also obtain a massive scalar particle, the Higgs boson. The masses of the W-, Z- and Higgs bosons have to be determined experimentally, together with the other free parameters of the SM: the masses of the fermions and the coupling strengths of the interactions.

The Higgs boson was the last SM particle to be observed, in 2012. With this discovery all the particles shown in Figure 1.1 have been experimentally detected, their masses have been determined and the energy dependent gauge couplings are known. Putting everything together, we consider the SM now complete.[3]

However, we do want to mention two specifics that are not included in the SM, firstly the existence of right-handed neutrinos. We know that neutrinos cannot be massless, since we have observed neutrino oscillations. The mechanism that generates these masses is unknown, although many different models are available. The study on neutrino masses and the mechanism to generate them, is considered beyond the standard model (BSM) physics for this thesis. To describe massless neutrinos that are compatible with the experimental data besides neutrino oscillations, we only need left-handed neutrinos. As such, right-handed neutrinos and any neutrino mass term will not be considered to be part of the SM for the remainder of this thesis.

Secondly there is the Θ_{QCD}-term, which we will consider BSM as well. Typically the Lagrangian is constructed by including all possible terms that respect the symmetries of the model. For the QCD sector there exists a term that does respect the $SU(3)$ symmetry, but is nevertheless left out. This term is

$$\Theta_{\text{QCD}} \frac{g_3^2}{32\pi^2} \tilde{G}^{a\mu\nu} G_{a\mu\nu}, \tag{1.2}$$

where the dual $SU(3)$ field strength tensor $\tilde{G}^{a\mu\nu}$ is defined in terms of the $SU(3)$ field strength tensor $G^a_{\mu\nu}$ and the Levi-Civita symbol ϵ as $\tilde{G}^{a\mu\nu} = \frac{1}{2}\epsilon^{\mu\nu\alpha\beta} G^a_{\alpha\beta}$, and Θ_{QCD} is the QCD vacuum angle. For the general conventions in this thesis, e.g. about the coupling constants, see Appendix A.1.

The QCD vacuum angle is the quantity that poses the problem: one would naively expect it to be of order $\mathcal{O}(1)$, as the SM provides no reason to expect otherwise. However, experimental constraints from the neutron electric dipole moment (EDM) put it at $\Theta_{\text{QCD}} < 10^{-10}$ [3, 4]. This is known as the strong-CP problem: we cannot explain within the SM why Θ_{QCD} is so small. In this work we will therefore not consider (1.2) as part of the SM.

There are more open issues that cannot be explained (properly) with the SM alone. We have already briefly mentioned the challenge of describing gravity in a QFT framework, but this is not the only open problem. Among these we will highlight the problems of baryogenesis and dark matter (DM) in Section 1.2, since these are the topics we have chosen for our study.

[3] A lot of details have been left out in this explanation, so we refer the interested reader to e.g. [2] for a more detailed account on the Higgs mechanism and the SM in general.

1.1.1 Charge conjugation, Parity and Time reversal

Besides gauge symmetries there are other symmetries that are relevant for the SM. These can be categorised in two types: continuous and discrete symmetries. An example of the first type is Lorentz symmetry, which states that the laws of physics should be the same for any observer in any inertial frame. The discrete symmetries charge conjugation (C), parity (P) and time reversal (T) are relevant for our study.

The C-operator transforms particles into antiparticles and vice versa. Under P the spatial coordinates are reversed and the T-operator reverses the time coordinate. The combination of those three operators gives a mirror image of sorts, where an anti-particle will move in the opposite spatial and time directions. A strong requirement for the SM is that any local QFT with a Hermitian Hamiltonian must by symmetric under CPT, in order for it to be Lorentz invariant. Since we require Lorentz symmetry for the SM, CPT invariance is also required.

However, the individual symmetries do not have to be respected by the SM. Since the weak interaction couples only to left-handed particles and not to right-handed ones, the weak interaction violates P [5]. Not much later, it was discovered that C is violated in weak decays as well. In fact, the weak interaction also violates CP, although this violation is much smaller. This was first shown through the decay of neutral kaons [6].

The unitary CKM matrix contains the information on the CP violation (CPV) through the weak interaction, as it translates between the quark gauge and mass eigenstates. As this is a unitary 3×3 matrix in family space, it can be specified with three mixing angles θ_{12}, θ_{13} and θ_{23}, and a phase δ. Using this, we can quantify the amount of CPV with the Jarlskog invariant J, defined as $J = c_{12}c_{13}^2c_{23}s_{12}s_{13}s_{23}\sin(\delta)$ for $c_{ij}, s_{ij} = \cos(\theta_{ij}), \sin(\theta_{ij})$ and δ the CP violating phase [7]. In the SM, the Jarlskog invariant is experimentally determined to be $J \approx 3 \cdot 10^{-5}$, portraying the small amount of CPV observed in the SM.

1.2 Beyond the SM physics

Based on our current understanding of particle physics and cosmology there is a huge lack of anti-matter in the observable Universe. In most cosmological models it is assumed that the Universe was in a hot, dense state for a very brief period, after which it rapidly expanded and cooled. During this expansion, the temperature of the Universe ultimately dropped enough for particles to decouple from the plasma and form stable states.

However, there appears to be an imbalance in this creation process, assuming the laws of physics have not changed over time. Observations show that the amount of matter outweighs the amount of antimatter significantly, although we expect that particles and anti-particles were created pairwise. Assuming that particle physics was ruled by the same laws we observe today, this means that there should be another

reason for this imbalance. Baryogenesis is the hypothetical process that takes place in the early Universe to account for the difference in the amount of matter versus anti-matter. Baryogenesis cannot happen unless the following conditions are satisfied:

- baryon number violation;
- C and CP violation;
- interactions out of thermal equilibrium.

These are also known as the Sakharov conditions [8].

Although there is C and CP violation in the SM, this is not enough to create the required imbalance to account for the observed matter/antimatter ratio, as J is quite small. We are therefore interested in BSM theories with more CPV, possibly also with baryon number violation to satisfy the first Sakharov condition.

In addition to baryogenesis there is another reason to go BSM: the problem of DM. There are several experimental signs for the existence of DM. The first and most famous one is the deviation in galaxy cluster radial velocities, which was first observed for the Coma cluster in 1933 by Fritz Zwicky [9, 10]. Based on the visible amount of matter we expect a far lower radial velocity for the galaxies within the cluster than the observations show. Several solutions were proposed for this mismatch, including the presence of 'dark' matter: matter that does not interact directly through the electromagnetic or strong force with SM particles, making it invisible to traditional detection methods other than gravitational detection.

At the time, the work of Zwicky did not gather much attention. However, in 1970 the team of Vera Rubin published similar observations about the rotational velocity of stars and gas in the Andromeda galaxy [12]. Since then several explanations besides DM have been considered, including modifications of general relativity and the existence of faint astrophysical objects [13].

Nowadays there is more experimental evidence for the existence of DM, besides the rotational velocities. The seeds of the present-day structures of galaxies, galaxy clusters and even larger structures have to be formed in the early Universe [14]. This structure formation cannot be explained without the presence of DM, as structure formation would not happen fast enough without DM to account for the present observable Universe. Another cosmological piece of evidence is the observed anisotropy power spectrum of the cosmic microwave backgrond (CMB). This spectrum can be explained with the ΛCDM model [15], which relies on the existence of DM.[4] Observations of the matter and mass distributions of merging galaxy clusters, such as the Bullet cluster, also point at the existence of DM in the form of particles [17]. Finally there are some very recent observations of galaxies without any DM [18, 19], that seriously challenge alternative explanations like modified gravity, since this requires gravity to behave differently in different parts of space. Note that it is also challenging to explain the existence of such galaxies with the ΛCDM model.

[4] Note that the ΛCDM model comes with its own challenges, see e.g. [16].

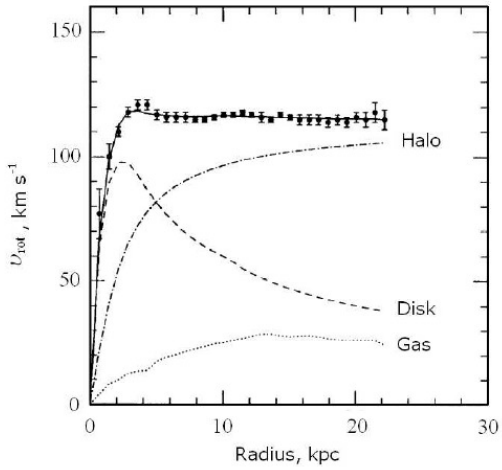

Figure 1.2 The observed rotation curve of galaxy NGC 6503 versus the predicted rotational velocity for the disk and gas in the galaxy, as a function of the distance to the center of the galaxy (radius). The predicted contribution from the dark-matter halo that surrounds the galaxy is shown by the dashed-dotted line [11].

In this thesis we will only consider the particle explanation of DM. A suitable DM particle, or DM candidate, must have the following properties in the ΛCDM model. First, a DM candidate has to be meta-stable compared to the lifetime of the Universe, dark (no direct strong or electromagnetic interactions with SM particles), cold (non-relativistic) and interacting only weakly with other particles.[5]

We call this a weakly interacting massive particle (WIMP). The total amount of DM can exist of one particle, or several different WIMPs.

The SM left-handed neutrinos are not a DM candidate because of the third requirement: due to their small masses they are fast moving and hence not cold. This means the SM does not contain a particle that is suitable as a DM candidate, so we look to BSM theories for this as well. Right-handed neutrinos are considered a possibility, but this depends on their properties, such as the mass and interaction strength.

Another possibility is the axion, a particle that is related to the strong-CP problem we discussed above. A solution to the strong-CP problem would be to introduce a new $U(1)$ symmetry that is then spontaneously broken, which drives the value of Θ_{QCD} towards zero and thereby explains its small value. This was first proposed by Peccei and Quinn in 1977 [20, 21]. As a result of this spontaneous symmetry breaking, we

[5] If DM is not cold, the primordial density fluctuations in the CMB would wash out and the DM would not be sufficiently bound to galaxies. Those two properties are in contrast with observations.

obtain a Goldstone boson: the axion. Due to the chiral anomaly of the $U(1)$ symmetry the axion is not massless, as one would expect from a Goldstone boson, but in fact acquires a small mass. If the axion would have a mass of $m_a \lesssim 10^{-3}$ eV (most likely 10^{-6} eV $< m_a < 10^{-4}$ eV), it could be a suitable DM candidate [13]. Note that it is difficult to match the properties of the axionic DM candidate with observations, specifically the amount of DM that is observed today.

Also supersymmetry (SUSY) can provide a DM candidate, as well as more CPV. A supersymmetry is a spacetime symmetry that links bosonic and fermionic degrees of freedom. Imposing such a symmetry on the SM results in additional particles, of which the neutralino could be a DM particle: it is charge and colour neutral, could be heavy enough and could be weakly interacting. In addition to providing a DM candidate, supersymmetric theories can also have more sources of CPV and thereby satisfy the Sakharov conditions.

Moreover, SUSY can potentially solve another problem: that of fine-tuning (FT). For any BSM theory that couples to the SM there is a potential FT problem in the Higgs sector. This is because the SM Higgs boson mass can receive large corrections from new particles at high energy scales. Depending on the mass of these new particles, the corrections on the Higgs boson mass can become many orders of magnitude larger than the mass itself. This raises the question why these large corrections cancel each other in such a way that the measured Higgs boson mass is obtained; it would be quite a coincidence that several large numbers add up to a very small number. As long as we lack an explanation for this coincidence, like the Peccei-Quinn solution to the small value of Θ_{QCD}, we consider this a FT problem that has to be addressed.

All in all, there are several reasons to study SUSY as a BSM theory and to look for experimental signs of SUSY.

1.3 Experimental searches for BSM physics

A very important experimental facility to study SM and BSM phsyics is the LHC at CERN. It is the world's largest and most powerful particle accelerator, where proton beams[6] can be collided to study the resulting particles, to gain more insight into particle physics and the SM, but also to search for evidence of BSM physics.

There are several experiments at the LHC: Alice, ATLAS, CMS and LHCb. The proton beams in the LHC are made to collide in each of these particle detectors. The remnants from the collision can be observed with these detectors. By measuring the energy, momentum and path of the particles that result from the collision, we can determine which kind of particles were produced. We can also extract SM parameters, such as the coupling constants, from these measurements. Currently some of the most precise measurements on the SM parameters are based on results from the different

[6] The LHC is also used for lead-lead and proton-lead collisions.

experiments at the LHC.

So far we have not observed a BSM particle in any LHC experiment. In order to understand what this means for SUSY, we have to take a look at the way the experimental analysis works. At the experiments we can measure observables such as the energy and momentum of the final state particles that are produced in a single proton-proton collision (an event). Also the missing (transverse) momentum, e.g. from neutrinos, is an important part of the event. With these observables we can reconstruct the event and run an analysis. The physics we want to study determines the specifics of the analysis.

First, we have to select relevant events, count them and obtain the observables per event. Then, we simulate what we expect the number of the relevant events to be, given a specific model. In our case, we would select a supersymmetric model and assume a value for the masses and coupling constants in the model. With this we can compare the expected number of events and the number of actually selected events. Depending on the comparison between the simulated events and the actual events, we can exclude the model with the chosen parameter values with a certain statistical confidence, typically 95%.

In practise, this is much more complicated. The events of interest are often very similar to other events, so one has to distinguish between signal and background. Also the assumptions on the model play a large role in the resulting exclusion limit. Since the masses and couplings of supersymmetric models typically depend on many free parameters, it is hard to translate the exclusion limits to concrete regions of parameter space that are excluded.

In order to obtain as much information about a BSM model as possible, we therefore aim to combine as much experimental data as possible and use data from more experiments than those at the LHC. Beside the high-energy experimental searches at the LHC, there are also several low-energy experiments that search for BSM physics. Precision measurements of such low-energy observables can be used to complement high-energy searches for new particles. Specifically we will study the muon anomalous magnetic moment $(g-2)_\mu$ and the EDM of the electron d_e^E.

There are several independent experiments that try to measure the value of $(g-2)_\mu$, such as the Brookhaven [22], Fermilab [23] and J-PARC [24] experiments. Of these, the first two have already published results that indicate BSM physics. The facility at J-PARC aims to publish its first results in the next few years. Currently the deviation between experiment and theory is roughly 4 standard deviations, making it a very interesting observable to study.

For the electron EDM (eEDM) a close comparison between SM prediction and experimental value is still 8 orders of magnitude away. However, it is still claimed that the current experimental limit places strong constraints on BSM theories [25,26]. Especially the parameters that violate CP can be constrained by this limit, as the eEDM is a CP violating observable [27]. This makes it an interesting complement to $(g-2)_\mu$, since they can be used to constrain different parameters of a model. We will

therefore study both observables in this thesis.

No eEDM has been measured so far, so the maximum value is limited by the experimental sensitivity. There are several independent groups that try to measure the eEDM: the Hinds group at Imperial College in London [28] and the ACME collaboration at Yale/Harvard [29] have both improved the limit on the eEDM over the past years. Both groups do not study the electron itself directly, but use atoms or molecules to extract the eEDM from the total EDM. Very recently the first results using yet another technique was published: the Cornell group measured the eEDM through the measurement of the EDM in trapped molecular HfH^+-ions [30].

The eEDM-NL collaboration in Groningen is a new initiative that was funded. They aim to use a new technique for measuring the eEDM through laser-cooled BaF molecules [31] and thereby to improve the eEDM limit by an order of magnitude. They will publish their first results in the coming years (2023-2024). In the meantime, the results from the ACME collaboration hold the strongest limit, which we will use for our studies on the eEDM.

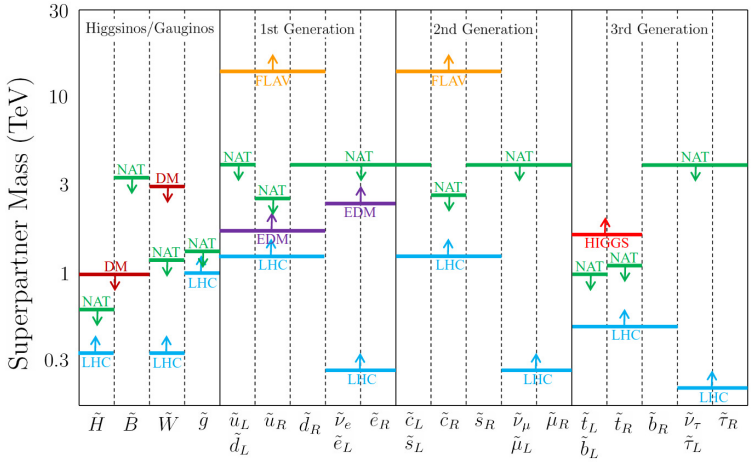

Figure 1.3 Claim on exclusion bounds based on eEDM limits: A sample of constraints on the superpartner spectrum from naturalness (NAT), dark matter (DM), collider searches (LHC), the Higgs boson mass (HIGGS), flavor violation (FLAV), and EDM constraints (EDM). The constraints assume a moderate value of $tan\beta = 10$. Taken from [26].

Although the eEDM value has not yet been determined and only upper experimental limits exist, it is often claimed that the current results do exclude many supersymmetric models. An example of such a claim can be found in Figure 1.3. As is mentioned in the paper, "*All of the constraints shown are merely indicative and subject to significant loopholes and caveats.*" We feel that this necessary nuance

is often lost in discussions on the exclusion power of the experimental eEDM limit. Supersymmetric models for which the eEDM has the same value as in the SM exist as well. Providing more insight into this nuance will be the main aim of our eEDM study in this thesis.

Additionally, we will study the fine-tuning of supersymmetric models that do not predict the same eEDM value as the SM. Note that fine-tuning and naturalness[7] are separate concepts and should be treated as such. Since naturalness is only properly defined for scenarios with one symmetry-breaking parameter, we will exclusively focus on studying the fine-tuning.

Since SUSY predicts a DM candidate, we will also use the results of experimental searches for DM in our studies. We can distinguish three types of interactions between a DM particle and a SM particle, see Figure 1.4, and therefore there are three different types of experiments.

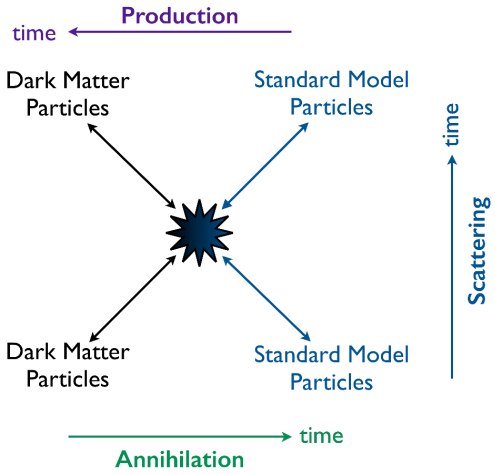

Figure 1.4 Types of DM detection: annihilation (indirect detection), scattering (direct detection) and production. From: `https://particleastro.brown.edu/dark-matter/`.

The production of DM particles is studied at the LHC, resulting in limits on supersymmetric candidates for DM.

Experiments that aim for indirect detection of DM typically search for an excess of SM particles produced by DM annihilation, e.g. neutrinos or photons. In this category there are many different experimental searches that study astrophysical objects or regions with a high DM density, such as the galactic center of the Milky Way or dwarf-galaxy satellites of the Milky Way. The biggest challenge for such experiments is to control the background, since it is hard to fully understand all possible astrophysical sources. We will therefore adopt a conservative approach in our work when

[7] In the sense of 't Hooft [32].

implementing these limits: we only consider the limit on $\langle \sigma v \rangle$ stemming from the observation of gamma rays originating from dwarf galaxies.

In DM direct detection (DMDD) one tries to observe the recoil energy from the scattering of a DM particle on a nucleus [33]. In order to do so, it is typically assumed that the local DM density ρ_0 and its distribution with respect to the center of the experiment are known. One also assumes that DM consists fully of one type of particle that saturates the relic density, and that we can reliably identify all sources of noise. Background reduction is therefore an important part of the experimental design. Finally the sensitivity of the experiment has to be high enough to measure the recoil energy precisely, even if it is low. So far there has not been a confirmed observation of a DM particle in any DMDD experiment.

Examples of DMDD experiments are the XENON1T experiment [34], LUX [35], PandaX [36], Darkside-50 [37] and Pico-60. Upgrades of these include the LUX-ZEPLIN collaboration [38], the XENONnT experiment and the Pico-40L and Pico-500 upgrades [39]. We will use the results of the different experimental searches for DM to place constraints on the models that we study.

1.4 Thesis outline

In this work we study observables in two supersymmetric models to gain more insight into the phenomenology of these models. The goal is to combine experimental data from different types of experiments, such that we can study the interplay of these constraints on the models. This will allow for a more complete picture than the study of separate observables.

In order to perform this study, a clear understanding of the underlying supersymmetric models is necessary. Therefore we will start with a short introduction to SUSY in Chapter 2, where we explain the general aspects of SUSY. We define the two supersymmetric models that we will study later on: the phenomenological MSSM (pMSSM) and the pMSSM with explicit CP violation (cpMSSM). We will pay special attention to the Higgs sectors of these models, since there are important differences between the Higgs sectors of the SM, the pMSSM and the cpMSSM. We will also discuss the new particle content and general properties of the two models.

Then in Chapter 3 we discuss and define the observables that will be the subject of our studies. We also look into measures to quantify the amount of fine-tuning in the (c)pMSSM.

The high-dimensional nature of supersymmetric models makes it difficult to study the dependence of the observables and the amount of fine-tuning directly as a function of the model parameters. Instead we set up a numerical analysis for each model, which we will do at the beginning of Chapters 4 and 5. This allows us to implement experimental observations as constraints on the models and to compute the value of observables.

In Chapter 4 we study the phenomenology of the pMSSM. We implement all available constraints, such as LHC results, and do a combined study of several observables. This allows us to discuss the properties of the part of parameter space that is not excluded by any experiment, is not too fine-tuned, but does allow for an explanation of the value of observables such as $(g-2)_\mu$ and the DM relic density. We focus this chapter on the question:

> *What is the phenomenology of the pMSSM spectra that survive all experimental constraints, are minimally fine-tuned and explain the latest (g-2)$_\mu$ results?*

To extend our (g-2)$_\mu$ study, we extend the pMSSM to include CPV in Chapter 5. We explain our in-house code to calculate the eEDM and how we adapt the available software packages to study the cpMSSM. We also discuss the first results of our study on the eEDM and FT in the cpMSSM, focussing on the question:

> *How does the current experimental limit on the eEDM constrain the cpMSSM, especially the phases, and does this limit imply a fine-tuned model?*

Finally, in Chapter 6 we present our conclusions regarding this question and discuss further research possibilities. Especially for the cpMSSM we identify several interesting directions for follow-up research.

Chapter 2

Theory

In this thesis we will study the minimal supersymmetric standard model (MSSM) as an extension of the SM. We will work with two slightly different sets of constraints on the MSSM, that result in two very different models phenomenologically. We will describe these models, their particle content and specifically their Higgs sector, before we use these models to study the observables that will be introduced in Chapter 3. A full account of the MSSM and related models would go beyond the purpose of this thesis, so we refer the interested reader to e.g. [40, 41]

2.1 A short introduction to supersymmetry

Modern particle physics is built on symmetries, as such the SM is as well. It therefore logically follows that any extension of the SM should be based on a new or extended symmetry that respects the existing gauge and spacetime symmetries. One possibility to extend the SM is through a supersymmetry. We will study the MSSM, which is the minimal implementation of supersymmetry in the SM.

A supersymmetry is a spacetime symmetry that connects bosonic and fermionic states with the same quantum numbers. In a supersymmetric version of the SM this results in an additional boson for each SM fermion and vice versa, such that all other quantum numbers are the same for the particle and its supersymmetric partner. These superpartners are called sparticles. Superpartners of fermions get the prefix 's' (selectron, squark, etc), while superpartners of bosons get the suffix 'ino' (gluino, higgsino, etc). An overview of the particles in the MSSM can be found in Table 2.1.

Note that also the degrees of freedom for each SM particle and its superpartner have to match. SM fermions can be in a left- or right-handed chiral state because they are spin-1/2 particles. We therefore define a similar property for their scalar superpartners to obtain the same number of degrees of freedom. These scalar superpartners of the left- and right-handed fermions then have different $SU(2)_L \times U(1)_Y$ quantum numbers as well.

Another important observation is that the MSSM necessarily has two Higgs doublets with opposite hypercharge. This is in order to obtain a gauge invariant supersymmetric Lagrangian (without anomalies) and is necessary to give mass to all up-type and down-type fermions. Both Higgs fields are listed as SM particles in Table 2.1.

There is no observed violation of lepton and baryon number in the SM, but these conservations are accidental in the SM. They are made explicit in the MSSM by requiring the conservation of R-partity[1] in all couplings [42, 43]. This quantity is defined as

$$R = (-1)^{2s+3B+L}, \tag{2.1}$$

where B and L are the baryon and lepton number, and s is the spin quantum number. All SM particles[2] have $R = 1$, while all superpartners have $R = -1$. R-parity

[1] R-parity is actually a remnant of a more general $U(1)$ symmetry, see e.g. [40] for more details.
[2] This definition includes both the Higgs doublets.

SM particle	Spin	MSSM superpartner	Spin
B and W-bosons	1	Bino, Wino	1/2
Higgs	0	Higgsino	1/2
Gluon	1	Gluino	1/2
(Left, right) up-type quarks	1/2	(Left, right) up-type squarks	0
(Left, right) down-type quarks	1/2	(Left, right) down-type squarks	0
(Left, right) charged leptons	1/2	(Left, right) charged sleptons	0
Neutrinos	1/2	Sneutrinos	0

Table 2.1 The particle content of the MSSM, including two Higgs doublets.

conservation has the important consequence that supersymmetric particles are always produced in pairs and the lightest supersymmetric particle (LSP) is stable. If this particle is also charge and colour neutral, it is therefore a DM candidate (see also Chapters 1 and 3 for more details on DM).

As is also mentioned in Chapter 1, the SM has a fine-tuning problem in the Higgs sector if we assume it couples to higher energy scales. A more detailed discussion of this subject is saved for Chapter 3. In short, the problematic scalar mass terms are protected if they are linked to fermionic mass terms, since these are themselves protected by a chiral symmetry. Unbroken supersymmetry offers this protection by linking all SM bosons, including the problematic Higgs, to SUSY fermions. Because the masses of a SM particle and its superpartner are the same, the fine-tuning problem is then solved.

However, we have not observed superpartners with the same mass as the SM particles. The only possibly realisation of supersymmetry is thus as a broken symmetry. The nature of this breaking is unknown, although several theories exist [40]. Consequently the masses of the particles and their superpartners are no longer equal and the FT problem could return. In the MSSM a practical approach to this breaking mechanism is taken: if we can describe the breaking in generic terms, it does not matter that we do not know the precise mechanism behind it. In order to save the protection offered by the fermionic mass terms, the breaking has to be soft, meaning that there are no reappearing quadratic divergences. This is done by adding explicit soft-breaking terms to the fully supersymmetric SM Lagrangian. Together they form the MSSM Lagrangian, that is described in more detail in e.g. [40, 41].

Unfortunately even this conservative implementation of SUSY results in 107 free parameters for the MSSM. Almost all of these are due to the soft-breaking terms; only the supersymmetry preserving Higgs mixing parameter μ is an exception. In this thesis we will focus on two more constrained versions of the MSSM to make a computational study of the parameter space feasible. To study these models, we will first look at the Higgs sector.

We start with a quick overview of the complex two Higgs doublet model, because this is the same as the Higgs sector of the MSSM.

2.2 The Higgs sector and EWSB in the MSSM

The Higgs sector of the MSSM contains two Higgs doublets, unlike the single Higgs doublet of the SM. In general, such a configuration would look like

$$\phi_1 = \begin{pmatrix} \phi_1^+ \\ \phi_1^0 \end{pmatrix}, \qquad \phi_2 = \begin{pmatrix} \phi_2^+ \\ \phi_2^0 \end{pmatrix}. \tag{2.2}$$

Barring any additional assumptions, the Higgs potential for such a model will look as follows

$$\begin{aligned} V(\phi_1,\phi_2) = {} & m_{11}^2(\phi_1^\dagger\phi_1) + \left(m_{12}^2(\phi_1^\dagger\phi_2) + \text{h.c.}\right) + m_{22}^2(\phi_2^\dagger\phi_2) \\ & + \frac{1}{2}\lambda_1(\phi_1^\dagger\phi_1)^2 + \frac{1}{2}\lambda_2(\phi_2^\dagger\phi_2)^2 + \lambda_3(\phi_1^\dagger\phi_1)(\phi_2^\dagger\phi_2) + \lambda_4(\phi_1^\dagger\phi_2)(\phi_2^\dagger\phi_1) \\ & + \left\{\frac{1}{2}\lambda_5(\phi_1^\dagger\phi_2)^2 + \lambda_6(\phi_1^\dagger\phi_2)(\phi_1^\dagger\phi_1) + \lambda_7(\phi_1^\dagger\phi_2)(\phi_2^\dagger\phi_2) + \text{h.c.}\right\}. \end{aligned} \tag{2.3}$$

In this expression the parameters m_{12}^2, λ_5, λ_6 and λ_7 can in general be complex. The others are real to ensure the potential is Hermitian. However, in the MSSM the two doublets necessarily have opposite hypercharge. This can be achieved by defining $H_1 = i\sigma^2\phi_1^*$ and $H_2 = \phi_2$, where σ^2 is the second Pauli matrix. This gives us

$$\begin{aligned} H_1 &= \begin{pmatrix} H_1^0 \\ H_1^- \end{pmatrix} = \begin{pmatrix} \phi_1^{0*} \\ -\phi_1^- \end{pmatrix}, \\ H_2 &= \begin{pmatrix} H_2^+ \\ H_2^0 \end{pmatrix} = \begin{pmatrix} \phi_2^+ \\ \phi_2^0 \end{pmatrix}. \end{aligned} \tag{2.4}$$

The corresponding potential can then be rewritten to the following expression:

$$\begin{aligned} V_{H_1,H_2} = {} & m_{11}^2\left(|H_1^0|^2 + |H_1^-|^2\right) + \left(m_{12}^2\left[H_1^0H_2^0 - H_1^-H_2^+\right] + \text{c.c}\right) + m_{22}^2\left(|H_2^0|^2 + |H_2^+|^2\right) \\ & + \frac{\lambda_1}{2}\left(|H_1^0|^2 + |H_1^-|^2\right)^2 + \frac{\lambda_2}{2}\left(|H_2^0|^2 + |H_2^+|^2\right)^2 \\ & + \lambda_3\left[(|H_1^0|^2 + |H_1^-|^2)(|H_2^0|^2 + |H_2^+|^2)\right] \\ & + \lambda_4(H_1^0H_2^0 - H_1^-H_2^+)(H_1^{0*}H_2^{0*} - H_1^{-*}H_2^{+*}) \\ & + \frac{\lambda_5}{2}(H_1^0H_2^0 - H_1^-H_2^+)^2 + \text{c.c.} \\ & + \lambda_6(H_1^0H_2^0 - H_1^-H_2^+)(|H_1^0|^2 + |H_1^-|^2) + \text{c.c.} \\ & + \lambda_7(H_1^0H_2^0 - H_1^-H_2^+)(|H_2^0|^2 + |H_2^+|^2) + \text{c.c.} \end{aligned} \tag{2.5}$$

The previous expressions are valid for any two Higgs doublet model. In the MSSM we typically write the potential in a different form. It is customary to define the two MSSM doublets with a relative phase η extracted. This way we can argue later that the vacuum expectation values (vev's) of both doublets can be chosen real. See also the discussion in Appendix **??** for other options. We thus have the following definition:

$$H_u = e^{i\eta} \begin{pmatrix} H_u^+ \\ H_u^0 \end{pmatrix} \qquad H_d = \begin{pmatrix} H_d^0 \\ H_d^- \end{pmatrix}, \tag{2.6}$$

The MSSM Higgs potential is then given by [40]

$$\begin{aligned} V(H_u, H_d) = &(|\mu|^2 + m_{H_u}^2)(|H_u^0|^2 + |H_u^+|^2) \\ &+ (|\mu|^2 + m_{H_d}^2)(|H_d^0|^2 + |H_d^-|^2) \\ &+ \left[be^{i\eta}(H_u^+ H_d^- - H_u^0 H_d^0) + \text{c.c.} \right] \\ &+ \frac{1}{8}(g^2 + g'^2)\left(|H_u^0|^2 + |H_u^+|^2 - |H_d^0|^2 - |H_d^-|^2 \right)^2 \\ &+ \frac{1}{2} g^2 |H_u^+ H_d^{0*} + H_u^0 H_d^{-*}|^2. \end{aligned} \tag{2.7}$$

By comparing the potential in (2.5) to the MSSM potential, we can identify the following tree-level relations between the different parameters:

$$\begin{aligned} H_1 &= H_d & \lambda_1 &= \frac{1}{4}(g^2 + g'^2) \\ H_2 &= e^{i\eta} H_u & \lambda_2 &= \frac{1}{4}(g^2 + g'^2) \\ m_{11}^2 &= |\mu|^2 + m_{H_d}^2 & \lambda_3 &= \frac{1}{4}(g^2 - g'^2) \\ m_{12}^2 &= -b & \lambda_4 &= -\frac{1}{2} g^2 \\ m_{22}^2 &= |\mu|^2 + m_{H_u}^2 & \lambda_5 &= \lambda_6 = \lambda_7 = 0. \end{aligned} \tag{2.8}$$

We will use the relations for λ_i later as described in Chapter 5, when we switch between the different conventions used by the software packages that we use there. A more detailed discussion of the complex two Higgs doublet model and the MSSM, including loop-corrected expressions, can be found in e.g. Appendix A of ref. [44].

From here on we will focus solely on the MSSM potential (2.7). We first note that we have the freedom to use $SU(2)_L$ gauge rotations. We can use this to rotate away a possible vev for one of the weak isospin components, allowing us to take for example $H_u^+ = 0$ at the minimum of the potential (meaning $\langle H_u^+ \rangle = 0$). The requirement

$\frac{\partial V}{\partial H_u^+} = 0$ then results in $\langle H_d^- \rangle = 0$ as well. We can now simplify the potential to

$$\begin{aligned} V(H_u, H_d) = &(|\mu|^2 + m_{H_u}^2)|H_u^0|^2 + (|\mu|^2 + m_{H_d}^2)|H_d^0|^2 \\ &- \left[be^{i\eta}\, H_u^0 H_d^0 + \text{c.c.}\right] + \frac{1}{8}(g^2 + g'^2)(|H_u^0|^2 - |H_d^0|^2)^2. \end{aligned} \tag{2.9}$$

If the Higgs doublets acquire non-zero vev's, a spontaneous symmetry breaking will occur. We define $\langle H_u^0 \rangle = v_u$ and $\langle H_d^0 \rangle = v_d$, and the ratio of them as $\tan\beta = \frac{v_u}{v_d}$. Note that we have explicitly taken out a phase in our expansion, such that v_u and v_d are real.

For the potential to be viable, it has to be bounded from below. In general, this means that the quartic term proportional to $g^2 + g'^2$ has to be positive. For any values $|H_u^0| \neq |H_d^0|$ this requirement is trivially met, but in the special case where $|H_u^0| = |H_d^0|$ we have to impose the following additional requirement to ensure the potential is bounded from below

$$2|b| < 2|\mu|^2 + m_{H_u}^2 + m_{H_d}^2. \tag{2.10}$$

This condition must be satisfied at all energy scales.

In order to achieve EWSB through this Higgs potential we require that its minimum is stable and does not lie at the origin. As a result at least one of the linear combinations of H_u^0 and H_d^0 has to have a negative squared mass term. We can write this as an eigenvalue problem:

$$V_H^{\text{quadr.}} = (H_d^{0*}\ H_u^0) \begin{pmatrix} m_{H_d}^2 + |\mu|^2 & -b^* e^{-i\eta} \\ -be^{i\eta} & m_{H_u}^2 + |\mu|^2 \end{pmatrix} \begin{pmatrix} H_d^0 \\ H_u^{0*} \end{pmatrix}. \tag{2.11}$$

Solving for the eigenvalues leads to the inequality

$$|b|^2 > (m_{H_u}^2 + |\mu|^2)(m_{H_d}^2 + |\mu|^2). \tag{2.12}$$

Noteworthy is that we cannot satisfy both the requirements in equations (2.10) and (2.12) simultaneously in the case that $m_{H_u}^2 = m_{H_d}^2$. To have EWSB $m_{H_u}^2$ and $m_{H_d}^2$ cannot both be zero. Since $m_{H_u}^2$ and $m_{H_d}^2$ are SUSY breaking parameters, this means that EWSB and SUSY breaking are intrinsically connected in the MSSM.

The SM Higgs doublet vev v is related to the masses m_Z and m_W of the SM Z- and W-bosons. To keep the same values for the observed masses also in the extended Higgs sector of the MSSM, we require that v is related to v_u and v_d as $v^2 = v_u^2 + v_d^2$. This means at tree-level that [45]

$$v^2 = v_u^2 + v_d^2 = \frac{4m_Z^2}{g^2 + g'^2}. \tag{2.13}$$

With these observations and definitions we now expand the Higgs doublets of equation (2.6) around the vev's in the following manner

$$e^{i\eta}\begin{pmatrix} H_u^+ \\ H_u^0 \end{pmatrix} = \frac{e^{i\eta}}{\sqrt{2}}\begin{pmatrix} 0 \\ v_u + \phi_u + i\sigma_u \end{pmatrix}, \qquad \begin{pmatrix} H_d^0 \\ H_d^- \end{pmatrix} = \frac{1}{\sqrt{2}}\begin{pmatrix} v_d + \phi_d + i\sigma_d \\ 0 \end{pmatrix} \tag{2.14}$$

and minimize the potential by requiring

$$\frac{\partial V}{\partial \phi_{u,d}} = 0, \qquad \frac{\partial V}{\partial \sigma_{u,d}} = 0. \tag{2.15}$$

At this minimum we have $\phi_{u,d} = \sigma_{u,d} = 0$, such that $v_{u,d}$ really is the vev of $H_{u,d}$. Defining $b = |b|\exp(i\phi_b)$, we can write the equations resulting from (2.15) as

$$\begin{aligned} |\mu|^2 + m_{H_u}^2 - |b|\cot(\beta)\cos(\phi_b + \eta) - \frac{1}{2}m_Z^2\cos(2\beta) + \frac{1}{v_u}\frac{\partial V^{\text{corr}}}{\partial \phi_u} &= 0, \\ |\mu|^2 + m_{H_d}^2 - |b|\tan(\beta)\cos(\phi_b + \eta) + \frac{1}{2}m_Z^2\cos(2\beta) + \frac{1}{v_d}\frac{\partial V^{\text{corr}}}{\partial \phi_d} &= 0, \\ \sin(\phi_b + \eta)|b| + \frac{1}{v_d}\frac{\partial V^{\text{corr}}}{\partial \phi_u} = \sin(\phi_b + \eta)|b| + \frac{1}{v_u}\frac{\partial V^{\text{corr}}}{\partial \phi_d} &= 0. \end{aligned} \tag{2.16}$$

These are known as the tadpole equations. Note that V^{corr} is not the tree-level potential as defined in (2.9), but contains the higher-order corrections.

This set of equations determines the conditions for EWSB. The two equations on the last line are not independent, which is due to gauge symmetry. Also η and ϕ_b are not independent, since they always appear as the combination $\eta + \phi_b$, and hence at tree-level we simply have $\eta = -\phi_b$. As a result, CP violation only enters through higher-order corrections, meaning the Higgs boson mass eigenstates are also CP-eigenstates at tree level. We do not explicitly discuss the higher-order corrections here and instead refer the interested reader to e.g. the appendix A of [44].

Any valid MSSM model has to satisfy these tadpole equations. For a model with N free parameters, one often chooses only $N-3$ parameters as model input and uses the tadpole equations to fix the remaining three. This allows some freedom in which parameters to use as input and which are left to be fixed. We will discuss this freedom in more detail in section 2.3, and in Chapter 4 when we set up our numerical analysis.

2.2.1 Higgs boson eigenstates without CP violation

There are eight degrees of freedom associated with two complex Higgs doublets. Three of these represent Goldstone bosons, which become the longitudinal polarisation modes of the Z^0- and $W^\pm$-bosons after EWSB. The five remaining Higgs scalar mass eigenstates contain two charged scalars H^+ and H^-, and three neutral states. Especially for the neutral states, the relation between mass and gauge eigenstates

depends heavily on the presence of CPV. We will therefore start our discussion with a model that contains no new CPV compared to the SM.

When there are no new sources of CPV, all MSSM parameters can be chosen real. Then the tadpole equations of (2.16) simplify (at leading order) to

$$|\mu|^2 + m_{H_u}^2 - b\cot(\beta) - \frac{1}{2}m_Z^2\cos(2\beta) = 0, \tag{2.17}$$

$$|\mu|^2 + m_{H_d}^2 - b\tan(\beta) + \frac{1}{2}m_Z^2\cos(2\beta) = 0. \tag{2.18}$$

An important consequence is that neutral Higgs bosons are CP eigenstates, also at higher orders: we obtain the CP-even states h^0 and H^0 (by convention $m_{h^0} \leq m_{H^0}$) and the CP-odd pseudo-scalar A^0. The gauge eigenstates can then be expressed in terms of the mass eigenstates as follows

$$\begin{pmatrix} H_u^0 \\ H_d^0 \end{pmatrix} = \frac{1}{\sqrt{2}}\begin{pmatrix} v_u \\ v_d \end{pmatrix} + \frac{1}{\sqrt{2}}R_\alpha \begin{pmatrix} h^0 \\ H^0 \end{pmatrix} + \frac{i}{\sqrt{2}}R_{\beta_0}\begin{pmatrix} G^0 \\ A^0 \end{pmatrix}, \tag{2.19}$$

where G^0 is the neutral Goldstone boson. With $G^\pm$ denoting the charged Goldstone bosons, we can also write

$$\begin{pmatrix} H_u^+ \\ H_d^{-*} \end{pmatrix} = R_{\beta_\pm}\begin{pmatrix} G^+ \\ H^+ \end{pmatrix}, \tag{2.20}$$

where we have defined $G^- = G^{+*}$ and $H^- = H^{+*}$. The rotation matrices R_i are defined as

$$R_\alpha = \begin{pmatrix} \cos\alpha & \sin\alpha \\ -\sin\alpha & \cos\alpha \end{pmatrix} \tag{2.21}$$

for the CP-even states, where for the CP-odd and charged states we have

$$R_{\beta_0} = \begin{pmatrix} \sin\beta_0 & \cos\beta_0 \\ -\cos\beta_0 & \sin\beta_0 \end{pmatrix}, \qquad R_{\beta_\pm} = \begin{pmatrix} \sin\beta_\pm & \cos\beta_\pm \\ -\cos\beta_\pm & \sin\beta_\pm \end{pmatrix}. \tag{2.22}$$

For vev's that minimize the tree-level potential we find $\beta_\pm = \beta_0 = \beta$ and $m_{G^0}^2 = m_{G^\pm}^2 = 0$. This results in the following expressions for the masses of the Higgs bosons at tree-level

$$m_{A^0}^2 = \frac{2b}{\sin(2\beta)} = 2|\mu|^2 + m_{H_u}^2 + m_{H_d}^2, \tag{2.23}$$

$$m_{h^0,H^0}^2 = \frac{1}{2}\left(m_{A^0}^2 + m_Z^2 \mp \sqrt{(m_{A^0}^2 - m_Z^2)^2 + 4m_Z^2 m_{A^0}^2\sin^2(2\beta)}\right), \tag{2.24}$$

$$m_{H^\pm}^2 = m_{A^0}^2 + m_W^2. \tag{2.25}$$

The tree-level mixing angle α is given by

$$\frac{\sin(2\alpha)}{\sin(2\beta)} = \frac{m_{h^0}^2 + m_{H^0}^2}{m_{h^0}^2 - m_{H^0}^2}, \qquad \frac{\tan(2\alpha)}{\tan(2\beta)} = \frac{m_{A^0}^2 + m_Z^2}{m_{A^0}^2 - m_Z^2}. \tag{2.26}$$

The value of α is typically chosen to be negative, with a range of $-\pi/2 < \alpha < 0$ for $m_{A^0} > m_Z$. The value of β is determined by the Lagrangian parameters of the MSSM, resulting in $0 < \beta < \pi/2$ for real and positive vev's.

These expressions are all tree-level results. Explicitly deriving the loop corrections for these results goes beyond the scope of this thesis, so we refer the interested reader to e.g. [46]. Note that these loop corrections are implemented in the software we use in our studies (see Chapters 4 and 5).

From equation (2.24) it is possible to estimate the mass of h^0 at tree level as $m_{h^0} \leq m_Z$, but loop corrections (see e.g. [46] for a review) change this number quite drastically:

$$m_{h^0} \lesssim 135\text{GeV}. \tag{2.27}$$

We deduce that h^0 is typically the SM Higgs boson, unless the two CP-even Higgs bosons are very close in mass. This configuration is almost excluded by experiments [47]. Therefore the requirement $m_{h^0} \approx 125$ GeV can be used to constrain the parameters of the model [44, 48, 49].

The opposite situation occurs when the phenomenology of the second Higgs boson H^0 (almost) completely decouples from the SM Higgs boson h^0. This happens when the couplings of h^0 to SM bosons and fermions are (almost) the same as the relevant SM Higgs boson couplings g^{SM}. For bosonic couplings we can express the h^0 and H^0 couplings in terms of the SM Higgs boson h, and the mixing angles α and β as follows [41]

$$g_{h^0VV^\dagger} = g^{\text{SM}}_{hVV^\dagger} \times \sin(\beta - \alpha), \tag{2.28}$$

$$g_{H^0VV^\dagger} = g^{\text{SM}}_{hVV^\dagger} \times \cos(\beta - \alpha). \tag{2.29}$$

Here we use $VV^\dagger$ to denote Z^0Z^0 or W^+W^-. We see that we can obtain the SM coupling in the limit $\alpha \to \beta - \pi/2$, because then only the h^0-coupling remains as g^{SM}.

Something similar happens for the couplings to fermions, where we have the fol-

lowing couplings in terms of g^{SM}

$$g_{h^0 b\bar{b}}, g_{h^0 \tau^+ \tau^-} \propto -\frac{\sin(\alpha)}{\cos(\beta)} = \sin(\beta-\alpha) - \tan(\beta)\cos(\beta-\alpha), \tag{2.30}$$

$$g_{h^0 t\bar{t}} \propto \frac{\cos(\alpha)}{\sin(\beta)} = \sin(\beta-\alpha) + \cot(\beta)\cos(\beta-\alpha), \tag{2.31}$$

$$g_{H^0 b\bar{b}}, g_{H^0 \tau^+ \tau^-} \propto \frac{\cos(\alpha)}{\cos(\beta)} = \cos(\beta-\alpha) + \tan(\beta)\sin(\beta-\alpha), \tag{2.32}$$

$$g_{H^0 t\bar{t}} \propto \frac{\sin(\alpha)}{\sin(\beta)} = \cos(\beta-\alpha) - \cot(\beta)\sin(\beta-\alpha). \tag{2.33}$$

If we take again the limit $\alpha \to \beta - \pi/2$ we find

$$\begin{aligned} g_{h^0 b\bar{b}},\ g_{h^0 \tau^+ \tau^-} &\propto g^{\mathrm{SM}}_{hb\bar{b}} \times 1, g^{\mathrm{SM}}_{h\tau^+ \tau^-} \times 1, \\ g_{h^0 t\bar{t}} &\propto g^{\mathrm{SM}}_{ht\bar{t}} \times 1, \\ g_{H^0 b\bar{b}},\ g_{H^0 \tau^+ \tau^-} &\propto g^{\mathrm{SM}}_{hb\bar{b}} \times \tan\beta, g^{\mathrm{SM}}_{h\tau^+ \tau^-} \times \tan\beta, \\ g_{H^0 t\bar{t}} &\propto g^{\mathrm{SM}}_{ht\bar{t}} \times -\cot\beta, \end{aligned} \tag{2.34}$$

such that again the h^0-couplings resemble the SM Higgs couplings very closely and the effect of H^0 differs by $\tan\beta$ and $1/\tan\beta$ factors for down-type and up-type fermions respectively. Since $\tan\beta$ is allowed to be substantially larger than unity in the MSSM, the hierarchy of the H^0-fermion couplings can be altered drastically with respect to the SM couplings. In a sense, the new physics that results from the second Higgs doublet decouples from the SM-like Higgs physics. This happens when $m_{A^0} \gg m_Z$, which is called the decoupling limit, as this implies $m_{H^0}, m_{A^0}, m_{H^\pm} \gg m_{h^0}$ and therefore a decoupling between the SM-like, light Higgs boson h^0 and the other Higgs bosons. We will study this scenario in more detail in Chapter 4, when we encounter it in our Δa_μ study.

2.3 The pMSSM

Instead of exploring the full MSSM with 105 free soft-SUSY breaking parameters, we will focus on more constrained models. The first is the pMSSM [50], which is derived from the MSSM by adding the following requirements:

- There are no new sources of CP violation;
- The first and second generation squark and slepton masses are degenerate;
- The sfermion mass matrices are diagonal;
- All trilinear couplings of the first and second generation sfermions are set to zero.

These requirements limit the MSSM in such a way that there is no new CP violation beyond the SM (first requirement) and flavour violation is minimised (third requirement) since there are strong upper bounds on this [51]. The other two constraints are motivated experimentally by rare decays, such as $\mu^- \to e^-\gamma$, $B_s \to s\gamma$ and $\tau^- \to \mu^-\gamma$, and minimise meson mixing effects through off-diagonal terms. They are also necessary to limit the number of free parameters to a manageable amount.

We have now reduced the number of free soft-SUSY breaking parameters to 19, that are shown in Table 2.2. With these constraints we obtain the Higgs sector as described above, since there is no additional CPV. With the soft-SUSY breaking

Symbol	Parameter description
$m_{\widetilde{Q}_1}$	Left-handed squark masses of the first and second generation
$m_{\widetilde{u}_R}$	Right-handed up-type squark masses of the first and second generation
$m_{\widetilde{d}_R}$	Right-handed down-type squark masses of the first and second generation
$m_{\widetilde{Q}_3}$	Left-handed squark mass of the third generation
$m_{\widetilde{t}_R}$	Right-handed top-squark mass
$m_{\widetilde{b}_R}$	Right-handed bottom-squark mass
$m_{\widetilde{L}_1}$	Left-handed slepton masses of the first and second generation
$m_{\widetilde{e}_R}$	Right-handed slepton masses of the first and second generation
$m_{\widetilde{L}_3}$	Left-handed slepton mass of the third generation
$m_{\widetilde{\tau}_R}$	Right-handed stau mass
M_1, M_2, M_3	Masses of the bino, wino and gluino
A_t, A_b, A_τ	Trilinear couplings for stop, sbottom and stau
$\tan(\beta)$	Ratio of the vacuum expectation values of the Higgs doublets
$m^2_{H_u}, m^2_{H_d}$	Soft squared Higgs masses

Table 2.2 The free soft-SUSY breaking parameters of the pMSSM.

parameters and the tadpole equations from (2.17), one can calculate the other two model parameters: $|\mu|$ and b. However, it is also possible to use $|\mu|$ and/or b as a free parameter if we sacrifice one of the 19 soft-SUSY breaking parameters in Table 2.2. In principle it is possible to take any four parameters from the set $m^2_{H_u}$, $m^2_{H_d}$, $\tan\beta$, b, $|\mu|$ and m_Z as free parameters and use the tadpole equations to determine the other two.[3] Using the relation (2.23) between m_{A^0}, b and $\tan\beta$, one can even use m_{A^0} as input parameter of the theory, although it is not a priori a parameter of the model. In the pMSSM a common choice is to take b and m_{A^0} as the parameters that will be fixed by the tadpole equations, as this allows us to use the resulting value of m_Z as a

[3] Note that the sign of μ always has to be specified as input, as it cannot be determined with the tadpole equations.

confirmation that the spectrum converges to a sensible result when we do a numerical analysis. We will discuss the parameters of the model in more detail in Chapter 4, when we set up the analysis.

2.4 pMSSM with CP violation: the cpMSSM

To study CP violating observables, the pMSSM is not a suitable model as it contains no new phenomenology compared to the SM for this sector. We will therefore look at a pMSSM-like model, where the requirement of no additional CPV has been lifted. The other requirements remain.

As a result, nine parameters can in principle obtain a non-zero CP violating phase: the gaugino masses M_1, M_2 and M_3, the trilinear couplings A_t, A_b and A_τ, the Higgs mass parameter μ, the soft-breaking parameter b and finally the Higgs doublets may gain a relative phase that we will denote by η. However, only 6 of these phases are independent.

Firstly, we observe that there are two left-over symmetries $U(1)$ in the MSSM Lagrangian. We can define two $U(1)$ as

$$\phi \to e^{iQ_A\omega_A}\phi, \qquad \phi \to e^{iQ_B\omega_B}\phi \tag{2.35}$$

for charges Q_A and Q_B under the $U(1)_A$ and $U(1)_B$ rotation respectively [20, 21, 52]. These rotations leave the Lagrangian invariant if we use the charges as listed in Table 2.3 and at the same time perform the following parameter transformations:

$$\begin{aligned} \mu &\to e^{2i(\omega_A+\omega_B)}\mu, \\ b &\to e^{4i\omega_A}b, \\ M_j &\to e^{2i(\omega_A-\omega_B)}M_j, \\ A_k &\to e^{2i(\omega_A-\omega_B)}A_k. \end{aligned} \tag{2.36}$$

Sparticles	Q_A	Q_B	Particles	Q_A	Q_B
sfermions	0	1	fermions	1	0
higgsinos	-1	-1	Higgs bosons	-2	0
gauginos	-1	1	gauge bosons	0	0

Table 2.3 The charges of the SM and MSSM particles under the $U(1)_A$ and $U(1)_B$ transformations, such that the MSSM Lagrangian (including soft-SUSY breaking terms) remains invariant. Note that for fermionic fields and sfermionic superpartner fields the given charges are for left-handed components, the right-handed components have opposite charges.

This allows us to rotate away two of the phases in the cpMSSM, for example the phases of b and μ, or the phases of b and M_3 are typical choices. The tadpole equations also fix three parameters of the cpMSSM, including one phase. Note also the discussion in Appendix A.2, as it is important to be careful in the treatment of η and b.

Similar to the pMSSM, we have freedom to choose which parameters are treated as free parameters and which parameters will be fixed by the tadpole equations. An important difference is that m_{A^0} cannot be used, since the Higgs sector of the cpMSSM does not contain a particle that we can identify as A^0. In Table 2.4 we show an overview of all the cpMSSM parameters, of which 25 are free (compared to 19 in the pMSSM).

Real parameters							Phases		
$m_{\widetilde{Q}_1}$	$m_{\widetilde{Q}_3}$	$m_{\widetilde{L}_1}$	$m_{\widetilde{L}_3}$	$\tan(\beta)$	$\lvert M_1\rvert$	$\lvert A_t\rvert$	ϕ_{M_1}	ϕ_{A_t}	η
$m_{\widetilde{u}_R}$	$m_{\widetilde{t}_R}$	$m_{\widetilde{e}_R}$	$m_{\widetilde{\tau}_R}$	$\lvert b\rvert$	$\lvert M_2\rvert$	$\lvert A_b\rvert$	ϕ_{M_2}	ϕ_{A_b}	ϕ_b
$m_{\widetilde{d}_R}$	$m_{\widetilde{b}_R}$	$m^2_{H_d}$	$m^2_{H_u}$	$\lvert\mu\rvert$	$\lvert M_3\rvert$	$\lvert A_\tau\rvert$	ϕ_{M_3}	ϕ_{A_τ}	ϕ_μ

Table 2.4 The total set of cpMSSM parameters: 21 pMSSM parameters and 9 new CP violating phases. Note that the tadpole equations (2.16) fix three of these parameters and we can rotate away two additional phases, so only 25 parameters are independent.

There are a lot of similarities between the pMSSM and the cpMSSM. Apart from the Higgs sector, the supersymmetric particle content of both models is the same, although there are relevant differences in the mixing matrices. We will therefore describe these sparticles and their mixing in a general way, with special attention paid to the most important differences between the pMSSM and cpMSSM. The Higgs sector deserves a separate treatment to explain the relevant differences between the two models.

Higgs sector

The Higgs sector changes significantly when CPV is allowed. In the pMSSM we can identify two CP-even Higgs bosons and one CP-odd Higgs boson, which do not mix. However, CP violation causes mixing between the CP eigenstates at higher orders. We can therefore no longer identify a CP-odd or CP-even Higgs boson beyond tree level. Instead, we define the three neutral Higgs bosons as H_1^0, H_2^0 and H_3^0, with $m_{H_1} < m_{H_2} < m_{H_3}$ by definition.

A large CP violating component would impact the decay of the lightest neutral Higgs boson H_1^0 into the weak gauge bosons $W^\pm$ and Z^0. So far there have been no observations of Higgs boson decays that differ significantly from the SM values [47]. Therefore the mixing of the CP-even and odd states is limited; the pseudo-scalar (or

A^0) component of the SM-like Higgs boson is limited to roughly 10%, depending on the other model parameters [53].

The gauge eigenstates can be defined as

$$\phi^0 = \left(\sqrt{2}(\mathrm{Re}\{H_d^0 - v_d/\sqrt{2}\}, \mathrm{Re}\{H_u^0 - v_u/\sqrt{2}\}, \mathrm{Im}(H_d^0), \mathrm{Im}(H_u^0))^T\right), \tag{2.37}$$

which still includes the neutral Goldstone boson. We can then define their mixing as follows [54]

$$-\phi^{0T}\mathcal{M}^2_{\phi^0}\phi^0 = -\phi^{0T}S^T S^* \mathcal{M}^2_{\phi^0} S^\dagger S\phi^0. \tag{2.38}$$

The mixing matrix S gives the decomposition of the three physical mass eigenstates in terms of the four interaction eigenstates, in such a way that the Goldstone boson G^0 is explicitly projected out.

We can define S in two ways, depending on the convention. One way is to define a rotation matrix $\mathcal{R}$ giving the decomposition of the three physical mass eigenstates in terms of the intermediate basis $\tilde{\Phi}^0 = (h^0, H^0, A^0)^T_{tree}$ of the tree-level mass eigenstates. We can also define the matrix $\mathcal{O}$ that gives the decomposition of the three physical mass eigenstates in terms of the intermediate basis $\tilde{\phi}^0 = (\sqrt{2}\mathrm{Re}\{H_d^0 - v_d/\sqrt{2}\}, \sqrt{2}\mathrm{Re}\{H_u^0 - v_u/\sqrt{2}\}, A^0_{tree})^T$.[4] We can then write

$$S\phi^0 = \begin{pmatrix} & & 0 \\ \mathcal{R}_{3x3} & & 0 \\ & & 0 \end{pmatrix} \begin{pmatrix} -\sin\alpha & \cos\alpha & 0 & 0 \\ \cos\alpha & \sin\alpha & 0 & 0 \\ 0 & 0 & \sin\beta & \cos\beta \\ 0 & 0 & -\cos\beta & \sin\beta \end{pmatrix} \phi^0 \tag{2.39}$$

$$\equiv \begin{pmatrix} & & 0 \\ \mathcal{O}_{3x3} & & 0 \\ & & 0 \end{pmatrix} \begin{pmatrix} 1 & 0 & 0 & 0 \\ 0 & 1 & 0 & 0 \\ 0 & 0 & \sin\beta & \cos\beta \\ 0 & 0 & -\cos\beta & \sin\beta \end{pmatrix} \phi^0, \tag{2.40}$$

where the conversion between $\mathcal{R}$ and $\mathcal{O}$ is given by

$$\begin{pmatrix} & & 0 \\ \mathcal{O}_{3x3} & & 0 \\ & & 0 \end{pmatrix} = \begin{pmatrix} -\mathcal{R}_{11}\sin\alpha + \mathcal{R}_{12}\cos\alpha & \mathcal{R}_{11}\cos\alpha + \mathcal{R}_{12}\sin\alpha & \mathcal{R}_{13} & 0 \\ -\mathcal{R}_{21}\sin\alpha + \mathcal{R}_{22}\cos\alpha & \mathcal{R}_{21}\cos\alpha + \mathcal{R}_{22}\sin\alpha & \mathcal{R}_{23} & 0 \\ -\mathcal{R}_{31}\sin\alpha + \mathcal{R}_{32}\cos\alpha & \mathcal{R}_{31}\cos\alpha + \mathcal{R}_{32}\sin\alpha & \mathcal{R}_{33} & 0 \end{pmatrix}. \tag{2.41}$$

In this thesis we will adopt the conventions of [55] and use $O = \mathcal{O}^T$ to relate the gauge and mass eigenstates, since this gives consistent expressions for the eEDM contributions in Section 3.1.2 and the given references. Note that we also use the software package FeynHiggs, where the convention is to use $\mathcal{R}$ for the mixing.

[4] Note the difference in convention with respect to [54]: we use $H_d = i\sigma^2\phi_1^*$ and therefore obtain different minus sign conventions in the definition of S.

2.4.1 Sparticle content and mixing

We have seen that the Higgs sector of the pMSSM and that of the cpMSSM are intrinsically different. Next, we turn to the supersymmetric particle content of these models. Here the mixing does not depend on CPV as intrinsically as in the Higgs sector, so we describe it in terms of complex parameters, which are taken real in the pMSSM. However, the phase η between the cpMSSM Higgs boson doublets affects the superpartners of the Higgs bosons as well. The chosen convention for η is often not clear in the literature. See also the discussion in Appendix A.2 on possible conventions.

We present the tree-level expressions for the sparticle mixing matrices, based on [40]. Beyond tree level the masses are sensitive to radiative corrections from SUSY particles. This makes it difficult to give general expressions, as the corrections themselves depend on the sparticle spectrum. This is one of the motivations behind spectrum generators to do analyses in a SUSY framework.

The neutral superpartners of the Higgs, the neutral higgsinos, mix together with the bino and neutral wino to form four different neutralinos $\widetilde{\chi}_1^0, \widetilde{\chi}_2^0, \widetilde{\chi}_3^0, \widetilde{\chi}_4^0$. The charged higgsinos and winos form two doubly degenerate charginos $\widetilde{\chi}_1^\pm, \widetilde{\chi}_2^\pm$. Finally also the sfermions mix, but this is restricted to one generation as flavour mixing is explicitly minimised in the pMSSM. Typically the L-R mixing occurs mainly in the third generation sfermions, for the first and second generation we can safely assume that $\widetilde{f}_L = \widetilde{f}_1$ and $\widetilde{f}_R = \widetilde{f}_2$ (or vice versa).

Neutralino mixing

In the basis of the Majorana fields $(\widetilde{B}, \widetilde{W}^0, \widetilde{H}_d^0, \widetilde{H}_u^0)$ the mass term of the neutralinos is given by

$$\mathcal{L} = -\frac{1}{2}\bar{\psi^0}\, M_{\widetilde{\chi}^0}\, P_L \psi^0 + \text{h.c.} \tag{2.42}$$

where $\bar{\psi^0} = (\bar{\widetilde{B}}, \bar{\widetilde{W}}^0, \bar{\widetilde{H}}_d^0, \bar{\widetilde{H}}_u^0)$. The mass matrix is then given by

$$M_{\widetilde{\chi}^0} = \begin{pmatrix} M_1 & 0 & -g' v_d/2 & g' v_u e^{-i\eta}/2 \\ 0 & M_2 & g v_d/2 & -g v_u e^{-i\eta}/2 \\ -g' v_d/2 & g v_d/2 & 0 & -\mu \\ g' v_u e^{-i\eta}/2 & -g v_u e^{-i\eta}/2 & -\mu & 0 \end{pmatrix}. \tag{2.43}$$

We can diagonalise the mass matrix by means of a unitary matrix N as

$$N^* M_{\widetilde{\chi}^0} N^{-1} = M_{\widetilde{\chi}^0}^{\text{diag}}. \tag{2.44}$$

In the pMSSM we can choose N to be a real and orthogonal matrix if we accept negative mass terms. This is common practice in the literature, so we will adopt the same convention. Note that one can always rotate the negative masses away

through chiral rotations, so this does not imply negative masses for the neutralinos. By definition we have mass ordering in this sector: $m_{\widetilde{\chi}_1^0} \leq m_{\widetilde{\chi}_2^0} \leq m_{\widetilde{\chi}_3^0} \leq m_{\widetilde{\chi}_4^0}$.

In the cpMSSM the terms proportional to M_1, M_2 and μ give rise to complex entries in the mixing matrix. In our conventions, also $e^{-i\eta}$ is complex. However, note that a typical choice is to take $\phi_b = 0$, resulting in $\eta = 0$ at tree level due to the tadpole equations. Therefore the factor $e^{-i\eta}$ is often removed in tree-level expressions. We opt to show it here, as we will work in a general scenario in Chapter 5.

In both models all neutralinos are colour and charge neutral, which makes $\widetilde{\chi}_1^0$ a DM candidate if it is the LSP. In particular for DM experiments, it is relevant what the composition of the LSP and the other neutralinos is in terms of the gauge eigenstates. We can determine this through the entries of N. The amount of bino, wino and higgsino mixing of the lightest neutralino is given by $|N_{11}|$, $|N_{12}|$ and $\sqrt{|N_{13}|^2 + |N_{14}|^2}$, respectively.

In general we expect the two lightest neutralinos to be dominantly gaugino for $|\mu| \gg |M_{1,2}| \gg M_Z$, where the heavier neutralinos are then mostly higgsino. This situation is reversed for $|\mu| \ll |M_{1,2}|$: then the lightest neutralinos will be mostly higgsino and the heaviest will be dominantly gaugino. Note that this is only true for parameters much larger than m_Z. If the values are close to m_Z we will see much more mixing. The composition of the neutralinos and charginos is very important for experimental exclusion power, as we will discuss in more detail in Chapters 4 and 5.

Chargino mixing

The charginos, denoted by $\widetilde{\chi}_i^\pm$ with $i = 1, 2$, are the charged mass eigenstates of the wino and higgsino interaction eigenstates, with $\widetilde{\chi}_1^\pm$ the lightest chargino.

We define the Dirac adjoint of the charge conjugated field, $(\overline{\psi^\pm})^C$ (suppressing the tildes for readability) as $(\overline{\psi^\pm})^C = \left((\overline{W^+})^C, (\overline{H_u^+})^C, (\overline{W^-})^C, (\overline{H_d^-})^C\right)$ such that the mass term is given by

$$\mathcal{L} = -\frac{1}{2}(\overline{\psi^\pm})^C M_{\widetilde{C}}\, P_L \psi^\pm + \text{h.c.} \tag{2.45}$$

for a 2×2 block form

$$M_{\widetilde{C}} = \begin{pmatrix} 0 & M_{\widetilde{\chi}^\pm}^T \\ M_{\widetilde{\chi}^\pm} & 0 \end{pmatrix}. \tag{2.46}$$

Then the chargino mass matrix at tree level reads

$$M_{\widetilde{\chi}^\pm} = \begin{pmatrix} M_2 & g v_u e^{-i\eta}/\sqrt{2} \\ g v_d/\sqrt{2} & \mu \end{pmatrix}. \tag{2.47}$$

We can find unitary matrices U and V such that the mass matrix $M_{\widetilde{\chi}^\pm}$ is diagonalised with positive real entries by $U^* M_{\widetilde{\chi}^\pm} V^{-1}$. Note that also in these mixing matrices the

phase η can be chosen to be 0 at tree level, although this is not our convention. The mass eigenstates of the positively (negatively) charged charginos are related to V (U) as

$$\begin{pmatrix} \widetilde{\chi}_1^+ \\ \widetilde{\chi}_2^+ \end{pmatrix} = V \begin{pmatrix} \widetilde{W}^+ \\ \widetilde{H}_u^+ \end{pmatrix}, \qquad \begin{pmatrix} \widetilde{\chi}_1^- \\ \widetilde{\chi}_2^- \end{pmatrix} = U \begin{pmatrix} \widetilde{W}^- \\ \widetilde{H}_d^- \end{pmatrix}. \tag{2.48}$$

The composition of the lightest chargino is predominantly higgsino when $m_Z \ll |\mu| \ll |M_2|$, predominantly wino when $m_Z \ll |M_2| \ll |\mu|$, or a mixture when the two parameters are close in value. An overview of the relative values of $|M_1|$, $|M_2|$ and $|\mu|$, and the resulting composition of the neutralinos and charginos is given in Table 2.5.

Parameter hierarchy	Chargino composition $\widetilde{\chi}_1^\pm, \widetilde{\chi}_2^\pm$	Neutralino composition $\widetilde{\chi}_1^0, \widetilde{\chi}_2^0, \widetilde{\chi}_3^0, \widetilde{\chi}_4^0$
$\lvert M_1\rvert < \lvert M_2\rvert < \lvert\mu\rvert$	$\widetilde{W}, \widetilde{H}$	$\widetilde{B}, \widetilde{W}, \widetilde{H}, \widetilde{H}$
$\lvert M_2\rvert < \lvert M_1\rvert < \lvert\mu\rvert$	$\widetilde{W}, \widetilde{H}$	$\widetilde{W}, \widetilde{B}, \widetilde{H}, \widetilde{H}$
$\lvert M_2\rvert < \lvert\mu\rvert < \lvert M_1\rvert$	$\widetilde{W}, \widetilde{H}$	$\widetilde{W}, \widetilde{H}, \widetilde{H}, \widetilde{B}$
$\lvert M_1\rvert < \lvert\mu\rvert < \lvert M_2\rvert$	$\widetilde{H}, \widetilde{W}$	$\widetilde{B}, \widetilde{H}, \widetilde{H}, \widetilde{W}$
$\lvert\mu\rvert < \lvert M_1\rvert < \lvert M_2\rvert$	$\widetilde{H}, \widetilde{W}$	$\widetilde{H}, \widetilde{H}, \widetilde{B}, \widetilde{W}$
$\lvert\mu\rvert < \lvert M_2\rvert < \lvert M_1\rvert$	$\widetilde{H}, \widetilde{W}$	$\widetilde{H}, \widetilde{H}, \widetilde{W}, \widetilde{B}$

Table 2.5 Rules of thumb for the dominant component in the chargino and neutralino composition for different parameter hierarchies in the set $|M_1|$, $|M_2|$ and $|\mu|$. Note that this is only true for parameters much larger than m_Z, otherwise there is much more mixing.

Sfermion mixing

We can define a six component vector for the sfermions as

$$\widetilde{\mathbf{f}} = \begin{pmatrix} \widetilde{f}_L \\ \widetilde{f}_R \end{pmatrix}, \tag{2.49}$$

where the sfermions $\tilde{f}$ can be the charged sleptons, up-type squarks or down-type squarks. The vectors $\widetilde{f}_L$ and $\widetilde{f}_R$ have three components each, for the three different generations. The mass terms can then be collected as

$$-\mathcal{L}_{\text{sfermion}} = \sum_{\tilde{f}} \widetilde{f}^\dagger \mathcal{M}^2_{\tilde{f}} \widetilde{f}, \tag{2.50}$$

where we can recognise the following general structure in the mass matrix

$$\mathcal{M}^2_{\tilde{f}} = \begin{pmatrix} \mathcal{M}^2_{\tilde{f}_{LL}} & \mathcal{M}^2_{\tilde{f}_{LR}} \\ \mathcal{M}^{2\dagger}_{\tilde{f}_{LR}} & \mathcal{M}^2_{\tilde{f}_{RR}} \end{pmatrix}. \tag{2.51}$$

Here we have defined $\mathcal{M}^{2\dagger}_{\tilde{f}_{LR}} = \mathcal{M}^2_{\tilde{f}_{RL}}$. The two matrices $\mathcal{M}^2_{\tilde{f}_{LL}}$ and $\mathcal{M}^2_{\tilde{f}_{RR}}$ are hermitian in generation space and the total matrix $\mathcal{M}^2_{\tilde{f}}$ is hermitian as well.

So far we have not made any assumptions regarding the sfermions. However, in the (c)pMSSM we explicitly assume no flavour mixing. We can therefore recast these expressions in 2×2 form and study each generation by itself. We can then specify mass matrices for the different types of sfermions as follows.

The slepton mass matrix $M^2_{\tilde{l}}$ reads in the $(\tilde{l}_L, \tilde{l}_R)$ basis

$$M^2_{\tilde{l}} = \begin{pmatrix} m^2_{\tilde{L}_i} - \left(\frac{1}{2} - s^2_{\theta_W}\right) M_Z^2 \cos(2\beta) + m_l^2 & m_l(A_l^* - \mu e^{i\eta} \tan\beta) \\ m_l(A_l - \mu^* e^{-i\eta} \tan\beta) & m^2_{\tilde{l}_R} - s^2_{\theta_W} M_Z^2 \cos(2\beta) + m_l^2 \end{pmatrix}. \tag{2.52}$$

Here $m^2_{\tilde{L}_i}, m^2_{\tilde{l}_R}$ is $m^2_{\tilde{L}_1}, m^2_{\tilde{e}_R}$ for the first and second generation, and $m^2_{\tilde{L}_3}, m^2_{\tilde{\tau}_R}$ for the third generation.

For the third generation, the up-type squark mass matrix $M^2_{\tilde{t}}$ reads in the $(\tilde{t}_L, \tilde{t}_R)$ basis

$$M^2_{\tilde{t}} = \begin{pmatrix} m^2_{\tilde{Q}_3} + \left(\frac{1}{2} - \frac{2}{3} s^2_{\theta_W}\right) M_Z^2 \cos(2\beta) + m_t^2 & m_t(A_t^* e^{-i\eta} - \mu \cot\beta) \\ m_t(A_t e^{i\eta} - \mu^* \cot\beta) & m^2_{\tilde{t}_R} + \frac{2}{3} s^2_{\theta_W} M_Z^2 \cos(2\beta) + m_t^2 \end{pmatrix}. \tag{2.53}$$

For the squarks of the first and second generation we find a similar matrix, where $m^2_{\tilde{Q}_3}, m^2_{\tilde{t}_R}$ is replaced with $m^2_{\tilde{Q}_1}, m^2_{\tilde{u}_R}$ and m_t is replaced with either m_u for the first and m_c for the second generation. As only the trilinear coupling of the third generation is non-zero in the (c)pMSSM, the corresponding matrices for the first and second generations lack the terms proportional to A_u, A_c.

Similarly, the down-type squark mass matrix $M^2_{\tilde{b}}$ reads in the $(\tilde{b}_L, \tilde{b}_R)$ basis

$$M^2_{\tilde{b}} = \begin{pmatrix} m^2_{\tilde{Q}_3} - \left(\frac{1}{2} - \frac{1}{3} s^2_{\theta_W}\right) M_Z^2 \cos(2\beta) + m_b^2 & m_b(A_b^* - \mu e^{i\eta} \tan\beta) \\ m_b(A_b - \mu^* e^{-i\eta} \tan\beta) & m^2_{\tilde{b}_R} - \frac{1}{3} s^2_{\theta_W} M_Z^2 \cos(2\beta) + m_b^2 \end{pmatrix}. \tag{2.54}$$

For the squarks of the first and second generation we find a similar matrix, where $m^2_{\tilde{Q}_3}, m^2_{\tilde{b}_R}$ is replaced with $m^2_{\tilde{Q}_1}, m^2_{\tilde{d}_R}$ and m_b is replaced with either m_d for the first and m_s for the second generation. As only the trilinear coupling of the third generation is non-zero in the (c)pMSSM, the corresponding matrices for the first and second generations lack the terms proportional to A_b, A_s.

Note that for the first and second generation the masses of the SM fermions are small compared to the SUSY parameters. They are therefore orders of magnitude smaller than the diagonal terms, which means there is hardly any L-R mixing for these generations. We do take the terms into account, as their relative importance can be as big as 10^{-4}, which makes them relevant enough for our calculations to include them. Since there is hardly any L-R mixing for the first and second generation, we can

define the mass eigenstates in terms of L,R eigenstates, e.g. $(\widetilde{e}_1, \widetilde{e}_2) = (\widetilde{e}_L, \widetilde{e}_R)$, and similarly for the other first and second generation squarks and sleptons. However, for the third generation the masses of the SM fermions are in fact large enough to induce significant mixing. We will always write the mass eigenstates of the third generation as $(\widetilde{\tau}_1, \widetilde{\tau}_2)$, $(\widetilde{t}_1, \widetilde{t}_2)$ and $(\widetilde{b}_1, \widetilde{b}_2)$ where the mass of the first sfermion is defined to be smaller than the mass of the second sfermion. As a result of the large mixing in the third generation, the $\widetilde{t}_1$ can in principle be the lightest sfermion.

We can diagonalise either of these sfermion mass matrices with unitary matrices $X^{\tilde{f}}$ as follows

$$(M^{\text{diag}}_{\tilde{f}})^2 = X^{\tilde{f}} M^2_{\tilde{f}} X^{\tilde{f}\dagger}. \tag{2.55}$$

The matrix $X^{\tilde{f}}$ is different for the up-type squarks, down-type squarks and the sleptons, and for the first and second generation versus the third generation. In this context, we also note that we have defined our theory such that the trilinear couplings A_l, A_u and A_d are zero for the first and second generation.

Note that it is the daggered 6×6 matrix $W^{\tilde{f}\dagger}$, not X, that is defined in [40] to diagonalise the mass matrix $\mathcal{M}^2_{\tilde{f}}$. In the equations for the couplings in Appendix A.4 we compare different conventions and rewrite this to the 2×2 matrices X.

After having defined the conventions of two supersymmetric models in this chapter, we can take a closer look at the observables that we want to study in the pMSSM and cpMSSM.

Chapter 3

Observables in the pMSSM and cpMSSM

In this chapter we will connect the (c)pMSSM as described in Chapter 2 to measurable observables: the anomalous magnetic moment of the muon, the electric dipole moment of the electron and dark matter observables such as Ωh^2 and $\langle \sigma v \rangle$. We will also study different measures of fine-tuning to see how fine-tuned the resulting spectrum and eEDM is for a chosen set of parameters in each model.

3.1 Electric and magnetic moments of leptons

We have chosen to focus our studies on two observables: the EDM of the electron and the anomalous magnetic moment of the muon (a_μ). We will see that they are closely related and each of them is an important BSM observable. The muon anomalous magnetic moment is important mainly because there exists a long-standing discrepancy between experiment and theory. We will investigate this discrepancy in an elaborate study in the pMSSM, combining it with DM and LHC limits.

The experimental limit on the eEDM is currently several orders of magnitude away from being sensitive to the SM prediction, but it can be used to constrain the CP-violating sector of BSM theories such as the cpMSSM. A typical claim is that the experimental lack of observing an eEDM results in either very large sparticle masses (at least of $\mathcal{O}$(TeV)) or very small phases [56–58]. However, this research is mostly done on supersymmetric models that are much more constrained than the cpMSSM. The same is true for the claim that the current limit constrains supersymmetric theories enough that they can no longer be called natural [25, 26, 59].

We will investigate the constraints resulting from the eEDM limit in the cpMSSM. We believe this is the most suitable model, as the pMSSM is the commonly accepted phenomenological supersymmetric framework for studies without CPV. To study the eEDM and Δa_μ we will first look into the definitions and (c)pMSSM contributions.

Both the magnetic moment and EDM represent an interaction of a particle's spin with the electromagnetic field (or separately the magnetic field $\vec{B}$ and electric field $\vec{E}$). We can express this classically in terms of the Hamiltonian

$$H = -\vec{\mu} \cdot \vec{B} - \vec{d} \cdot \vec{E}, \tag{3.1}$$

where we define the electric dipole $\vec{d}$ and magnetic moment $\vec{\mu}$ for a lepton l as

$$\vec{d_l} = d_l \vec{\sigma} = 2 d_l \vec{S}, \tag{3.2}$$

$$\vec{\mu}_l = g_l \frac{q_l}{2m_l} \vec{S} = g_l \frac{-e}{2m_l} \vec{S}, \tag{3.3}$$

and where $\vec{S} = \vec{\sigma}/2$ is the spin of the particle in terms of the Pauli spin matrices. We have expressed the magnetic moment in terms of the g-factor g [2, 45]. For a lepton we predict that the g-factor without quantum corrections is the tree-level QED value: $g_l = 2$.

We are interested in the anomalous magnetic moment, which is defined as the deviation from the tree-level result:

$$a_l = \frac{g_l - 2}{2}. \tag{3.4}$$

When using a QFT framework we can rewrite the Hamiltonian of equation (3.1) to obtain the following (effective) Lagrangian density for a lepton field ψ [2]

$$\mathcal{L} = \frac{1}{2}\bar{\psi}\sigma_{\nu\rho}\left(\frac{a_l e}{2m_l} - i\gamma_5 d_l\right)\psi F^{\nu\rho}. \tag{3.5}$$

Here we have defined $\sigma^{\mu\nu}$ as the commutation relation $\frac{i}{2}[\gamma^\mu, \gamma^\nu]$ of the Dirac gamma matrices and $F^{\mu\nu}$ is the electromagnetic field tensor. The factor γ_5 for the EDM reflects its CPV nature and is thus absent for the magnetic moment.

Important to note is that a non-zero value for d violates both parity and time reversal symmetry: T will flip spin and the magnetic field, while P flips the electric field. Therefore $-d(\vec{S}\cdot\vec{E}) \to +d(\vec{S}\cdot\vec{E})$ under T or P. Assuming CPT invariance, the EDM then also violates CP.[1]

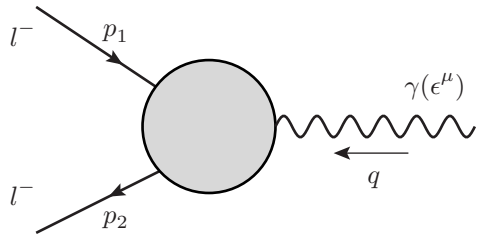

Figure 3.1 *General structure for the electromagnetic interaction between a charged lepton and a photon.*

Looking at (3.5) we see that both the EDM and magnetic moment are interactions between a lepton and the electromagnetic field. One may ask how to distinguish which Feynman diagrams contribute to which observable. In fact, the same diagram can contribute to both and we have to identify what part of the diagram contributes to which observable. In general an interaction between the electromagnetic field and a lepton can be described by the Feynman diagram in Figure 3.1.

[1] This statement is only true for dipoles of elementary particles. Molecules can also have large EDMs, but those do not violate CP, as the vector representation of the group describing a molecule has a reducible representation. Only when a system corresponds to an irreducible representation does a nonzero EDM imply CPV.

The corresponding matrix element is

$$i\mathcal{M} = -ie\ \bar{u}(p_2)\ \Gamma^{\mu}\ u(p_1)\ \epsilon_{\mu}(q), \tag{3.6}$$

where we have defined the vertex structure Γ^{μ}, such that at tree level (3.6) reduces to $ie\ \bar{u}(p_2)\ \gamma^{\mu}\ u(p_1)\ \epsilon_{\mu}(q)$. Different parts of Γ^{μ} can be identified as contributing to different observables.

We define projection operators to project on the relevant structure to find the part of a diagram that contributes to the observable of interest. In Appendix C we describe this in more detail. We use the results from that Appendix to obtain analytic expressions for the contributions in the (c)pMSSM to a_{μ} and d_e, which we will present in Sections 3.1.1 and 3.1.2, respectively.

To study the BSM contributions we compare the SM prediction to experimental results. By far the largest contribution to a_{μ}^{SM} is the famous Schwinger one-loop QED correction $\alpha/2\pi$ [60]. There are many other quantum corrections, composed of quantum-electrodynamic, weak and hadronic contributions, that influence this observable. Especially the hadronic contributions, susceptible to QCD uncertainties, are subject of recent discussion.

According to the Muon g-2 theory initiative, the full SM prediction reads [61–82]

$$a_{\mu}^{\mathrm{SM}} = \frac{(g-2)_{\mu}}{2} = 116\,591\,810(43) \times 10^{-11}, \tag{3.7}$$

where the value between parentheses represents the theoretical uncertainty. There is a long-standing discrepancy between this SM prediction and the experimental result for a_{μ} [22, 83, 84].

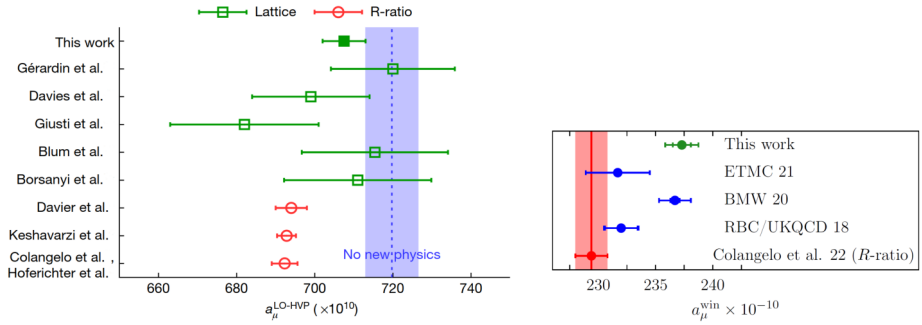

Figure 3.2 On the left: The leading-order hadronic vacuum polarisation contribution to Δa_{μ} in different calculational methods; taken from [85], where references for the different values can be found as well. On the right: Comparison between different lattice results for the so-called window observable for Δa_{μ} ; taken from [86].

However, another group recently published calculations based on lattice QCD that show that the difference between SM prediction and experimental result could

be much smaller than previously assumed [85]. In the left panel of Figure 3.2 we show the different values for the leading-order hadronic vacuum polarisation contribution.

Even more recently new results were published [86] that focus on the consistency of the lattice calculations for the hadronic contributions to Δa_μ , see the right panel of Figure 3.2. Also new data-driven calculations were published recently [87]. So far there seems to be a tension between the lattice calculations and the data-driven calculations. This shows that there is no complete consensus yet about the SM prediction and we have to be careful when interpreting BSM contributions.

Experimentally there have also been interesting developments. Last year, new experimental data from the Fermilab experiment were published [23, 88–90]. Combined with the earlier results from Brookhaven [22, 83, 84] the current experimental value is

$$a_\mu^{\text{exp}} = 116\,592\,061(41) \times 10^{-11}, \tag{3.8}$$

showing that the deviation from the SM prediction based on (3.7) is now

$$\Delta a_\mu = a_\mu^{\text{exp}} - a_\mu^{\text{SM}} = 251(59) \times 10^{-11}. \tag{3.9}$$

This result amounts to a 4.2σ deviation between SM and experiment, although it is important to keep the discussion about a_μ^{SM} in mind. An independent experiment with different techniques than those employed by the Fermilab experiment is being constructed at J-PARC [24, 91]. We will study the deviation (3.9) in more detail in Chapter 4, where we look for pMSSM contributions that bridge the gap between SM expectation and experimental observations, and study the phenomenology of the corresponding pMSSM models.

There is also a deviation between the SM prediction for a_e and the experimental value. However, as this deviation is much smaller, we will focus only on the muon. For a recent study on a_e in the MSSM, see e.g. [92].

For the eEDM, the SM prediction is harder to obtain, since only at four-loop order there is a non-zero SM contribution to the eEDM. This is because the only source of CPV in the SM is the CKM matrix[2]. At one-loop order, there is no possible diagram of the type of Figure 3.1 that contains the CKM matrix. At two loops, we can draw diagrams of the kind shown in Figure 3.3a, which do not contribute to an EDM as the CPV phases of the unitary CKM matrix cancel each other. Unexpectedly, the contributing diagrams at three-loop order (Figure 3.3b) add up to zero as well [93]. Therefore the first contributing diagrams are of four-loop order, resulting in a very small SM prediction for the eEDM [94]

$$d_e^E \leq 10^{-38}\text{e cm}. \tag{3.10}$$

The typical unit for an EDM is [e cm], corresponding to $1/1.973269788 \cdot 10^{-14}$ e GeV^{-1} [45].

[2] We assume only left-handed neutrinos here. If right-handed neutrinos, and therefore neutrino masses, are added, there is another source of CPV in the lepton sector.

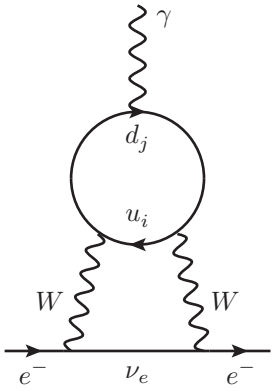

(a) Two-loop diagram for the electron EDM, which does not contribute to d_e due to the unitary nature of the CKM matrix.

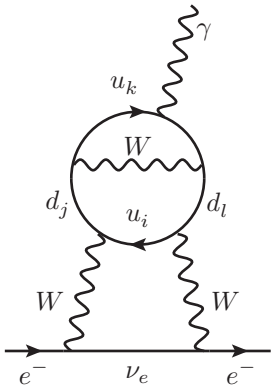

(b) Three-loop diagram for the eEDM. Summing all diagrams of third order also results in a zero contribution.

Figure 3.3 Examples of the two- and three-loop SM diagrams that have a zero contribution to the eEDM.

In the SM we assume that $m_\nu = 0$ and as such there are no neutrino oscillations possible. However, we have experimentally observed such oscillations, meaning that the masses of the neutrinos in fact should be non-zero. There are many different models to generate these masses and depending on the model, this could lead to an additional contribution for the eEDM if there is a CP violating phase associated with the neutrino oscillations. An example of this would be a Majorana mass term, resulting in a possible contribution to the eEDM as shown in Figure 3.4. Depending on the model, the expected eEDM could go up to roughly $d_e \leq 10^{-32}$ e cm [95]. In this work we will mainly focus on the current experimental limit to constrain the cpMSSM parameter space. For this we will use the SM prediction without neutrino masses, i.e. $d_e^E \approx 10^{-38}$e cm.

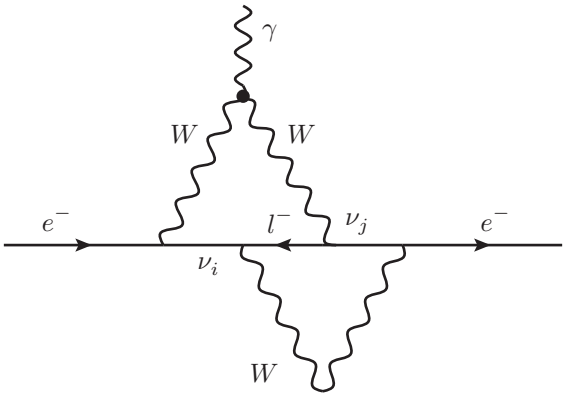

Figure 3.4 An example of a two-loop diagram including Majorana neutrinos that would give a non-zero contribution to the eEDM.

Experimental searches for the eEDM typically do not measure the eEDM directly, but study molecules or atoms to extract the value of the eEDM. For diamagnetic and paramagnetic systems the enhancement factor can be large enough that the eEDM contributes significantly to the total EDM. Besides the contributions from the electron, also nuclear interactions contribute. Using an effective field theory framework, one can calculate these interactions based on the underlying high-energy theory, such as the cpMSSM. For paramagnetic systems such as ThO and BaF, the electron-nucleon interactions are the dominant contribution besides the eEDM. For diamagnetic systems such as mercury, and the neutron, it is the pion-nucleon interactions that are relevant [96].

Currently the ACME collaboration at Yale/Harvard has the most precise measurement using ThO molecules [29, 97]. However, no eEDM has been found, which puts the experimental limit at

$$d_e \leq 1.1 \times 10^{-29} \text{e cm}, \tag{3.11}$$

with a 90% confidence level. In Groningen the NL-eEDM collaboration (see also Chapter 1) aims to measure the eEDM using BaF molecules [31], which could push the limit towards $d_e \leq 10^{-30}$ e cm. The first results are due in 2023-2024. In the meantime, we take the limit of (3.11) as an experimental constraint on the cpMSSM to restrict the parameter space.

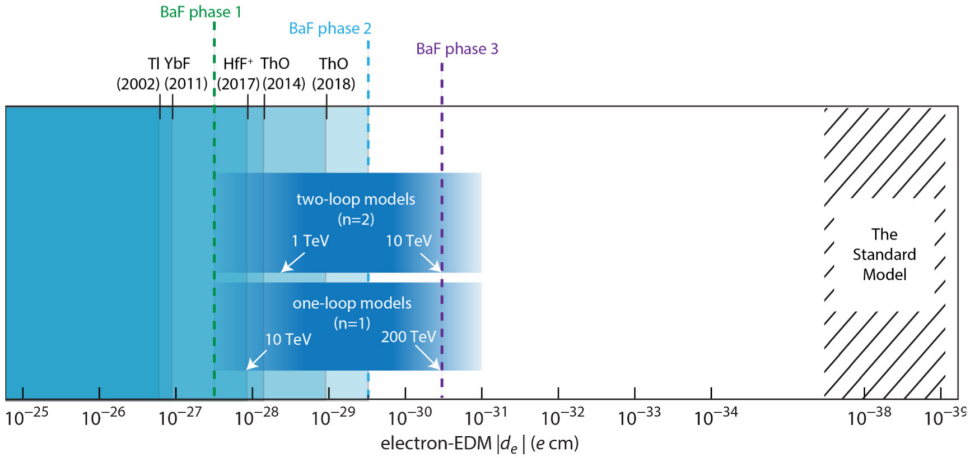

Figure 3.5 The magnitude of the eEDM on the horizontal axis, together with current experimental limits and the ranges predicted by BSM models that generate the eEDM at the one- and two-loop level. The energy scale of the new particles that are probed is indicated in TeV. Obtained from internal communication with Steven Hoekstra.

Related to the experimental searches are exclusion predictions such as shown in Figure 3.5. However, it is not straightforward to put a value of the eEDM to a class of models. We will therefore investigate such claims in more detail in Chapter 5. For example, we will see that the cpMSSM allows for $d_e^E \approx 10^{-32}$ e cm, although the eEDM is generated already at 1-loop level.

It is important to note that more experimental observables are necessary to properly constrain the parameter space of the CPV phases. Even with independent measurements of several systems it is not possible to constrain all 6 free phases of the cpMSSM, let alone additional phases of more complicated models. This is because the observables are related and ultimately depend on three factors: the eEDM, the pion-nucleon interactions and the electron-nucleon interactions.

3.1.1 Analytic expressions for a_μ at first and second order

Typically the deviation of a_μ from the SM prediction is studied in models without CPV, partially because the available software does not always allow for CPV phases and partially because this was historically more interesting. We will therefore study a_μ in the pMSSM to use the available state-of-the-art calculations, and do a smaller study in the cpMSSM. In this chapter we will present the analytic expressions for the cpMSSM contributions. These expressions can be evaluated for purely real parameters to obtain the pMSSM contributions. The additional contributions that are taken into account by the software package GM2Calc, which we use for our pMSSM study

in Chapter 4, are presented in [98, 99].

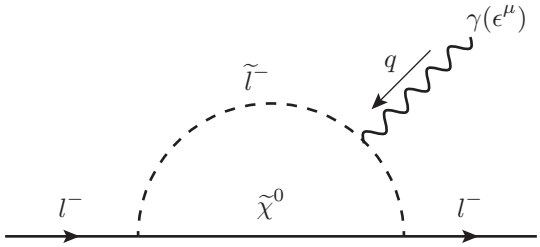

Figure 3.6 *The 1-loop lepton-neutralino-sfermion diagram, assuming no flavour violation. Observables are defined in the limit $q \to 0$.*

At first order there are two contributing diagrams: the neutralino-smuon loop (Figure 3.6 for $l = \mu$) and the chargino-sneutrino loop (Figure 3.7 for $l = \mu$) [100].

Using the conventions as described in Appendix A, the expressions for these one-loop contributions read [101]

$$a_\mu^{\widetilde{\chi}^0} = \frac{m_\mu}{16\pi^2} \sum_{i=1}^{4} \sum_{m=1}^{2} \left[-\frac{m_\mu}{12 m^2_{\widetilde{\mu}_m}} \left(|G^L_{im}|^2 + |G^R_{im}|^2 \right) F_1^N \left(\frac{m^2_{\widetilde{\chi}^0_i}}{m^2_{\widetilde{\mu}_m}} \right) \right. \\ \left. - \frac{m_{\widetilde{\chi}^0_i}}{3 m^2_{\widetilde{\mu}_m}} \mathrm{Re}\left[G^L_{im} (G^R_{im})^* \right] F_2^N \left(\frac{m^2_{\widetilde{\chi}^0_i}}{m^2_{\widetilde{\mu}_m}} \right) \right], \tag{3.12}$$

$$a_\mu^{\widetilde{\chi}^\pm} = \frac{m_\mu}{16\pi^2} \sum_{k=1}^{2} \left[\frac{m_\mu}{12 m^2_{\widetilde{\nu}_\mu}} \left(|c^L_k|^2 + |c^R_k|^2 \right) F_1^C \left(\frac{m^2_{\widetilde{\chi}^\pm_k}}{m^2_{\widetilde{\nu}_\mu}} \right) \right. \\ \left. + \frac{2 m_{\widetilde{\chi}^\pm_k}}{3 m^2_{\widetilde{\nu}_\mu}} \mathrm{Re}\left[c^L_k c^R_k \right] F_2^C \left(\frac{m^2_{\widetilde{\chi}^\pm_k}}{m^2_{\widetilde{\nu}_\mu}} \right) \right]. \tag{3.13}$$

The loop functions F can be found in Appendix B. Note the complex conjugate and minus sign that differ from [101] for the neutralino contribution, which is due to our convention for G^R_{im}.

At two loop, the numerical values of the various contributions differ considerably. The photonic Barr-Zee diagrams are the source of the largest possible two-loop contribution. Here a Higgs boson and a photon connect to either a chargino, sfermion or fermion loop [102] [3]. In Figure 3.8 we show the Barr-Zee diagrams we take into account.

[3] Two-loop corrections from sfermion loops contribute with a few percent here as well, since we assume heavy squark masses [103, 104].

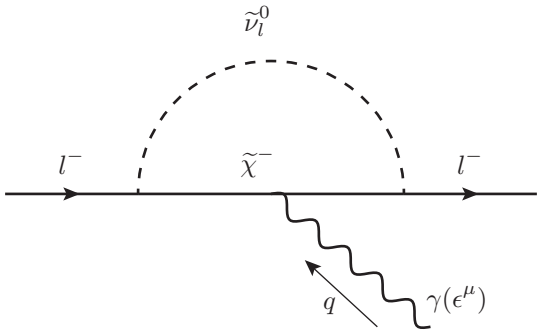

Figure 3.7 *The 1-loop lepton-chargino-sneutrino diagram, assuming no flavour violation. Observables are defined in the limit $q \to 0$.*

The neutral Higgs contributions from these Barr-Zee diagrams are as follows [105]

$$
\begin{aligned}
(a_\mu)^H = \sum_{q=t,b} \Bigg\{ & -\frac{3\alpha_{\rm em}\, Q_q^2\, m_\mu^2}{16\pi^3} \sum_{i=1}^{3} \frac{g^S_{H_i\mu^+\mu^-}}{M^2_{H_i}} \sum_{j=1,2} g_{H_i\tilde{q}_j^*\tilde{q}_j}\, F(\tau_{\tilde{q}_j i}) \\
& + \frac{3\alpha_{\rm em}^2\, Q_q^2\, m_\mu^2}{4\pi^2 s_W^2 M_W^2} \sum_{i=1}^{3} \left[-g^S_{H_i\mu^+\mu^-} g^S_{H_i\bar{q}q}\, f(\tau_{qi}) + g^P_{H_i\mu^+\mu^-} g^P_{H_i\bar{q}q}\, g(\tau_{qi}) \right] \Bigg\} \\
& - \frac{\alpha_{\rm em}\, m_\mu^2}{16\pi^3} \sum_{i=1}^{3} \frac{g^S_{H_i\mu^+\mu^-}}{M^2_{H_i}} \sum_{j=1,2} g_{H_i\tilde{\tau}_j^*\tilde{\tau}_j}\, F(\tau_{\tilde{\tau}_j i}) \\
& + \frac{\alpha_{\rm em}^2\, m_\mu^2}{4\pi^2 s_W^2 M_W^2} \sum_{i=1}^{3} \left[-g^S_{H_i\mu^+\mu^-} g^S_{H_i\tau^+\tau^-}\, f(\tau_{\tau i}) + g^P_{H_i\mu^+\mu^-} g^P_{H_i\tau^+\tau^-}\, g(\tau_{\tau i}) \right] , \\
& + \frac{\alpha_{\rm em}^2\, m_\mu^2}{2\sqrt{2}\pi^2 s_W^2 M_W} \\
& \quad \times \sum_{i=1}^{3} \sum_{j=1,2} \frac{1}{m_{\chi_j^\pm}} \left[-g^S_{H_i\mu^+\mu^-} g^S_{H_i\chi_j^+\chi_j^-}\, f(\tau_{\chi_j^\pm i}) + g^P_{H_i\mu^+\mu^-} g^P_{H_i\chi_j^+\chi_j^-}\, g(\tau_{\chi_j^\pm i}) \right] .
\end{aligned}
\tag{3.14}
$$

Here $\alpha_{\rm em}$ is the electromagnetic fine-structure constant, $\tau_{xi} = m_x^2/M^2_{H_i}$ and Q_q is the charge in units of e, which is $2/3$ and $-1/3$ for up- and down-type quarks respectively. Expressions for the two-loop functions $F(\tau)$, $f(\tau)$ and $g(\tau)$ can be found in Appendix B. The couplings are defined in Appendix A.4. We implement $\tan\beta$ resummation for the third generation fermions, to take higher-order corrections for large values of $\tan\beta$ into account. This can be found in Appendix A.5.

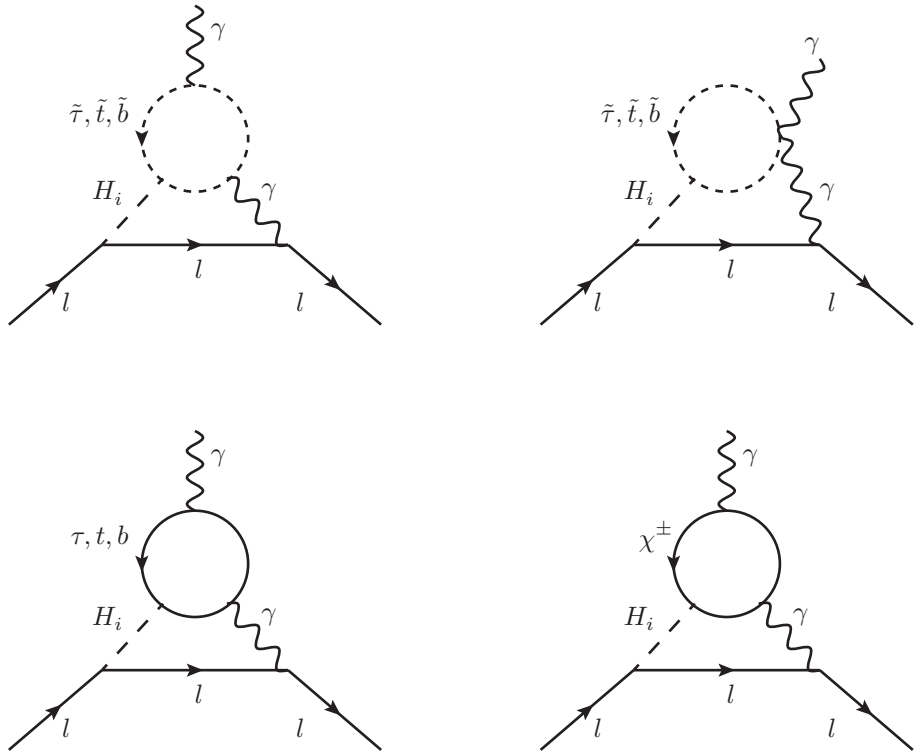

Figure 3.8 *Barr-Zee diagrams for a charged lepton l, where the H_i lines denote all three neutral Higgs bosons.*

It is noteworthy that the Barr-Zee contributions given in (3.14) can be as large as the 1-loop contributions in specific models. This is because the parameters that play a role in (3.12) and (3.13) are different and independent from those in (3.14) Specifically two-loop diagrams with a top or tau contribute significantly to Δa_μ , see e.g. [106, 107] for a discussion in the two Higgs doublet model.

Other contributions, such as the bosonic 2-loop diagrams, are of less importance. They are taken into account in the software package GM2Calc, which can be used to calculate Δa_μ in BSM models without CPV. See [99] for a full account on all contributions that are taken into account in this software package. Since these contributions are always smaller than the Barr-Zee contributions, we have decided to leave such improvements for a future study.

Finally the charged Higgs bosons can contribute through a process similar to the

neutral Higgs boson Barr-Zee diagrams. Again we have opted to leave this for future extensions of our in-house code, as these have been shown to be much smaller than the neutral Barr-Zee contributions [57, 108].

3.1.2 Analytic expressions for the eEDM

Since the eEDM violates CP, the pMSSM contribution would be explicitly zero. We will therefore study it in the cpMSSM. The diagrams necessary to calculate the eEDM contribution in the cpMSSM are similar to those presented for a_μ, we only project on a different structure using the EDM projection operator described in Appendix C. This gives the following results.

At first order there are two diagrams contributing to the eEDM: the neutralino-selectron diagram as shown in Figure 3.6, and the chargino-sneutrino diagram as shown in Figure 3.7. These are the same diagrams as for a_μ, but now for $l = e$.

Using the expressions for the couplings as in Appendix A.4 we can write the 1-loop contribution to the eEDM as

$$\left(\frac{d_e^E}{e}\right)^{\tilde{\chi}^0} = \frac{-1}{16\pi^2}\sum_{i=1}^{4}\sum_{m=1}^{2}\frac{m_{\tilde{\chi}_i^0}}{m_{\tilde{e}_m}^2}\mathrm{Im}\Big[\Big(G_{im}^R\Big)^* G_{im}^L\Big]\Big[B(m_{\tilde{\chi}_i^0}^2/m_{\tilde{e}_m}^2)\Big]\,, \tag{3.15}$$

$$\left(\frac{d_e^E}{e}\right)^{\tilde{\chi}^\pm} = \frac{1}{16\pi^2}\sum_{k=1}^{2}\frac{m_{\tilde{\chi}_k^\pm}}{m_{\tilde{\nu}_e}^2}\mathrm{Im}\Big[c_k^R c_k^L\Big]\Big[A(m_{\tilde{\chi}_k^\pm}^2/m_{\tilde{\nu}_e}^2)\Big]\,. \tag{3.16}$$

This expression agrees with [57], but instead of a general sfermion $\tilde{f}$ we use the selectron $\tilde{e}$ in the cpMSSM, since minimal flavour violation is assumed.

For higher orders we take the Barr-Zee diagrams as shown in Fig. 3.8 into account. We find that the eEDM $(d_e^E)^H$ is induced by CP-violating phases of third-generation fermions and sfermions, and of charginos. The Barr-Zee contribution to the eEDM is given by [57]

$$\begin{aligned}
\left(\frac{d_e^E}{e}\right)^H = \sum_{q=t,b} \Bigg\{ & \frac{3\alpha_{\rm em}\, Q_q^2\, m_e}{32\pi^3} \sum_{i=1}^{3} \frac{g^P_{H_i e^+ e^-}}{M^2_{H_i}} \sum_{j=1,2} g_{H_i \tilde{q}_j^* \tilde{q}_j}\, F(\tau_{\tilde{q}_j i}) \\
& + \frac{3\alpha_{\rm em}^2\, Q_q^2\, m_e}{8\pi^2 s_W^2 M_W^2} \sum_{i=1}^{3} \left[g^P_{H_i e^+ e^-} g^S_{H_i \bar{q} q}\, f(\tau_{qi}) + g^S_{H_i e^+ e^-} g^P_{H_i \bar{q} q}\, g(\tau_{qi}) \right] \Bigg\} \\
& + \frac{\alpha_{\rm em}\, m_e}{32\pi^3} \sum_{i=1}^{3} \frac{g^P_{H_i e^+ e^-}}{M^2_{H_i}} \sum_{j=1,2} g_{H_i \tilde{\tau}_j^* \tilde{\tau}_j}\, F(\tau_{\tilde{\tau}_j i}) \\
& + \frac{\alpha_{\rm em}^2\, m_e}{8\pi^2 s_W^2 M_W^2} \sum_{i=1}^{3} \left[g^P_{H_i e^+ e^-} g^S_{H_i \tau^+ \tau^-}\, f(\tau_{\tau i}) + g^S_{H_i e^+ e^-} g^P_{H_i \tau^+ \tau^-}\, g(\tau_{\tau i}) \right] \\
& + \frac{\alpha_{\rm em}^2\, m_e}{4\sqrt{2}\pi^2 s_W^2 M_W} \\
& \quad \times \sum_{i=1}^{3} \sum_{j=1,2} \frac{1}{m_{\chi_j^\pm}} \left[g^P_{H_i e^+ e^-} g^S_{H_i \chi_j^+ \chi_j^-}\, f(\tau_{\chi_j^\pm i}) + g^S_{H_i e^+ e^-} g^P_{H_i \chi_j^+ \chi_j^-}\, g(\tau_{\chi_j^\pm i}) \right] ,
\end{aligned} \tag{3.17}$$

with $\tau_{xi} = m_x^2/M^2_{H_i}$ and Q_q again the charge in units of e. Expressions for the couplings g and loop functions $F(\tau), f(\tau)$ and $g(\tau)$ are again given in Appendices A.4 and B respectively. To include higher-order effects, e.g. from gluino exchange, we will also implement $\tan(\beta)$ resummation, as is described in Appendix A.5. Note that this resummation is questionably called threshold correction, e.g. in [57].

Note that for both the one-loop and two-loop contributions the phase between the two Higgs doublets, η, plays an important role, even though there is no direct dependence. At first order the neutralino and chargino mixing matrices and masses depend on η. At second order again the chargino mixing matrices and masses are relevant, but also the mixing matrices and masses of the neutal Higgs bosons depend on η. This makes η one of the most relevant parameters for d_e. We will see this in more detail in Chapter 5.

Similar to the Δa_μ calculation, there are other two-loop and higher-order corrections known that we do not take into account in our own in-house code. See e.g. [108] for a full account of the two-loop contributions. These are part of a future extension of our in-house code, which will allow for a more complete comparison with the code CPsuperH, that does include the charged Higgs boson Barr-Zee contribution [109]. However, such contributions have been shown to be much smaller (at least one order of magnitude) than the contributions we have taken into account [108, 110].

3.2 Dark matter

As discussed in Chapter 1, one of the goals of a BSM theory is to explain the observations on DM. There are several observables related to DM: the DM relic density, the velocity-weighted annihilation cross-section for DM indirect detection and the spin-dependent and spin-independent cross sections for DMDD. In this Section we will discuss these observables in the (c)pMSSM. Note that we thus assume a particle interpretation of DM.

Assuming DM particles obey the same laws of physics as SM particles, the first DM particles were created in the early Universe when the temperature was still high enough for pairwise creation. In the ΛCDM we assume that the early Universe is radiation dominated and in a thermal equilibrium, such that the number density n of DM particles at that time can be described with the Boltzmann equation [111]

$$\frac{dn}{dt} = -3Hn - \langle\sigma_{\text{ann}}v\rangle(n^2 - n_{\text{eq}}^2), \tag{3.18}$$

where H is the Hubble constant describing the expansion of the Universe and $\langle\sigma_{\text{ann}}v\rangle$ is the velocity-weighted annihilation cross section for DM particles annihilating into SM particles. If not for the expanding Universe, this equation means that any $n^2 \neq n_{\text{eq}}^2$ would drive the number density of DM particles towards an equilibrium: if the number density exceeds the equilibrium value n_{eq}, more particles annihilate and n decreases. Vice versa if n is smaller than the equilibrium value, there is more particle creation. Once the particles reach the equilibrium state, n will only decrease due to the expansion of the Universe. In other words, after some time the number density per comoving volume stays constant. We call this a thermal freeze-out of DM. The remaining DM, or the relic density $\Omega_{\text{DM}}h^2$, can be calculated and is typically expressed in terms of the scaled Hubble parameter h, as this is now a constant number. We define h as [112]

$$H = 100\ h\ \text{km s}^{-1}\text{Mpc}^{-1}. \tag{3.19}$$

Observations from the Planck satellite on the CMB put the total observed $\Omega_{\text{DM}}h^2$ at a value of $\Omega_{\text{Planck}}h^2 = 0.120 \pm 0.001$ [15].

We can calculate the expected value $\Omega_{\text{DM}}h^2$ for a certain DM candidate. If this theoretical value exceeds $\Omega_{\text{Planck}}h^2$ it is said that this DM candidate is over-abundant and therefore disfavoured. If the calculated value stays below $\Omega_{\text{Planck}}h^2$, the candidate is under-abundant, as it cannot account for all the observed DM. We can thus use the observed value of the relic density as a constraint on our models. However, we have to be careful, as the annihilation mechanism can be more complicated when co-annihilation plays a role. This is when another particle annihilates with the DM particle as $\widetilde{\chi}^0 + X \to \text{SM} + \text{SM}$. For N kinds of particles that can participate in the annihilation (including the DM particle), we find [113]

$$\frac{dn}{dt} = -3Hn - \langle\sigma_{(\text{co})\text{ann}}v\rangle(n^2 - n_{\text{eq}}^2), \tag{3.20}$$

where the co-annihilation cross section for co-annihilation partners i and j is given by

$$\langle \sigma_{(\mathrm{co})\mathrm{ann}} v \rangle = \sum_{i,j=1}^{N} \langle \sigma_{ij} v_{ij} \rangle \frac{n_i^{\mathrm{eq}}}{n^{\mathrm{eq}}} \frac{n_j^{\mathrm{eq}}}{n^{\mathrm{eq}}}, \tag{3.21}$$

where v_{ij} is the relative velocity between particle i and j. This describes all annihilation and co-annihilation into SM particles. However, co-annihilation is suppressed depending on the temperature T and mass of the co-annihilation partner i as

$$\frac{n_i^{\mathrm{eq}}}{n^{\mathrm{eq}}} \propto \exp\left(-\frac{m_i - m_{\mathrm{DM}}}{T}\right). \tag{3.22}$$

Therefore only particles similar in mass to the DM particle will contribute to the co-annihilation process. In the (c)pMSSM these are typically the gauginos and lightest stop, but in Chapter 4 we will also see slepton co-annihilation.

Note that the observable that we use for DM indirect detection is actually the present-day velocity-weighted annihilation cross section $\langle \sigma v \rangle$. On the other hand, the $\langle \sigma_{(\mathrm{co})\mathrm{ann}} v \rangle$ in the expressions above, is calculated in the early Universe and can thus differ from the present day value.

In most cases these two cross sections will be roughly the same, as they do not change over time. There is an exception however, which is when the main contribution comes from an s-channel resonance. This resonance could exist because of the higher temperatures (and thus energies) present in the early Universe, which are not present today. The resonance will have disappeared over time due to the reduced temperature, resulting in a different cross section. The result for $\Omega_{\mathrm{DM}} h^2$ is based on the early Universe cross section $\langle \sigma_{(\mathrm{co})\mathrm{ann}} v \rangle$, meaning that the same value of $\Omega_{\mathrm{DM}} h^2$ can result in different values of $\langle \sigma v \rangle$. We will see this in Chapter 4, where we study $\langle \sigma v \rangle$ and $\Omega_{\mathrm{DM}} h^2$ as part of our analyses.

Since direct evidence of a DM particle is currently lacking, one typically uses the experimental results as a constraint on the theoretical model. The difficulty with the MSSM is that each set of parameter values results in a different spectrum, including a different DM candidate. This makes it challenging to use the DMDD limits directly to exclude regions of the parameter space. Instead, we calculate the expected DMDD rate for a given spectrum, which is represented by a given set of parameter values. We can then compare this spectrum and its DM candidate to the current experimental limits to check if the hypothetical detection rate exceeds the signal limit for a given experiment. If the prediction does exceed the signal limit, the considered candidate is excluded.

The direct detection rate for a DM particle depends on the cross section for elastic scattering between the DM particle and a nucleus, σ, which has to be calculated in the assumed model. Because the scattering is elastic and the momentum transfer is low, one typically uses an effective field theory (EFT) framework to determine σ, where the (heavy) mediator is integrated out. In this framework there are different types of

contributions relevant for the cross section: scalar, axial-vector and pseudoscalar (the tensor and vector contributions are not relevant for Majorana particles such as the neutralino). The pseudoscalar contribution is typically not relevant for pMSSM-like models, since it is usually strongly suppressed in the non-relativistic limit. Interactions of the scalar kind will then contribute to the spin-independent (SI) cross section, while the axial-vector contributions are relevant for the spin-dependent (SD) cross section for the interaction between a WIMP and a nucleus. For more details on this calculation we refer the interested reader to e.g. [114] for a pedagogical review.

We will use both the spin-dependent and spin-independent cross section for protons and neutrons in our analyses. We can then compare this to the current experimental limits on $\sigma^{\mathrm{SD}}_{\mathrm{p,n}}$ and $\sigma^{\mathrm{SI}}_{\mathrm{p,n}}$.

3.3 Fine-tuning

For a given SUSY model it is also possible to define a quantity called the FT of the model. This is not an observable, but we can use it to study the validity of our models. We will therefore define the FT measures that we use and motivate them. But first we will define what we mean by fine-tuning.

The SM Higgs particle has an observed mass of 125 GeV. Within the SM there is nothing special about this value. However, if there exists a BSM theory at higher energies, the SM will couple to this new theory and the Higgs boson mass will receive quantum corrections that can potentially become much larger than the mass itself. These corrections depend on the mass of the BSM particles and are quadratic in nature[4]. The instability of a scalar mass with respect to high scale physics was already studied in the 80's, e.g. in [116–119]. For a model to still result in the correct Higgs boson mass of 125 GeV, one would need a lot of FT to obtain the correct mass instead of a value that is close to the scale of the new theory.

In an unbroken version of SUSY, this is actually not a problem. Unbroken SUSY links the mass of scalar particles, like the Higgs boson, to fermionic SUSY particles. Fermions are protected by a chiral symmetry [32], which makes it natural for their masses to be small. Linking the Higgs boson mass to a protected fermionic mass would solve the FT problem, regardless of any other BSM theory. We can also see this in the loop corrections that the Higgs boson mass receives: for each bosonic loop correction in a supersymmetric theory, there is also a fermionic loop correction with the opposite sign, and vice versa. This was originally one of the reasons to study SUSY.

Nowadays we only study broken versions of SUSY, as we know that an unbroken version is not realised in nature. For the MSSM we even find that EWSB and SUSY breaking are closely related, as we cannot have the former without the latter. What does this mean for the FT in the theory? The Higgs boson mass is no longer directly

[4] This is unrelated to the renormalisation that is used to compute the Higgs boson mass. See e.g. [115] for a clear explanation on the origin of the quantum corrections.

protected by the chiral symmetry of the fermionic masses. However, the Higgs boson mass does depend on the free parameters of the supersymmetric theory. This results in a different FT problem[5]: if the parameters are very large compared to the Higgs boson mass, we could again need a large amount of FT to obtain the correct mass. If the model is too fine-tuned, it is said to be unnatural and therefore not favoured.

It is often claimed that the MSSM cannot be realised in nature in a natural way, because the masses of the relevant SUSY particles are too large (> 1 TeV). However, recent studies have shown that this claim is too general and one should be careful of the nuances [120, 121]. On top of that, it is unclear how much FT one should allow before considering a model unnatural, as there is no consensus on this amount.

Different FT measures give different results. This makes the FT discussion not only model- but also measure-dependent. One can choose for a measure that takes the relation between the low scale SUSY parameters (such as μ, $m^2_{H_d}$ and $m^2_{H_u}$) and the high scale theory into account. For instance the Barbieri-Giudice measure [122], that is widely used, is such a measure. However, we will use a more agnostic approach by looking only at the low scale (c)pMSSM model.

The electroweak (EW) FT measure [123] is more suitable for this, as it only takes the dependence of the Z-boson mass on the model parameters into account. It is motivated by the relation between m_Z and the Higgs sector in the pMSSM [see also (2.17)], which is as follows when we include the loop corrections:[6]

$$\frac{m_Z^2}{2} = \frac{(m^2_{H_d} + \Sigma_d^d) - (m^2_{H_u} + \Sigma_u^u)\tan^2(\beta)}{\tan^2(\beta) - 1} - |\mu|^2. \tag{3.23}$$

Here Σ_d^d and Σ_u^u contain a sum of different contributions, that arise from the loop corrections to the Higgs potential [124]. We now define the EW FT measure Δ_{EW} as follows

$$\Delta_{\text{EW}} \equiv \max_i \left| \frac{C_i}{m_Z^2/2} \right|, \tag{3.24}$$

where the C_i are defined as

$$C_{m_{H_d}} = \frac{m^2_{H_d}}{\tan^2\beta - 1}, \quad C_{m_{H_u}} = \frac{m^2_{H_u}\tan^2\beta}{\tan^2\beta - 1}, \quad C_\mu = -|\mu|^2 \tag{3.25}$$

$$C_{\Sigma_d^d} = \frac{\max(\Sigma_d^d)}{\tan^2\beta - 1}, \quad C_{\Sigma_u^u} = \frac{\max(\Sigma_u^u)\tan^2\beta}{\tan^2\beta - 1}. \tag{3.26}$$

Note that the terms Σ_d^d and Σ_u^u contain contributions from parameters that are real in the pMSSM, but can become complex in the cpMSSM. At leading order, it is sufficient

[5] Note that this is really different, as we have explicitly allowed only soft breaking terms in the SUSY Lagrangian.

[6] Since m_Z was known long before m_h was measured, the FT measure is historically defined in terms of the Z-boson mass.

to include the absolute value of those parameters. However, for a complete study it is necessary to also include the higher-order corrections that depend on the full, and thus in general complex, parameters. This would go beyond the scope of this thesis, so we have included the leading-order terms by taking the absolute values of those parameters for a first-order calculation of Δ_{EW} in the cpMSSM.

With these definitions we can evaluate how the mass of the Z-boson depends on the model parameters and how fine-tuned this must be to obtain the observed $m_Z = 91.2$ GeV [45]. For the EW FT measure a value of $\Delta_{\text{EW}} = 100$ corresponds to a parameter FT of $\mathcal{O}(1\%)$.

To study the FT in the CPV sector of the cpMSSM explicitly, the EW FT measure is not suited. Instead, we will use the observable eEDM to determine the degree of FT for these phases by defining

$$\Delta_{\text{CPV}} \equiv \Delta_\phi = \max_i \left| \frac{\partial \log d_e}{\partial \phi_i} \right| \equiv \max_i \Delta_{\phi_i}, \tag{3.27}$$

where d_e is the eEDM and ϕ_i is one of the CPV phases of the cpMSSM. By taking the logarithmic derivative in d_e, we ensure that the amount of FT is an absolute number that can be interpreted on its own. For a linear derivative we would have to compare the resulting value to the value of d_e. In Chapter 5 we will study this definition of FT in more detail and discuss whether this choice is indeed suitable for the cpMSSM, or if other definitions should be considered.

We do not take a double logarithmic derivative to avoid an artificial transition between $\phi_i = 0$ and $\phi_i \approx 0$. A phase that is truly 0 would have a FT of 0 as well in a double logarithmic definition, which means that the FT of that point would only depend on non-zero phases. We believe this is more difficult to interpret and thus opt for a linear derivative in the phases. See e.g. [125] for a more thorough discussion on the different definitions on FT in BSM models.

We will implement Δ_{CPV} as a numerical derivative that is normalised to the eEDM. Using $x = \phi_i$, for phases $\phi_i > 10^{-6}$ we compute this as

$$\frac{\partial d_e}{\partial x} = \frac{d_e(x + x\epsilon) - d_e(x - x\epsilon)}{2x\epsilon}, \tag{3.28}$$

and in other case we use

$$\frac{\partial d_e}{\partial x} = \frac{d_e(x + h) - d_e(x - h)}{2h}. \tag{3.29}$$

for $h = 1 \times 10^{-6}$, to ensure numerical stability.

To find a value of ϵ for which the numerical derivative of (3.28) is stable, we have run several tests. We compare the two-point derivative with the five-point derivative, defined as

$$\frac{\partial d_e}{\partial \phi_i} = \frac{-d_e(x + 2x\epsilon) + 8d_e(x + x\epsilon) - 8d_e(x - x\epsilon) + d_e(x - 2x\epsilon)}{12x\epsilon}. \tag{3.30}$$

When both methods give the same result, we consider the calculation stable. We have tested this for several values of ϵ, in Figure 3.9 the results are shown. After these tests we have implemented the two-point derivative of (3.28) and (3.29) in our code for the value $\epsilon = 10^{-2}$.

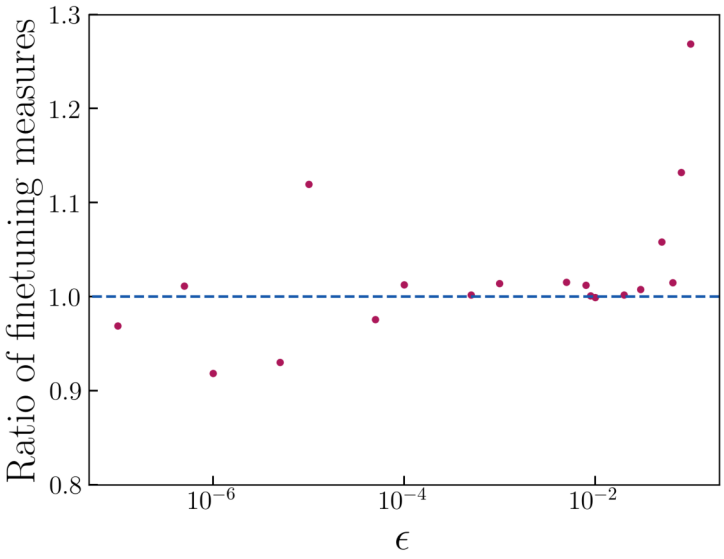

Figure 3.9 The ratio of the the two-point and five-point derivative for calculating $\partial d_e/\partial\phi_i$. When both methods give the same result, we consider the numerical derivative stable, as is the case for $\epsilon \approx 10^{-2}$.

A high value of FT corresponds to a region of the parameter space where the eEDM is not stable in terms of the CPV phases. Note that FT and naturalness are different concepts and thus a point with low or high FT can still be unnatural. We refer to [32] for a discussion on the concept of naturalness in the case of a one-parameter problem. It is not immediately clear how one could extend this definition of naturalness to a model such as the cpMSSM, where several parameters can violate CP symmetry. We will therefore only focus on studying the FT of our models.

We will study the EW FT in the pMSSM in Chapter 4 and the FT in the CPV sector in Chapter 5. Since any FT measure can be defined up to a constant, it is not a priori clear how to combine both FT measures to a single value. We will therefore focus on Δ_{CPV} for the CP violating sector of the cpMSSM.

Note that Δ_{CPV} is inherently different than Δ_{EW}, as it is only suitable for certain models. While the contributions to Δ_{EW} may vary for different models, the general definition is the same. On the other hand, Δ_{CPV} is undefined for supersymmetric models without CPV. Furthermore, the EW FT is related to a general observable,

the mass of the Z-boson, while Δ_{CPV} is related to a specific observable of our choice and any other CPV observable could have been chosen instead. Additionally, only an upper bound for $|d_e^E|$ is known, contrary to observables as m_Z and $\Omega_{\text{DM}}h^2$. It is important to keep this in mind for the discussion in Chapters 4 and 5.

Chapter 4

Dark Matter, fine-tuning and $(g-2)_\mu$

As we have seen in Chapter 3, the anomalous magnetic moment of the muon is an interesting observable to study, as there is currently a discrepancy between theory and experiment of roughly 4σ. In this Chapter we will study the pMSSM contribution to $(g-2)_\mu$ to explain this difference. Additionally, we will study DM observables and fine-tuning, such that we can look into the phenomenology of the regions of the pMSSM parameter space that account for the DM relic abundance, the observed $(g-2)_\mu$ discrepancy and are minimally fine-tuned. The contents in this Chapter are based on [126].

The LHC has been searching for over a decade for signs of physics that originate from BSM scenarios, including searches for signals that originate from SUSY particle production. These high-energy searches are complemented by low-energy experiments such as DM experiments, or experiments that search for small deviations in known SM processes from their SM prediction. In the former category, the XENON1T [127, 128], PandaX-II [129, 130] and PICO [131–133] experiments provide limits on the DM-nucleus scattering cross section, whereas the Planck collaboration provides a precise measurement of the DM relic abundance [15]. In the latter category, the anomalous magnetic moment of the muon $(g-2)_\mu$ plays an important role. There is a long-standing discrepancy between the experimental result [22, 83, 84] and the SM prediction for the muon anomalous magnetic moment. Note that there is still some discussion on the calculation of the SM prediction, as mentioned in Section 3.1. In this Chapter we will focus on our work from [126]. Keeping this in mind, the deviation from the SM predication based on (3.7) is

$$\Delta a_\mu = a_\mu^{\text{exp}} - a_\mu^{\text{SM}} = 251(59) \times 10^{-11}. \tag{4.1}$$

The pMSSM predicts a DM candidate and can simultaneously provide an explanation for the $(g-2)_\mu$ discrepancy [1]. Furthermore, the MSSM provides a solution to the FT problem in the Higgs sector that any BSM model introduces, even after taking into account the constraints on colored sparticles originating from the LHC. It is clear that for a rich model such as the pMSSM, the interplay between the various experimental results is of crucial importance. In this context, several studies have been performed to study a subset of these constraints. For instance, the interplay between the LHC limits and the $(g-2)_\mu$ discrepancy has been studied in e.g. Ref. [134–141]. DMDD searches are complementary in regions of the pMSSM parameter space where the LHC has little sensitivity, for example in compressed regions.[2] Papers that explore the DM implications of spectra that explain the $(g-2)_\mu$ discrepancy include Refs. [140–145], where the relic density requirement is not always taken into account. Likelihood analyses or global fits, where all experimental data

[1] A simultaneous explanation of the muon and electron anomalous magnetic moments in the MSSM context is provided in Ref. [92].

[2] In compressed regions some sparticles are nearly degenerate in mass, e.g. $m_{\tilde{t}_1} \approx m_{\tilde{t}_2}$.

that constrain the pMSSM parameter space are taken into account, have been performed in e.g. Ref. [145–151]. The degree of FT in constrained models that explain the $(g-2)_\mu$ discrepancy is studied in [152, 153], whereas the role of FT in spectra with the right DM properties is studied in Ref. [120, 121, 154–156].

In this work we perform for the first time a study of the phenomenology of the pMSSM that simultaneously accounts for the DM relic abundance and the observed discrepancy of $(g-2)_\mu$, that includes all DMDD and LHC limits, and that constrains the model-parameter space to models that are minimally fine-tuned. The resulting spectra may be obtained from [157]. First, we will explain the analysis setup for this study.

4.1 Analysis setup

We study model points in the pMSSM as defined in Section 2.3, which has 19 free parameters. In modern particle physics it is customary to use computational techniques to support more traditional methods of calculations. This is especially the case for supersymmetric models such as the pMSSM, because of the many free parameters of the model. Ultimately we aim to find model points that satisfy all available constraints on the observables defined in Chapter 3. In order to do so, one has to find the masses and couplings, or the spectrum, for a chosen set of values of the Lagrangian parameters. This is not a simple task. The pMSSM parameters are defined at the energy scale of the model, or SUSY scale, which is typically taken to be

$$m_{\text{SUSY}} = \sqrt{m_{\tilde{t}_1} m_{\tilde{t}_2}} \tag{4.2}$$

in terms of the two top squark masses. On the other hand, the model has to satisfy constraints that are defined at the electroweak scale. This includes LEP and LHC limits on the masses and couplings, but also successful EWSB is a requirement, so the spectrum has to satisfy the tadpole equations (2.17). To make sure that the model point satisfies the constraints at both energy scales, we use a spectrum generator.

A spectrum generator is designed to solve the renormalisation group equations (RGEs) that describe the energy dependence of the model parameters. The user can define properties of the model, e.g. unification of certain parameters at a defined energy scale, or the requirement that there is no flavour violation. Also the boundary conditions at the low (electroweak) and high energy scale are defined in the spectrum generator. For a chosen set of input parameters, the spectrum generator will then try to find a consistent solution of the RGEs at both energy scales. If such a solution indeed exists, the masses, mixing matrices and couplings are calculated as well.

There are several public spectrum generators available, each with its own benefits and downsides. For instance the codes CPsuperH, FeynHiggs, ISAJET, SoftSUSY, SPheno and SUSPECT can all be used as a spectrum generator. Most codes take roughly the same approach and differ only in higher-order corrections (see e.g. [158]

for a nice overview). The exception is CPsuperH: most codes include running to satisfy the boundary conditions at both energy scales, but CPsuperH uses an effective potential approach [159] to calculate the resulting spectrum. Depending on the values of the input parameters, this can lead to significant differences between the resulting spectra from CPsuperH and other spectrum generators (see Appendix D for a comparison between the results of several spectrum generators). Consequently, we have to pick a spectrum generator that suits the model and region of parameter space that we want to study.

For the pMSSM there are several spectrum generators available and their differences are well-known [158]. We choose SoftSUSY for the general spectrum and FeynHiggs to calculate the Higgs masses, as this gives the best result for the region of parameter space that we are interested in. Once the masses and couplings are all calculated, we can use them to calculate other observables. In Table 4.1 we show an overview of the software that we have used[3]. Not all of the software packages are suited for the cpMSSM, which is indicated by a star for suitable software.

Our analysis setup for the $(g-2)_\mu$ study is as follows. We use the Gaussian particle filter [200] to search the pMSSM parameter space for interesting areas. First, we use random sampling to search the parameter space for spectra that do not result in nonphysical results (e.g. when no converging spectrum can be found for a correct Z-boson mass). Next, we sample around these points to search for points that satisfy one or more experimental constraints. Using the Gaussian particle filter, we can then search for areas where all constraints are satisfied.

The particle filter allows to zoom in on regions of parameter space that look promising after generating a first set of data points. Once the spectrum and observables are calculated for each point, we search for points that meet some or all criteria and use these as seeds for a new iteration. With the Gaussian particle filter we can smartly search the parameter space for more points that allow the criteria, or for points that meet more criteria. Note that the width of the Gaussians can be chosen by hand: for a small width the new data points will likely be very similar to the seeds. Although this allows for the fast generation of many data points, it is easy to then overlook regions of parameter space. A balance between iterations that use a larger width to find new regions and iterations with a small width for in-depth study, is therefore necessary.

To create the SUSY spectra we use SoftSUSY 4.0 , the Higgs mass is calculated using FeynHiggs 2.14.2 , and SUSYHIT is used to calculate the decay of the SUSY and Higgs particles. Vevacious is used to check that the models have at least a meta-stable minimum state that has a lifetime that exceeds that of our universe and that this state is not color/charge breaking [4]. We use SUSY-AI and SModelS to determine the LHC exclusion of a model point. LHC cross sections for sparticle production at NLO accuracy are calculated using Prospino. HiggsBounds 5.1.1 is

[3] This includes software for the eEDM study, that we present in Chapter 5

[4] These scenarios appear in the $(g-2)_\mu$ context for large $|\mu| \tan\beta$, see e.g. Ref. [201].

Name	References	Purpose
CPsuperH$^{(*)}$	[55, 109, 160]	Benchmark check
DDCalc*	[161, 162]	Future DMDD constraints
FeynHiggs*	[163, 164]	Improved Higgs mass
GM2Calc	[98, 99]	muon anomalous magnetic moment
HiggsBounds*	[165–171]	LEP, Tevatron and LHC constraints on Higgs
HiggsSignals*	[172, 173]	Higgs constraints
Lilith*	[174, 175]	Higgs likelihood analysis
MicrOMEGAS$^{(*)}$	[176–182]	DM observables
Prospino	[183]	LHC cross sections NLO
SARAH*	[184]	Generator CPV version of SPheno
SModelS*	[185–189]	LHC exclusion limits
SPheno$^{(*)}$	[190, 191]	Spectrum generator (CPV)
SUSY-AI	[192]	LHC exclusion limits
SUSYHIT	[193]	Decay of SUSY and Higgs particles
SoftSUSY 4.0	[194]	Spectrum generator
SuperIso	[195, 196]	Flavour observables
Vevacious	[197–199]	Stable minimum of the Higgs potential

Table 4.1 An overview of the software we have used in this work. Software that can be used for the cpMSSM is shown with a $*$. If modifications are necessary, the star is between brackets.

used to determine whether the SUSY models satisfy the LEP, Tevatron and LHC Higgs constraints . MicrOMEGAs 5.2.1 is used to compute the DM relic density ($\Omega_{\rm DM}h^2$), the present-day velocity-weighted annihilation cross section ($\langle\sigma v\rangle$) and the spin-dependent and spin-independent dark-matter – nucleon scattering cross sections ($\sigma_{\rm SD,p}$ and $\sigma_{\rm SI,p}$). For DM indirect detection we only consider the limit on $\langle\sigma v\rangle$ stemming from the observation of gamma rays originating from dwarf galaxies, which we implement as a hard cut on each of the channels reported on the last page of Ref. [202]. The current constraints on the dark-matter – nucleon scattering cross sections originating from various DMDD experiments are determined via MicrOMEGAs, while future projections of constraints are determined via DDCalc 2.0.0.

Flavour observables are computed with SuperIso 4.1. The muon anomalous magnetic moment and its theoretical uncertainty is determined including two-loop corrections and $\tan\beta$ resummation with GM2Calc. We use an in-house code (see Ref. [120]) to calculate the EW finetuning measure as defined in (3.24).

Note that it is inherent to such studies that some areas of parameter space will

be sampled more often than others, due to the random nature of the data sampling. Using the Gaussian particle filter we then focus on interesting areas. As a result, some regions can seem more important than others as there are more model points. This is however a result of the sampling algorithm and has no physical interpretation. It is always possible to generate more points in a certain area, by sampling closely around an existing point. Hence we stress that for any result we show here, the density of points cannot be interpreted in terms of physics directly.

4.1.1 Constraints

We will use an upper bound of $\Delta_{\text{EW}} < 100$ (implying no worse than $\mathcal{O}(1\%)$ fine-tuning on the mass of the Z-boson) to determine whether a given set of pMSSM parameters is fine-tuned. Using this measure, one generically finds that minimally fine-tuned scenarios have low values for $|\mu|$, where $\Delta_{\text{EW}} = 100$ is reached at $|\mu| \simeq$ 800 GeV [120,156,203–208]. The masses of the gluino, sbottom, stop and squarks are allowed to get large for models with low Δ_{EW} [121,209,210]. Therefore, we assume that the masses of these sparticles are above 2.5 TeV (for the gluino), above 1.2 TeV (for the stops and sbottoms) and above 2 TeV (for the squarks), such that they evade the ATLAS and CMS limits [5].

As one can see in the expressions in (3.12) and (3.13), the neutralino-smuon and chargino-sneutrino contributions are controlled by $|M_1|$, $|M_2|$, $\tan\beta$ and $|\mu|$ (through $m_{\widetilde{\chi}_i^0}$ and $m_{\widetilde{\chi}_k^\pm}$), as well as $m_{\widetilde{L}_1}$ and $m_{\widetilde{e}_R}$ (through $m_{\widetilde{\mu}_m}$ and $m_{\widetilde{\nu}_\mu}$). They are enhanced when $\tan\beta$ grows large and when simultaneously light ($\mathcal{O}(100)$ GeV) neutralinos/charginos and smuons/sneutrinos exist in the sparticle spectrum. The Barr-Zee contributions from (3.14) are enhanced by large values of $\tan\beta$, small values of m_A and large Higgs-sfermion couplings. In general, the one-loop chargino-sneutrino contribution dominates over the neutralino-slepton contribution [101], unless there is a large smuon left-right mixing induced by a sizable value for $|\mu|$ [201]. These latter spectra will however result in slightly higher FT values, which is a direct consequence of a higher value of $|\mu|$.

The lightest SM-like Higgs boson is required to be in the mass range of 122 GeV $\leq m_h \leq$ 128 GeV to take the calculational uncertainties into account. Spectra that do not satisfy the LHC bounds on sparticle masses, branching fractions of B/D-meson decays, the DMDD, or DM indirect detection bounds are removed. Our spectra are furthermore required to satisfy the LEP limits on the masses of the charginos, light sleptons and staus ($m_{\widetilde{\chi}_1^\pm} > 103.5$ GeV, $m_{\widetilde{l}^\pm} > 90$ GeV and $m_{\widetilde{\tau}^\pm} > 85$ GeV) [211,212], and the constraints on the invisible and total width of the Z-boson ($\Gamma_{Z,\text{inv}} = 499.0 \pm 1.5$ MeV and $\Gamma_Z = 2.4952 \pm 0.0023$ GeV) [213]. We assume that the DM abundance is determined by thermal freeze-out and require that the lightest neutralino saturates $\Omega_{\text{DM}}h^2$ with the observed value of 0.12 [15] within 0.03 to allow for a theoretical

[5] Note that those limits are shown to be significantly less stringent for pMSSM spectra with rich sparticle decays, see e.g. Ref. [151].

uncertainty on the relic-density calculation.

The spectra surviving all these constraints are available via [157] [6].

4.2 Phenomenology of the surviving model points

The main experimental constraints on our models that explain the $(g-2)_\mu$ discrepancy Δa_μ come from DMDD experiments and the LHC. To understand which spectra are still viable it is crucial to understand the phenomenology of them, since the experimental exclusion power varies depending on the composition of the neutralinos and charginos.
In this section, we therefore take a look at the different scenarios and contributing compositions, and describe in detail the properties of these spectra. Knowing these properties is also relevant for considering future experimental setups, e.g. for LHC studies where the exclusion power heavily depends on the assumed model.

We first discuss the DM phenomenology of the lightest supersymmetric particle (LSP). As explained in Chapter 2, the mass eigenstate of the DM particle is a mixture of bino, wino and higgsino interaction eigenstates. To obtain the correct relic density in the pMSSM with a pure state, one can either have a higgsino with a mass of $m_{\tilde{\chi}_1^0} \simeq 800$ GeV or a wino with $m_{\tilde{\chi}_1^0} \simeq 2.5$ TeV. Spectra that saturate the relic density with lower DM masses necessarily are predominantly bino-like, mixed with higgsino/wino components. Negligible higgsino/wino components are found in so-called funnel regions [214, 215], i.e. regions where the mass of the DM particle is roughly half of the mass of the Z boson, SM-like Higgs boson or heavy Higgs boson. In such a scenario, the mass of the neutralino can even get below 100 GeV with $M_1 < 100$ GeV, and in particular the early-universe DM annihilation cross section is enhanced for $m_{\tilde{\chi}_1^0} \simeq m_{h^0}/2$ and $m_Z/2$. Moreover, spectra with another particle close in mass to the LSP can satisfy the relic density constraint without having a large wino/higgsino component too, due to the co-annihilation mechanism [216].

Requiring that our spectra are simultaneous minimally fine-tuned and satisfy the Δa_μ constraint removes two types of solutions where the DM relic density constraint is satisfied. Firstly, the case where the lightest neutralino is predominantly wino-like results in a fine-tuned spectrum: to obtain the right relic density $M_2 \simeq 2.5$ TeV for a pure wino, so $|\mu| > 2.5$ TeV in that scenario. Secondly, the pure-higgsino solutions with the right Ωh^2 do result in $\Delta_{\text{EW}} < 100$, but do not allow for an explanation of Δa_μ, which will explicitly be shown in Section 4.2.4. Therefore we will see that our solutions feature predominantly bino-like LSPs. Due to the combined Δa_μ constraint

[6] This repository contains both the raw data and a single CSV file that summarizes the SUSY parameters, masses, and the phenomenology explained in Section 4.1 of all the surviving spectra. Each line in the CSV file corresponds to one particular spectrum, whose name is uniquely specified and corresponds to the names of the directories of the raw data. The contents of the CSV file is further explained in [157].

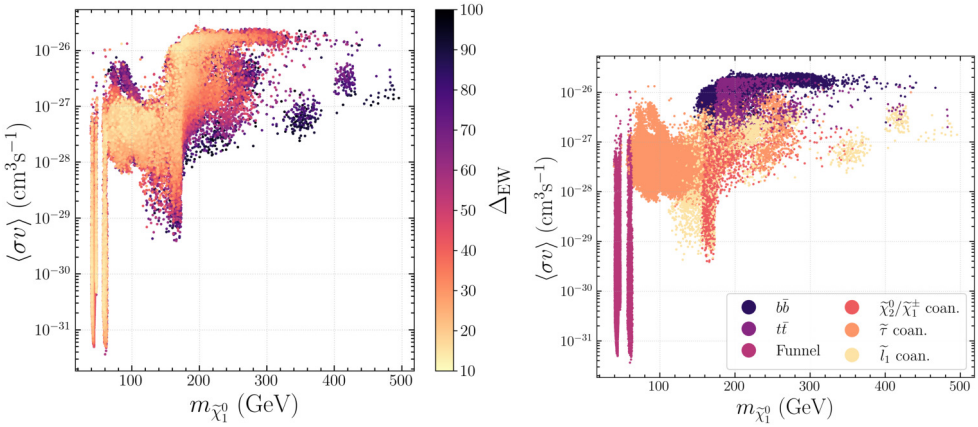

Figure 4.1 The mass of the DM particle ($m_{\tilde{\chi}_1^0}$) vs the velocity-weighted annihilation cross section ($\langle\sigma v\rangle$). The value of $\Delta_{\rm EW}$ is shown as a color code on the left, where the points are ordered such that spectra with lower values of $\Delta_{\rm EW}$ lie on top of those with higher values of $\Delta_{\rm EW}$. On the right we show the dominant early-universe annihilation process that contributes to the value of $\Omega_{\rm DM}h^2$. In both plots, we only show points that satisfy all experimental constraints, and have $133 \times 10^{-11} < \Delta a_\mu < 369 \times 10^{-11}$, allowing for a 2σ uncertainty.

(requiring high $\tan\beta$), DMDD limits and the FT requirement, the composition has a small higgsino component ($< 20\%$) and a negligible wino component.
On the left-hand side of Fig. 4.1 we show the spectra that survive all constraints and have $\Delta_{\rm EW} < 100$. Lower values for $\Delta_{\rm EW}$ are generally found for lower DM masses. The mass of the DM particle does not exceed 500 GeV, which is a direct result of the combined requirements of having $\Delta_{\rm EW} < 100$ and a sufficiently high contribution to Δa_μ. The lowest-obtained value is $\Delta_{\rm EW} = 12.3$. From the right-hand side of Fig. 4.1, we can distinguish three different types of DM early-universe annihilation mechanisms: the funnel regions, the coannihilation regions and the bino-higgsino solution (indicated with $b\bar{b}$ and $t\bar{t}$). For clarity we show in Fig. 4.2 the same plot split out per annihilation channel, where it clearly can be seen that for example the $t\bar{t}$ and $b\bar{b}$ annihilation regimes overlap.

Before discussing the phenomenology of each of these regions in more detail, we first discuss the compositions of the LSP, the second-to-lightest neutralino and the lightest chargino. As anticipated in the previous section, and as shown in Fig. 4.3, we find that the LSP is predominantly bino-like and has a small higgsino component. Larger higgsino components are generally found for spectra that show larger values of $\langle\sigma v\rangle$. The second-to-lightest neutralino and the lightest chargino are either wino-like, higgsino-like, or mixed wino-higgsino states. It might be surprising to read that spectra with bino-higgsino LSPs are allowed to have wino-like $\tilde{\chi}_2^0/\tilde{\chi}_1^\pm$, as one would

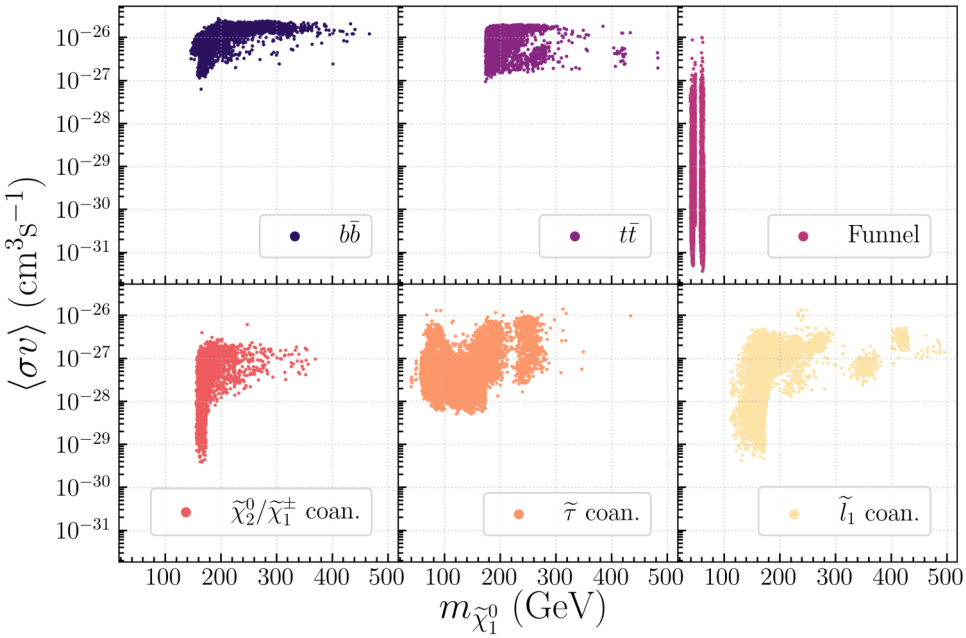

Figure 4.2 The mass of the DM particle ($m_{\widetilde{\chi}_1^0}$) vs the velocity-weighted annihilation cross section ($\langle\sigma v\rangle$). The same points as in Fig. 4.1 are shown, but split out individually for each early-universe annihilation process.

expect that in general these sparticles would be predominantly higgsino-like. This is shown in Figure 4.4 for the second neutralino $\widetilde{\chi}_2^0$.

Such configurations can however be found in spectra for which $|M_1|$, $|M_2|$ and $|\mu|$ are all of $\mathcal{O}(100)$ GeV with M_2 being smaller than $|\mu|$, and that have moderate to large values of $\tan\beta$ ($10 \lesssim \tan\beta \lesssim 20$). From Eq. (2.43) one may infer that for such spectra, little mixing can take place between the bino and wino. This results in negligible wino components of the LSP, whereas $\widetilde{\chi}_1^\pm$ and $\widetilde{\chi}_2^0$ can be predominantly wino-like. Moreover, decreasing $|\mu|$ for such models will not only result in a higher higgsino-component of the LSP, but counter-intuitively also in a *higher* wino component, while the wino component of $\widetilde{\chi}_1^\pm$ and $\widetilde{\chi}_2^0$ then *decreases*. The composition of the $\widetilde{\chi}_1^\pm$ and $\widetilde{\chi}_2^0$ sparticles is relevant for the LHC phenomenology, as those spectra where these are predominantly higgsino-like are typically difficult to probe at the LHC due to low production cross sections compared to the pure wino $\widetilde{\chi}_1^\pm/\widetilde{\chi}_2^0$ case.

In what follows, we will explore the DM phenomenology of each of these regimes in some more detail (Section 4.2.1-4.2.3). We also discuss their LHC phenomenology, and explain why our solutions elude the LHC constraints. This allows us to identify gaps in the LHC search program for supersymmetric particles. We end our discussion

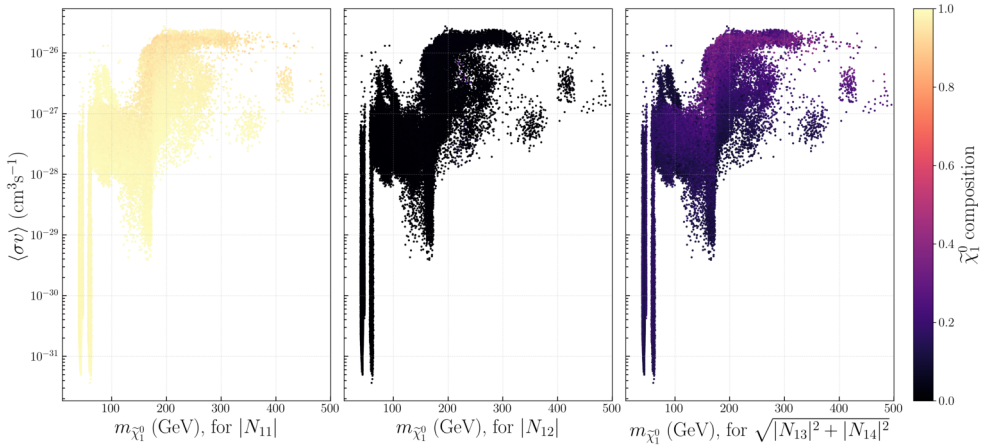

Figure 4.3 The mass of the DM particle ($m_{\tilde{\chi}_1^0}$) vs the velocity-weighted annihilation cross section ($\langle\sigma v\rangle$). The composition of the LSP is shown as a color code, with the bino component $|N_{11}|$ indicated on the left, the wino component $|N_{12}|$ in the middle, and the higgsino component $\sqrt{|N_{13}|^2+|N_{14}|^2}$ on the right.

on the phenomenology of the found solutions by discussing the sensitivity of DMDD experiments in Section 4.2.4.

4.2.1 LHC phenomenology for the funnel regimes

We start with discussing the DM phenomenology of the funnel regions, of which there are two in our spectra [7]. The first one centers around $m_{\tilde{\chi}_1^0} \simeq 40$ GeV, which is slightly less than $m_Z/2$. This can be explained as follows. The velocities of the DM particles were much higher in the early universe than what they are in the present-day universe. This means that DM annihilations via s-channel Z exchanges could happen on-resonance in the early universe, whereas in the present-day universe these exchanges only happen off-resonance. This also explains the fact that the value for $\langle\sigma v\rangle$ is allowed to get orders of magnitude smaller than the value that one usually expects for a thermal relic (around $\langle\sigma v\rangle = 3\cdot 10^{-26}$ cm^{3}s^{-1} for a DM mass of 100 GeV). These models are characterized by small wino/higgsino components of the LSP - otherwise the early-universe annihilation would be too efficient, resulting in a too-low value of $\Omega_{\rm DM}h^2$. The second funnel region is centered around $m_{\tilde{\chi}_1^0} \simeq 60$ GeV, slightly less than $m_h/2$. These DM particles annihilated in the early universe predominantly via s-channel SM-like Higgs exchanges. No solutions are found for spectra with DM masses in-between the two funnel regions. Here, the wino/higgsino component ne-

[7] The heavy Higgs funnel is not identified here, and will be left for future study.

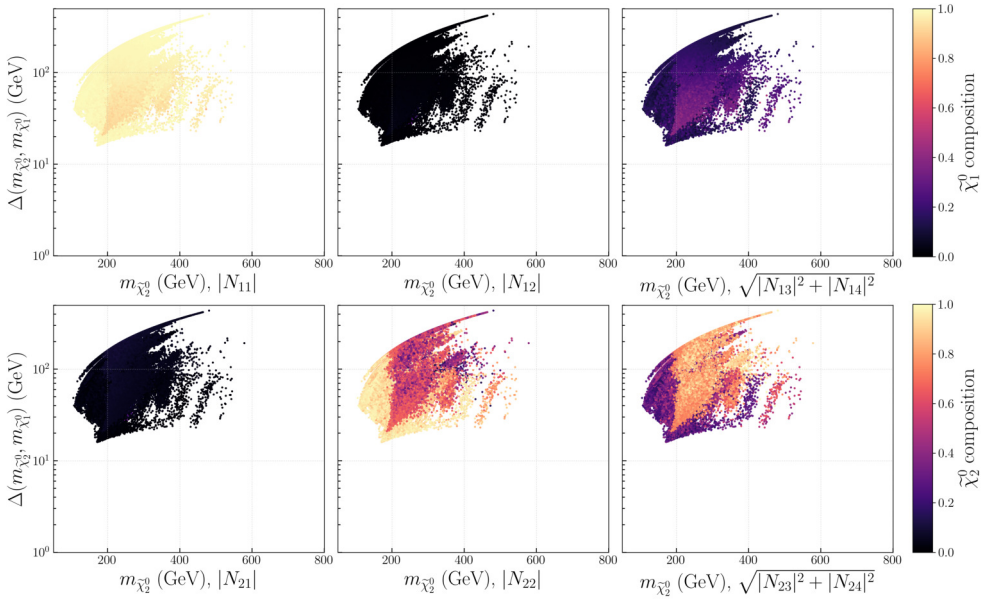

Figure 4.4 The mass difference between the DM particle and the lightest chargino. The composition of the first (second) neutralino is shown as a color code on the top (bottom) row, with the bino component $|N_{11}|$ indicated on the left, the wino component $|N_{12}|$ in the middle, and the higgsino component $\sqrt{|N_{13}|^2+|N_{14}|^2}$ on the right.

cessarily needs to increase to satisfy the $\Omega_{\rm DM}h^2$ requirement, and these spectra are excluded by DMDD experiments. The minimal value of $\Delta_{\rm EW}$ for these spectra is 13.2.

We now consider the compositions of $\widetilde{\chi}_1^0$, $\widetilde{\chi}_2^0$ and $\widetilde{\chi}_1^\pm$, and identify the mass difference between the LSP and the next-to-lightest SUSY particles in the funnel regimes, as this is important to understand the LHC phenomenology of these regions. The two funnel regimes are characterized by light ($m_{\widetilde{\chi}_1^0} < 100$ GeV) bino-like LSPs. The $\widetilde{\chi}_1^\pm$ and $\widetilde{\chi}_2^0$ are degenerate in mass. They are wino mixtures for masses around $100-200$ GeV, while they become higgsino-like for heavier $\widetilde{\chi}_1^\pm/\ \widetilde{\chi}_2^0$ (up to $m_{\widetilde{\chi}_1^\pm/\widetilde{\chi}_2^0} \simeq 500$ GeV). The mass gap between $\widetilde{\chi}_1^0$ and $\widetilde{\chi}_2^0$ or $\widetilde{\chi}_1^\pm$ ($\Delta(m_{\widetilde{\chi}_2^0}, m_{\widetilde{\chi}_1^0})$ or $\Delta(m_{\widetilde{\chi}_1^\pm}, m_{\widetilde{\chi}_1^0})$) is at least around 50 GeV, and exceeds 100 GeV for $m_{\widetilde{\chi}_1^\pm} \gtrsim 150$ GeV (see Fig. 4.5, left panel).

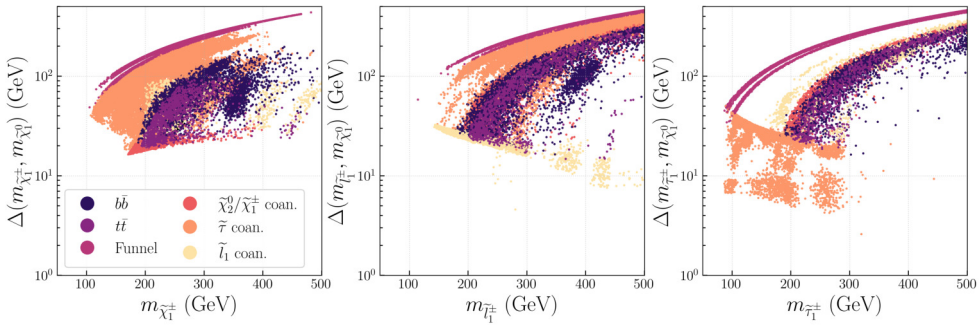

Figure 4.5 The mass difference between the DM particle and the lightest chargino (left), lightest smuon (middle) and lightest stau (right) versus the mass of the heavier particle. The color code represents the dominant early-universe annihilation channel.

The masses of the first and second generation sleptons are heavier than (at least) the masses of $\widetilde{\chi}_2^0$ and $\widetilde{\chi}_1^\pm$. Three different sorts of decays for $\widetilde{\chi}_2^0$ can be identified that are relevant final-state topologies for LHC searches:

1. $\widetilde{\chi}_2^0 \to h^0 \widetilde{\chi}_1^0$ when $\Delta(m_{\widetilde{\chi}_2^0}, m_{\widetilde{\chi}_1^0}) > m_{h^0}$,
2. $\widetilde{\chi}_2^0 \to Z \widetilde{\chi}_1^0$ when $\Delta(m_{\widetilde{\chi}_2^0}, m_{\widetilde{\chi}_1^0}) > m_Z$,
3. off-shell decays when $\Delta(m_{\widetilde{\chi}_2^0}, m_{\widetilde{\chi}_1^0}) < m_Z$.

For $\widetilde{\chi}_1^\pm$, there are only two sorts of decays

1. $\widetilde{\chi}_1^\pm \to W^\pm \widetilde{\chi}_1^0$ when $\Delta(m_{\widetilde{\chi}_1^\pm}, m_{\widetilde{\chi}_1^0}) > m_W$,
2. off-shell decays when $\Delta(m_{\widetilde{\chi}_1^\pm}, m_{\widetilde{\chi}_1^0}) < m_W$.

We now determine why our points in the funnel region survive the LHC constraints. Given that the first and second generation sleptons in these spectra are heavier than $\widetilde{\chi}_2^0$ and $\widetilde{\chi}_1^\pm$, searches for $\widetilde{\chi}_2^0 \widetilde{\chi}_1^\pm$ production with on-shell decays of $\widetilde{\chi}_2^0 \to Z \widetilde{\chi}_1^0$, such as those in Ref. [217–220], are most sensitive to our spectra. However, whenever $\Delta(m_{\widetilde{\chi}_2^0}, m_{\widetilde{\chi}_1^0}) > m_{h^0}$, we find that in our models there exists a mixture between $\widetilde{\chi}_2^0 \to h^0 \widetilde{\chi}_1^0$ and $\widetilde{\chi}_2^0 \to Z \widetilde{\chi}_1^0$ decays. This is part of the reason why our models evade the LHC limits: the sensitivity of the experiments drops when $\widetilde{\chi}_2^0$ can decay into the SM-like Higgs boson [218, 221]. A second reason why these spectra evade the LHC limits is that the simplified limits of the searches mentioned above assume a wino-like $\widetilde{\chi}_2^0 \widetilde{\chi}_1^\pm$ pair, whereas we deal with mixed wino-higgsino pairs.

To interpret the above-mentioned analyses, we show in the left panel of Fig. 4.6 the average cross section per 10 by 10 GeV bin for $\widetilde{\chi}_2^0 \widetilde{\chi}_1^\pm$ production. We determined whether a given model point is excluded by parameterizing the upper

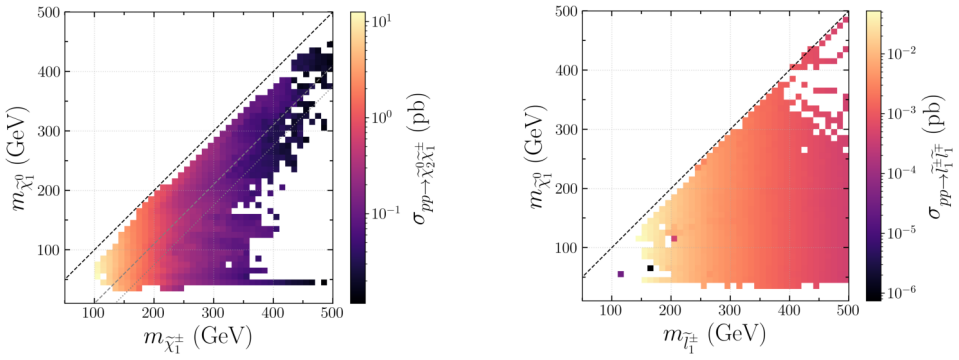

Figure 4.6 The mass of the DM particle versus the mass of the lightest chargino (left) and smuon (right), combined in 10 by 10 GeV bins. The average production cross section of $\sigma_{pp\to\tilde{\chi}_2^0\tilde{\chi}_1^\pm}$ (left) and $\sigma_{pp\to\tilde{l}_1^\pm\tilde{l}_1^\mp}$ (right) is shown in color code for each bin. The dashed black line in the plot on the left-hand side shows the limit where $m_{\tilde{\chi}_1^0} = m_{\tilde{\chi}_1^\pm}$, whereas the gray dashed (dotted) lines show $m_{\tilde{\chi}_1^\pm} = m_{\tilde{\chi}_1^0} + m_Z$ ($m_{\tilde{\chi}_1^\pm} = m_{\tilde{\chi}_1^0} + m_{h^0}$). The dashed black line in the plot on the right-hand side shows $m_{\tilde{\chi}_1^0} = m_{\tilde{l}_1^\pm}$.

bounds on the cross sections as shown in Ref. [219], Fig. 7 and 8, Ref. [218], Fig. 11 and Ref. [220], Fig. 5 and 6. We find that our cross sections in the regime where $m_Z < \Delta(m_{\tilde{\chi}_2^0}, m_{\tilde{\chi}_1^0}) < m_{h^0}$ do no not exceed the 95% confidence level (CL) limits. We expect this situation to change if more LHC data is collected, making the LHC sensitive to this part of the funnel parameter space. The models with off-shell decays are slightly more constrained by the current results of the LHC experiments. Particularly Ref. [220] excludes some of our spectra in this regime that have $m_{\tilde{\chi}_1^\pm}$ up to 210 GeV and $\Delta(m_{\tilde{\chi}_2^0}, m_{\tilde{\chi}_1^0}) < 55$ GeV. These spectra are explicitly removed from the plots. The LHC shows limited sensitivity to the models in the mass range of 55 GeV $< \Delta(m_{\tilde{\chi}_1^\pm}, m_{\tilde{\chi}_1^0}) < m_Z$. To gain full sensitivity to the funnel regions, this mass range is an important domain to cover in the LHC searches.

4.2.2 LHC phenomenology for the coannihilation regimes

The second regime is the coannihilation regime, whose DM phenomenology we now discuss. It starts to open up at DM masses of roughly 70 GeV, as no charged sparticles (and therefore no coannihilation partners other than the sneutrino) can exist with masses below 85 GeV due to the LEP/LHC bounds. Three different types of coannihilation partners are identified: first-/second-generation sleptons, third-generation sleptons, and charginos or heavier neutralinos. Interestingly, only with the help of slepton coannihilations the DM particle can have a mass between $\mathcal{O}(70-150)$ GeV and still give the right $\Omega_{\text{DM}}h^2$. To obtain the right relic density in this regime without

a slepton-coannihilation partner, one generally needs high higgsino fractions, which increases the value of $\sigma_{\mathrm{SI,p}}$ beyond the exclusion limit of the DMDD experiments. The lowest values of Δ_{EW} are found in the stau-coannihilation regime ($\Delta_{\mathrm{EW}} = 12.3$), while the first-/second-generation slepton and chargino/neutralino regimes result in lowest values $\Delta_{\mathrm{EW}} = 14.4$ and $\Delta_{\mathrm{EW}} = 16.4$ respectively. The coannihilation regimes are all characterized by small mass differences between the LSP and its coannihilation partner(s).

The first type of coannihilation is that of first-/second-generation sleptons ($\widetilde{l}_1^{\pm}$). The compression between $m_{\widetilde{l}_1^{\pm}}$ and $m_{\widetilde{\chi}_1^0}$ is increased for higher LSP masses such that the right $\Omega_{\mathrm{DM}}h^2$ can still be obtained, see Figure 4.5. By computing the production cross sections $\sigma_{pp\to\widetilde{\chi}_2^0\widetilde{\chi}_1^{\pm}}$ and $\sigma_{pp\to\widetilde{l}_1^{\pm}\widetilde{l}_1^{\mp}}$ (see Fig. 4.6), and comparing these to the results of Fig. 20 of Ref. [221], we see that spectra with $\Delta(m_{\widetilde{\chi}_2^0}, m_{\widetilde{\chi}_1^0}) > m_Z$ are under strong constraints from searches for $\widetilde{\chi}_2^0\widetilde{\chi}_1^{\pm} \to \widetilde{l}\widetilde{l}l\nu_l$. We explicitly remove those points from our data, leaving only models with $\Delta(m_{\widetilde{\chi}_2^0}, m_{\widetilde{\chi}_1^0}) < m_Z$. The $\widetilde{\chi}_1^{\pm}$ and $\widetilde{\chi}_2^0$ sparticles of the surviving models are typically higgsino-like with a small wino component, and have masses between 180 and 500 GeV.

The second coannihilation regime is characterized by low $\widetilde{\tau}_1^{\pm}$ masses. The masses of $\widetilde{\chi}_1^{\pm}/\widetilde{\chi}_2^0$ can still be as light as 105 GeV in this regime, where they are predominantly wino-like. The higgsino component of these particles increases when their masses increase, up to $m_{\widetilde{\chi}_1^{\pm}/\widetilde{\chi}_2^0} \simeq 500$ GeV. Although we have a large production cross section for the wino-like $\widetilde{\chi}_1^{\pm}/\widetilde{\chi}_2^0$ pair, these models are not constrained by the LHC experiments due to the presence of the light staus. The staus are often lighter than $\widetilde{\chi}_1^{\pm}$ and $\widetilde{\chi}_2^0$, and the searches for $\widetilde{\tau}_1^{\pm}$-mediated decays of $\widetilde{\chi}_1^{+}\widetilde{\chi}_1^{-}/\widetilde{\chi}_1^{\pm}\widetilde{\chi}_2^0$ production have no sensitivity when $\Delta(m_{\widetilde{\chi}_1^0}, m_{\widetilde{\tau}_1^{\pm}}) < 100$ GeV [222, 223]. The latter holds for our spectra in the second coannihilation regime, since the mass differences between the LSP and $\widetilde{\tau}_1^{\pm}$ are between $5 - 50$ GeV in that case (see also Figure 4.5, right panel). Additionally, relatively few LHC searches for low-mass $\widetilde{\tau}^{\pm}$ particles exist. Small $\widetilde{\tau}^{+}\widetilde{\tau}^{-}$ production cross sections and low signal acceptances make these searches difficult, so the experiments have no constraining power in the compressed regime [224, 225].

We suggest a dedicated low mass $\widetilde{\tau}^{\pm}$ search without an assumed mass degeneracy between $\widetilde{\tau}_1^{\pm}$ and $\widetilde{\tau}_2^{\pm}$ to probe the sensitivity of the LHC to these scenarios.

The last coannihilation regime has a $\widetilde{\chi}_1^{\pm}$ or $\widetilde{\chi}_2^0$ that is close in mass to the LSP. Interestingly, although the mass compression for the slepton coannihilation regimes needs to increase to obtain the right relic density for higher DM masses, for the gaugino-coannihilation regime it needs to decrease instead (see Figure 4.5, left panel). Regarding the LHC phenomenology, note that although the slepton masses in these regions can be $\mathcal{O}(200)$ GeV, the results from the $\widetilde{l}_{R,L}^{+}\widetilde{l}_{R,L}^{-}$ searches with $\widetilde{l}^{\pm} = \widetilde{e}^{\pm}, \widetilde{\mu}^{\pm}$ or $\widetilde{\tau}^{\pm}$ (e.g. [225–227]) are not directly applicable here, as often one or more of the chargino/heavier neutralino states is lighter than the sleptons. Therefore, the slepton

will not decay with a 100% branching ratio to $\widetilde{\chi}_1^0 l^\pm$, although this is assumed in the above-mentioned searches. Instead, in this regime, only the $\widetilde{\chi}_1^\pm \widetilde{\chi}_2^0$ searches are of relevance, similar to the case in the funnel region discussed above. The mass compression between the LSP and wino-higgsino like $\widetilde{\chi}_1^\pm/\widetilde{\chi}_2^0$ sparticles is generally around 15-20 GeV, and Ref. [220] excludes our solutions with $m_{\widetilde{\chi}_1^\pm}$ up to 140 − 180 GeV.

4.2.3 LHC phenomenology for the bino-higgsino LSP

The last regime we identify consists of bino-higgsino LSPs and is labeled with $b\bar{b}$ and $t\bar{t}$. These early-universe annihilation channels are mediated by either s-channel Z or h^0/H^0 exchanges. The $t\bar{t}$ annihilation channel opens up when $m_{\widetilde{\chi}_1^0}$ becomes larger than the mass of the top quark m_t, as then the invariant mass of the two LSPs is enough to create a $t\bar{t}$ pair [8]. For the Z-exchange channel this annihilation becomes favored over the annihilation into a lighter fermion pair, since any Z-mediated annihilation of two Majorana fermions is helicity suppressed at tree level [228]. This is explained as follows. The two identical LSPs form a Majorana pair. Such a pair is even under the operation of charge-conjugation $C = (-1)^{L+S}$ with S the total spin and L the total orbital angular momentum, so L and S must either both be even, or both be odd. Taking the limit of zero velocity, as the present-day velocity of DM particles is non-relativistic, we may assume $L = 0$ and even S. The final-state fermion pair can have a total spin of $S = 1$ or $S = 0$, but only the latter is allowed for the Majorana-pair annihilation in the non-relativistic limit. For a Dirac-field pair, an $S = 0$ configuration is obtained if the fermion and anti-fermion are from different Weyl spinors: a left- and right-handed one. In the SM, a coupling with this combination only arises (at tree level) by a mass insertion. Therefore, the transition amplitude is proportional to the mass of the final-state fermions, and a decay to a heavier pair of fermions is generally preferred. In spectra where $\tan\beta$ is large we also see the heavy-Higgs-mediated decays to $b\bar{b}$, as the bottom-Yukawa coupling is enhanced. As can be seen in Fig. 4.5, in the regime of $m_{\widetilde{\chi}_1^0} \gtrsim m_t$, the masses of $\widetilde{\chi}_1^\pm$ and $\widetilde{\chi}_2^0$ are relatively close to that of the LSP, so due to the coannihilation mechanism these spectra tend to show slightly lower values of $\langle\sigma v\rangle$ than naively would be expected.

The minimal value of $\Delta_{\rm EW}$ is around 14.2 for these models. The $\widetilde{\chi}_2^0$ and $\widetilde{\chi}_1^\pm$ are predominantly higgsino-like with masses from 180 to 500 GeV. Due to their small production cross section, the LHC searches do not have exclusion power in this regime.

[8] The annihilation to a W^+W^- pair is possible when $m_{\widetilde{\chi}_1^0} > m_W$. However, this is constrained by DMDD due to the high wino/higgsino fraction that is necessary for this channel.

4.2.4 Dark-matter direct detection experiments

In the previous subsections we discussed the phenomenology of the viable spectra at the LHC. We now comment on the sensitivity of DMDD experiments. We have seen that the LSP in our spectra is always bino-like with a small higgsino component (Fig. 4.3). We find that the relative size of the wino component of the LSP is constrained by DMDD experiments: higher wino components result in larger values of $\sigma_{\mathrm{SI,p}}$ and $\sigma_{\mathrm{SD,p}}$. Surprisingly, this indirectly also places a lower bound on $|\mu|$: decreasing $|\mu|$ for our models will not only result in a higher higgsino-component, but also in a higher wino component of the LSP, as more mixing between the wino and bino components is then allowed. Therefore, decreasing $|\mu|$ for these scenarios is limited by the constraints imposed by the DMDD experiments.

The resulting values for $\sigma_{\mathrm{SI,p}}$ and $\sigma_{\mathrm{SD,p}}$ of the surviving models may be seen in Fig. 4.7. While the value of $\sigma_{\mathrm{SI,p}}$ varies by over 7 orders of magnitude, $\sigma_{\mathrm{SD,p}}$ is relatively constrained. We moreover observe that $\sigma_{\mathrm{SD,p}}$ is directly correlated with Δ_{EW}: lower values of $\sigma_{\mathrm{SD,p}}$ result in higher values of Δ_{EW}. The value of $\sigma_{\mathrm{SD,p}}$ decreases with smaller higgsino fractions in the LSP, while for a given fixed LSP mass Δ_{EW} increases since $|\mu|$ needs to increase in order to lower the higgsino fraction in the LSP. In this figure we also indicate the projected limit of the PICO-40L and the PICO-500 experiments [39]. We observe that the latter one is sensitive to all of our solutions with $\Delta_{\mathrm{EW}} < 62$. The LUX-ZEPLIN experiment [38, 229] (whose projected limit is not shown in Fig. 4.7) will ultimately probe all of our solutions with $\Delta_{\mathrm{EW}} < 100$ once it reaches its full potential.

This shows an important message, namely that

future DMDD experiments that probe $\sigma_{\mathrm{SD,p}}$ will be sensitive to all our solutions, irrespective of the masses and compositions of the rest of the sparticle spectrum.

That the Δa_μ requirement is crucial to obtain this conclusion is shown in the bottom panel of Fig. 4.7, where we show both the spectra from this work and those from Ref. [120] without imposing the Δa_μ constraint. One may observe that in this case spectra survive with $m_{\tilde{\chi}_1^0} > 500$ GeV that show very small values of $\sigma_{\mathrm{SD},p}$. These pure higgsino solutions have vanishing couplings to the Z-boson and therefore evade detection at future DMDD experiments, but do not satisfy the Δa_μ requirement.

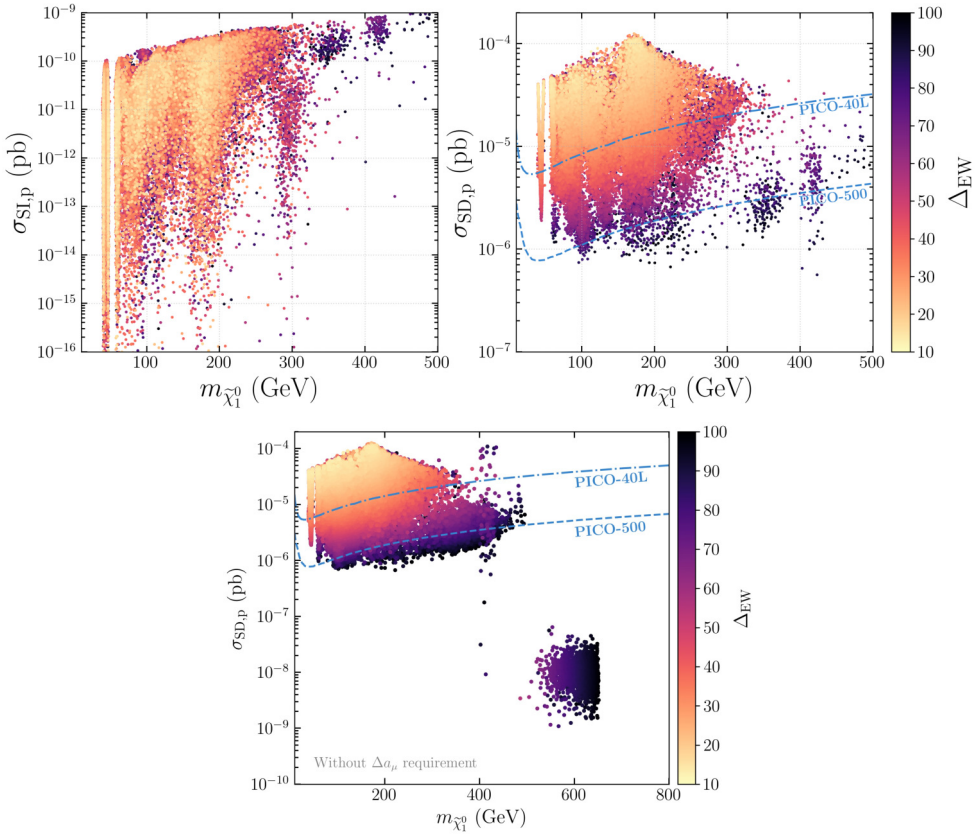

Figure 4.7 Top right (left): The mass of the DM particle versus the spin-(in)dependent cross section $\sigma_{\mathrm{SD,p}}$ ($\sigma_{\mathrm{SI,p}}$). The value of Δ_{EW} is shown in color code. We also show the projected PICO-40L and PICO-500 central limits on $\sigma_{\mathrm{SD,p}}$ [39]. The points are ordered such that those with lower values of Δ_{EW} lie on top of those with higher values. Bottom: The mass of the DM particle versus $\sigma_{\mathrm{SD,p}}$ for spectra satisfying all constraints listed in Section 4.1 except the Δa_μ requirement. This plot contains the data of the present study combined with that from Ref. [120], where the requirement on a_μ was not taken into account.

4.3 Conclusion

In this study we have analyzed for the first time the spectra in the pMSSM that are minimally fine-tuned, result in the right $\Omega_{\rm DM}h^2$ *and* simultaneously offer an explanation for Δa_μ. We have made these spectra publicly available under [157].
In terms of DM phenomenology, we have distinguished three interesting branches of solutions: the funnel regimes, three types of coannihilation regimes, and the generic bino-higgsino solution. All these solutions have in common that the LSP is predominantly bino-like with a small higgsino component. The mass of the DM particle ranges between $39-495$ GeV. We discussed the phenomenology at the LHC for each of the regimes. The first and second regime are relatively more constrained by $\widetilde{\chi}_2^0\widetilde{\chi}_1^\pm$ searches at the LHC than the last regime, which is due to the lower wino-components and higher masses of the $\widetilde{\chi}_2^0/\widetilde{\chi}_1^\pm$ sparticles that are typical in the last regime. On the other hand, in particular when the coannihilation partner of the LSP is a light stau, the LHC searches show little to no sensitivity to our found solutions. Our solutions motivate further the ongoing efforts at the LHC to probe pMSSM spectra that feature (compressed) higgsino-like production of $\widetilde{\chi}_2^0\widetilde{\chi}_1^\pm$ pairs. In addition, to increase the sensitivity of the LHC to our found solutions, we find that a dedicated low-mass $\widetilde{\tau}^\pm$ search without an assumed mass degeneracy between $\widetilde{\tau}_1^\pm$ and $\widetilde{\tau}_2^\pm$ would be needed, but also that the mass-gap region of 55 GeV $< \Delta(m_{\widetilde{\chi}_2^0}, m_{\widetilde{\chi}_1^0}) < m_Z$ is not probed at the LHC. Proposing a the details of a dedicated search for these regimes, however, lies beyond the scope of this work.

We find that DMDD experiments such as the LUX-ZEPLIN [38, 229] that probe $\sigma_{\rm SD,p}$ will ultimately be sensitive to all of our minimally fine-tuned spectra. The requirement of satisfying Δa_μ is crucial to arrive at this conclusion. This requirement excludes models with a higher-mass higgsino with $m_{\widetilde{\chi}_1^0} = 550-650$ GeV as the LSP, and these spectra would evade detection by future DMDD experiments.

Chapter 5

The electron electric dipole moment

In this Chapter we will expand our previous $(g-2)_\mu$ study to the cpMSSM, allowing us to study the eEDM. Our aim is to study the degree of fine-tuning in the cpMSSM, specifically for model points that agree with the experimental limit on the eEDM. The central question is: how are the eEDM and the degree of fine-tuning correlated?

Many studies have been done on the eEDM in supersymmetric models [56–58,94,110]. However, such studies typically assume many constraints on the MSSM in order to limit the number of free parameters that are involved. Nowadays it is possible to run computations with more free parameters, allowing for more complicated models such as the cpMSSM. This also allows for a more nuanced study of the eEDM in relation to LHC and DM observables. Previous studies claim that the experimental limit on the eEDM can only be satisfied when the sparticle masses are at least of $\mathcal{O}(1\text{ TeV})$, or the phases are at most of $\mathcal{O}(10^{-5})$ (see e.g. [58]). We will test this claim in the cpMSSM, as we expect the additional free parameters to allow for a more complicated phenomenology.

5.1 Analysis setup

As we have already generated many data points in the pMSSM for our study in Chapter 4, we will use these as a start for the eEDM study in the cpMSSM. The general set-up is similar: we generate data points, compute the spectrum for each data point, calculate the observables and remove all points that do not satisfy the constraints. To generate the data points, we sample around the points from the $(g-2)_\mu$ data set and extend the new points to the cpMSSM by adding phases.

However, the available software to study the cpMSSM is not as extensive as for the pMSSM. We have therefore written our own code to calculate the value of the eEDM for a model point and to calculate the degree of FT as defined in (3.27). To generate a spectrum in the cpMSSM we use an adapted version of SPheno: SPheno-CPV, which we will explain in more detail in Section 5.1.2.

5.1.1 Obtaining input

We start with the model points from the $(g-2)_\mu$ study that survive all constraints listed in Section 4.1.1 and extend these to the cpMSSM. We extract the pMSSM input parameters from the $(g-2)_\mu$ output data and use SPheno-CPV to generate the cpMSSM spectra. In Table 2.4 we present an overview of the cpMSSM parameters, of which $\text{Re}\, b, \text{Im}\, b$ and $|\mu|$ are determined by the tadpole equations. Note that this implies that $m^2_{H_u}$ and $m^2_{H_d}$ are input parameters for this study, in contrast to our analysis in the pMSSM.

We want to avoid duplication of the $(g-2)_\mu$ data. Therefore, we also slightly vary the absolute values of the pMSSM parameters, instead of only extending the data points with phases. Per data point, we use a Gaussian distribution around each

parameter and sample from this distribution to obtain a new value for the pMSSM parameter. Then we extend the data point with a value for each phase.

- First we translate the pMSSM parameters to absolute values and phases. Then we use for each pMSSM parameter P_i a Gaussian distribution of the form

$$p(x) = \frac{1}{\sqrt{2\pi\sigma_i^2}} e^{-\frac{(x-\mu_i)^2}{2\sigma_i^2}}, \tag{5.1}$$

  where we choose $\mu_i = P_i$ and $\sigma_i = w_i P_i$. The width w_i is a manual setting that can be chosen for each parameter individually, where a typical value is of order $\mathcal{O}(0.1 - 0.01)$. We choose such a small width to avoid a large deviation from the original $(g-2)_\mu$ values, as the original parameters resulted in a correct spectrum.
- Next we extend the obtained data to the cpMSSM by adding the phases $\eta, \phi_\mu, \phi_{A_t}, \phi_{A_b}$, $\phi_{A_\tau}, \phi_{M_1}, \phi_{M_2}$ and ϕ_{M_3}. We do this by generating a random value for each phase, such that the sign of the pMSSM parameter remains the same. We generate a number P_i' from the probability distribution 5.1 for each pMSSM parameter P_i. For parameters that are still real in the cpMSSM, we obtain the new parameter C_i as follows

$$C_i' = \text{sign}(P_i)|P_i'|, \tag{5.2}$$

  while for parameters that do obtain a phase, we multiply P_i' with a randomly generated phase to obtain

$$C_i' = \text{sign}(P_i)|P_i'|e^{i\phi_i}. \tag{5.3}$$

  The phases ϕ_i and η are taken from a logarithmic distribution that is bound to

$$10^{-6} < |\phi_i|, |\eta| < B_i, \tag{5.4}$$

  where one can choose the value of B_i. We choose 10^{-6} to avoid problems with numerical stability, which show up for lower values. The default setting is to use

$$B_\eta, B_\mu = \pi, \tag{5.5}$$

$$B_i = \pi/2 \quad \text{for } i \neq \mu, \tag{5.6}$$

  as this fully covers the parameter space of the cpMSSM. For specific studies we limit the phases, e.g. in Section 5.4 we use a data set with $10^{-6} < |\phi_\mu, \eta| < 10^{-2}$.

Note that we sample η and ϕ_μ in a larger range than the other phases. For η this is because the parameter does not occur in the pMSSM at all and we thus have to sample the entire range here. For μ we solve for $|\mu|$ in the tadpole equations, meaning we have to sample ϕ_μ in such a way that we complement this. We therefore do not take sign(μ) from the pMSSM data, but sample it with ϕ_μ.

In Figure 5.1 we show an overview of the process to create cpMSSM input data from the $(g-2)_\mu$ data points that survive all constraints. Next, we will generate the spectrum and calculate the observables for each data point.

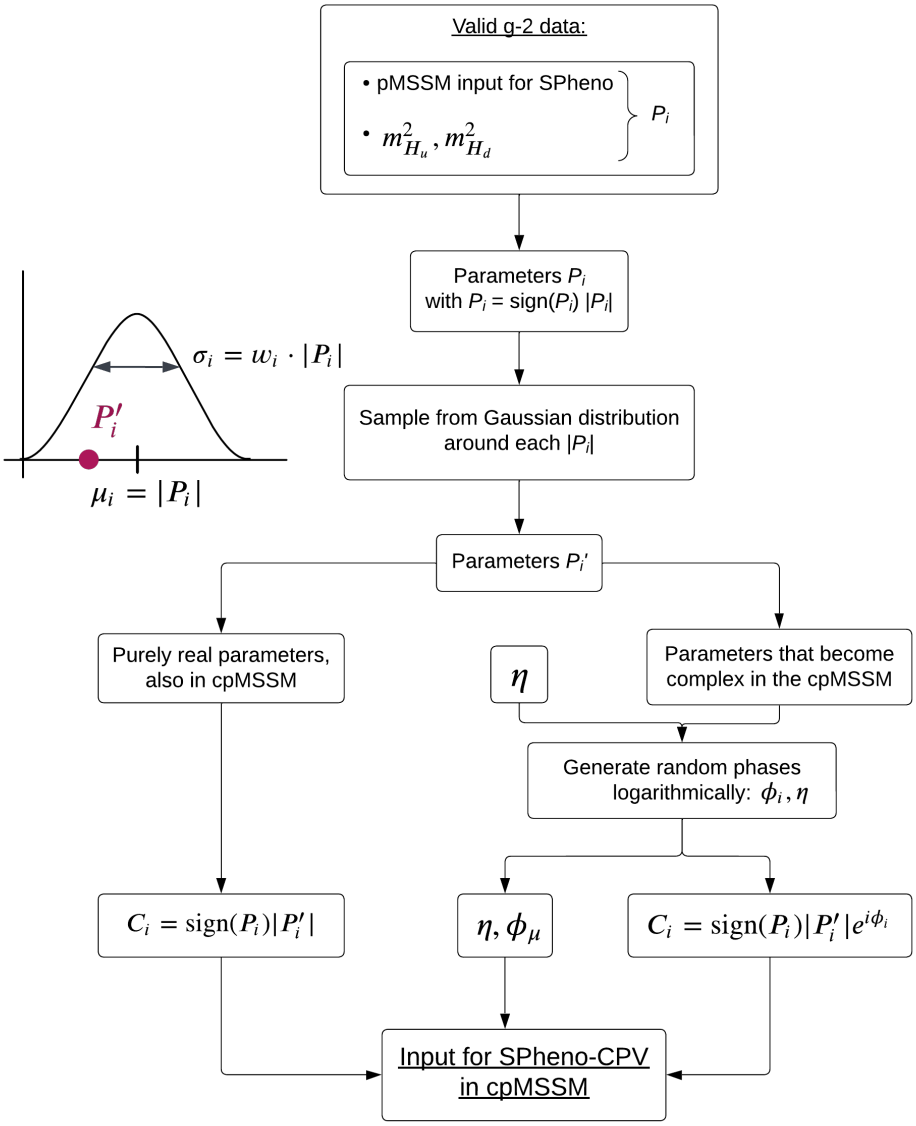

Figure 5.1 Flow chart to show the process of creating input for SPheno-CPV from the $(g-2)_\mu$ data.

5.1.2 Generating spectra and calculating observables

To generate a spectrum for the cpMSSM points, we need a spectrum generator that can take the complex parameters fully into account. Our previous choice in Chapter 4, SoftSUSY, is not suitable to deal with complex input parameters. Similarly ISAJET, SPheno and SUSPECT are not compatible. Although FeynHiggs has the option to study complex input, it only generates the spectrum of the Higgs bosons instead of a full spectrum that includes all supersymmetric masses and couplings.

This leaves CPsuperH, which was specifically designed to study supersymmetry with CPV and hence seems to be a good choice. However, it was never meant to be used for the parameter values that we would like to study in the cpMSSM. At the time that this software was designed, it was not known what the mass of the SM Higgs boson would be, and it was generally expected to be much lighter than 125 GeV. Combined with the effective potential approach that is implemented for the spectrum calculation, this can lead to significant deviations from the results of other spectrum generators. A comparative study can be found in Appendix D, where we use the same input and generate a spectrum with CPsuperH and SPheno in the pMSSM. Since the differences between the spectra are significant for the sparticle masses and mixing matrices, also for the regions of parameter space that we want to study, we conclude that CPsuperH is not suited for our study of the cpMSSM.

Instead we have opted to use the SARAH package to generate a new version of the SPheno code that is specifically designed for the cpMSSM. In Appendix E we show the model files that we have defined to generate this code. We have compared the results of this new CPV version of SPheno (SPheno-CPV) with the original SPheno for real values of the parameters and find only small differences. These differences are to be expected in the pMSSM, as SPheno-CPV does not include the same loop-level calculations as SPheno itself. For details, see [190, 191] for SPheno and [184, 230–232] for SPheno-CPV as generated by SARAH.

Furthermore we have compared the results of CPsuperH and SPheno-CPV. We do this for a set of input parameters for which we would expect similar results, namely for a set with minimal mass splitting between the two sfermions of the same generation. The pMSSM spectra are similar ($\mathcal{O}(10\%)$ differences between the two spectra) for these parameter sets. We find that indeed also the cpMSSM spectra are within a 10% uncertainty. All in all we conclude that SPheno-CPV is reliable enough for our study of the eEDM in the cpMSSM.

With the spectra from SPheno-CPV we set up the rest of our analysis. See Figure 5.2 for an overview. We use FeynHiggs 2.18 to lower the uncertainty on the Higgs boson masses. As it is an implicit assumption in FeynHiggs that the parameter b is real, we rotate the phases of the spectrum before running FeynHiggs. See Section 2.4 for a discussion about this rotation.

We use Micromegas 5.2.13 to calculate the DM observables and DMDD exclusion limits. However, it was necessary to make some changes in order to use our own generated spectrum as input for the Micromegas calculations. Without these changes,

Micromegas uses an integrated version of CPsuperH to generate its own spectrum for the DM observables. As we explicitly want to avoid using CPsuperH, we have made it possible to use input from an SLHA formatted file instead of using input from CPsuperH.

For the calculation of d_e^E we have written a Python code, which includes the 1-loop contributions and 2-loop Barr-Zee contributions. Also the $\tan\beta$ resummation (or threshold corrections) are taken into account [55]. We have verified that our code gives the same results as CPsuperH if we calculate d_e^E directly from the masses, mixing matrices and couplings as in Section 3.1.2. Finally we calculate the FT as defined in Section 3.3, both Δ_{EW} and Δ_ϕ, with two in-house scripts.

As explained in 4.1, sampling can leave artefacts in the data. We stress again that for any result we show, the density of points cannot be interpreted in terms of physics directly.

5.1.3 Constraints

Some of the resulting spectra are excluded, now that phases have been added to the original pMSSM parameters. Therefore we apply the following constraints (again) on the spectra:

- 122 GeV $< m_{h_1^0} <$ 128 GeV;
- LEP and LHC constraints as explained in Section 4.1.1;
- DMDD and DM indirect detection constraints: Xenon, DarkSide;
- Lilith Higgs constraints with a 2σ uncertainty;
- HiggsBounds limits with a 2σ uncertainty.

All the spectra that we discuss in the remainder of this chapter survive these constraints.

Note that, contrary to the analysis in Chapter 4, we do not include the constraints on the DM relic density. Due to the nature of our data set, we generate very few points ($\mathcal{O}(10^3)$) that satisfy $\Omega_{\text{DM}}h^2 = 0.12 \pm 0.03$. In hindsight this is due to our usage of the $(g-2)_\mu$ data set as starting point for the cpMSSM data points. As is explained in Chapter 4, we have searched very specifically for points that satisfy the DM constraints in the $(g-2)_\mu$study. Satisfying this constraint depends profoundly on the interplay of the pMSSM parameters, due to the involved funnel structures and co-annihilation mechanisms. As a result, those points are very sensitive to a small change in the parameter values, effectively creating a kind of fine-tuning. Small changes in the pMSSM parameters therefore have a vast effect on the value of $\Omega_{\text{DM}}h^2$.

All in all, a full study in the cpMSSM parameter space is necessary to properly probe solutions that satisfy both the eEDM and DM constraints. We will discuss this further in Section 6.3, as we are currently working on an extension of our study.

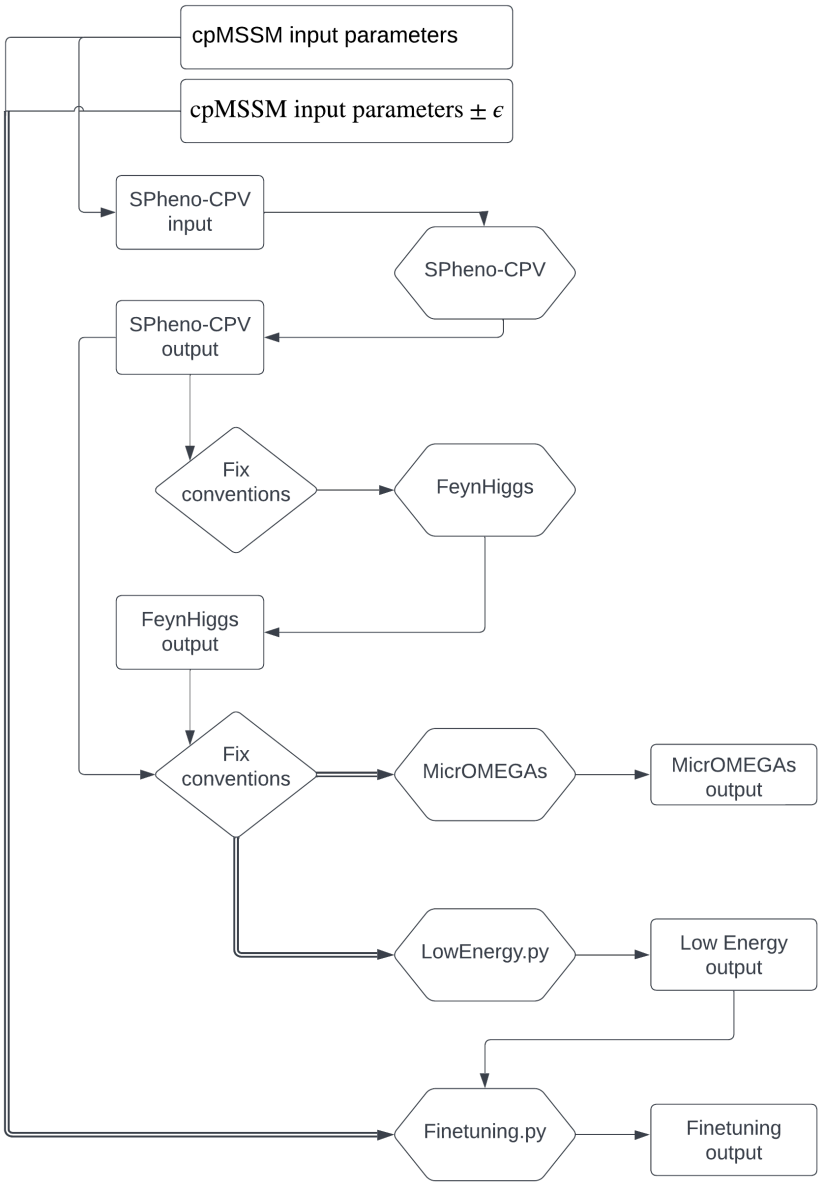

Figure 5.2 Flow chart of the different software packages and necessary adaptations of their output to be suitable as input for the next package. Note that the conventions for SPheno-CPV, FeynHiggs and MicrOMEGAs are different. The packages LowEnergy.py and Finetuning.py are in-house codes to calculate the low energy observables and the FT, respectively.

5.1.4 Set-up for the different runs

In order to study the effect of the different phases on the eEDM, we have created several data sets with slightly different properties by sampling the phases in specific domains. This allows us to study the properties of the cpMSSM in specific scenarios. The runs have the same general properties, as described above. In Table 5.1 we show the specific properties of the different runs.

Name of the run	Properties
Iter10	$10^{-6} < \|\eta\|, \|\phi_\mu\| < 10^{-2}$
Iter11	$10^{-6} < \|\eta\|, \|\phi_\mu\|, \|\phi_{M_2}\| < 10^{-2}$
Iter12	$10^{-6} < \|\phi_i\| < \pi/2$, $10^{-6} < \|\eta\|, \|\phi_\mu\| < \pi$
Iter13	$10^{-6} < \|\eta\|, \|\phi_\mu\|, \|\phi_{M_2}\|, \|\phi_{M_1}\| < 10^{-2}$

Table 5.1 The additional constraints that have been used to generate the data for different runs, allowing us to study the eEDM in specific scenarios.

5.2 Studying the individual phases

First we want to gain some basic understanding of the cpMSSM and the relation between the parameters and the eEDM. This will also help us understand the relationship between the FT and the eEDM better, as we use a definition that contains the derivative of d_e^E with respect to the phases. In order to do so, we have studied the influence of the individual phases on the eEDM.

For the first part of this study we have selected two data points, of which the parameter values are given in Appendix G. Note that the data points are chosen for their low values of d_e^E, namely $9.0054 \cdot 10^{-33}$ e cm (point 1) and $6.2557 \cdot 10^{-34}$ e cm (point 2). Only the phase ϕ_{M_3} or ϕ_{A_b} was given a small but nonzero value, for point 1 and point 2 respectively. This allows us to study the impact of an individual phase, as the other phases do not contribute, or hardly contribute, to d_e^E.

For each data point we have generated new data sets by varying one single phase between 0 and 2π. Each set thus has the parameters as listed in Tables G.1 and G.2, except the phase we are studying in that set. We have also generated sets where the phase was varied between 10^{-8} and 10^{-2} to study the behaviour for small values of the phases.

We note that some phases have a much larger influence on d_e^E than others. In Figure 5.3 we show the results of the data sets where ϕ_{A_t} and ϕ_μ were varied between 0 and 2π. We clearly see that ϕ_μ has a much larger effect, as the value of the eEDM in this dataset is $d_e^E \approx 10^{-24}$ e cm, regardless of the original data point.
For ϕ_{A_t} this is only $d_e^E \approx 10^{-28}$ e cm and the original data point has a bigger effect on the resulting dependence.

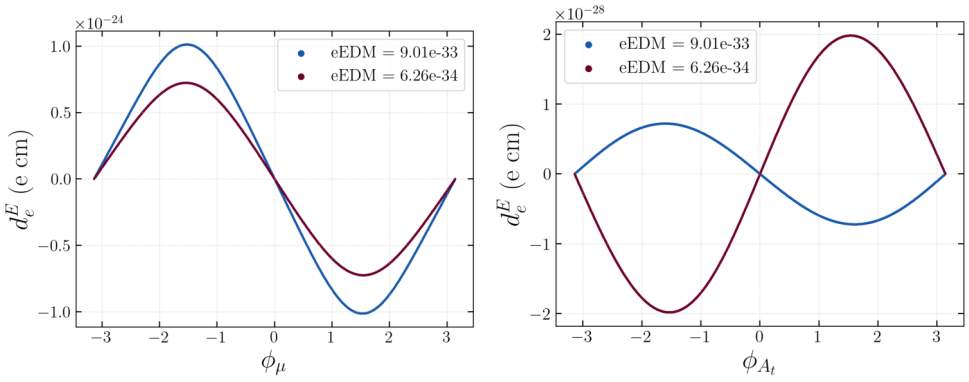

Figure 5.3 The dependence of the eEDM d_e^E on the phase ϕ_μ (ϕ_{A_t}) is shown on the left (right), where all other parameters have been kept constant. The value of the eEDM shown in the legend, is the value of the original data point.

If we zoom in to small values of the phases, between 10^{-2} and 10^{-8}, we also see that ϕ_μ has more impact. This is shown in Figure 5.4. Only for very small values of ϕ_μ do we see that the two lines slightly diverge, as the blue line shows some saturation of d_e^E. We can conclude that ϕ_μ has a larger impact on d_e^E than ϕ_{M_3} for the entire range of ϕ_μ that is scanned. On the other hand, we see that ϕ_{A_t} only affects d_e^E for values $\phi_{A_t} > 10^{-4}$ (blue line) or $\phi_{A_t} > 10^{-6}$ (raspberry pink line). For lower values of the phase ϕ_{A_t}, it is the value of ϕ_{M_3} (blue line) or ϕ_{A_b} (raspberry pink line) that determines d_e^E. Also note that d_e^E changes sign for $\phi_{A_t} \approx 5 \cdot 10^{-6}$, resulting in a sudden drop in $|d_e^E|$ in the pink line.

Note that the FT for the complex parameters is defined as a derivative with respect to the phases. Based on these first studies, we expect that parameters like ϕ_μ will impact the FT much more than e.g. ϕ_{A_t}. To show the relevance of the different parameters we have added the full study of each parameter in Appendix G, both for large and small values of each phase.

For the second part of the study on the impact of individual phases, we have generated new input as described in Section 5.1.1, but with only one phase. The other phases are set to 0. This means we vary the absolute values of the pMSSM parameters slightly, as we take a different random value from the Gaussian distribution (5.1) each time. Doing so allows us to eliminate the impact of the specific pMSSM parameter values that were used in the study described above. The results for ϕ_μ, ϕ_{A_t} and η are shown in Figure 5.5 and the full results can be found in Appendix G.

Similar to the first part of the study, we see that η and ϕ_μ influence d_e^E much more: the spread in the values of d_e^E is much lower for these phases. A wide spread in d_e^E for the same value of the phase, means that d_e^E is mostly determined by the real

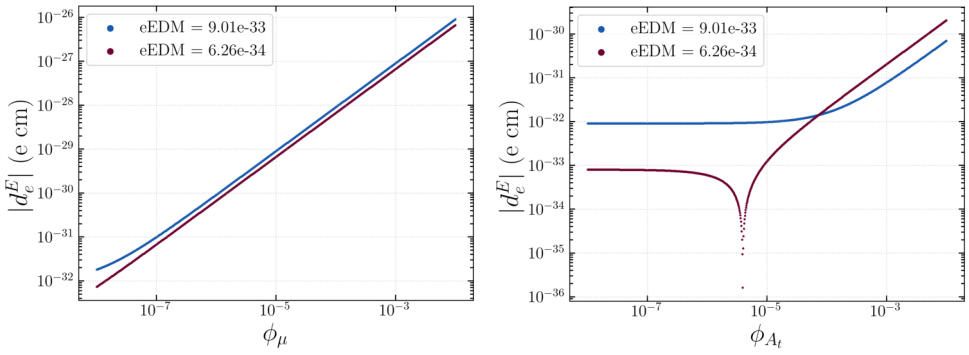

Figure 5.4 The dependence of the eEDM $|d_e^E|$ on the phase ϕ_μ (ϕ_{A_t}) is shown in the left (right) panel, where all other parameters have been kept constant; this time for small values of ϕ_μ (ϕ_{A_t}). The value of the eEDM shown in the legend, is the value of the original data point. Note that d_e^E changes sign for $\phi_{A_t} \approx 5 \cdot 10^{-6}$, resulting in a sudden drop in $|d_e^E|$ (raspberry pink line).

pMSSM parameters. On the other hand, a small spread such as we see for η and ϕ_μ means that the phases have the biggest influence and dominate the behaviour of d_e^E.

From this first study we can already conclude that there is a hierarchy in the phases: η and ϕ_μ dominate the behaviour of d_e^E, followed by ϕ_{M_2} and then ϕ_{M_1}. The phases ϕ_{M_3}, ϕ_{A_b}, ϕ_{A_t} and ϕ_{A_τ} have the least impact. This makes sense if we consider the expressions for the 1-loop and 2-loop contributions in (3.15) and (3.16), and (3.17) respectively. The parameters from the 1-loop contributions influence d_e^E much more, as expected.

5.3 1-loop versus 2-loop contributions

For the supersymmetric contributions to Δa_μ it is well known that the two-loop contributions can grow to be as large as the one-loop contributions [106,107]. Depending on the model, this is also true for the supersymmetric contributions to d_e^E.

In Figure 5.6 we show the results from one of our scans in the cpMSSM. Each point represents one set of input parameters, as described in Section 2.4. We observe that the total two-loop contribution can grow as large as the one-loop contribution. Moreover, since these contributions can have an opposite sign, we see that significant cancellations can occur. We recognise this in the bright diagonal band starting at $|d_e^E|^{\text{one loop}} \approx 10^{-27}$ e cm and continuing down to $|d_e^E|^{\text{one loop}} \approx 10^{-31}$ e cm. Remarkably, the resulting total value of $|d_e^E|$ can be two to three orders of magnitude smaller than the individual contributions.

So far, we have not found specific properties of these cancellation spectra. They

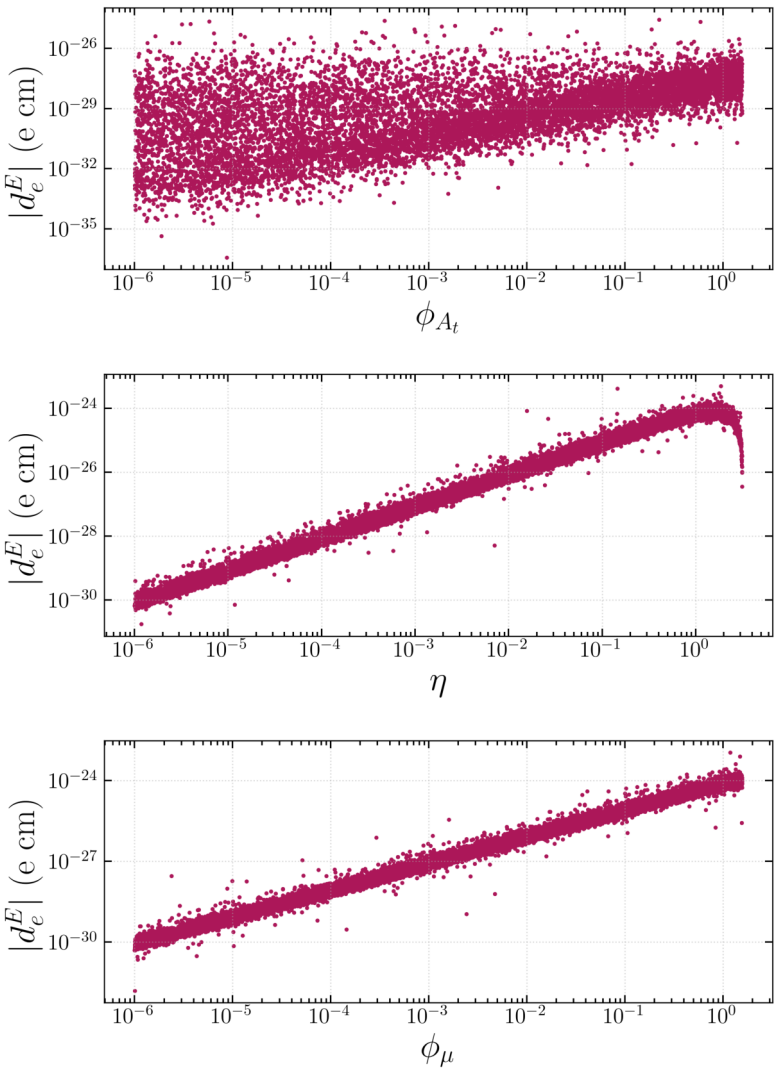

Figure 5.5 The dependence of the eEDM $|d_e^E|$ on the phases ϕ_μ, ϕ_{A_t} and η, for different values of the real pMSSM parameters. Only the phase that is shown has a non-zero value.

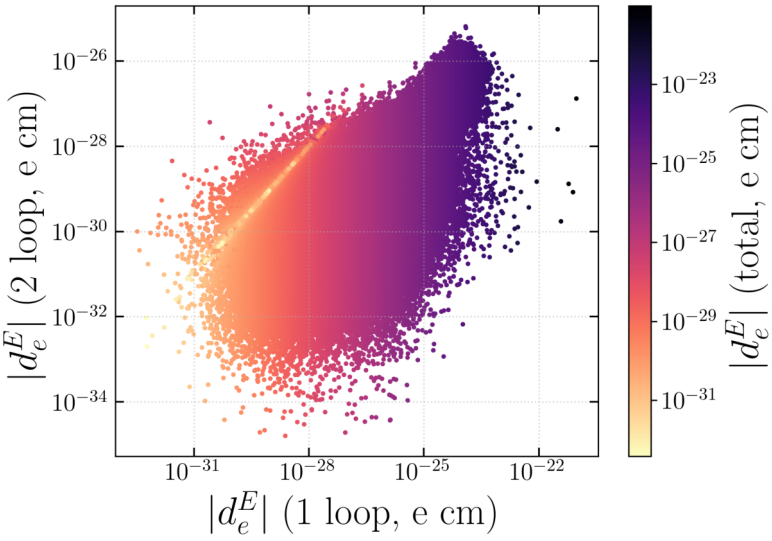

Figure 5.6 The absolute values of the one-loop and two-loop contributions to the eEDM, with the absolute value of the total eEDM as colour coding. Points with low values of $|d_e^E|$ (total) are put on top of those with large values of $|d_e^E|$ (total).

occur nevertheless due to our random sampling algorithm: given enough data points, one will always find spectra for which the one-loop and two-loop contributions have opposite signs. We are currently working on a more thorough understanding of these spectra.

5.4 Fine-tuning and the electron EDM

We have seen that the value of d_e^E directly depends on each of the phases, although not every phase has the same impact. We study this through the FT Δ_ϕ, which is defined as a derivative with respect to the individual phases in (3.27).

As shown in Figure 5.7, a first study on the impact of the phases and the eEDM on the FT shows that lower values of Δ_ϕ seem to occur mostly for larger values of $|d_e^E|$. We also confirm our earlier impression that some phases are of much more significance to $|d_e^E|$: only for small values of η and ϕ_μ do we obtain small values of $|d_e^E|$ (or around $|\eta|, |\phi_\mu| \approx \pi$). Note that some regions have a lower density of points, e.g. $-\pi/2 < \phi_{A_t} < \pi/2$. This is due to the nature of the sampling, in this case not as many points with $\mathrm{Re}(A_t) > 0$ are computed successfully and survive the constraints. This could be resolved by sampling more points in the areas with low density, given enough time. Important is that the points exist, which means it is always possible to

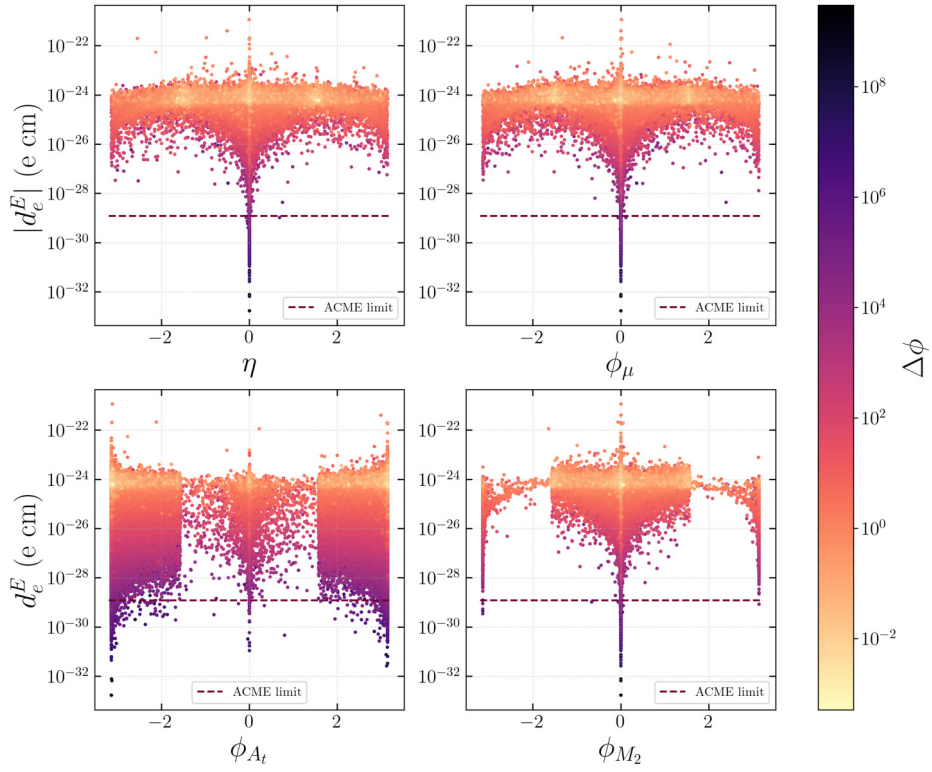

Figure 5.7 The dependence of the eEDM $|d_e^E|$ on the phases η, ϕ_μ, ϕ_{A_t} and ϕ_{M_2} for a data set where the phases are randomly sampled as $10^{-6} < |\eta|, |\phi_\mu| < \pi$ and $10^{-6} < |\phi_i| < \pi/2$. The amount of fine-tuning is shown as colour coding, with the data points ordered such that lower values of Δ_ϕ are put on top of those with higher values of Δ_ϕ.

generate more in this area.

If we look at the FT as shown in Figure 5.8, left panel, we find a direct relationship between Δ_ϕ and $|d_e^E|$: for smaller values of the eEDM we only find solutions with a large degree of FT. Note that we remove points where we run into the computational limits and obtain one or more NaN values in Δ_{ϕ_i}.

Since we find low values of $|d_e^E|$ for small values of η and ϕ_μ, we have also generated a data set where these two phases are sampled in a smaller domain: $10^{-6} < |\eta|, |\phi_\mu| < 10^{-2}$. We can clearly see in Figure 5.9 that the values of the eEDM are no longer dominated by these phases for this study and ϕ_{M_2} takes over this role of dominant phase. However, we still find that low values of Δ_ϕ seem to be correlated to high values of $|d_e^e|$, which we can confirm by looking at Figure 5.8, right panel.

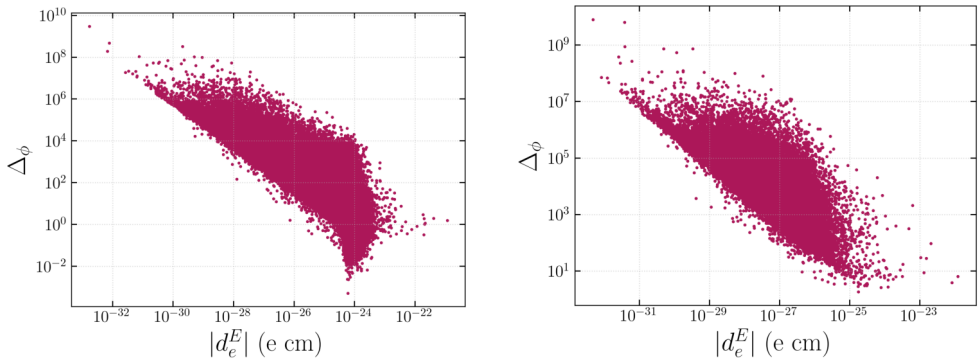

Figure 5.8 On the left: the FT of the CPV sector as a function of $|d_e^E|$ for a data set where phases where sampled randomly as $10^{-6} < |\eta|, |\phi_\mu| < \pi$ and $10^{-6} < |\phi_i| < \pi/2$ (iter12). On the right, the same but for a data set where we take $10^{-6} < |\eta|, |\phi_\mu|, |\phi_{M_1}|, |\phi_{M_2}| < 10^{-2}$. All other phases are randomly sampled as $10^{-6} < |\phi_i| < \pi/2$. (iter13).

We repeat this process twice more: with a study in which $10^{-6} < |\eta|, |\phi_\mu|, |\phi_{M_2}| < 10^{-2}$ and then with a study in which $10^{-6} < |\eta|, |\phi_\mu|, |\phi_{M_1}|, |\phi_{M_2}| < 10^{-2}$, which are iterations 11 and 13. The results are shown in Figures 5.10 and 5.11 respectively.

Name of the run	min (Δ_ϕ)	min (Δ_ϕ) with constraint	max(Δ_ϕ)
Iter10	$4.66 \cdot 10^{-13}$	$4.81 \cdot 10^{-1}$	$6.38 \cdot 10^{10}$
Iter11	$1.00 \cdot 10^{-5}$	$1.53 \cdot 10^{3}$	$9.44 \cdot 10^{9}$
Iter12	$3.44 \cdot 10^{-7}$	$4.53 \cdot 10^{3}$	$3.01 \cdot 10^{9}$
Iter13	$4.88 \cdot 10^{-4}$	$1.83 \cdot 10^{3}$	$8.00 \cdot 10^{9}$

Table 5.2 The minimum and maximum values of Δ_ϕ for each data set, compared to the minimum value of Δ_ϕ when the experimental constraint on d_e^E is satisfied.

Important to note is that the eEDM does not go further down as we restrict more phases. However, we have obtained values $|d_e^E| < 10^{-33}$ in our study of individual phases. By restricting ourselves to phases of at least $\phi_i > 10^{-6}$, we do not find such results here. Allowing some zero-valued phases would be an interesting follow-up study.

In our current study we observe that $|d_e^E|$ is determined mostly by the other, real pMSSM parameters at this point. Since we started with a data set that satisfies $1.33 \cdot 10^{-9} < \Delta a_\mu < 3.69 \cdot 10^{-9}$ and the contributions to Δa_μ and $|d_e^E|$ are very similar, we can explain this behaviour. The same parameters that allow us to obtain the correct value of Δa_μ in the pMSSM, prevent us from finding lower values of $|d_e^E|$ in the cpMSSM. Larger sparticle masses result in a too low value of Δa_μ and are

therefore not a part of the $(g-2)_\mu$ data set. This does not allow us to check the claim that larger sparticle masses result in a smaller value for d_e^E, although we do expect this based on the expressions in equations (3.15), (3.16) and (3.17).

For a more general result, we are therefore currently setting up two new studies: one where we only satisfy the upper bound $\Delta a_\mu < 3.69 \cdot 10^{-9}$ and add phases in the same way, and one where we sample the cpMSSM as generally as possible. As such studies take a lot of computer time, we have chosen to focus on the combined $(g-2)_\mu$ and eEDM study first as core topic of this thesis.

The choice to start with the $(g-2)_\mu$ data set also impacts Δ_ϕ. Typically this FT due to the phases is lower for higher sparticle masses. However, such values are not allowed for $1.33 \cdot 10^{-9} < \Delta a_\mu < 3.69 \cdot 10^{-9}$. An extended study will provide more insight into the correlation between the sparticle masses and the FT due to the phases, as well as the impact on Δ_{EW} if we allow higher sparticle masses.

With the data sets that we do have on hand, we take a final look at the eEDM and the FT. In Table 5.2 we show the maximum values of Δ_ϕ that we find in our data sets, and the minimum values of Δ_ϕ with and without the experimental constraint on $|d_e^E| < 1.1 \cdot 10^{-29}$.

We see that for typical data sets the minimum amount of FT is 10^3 when we satisfy the constraint on d_e^E, which corresponds to FT of 0.1% in the eEDM.

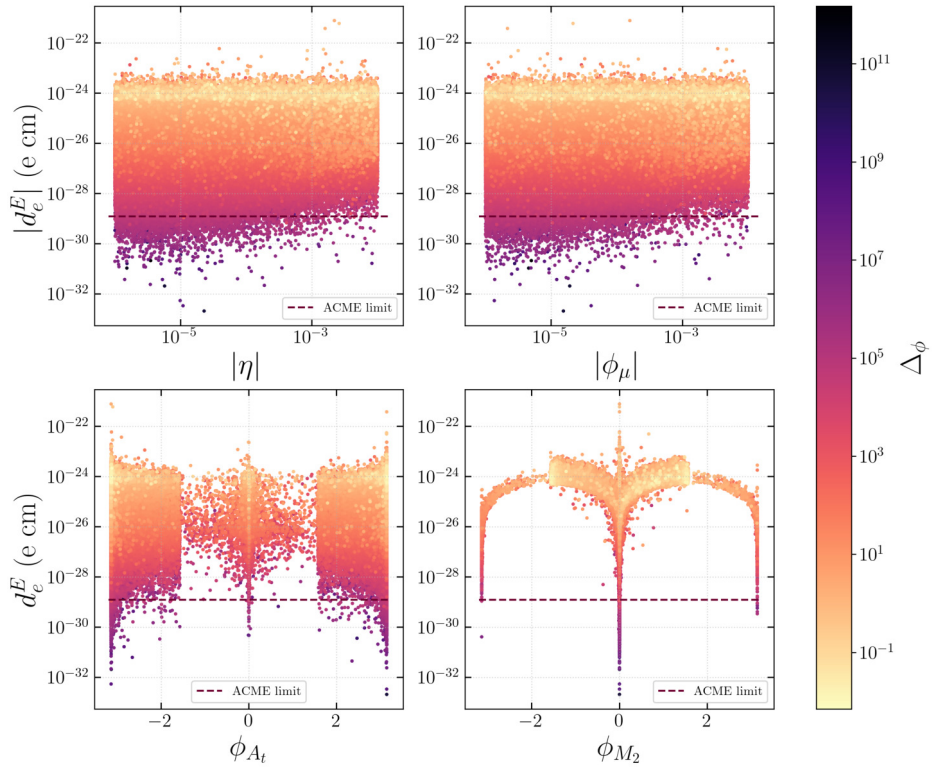

Figure 5.9 The dependence of the eEDM $|d_e^E|$ on the phases η, ϕ_μ, ϕ_{A_t} and ϕ_{M_2} for a data set where η and ϕ_μ are sampled as $10^{-6} < |\eta|, |\phi_\mu| < 10^{-2}$ and all other phases are randomly sampled as $10^{-6} < |\phi_i| < \pi/2$. The amount of fine-tuning is shown as colour coding, with the data points ordered such that lower values of Δ_ϕ are put on top of those with higher values of Δ_ϕ.

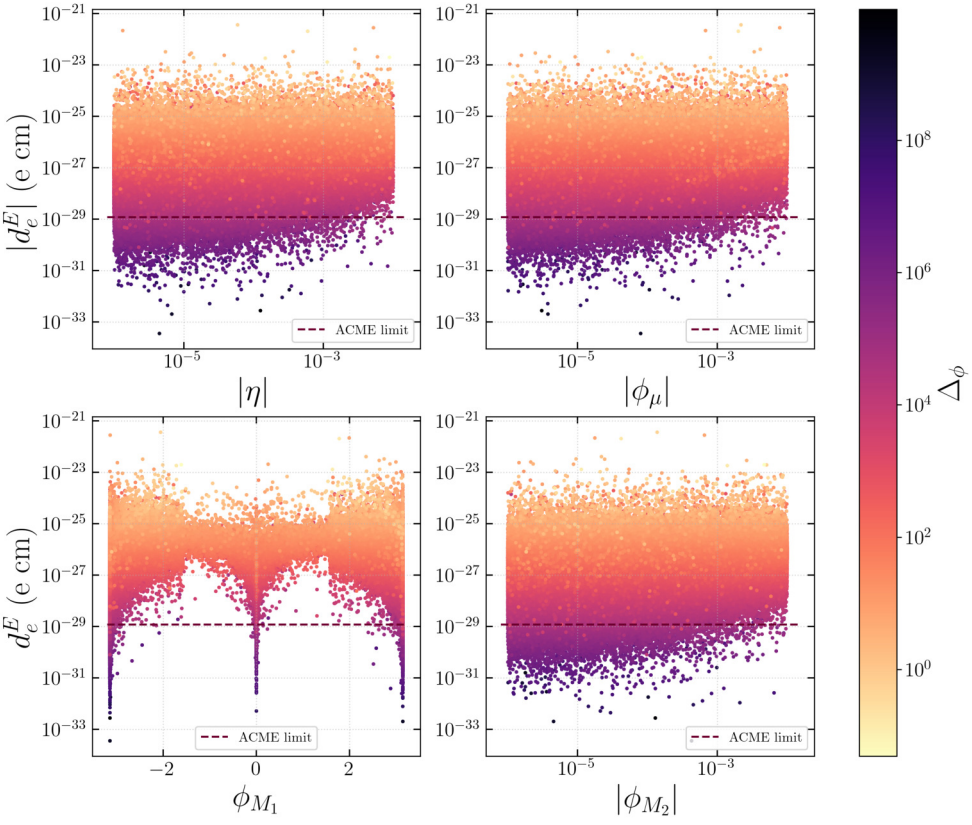

Figure 5.10 The dependence of the eEDM $|d_e^E|$ on the phases η, ϕ_μ, ϕ_{M_1} and ϕ_{M_2} for a data set where η, ϕ_μ, ϕ_{M_1} and ϕ_{M_2} are sampled as $10^{-6} < |\eta|, |\phi_\mu|, |\phi_{M_2}| < 10^{-2}$. All other phases are randomly sampled as $10^{-6} < |\phi_i| < \pi/2$. The amount of fine-tuning is shown as colour coding, with the data points ordered such that lower values of Δ_ϕ are put on top of those with higher values of Δ_ϕ.

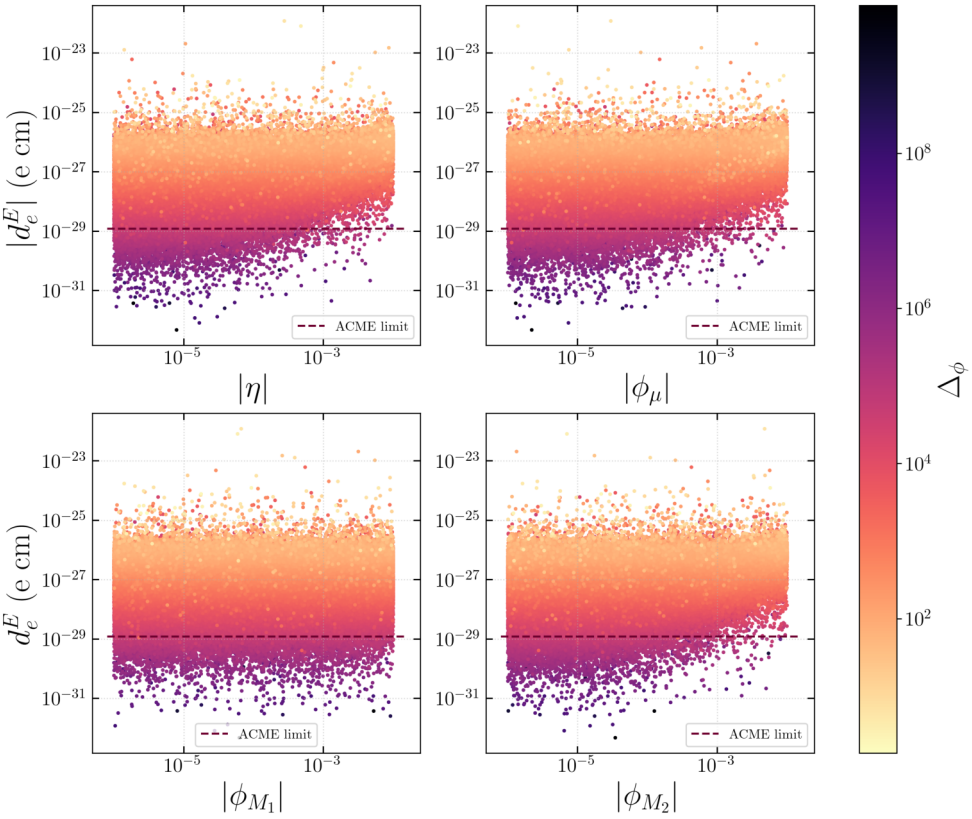

Figure 5.11 The dependence of the eEDM $|d_e^E|$ on the phases η, ϕ_μ, ϕ_{M_1} and ϕ_{M_2} for a data set where η, ϕ_μ, ϕ_{M_1} and ϕ_{M_2} are sampled as $10^{-6} < |\eta|, |\phi_\mu|, |\phi_{M_1}|, |\phi_{M_2}| < 10^{-2}$. All other phases are randomly sampled as $10^{-6} < |\phi_i| < \pi/2$. The amount of fine-tuning is shown as colour coding, with the data points ordered such that lower values of Δ_ϕ are put on top of those with higher values of Δ_ϕ.

5.4.1 Alternative fine-tuning measures

We have studied the FT in the CP violating sector of the cpMSSM through a specific measure: Δ_ϕ. Similarly to the FT measure in the EW sector, there are more possibilities and there is no consensus yet in the community about a measure. The choice for Δ_ϕ as defined in (3.27) is based on a general approach to FT measures [125]. We can now comment on this choice, knowing more about the behaviour of d_e^E in the cpMSSM.

We can define three regions for each phase: in the first, the behaviour of d_e^E depends linearly on that phase. For example in Figure 5.4 we see that this region for the phase ϕ_{A_t} is roughly $\phi_{A_t} > 10^{-4}$ for the blue line. For values $\phi_{A_t} \gg 10^{-4}$ we see in Figure 5.3 that for $|\phi_{A_t}| \approx \mathcal{O}(1)$ the relation between d_e^E and ϕ_{A_t} is sine-like.[1] For values $\phi_{A_t} < 10^{-4}$ the behaviour changes as well, as ϕ_{A_t} no longer influences d_e^E. This is the third region. Note that the exact domains of the regions depend strongly on the parameters of the data point. For e.g. ϕ_μ we identify completely different regions based on Figures 5.3 and 5.4.

Our current definition does not take the different regions into account at all, but is instead based on the second region. Consequently, the FT for small values of ϕ_i is overestimated in the first and third region. The relative change in d_e^E is divided by the absolute change in ϕ_i, although the dependence is linear. This results in a biased definition towards high FT for small phases (and thus small values of d_e^E).

A logarithmic derivative with respect to ϕ_i would cover those regions better, but is problematic for $\phi_i = \pi$ as this does not take the sine-like behaviour into account. The behaviour that $\phi_i = \pi$ results in the same eEDM as $\phi_i = 0$ should be reflected in the FT, but this is not possible for a straightforwardly defined logarithmic derivative with respect to ϕ_i . We therefore propose a new definition for the CPV FT measure.

Having studied the FT measure Δ_ϕ, we now propose to use the following definition for a new FT measure

$$\Delta_{\text{CPV}} = \Delta_{\sin\phi} = \max_i \left| \sin\phi_i \frac{\partial \log d_e}{\partial \phi_i} \right|, \tag{5.7}$$

which avoids trouble at $\phi = 0$ but takes the nature of the first and third regions better into account. With this definition we can take another look at the FT, for example in iter13 as shown in the left panel of Figure 5.12.

We find that the bias towards high FT for small phases has disappeared with the implementation of the new definition. This is confirmed by the plots shown in Figure 5.13, where we see the relation between $|d_e^E|$, the phases $\eta, \phi_\mu, \phi_{M_1}$ and ϕ_{M_2}, and the FT.

However, we can find no clear relation between the FT as defined in (5.7) and the cancellation points as shown in Figure 5.6, as is shown in the right panel of

[1] In fact, the behaviour in the first and second region can both be captured by a sinusoid. Nevertheless, we distinguish these regions to clarify the discussion on the fine-tuning definition, which is different in all three regions.

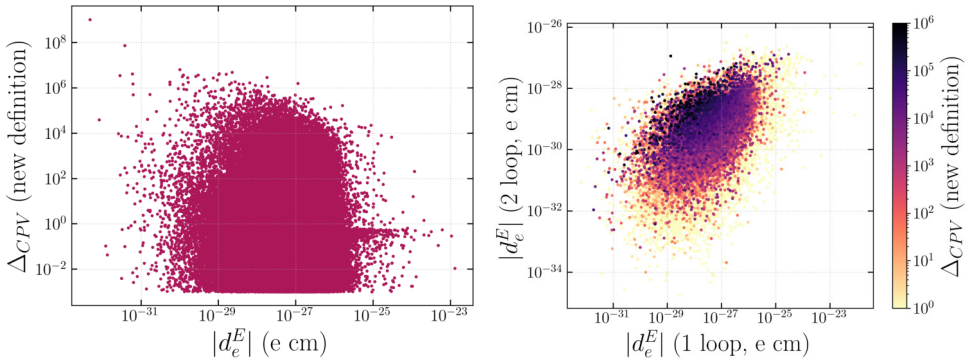

Figure 5.12 On the left: the relation between $|d_e^E|$ and the FT, based on the new Δ_{CPV} definition (5.7). On the right: the 1-loop and 2-loop contribution to $|d_e^E|$, with the new definition of Δ_{CPV} as colour coding. Points are ordered such that points with a high value of Δ_{CPV} are put on top of those with a low value of Δ_{CPV}.

Figure 5.12. Instead, the line is smeared and there is a larger area with points that have a high FT. We do feel that points with a significant cancellation between the 1-loop and 2-loop contributions are fine-tuned, in the sense that a small variation in the parameters will have a large effect on the value of d_e^E. A proper FT measure should take this into account.

We also find that points with a low FT exist for all values of the 1-loop and 2-loop contributions. Since points are ordered such that points with a high value of Δ_{CPV} are put on top of those with a low value of Δ_{CPV}, the homogeneously distributed low-FT points are not immediately visible in Figure 5.12.

Although both definitions for Δ_{CPV} can be properly motivated, the differences are huge. With the definition as in (5.7), the correlation between d_e^E and Δ_{CPV} is completely gone. This shows that it is of the utmost importance to be clear about the definition of the FT measure that is used. The first definition of Δ_ϕ as a measure for the FT in the phases does not properly display the cancellation between the 1-loop and 2-loop contributions, and together with its bias for small phases, we believe this definition is unsuitable to study what we define as FT. The second definition is better as it does not have a bias, but nevertheless it does not satisfy the requirements for a proper FT measure in our opinion.

Finally we want to remark that neither of these definitions are related to naturalness (in the sense of 't Hooft [32]). One small phase is in fact very natural, as the CP symmetry is restored for $\phi = 0$. However, the cpMSSM contains several CP violating parameters and therefore the definition of naturalness cannot straightforwardly be applied here.

In our opinion, a discussion on the concept of naturalness in the case of several relevant parameters is necessary before any statement can be made on the naturalness

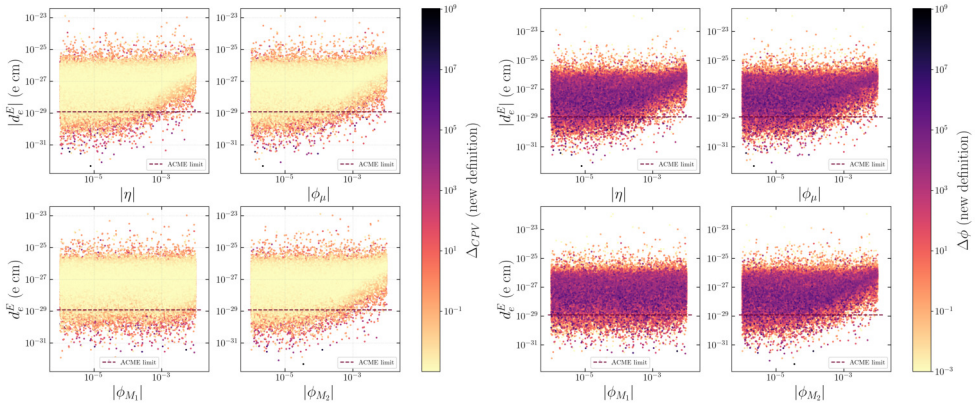

Figure 5.13 The dependence of the eEDM $|d_e^E|$ on the phases η, ϕ_μ, ϕ_{M_1} and ϕ_{M_2} for a data set where η, ϕ_μ, ϕ_{M_1} and ϕ_{M_2} are sampled as $10^{-6} < |\eta|, |\phi_\mu|, |\phi_{M_1}|, |\phi_{M_2}| < 10^{-2}$. All other phases are randomly sampled as $10^{-6} < |\phi_i| < \pi/2$. The amount of fine-tuning is shown as colour coding, with the data points in the left (right) panel ordered such that lower (higher) values of Δ_ϕ are put on top of those with higher values of Δ_ϕ.

of a cpMSSM model point and hence, whether such a point is favourable or not. We therefore urge to carefully consider exclusion limits such as shown in Figure 1.3.

5.5 Conclusion

We have created a spectrum generator using SARAH, allowing us to research the real and complex parameter space of the cpMSSM. We have combined this approach with the calculational tool FeynHiggs, resulting in a smaller uncertainty on the Higgs boson masses in this model. To implement constraints from DM searches, we have adapted the software package MicrOMEGAS, and to study the eEDM we have developed our own code to calculate d_e^E and the amount of FT on it. We have performed a first study, starting from the results from the $(g-2)_\mu$ study.

For parameter sets that satisfy the experimental constraints, such as the LEP and LHC data, and the DM constraints, we have identified parameter sets that also satisfy the experimental constraint on the eEDM, currently at $|d_e^E| < 1.1 \cdot 10^{-29}$ e cm with the ACME experiment. We find that the eEDM constraint limits the amount of CPV mostly through the phase of the Higgs parameter μ and the phase between the Higgs doublets η. By limiting the domain of ϕ_μ and η, we find more data points that satisfy the eEDM constraint. We also observe that the pMSSM parameters start to dominate the value of d_e^E when we limit the possible values of the phases, which is to be expected for our set up that is based on the data points from the $(g-2)_\mu$ study as the contributions to Δa_μ and $|d_e^E|$ are very similar. The same parameters that allow

us to obtain the correct value of Δa_μ in the pMSSM, prevent us from finding lower values of $|d_e^E|$ in the cpMSSM through larger sparticle masses.

Reaching lower values for the eEDM comes with a price, at least when defining FT in the phases as Δ_ϕ. We clearly see a direct relation between the value of $|d_e^E|$ and the phase FT Δ_ϕ: for lower values of $|d_e^E|$ we find more fine-tuned solutions. This is to be expected based on the dependence of d_e^E on the individual phases. We see that for typical data sets the minimum amount of FT is 10^3 when we satisfy the constraint on $|d_e^E|$, which corresponds to FT of 0.1% in the eEDM.

Using a different FT measure, such as $\Delta_{\sin\phi}$, changes this picture completely. There is no longer a dependence between $|d_e^E|$ and $\Delta_{\sin\phi}$. However, the FT between the 1-loop and 2-loop contributions is not captured fully by this measure. We therefore suggest a more extensive study that includes different measures, to search for a measure that properly captures the FT in the phases: when a small change in ϕ results in a large (small) change in $|d_e^E|$, the FT should also be large (small).

We are therefore careful with our interpretation and only note that the FT in the CP violating sector as defined in Δ_{CPV} is potentially high enough to take into account as a warning sign: the connection between $|d_e^E|$ and the phases is strong for the spectra that we studied, meaning further study is necessary and we cannot discard the FT in this sector as irrelevant. We do note that small values for the phases are not necessarily unnatural, as such a conclusion needs further consideration on the definition of naturalness.

With these preliminary results, collaborators are currently expanding this study to include the regions of parameter space in the cpMSSM that satisfy only the upper bound $\Delta a_\mu < 3.69 \cdot 10^{-9}$. We expect this will allow the combination of satisfying the $\Omega_{\text{DM}}h^2$ constraint more easily, as well as the constraint on $|d_e^E|$. This also permits a study on the resulting points to gain more phenomenological insight into the relevant regions of the cpMSSM parameter space and their FT for points where both experimental constraints are met.

Chapter 6

Conclusion and outlook

We have studied two related supersymmetric models: the pMSSM and the cpMSSM. Our aim was to identify data points in the parameter space of each model that satisfy all available experimental constraints. This was done by generating the mass spectrum, coupling constants and mixing matrices for each data point, calculating the observables based on this spectrum and comparing the observables to experimental data.

6.1 Conclusions on the $(g-2)_\mu$ study

In Chapter 4 we performed a study where we have analyzed for the first time the spectra in the pMSSM that are minimally fine-tuned, result in the right $\Omega_{\rm DM}h^2$ *and* simultaneously offer an explanation for Δa_μ. We made these spectra publicly available under [157].

In terms of DM phenomenology, we have distinguished three interesting branches of solutions: the funnel regimes, three types of coannihilation regimes, and the generic bino-higgsino solution. All these solutions have in common that the LSP is predominantly bino-like with a small higgsino component. The mass of the DM particle ranges between $39-495$ GeV. We discussed the phenomenology at the LHC for each of the regimes. The first and second regime are relatively more constrained by $\widetilde{\chi}_2^0\widetilde{\chi}_1^\pm$ searches at the LHC than the last regime, which is due to the lower wino-components and higher masses of the $\widetilde{\chi}_2^0/\widetilde{\chi}_1^\pm$ sparticles that are typical in the last regime. On the other hand, in particular when the coannihilation partner of the LSP is a light stau, the LHC searches show little to no sensitivity to our found solutions.

Our solutions motivate further the ongoing efforts at the LHC to probe pMSSM spectra that feature (compressed) production of higgsino-like $\widetilde{\chi}_2^0\widetilde{\chi}_1^\pm$ pairs. In addition, to increase the sensitivity of the LHC to our found solutions, we found that a dedicated low-mass $\widetilde{\tau}^\pm$ search without an assumed mass degeneracy between $\widetilde{\tau}_1^\pm$ and $\widetilde{\tau}_2^\pm$ would be needed, just as a dedicated search strategy for the mass-gap region of $55\text{ GeV} < \Delta(m_{\widetilde{\chi}_2^0}, m_{\widetilde{\chi}_1^0}) < m_Z$, which is not yet probed at the LHC.

We found that DMDD experiments such as the LUX-ZEPLIN experiment [38, 229] that probe $\sigma_{\rm SD,p}$ will ultimately be sensitive to all of our minimally fine-tuned spectra. The requirement of satisfying Δa_μ is crucial to arive at this conclusion. This requirement excludes models with a higher-mass higgsino with $m_{\widetilde{\chi}_1^0} = 550-650$ GeV as the LSP, and these spectra would evade detection by future DMDD experiments.

6.2 Conclusions on the eEDM study

To study the cpMSSM we found that no readily available software is suited for this model. Instead we have created a new spectrum generator using SARAH, allowing us to research the real and complex parameter space of the cpMSSM. We have combined

this approach with the calculational tool FeynHiggs, resulting in a smaller uncertainty on the Higgs boson masses in this model. To implement constraints from DM searches, we have adapted the software package MicrOMEGAS, and to study the eEDM we have developed our own code to calculate d_e^E and the amount of FT on it.

The first step of this project was to study the interplay between $(g-2)_\mu$ and the eEDM. We have therefore extended the pMSSM data that satisfies all experimental constraints as described in Chapter 4. We found that the interplay between both observables is so strong, that a small deviation in the values of the real pMSSM parameters will result in a significantly different value for $\Omega_{\mathrm{DM}}h^2$. We have therefore opted to lift this constraint for the eEDM study.

Using the new cpMSSM data set, we have identified cpMSSM parameter sets that also satisfy the experimental constraint on the eEDM, currently at $|d_e^E| < 1.1 \cdot 10^{-29}$ e cm with the ACME experiment. Starting from pMSSM data points that additionally satisfy the experimental bounds on $(g-2)_\mu$, we found that the eEDM constraint limits the amount of CPV mostly through the phase of the Higgs parameter μ and the phase between the Higgs doublets η. We emphasize the different conventions for η, μ and b: if one chooses to rotate η away, the parameter b will in general be complex beyond tree level.

We have not been able to test the often-made assumption that low values of $|d_e^E|$ can be obtained by taking large values for the sparticle masses, as these masses are already constrained to low values due to the requirement of $1.33 \cdot 10^{-9} < \Delta a_\mu < 3.69 \cdot 10^{-9}$.

We found that even with relatively small sparticle masses, necessary to satisfy the constraint on Δa_μ, the phases do not have to be smaller than 10^{-2} to also satisfy the limit $|d_e^E| < 1.1 \cdot 10^{-29}$ e cm. However, reaching these low values for the eEDM comes with a price. We clearly see a direct relation between the value of $|d_e^E|$ and the phase FT measure Δ_ϕ: for lower values of $|d_e^E|$ we find more fine-tuned solutions. This is to be expected based on the dependence of $|d_e^E|$ on the individual phases.

Studying this dependence in more detail, we have motivated a proposal for a second definition for the FT in the phases as given by the FT measure $\Delta_{\sin\phi}$. Using this new definition, we do not find any correlation between $|d_e^E|$ and the FT. We conclude that a careful consideration of the definition of the FT measure is necessary in any FT study. We propose to search for a definition that captures the true meaning of FT: small changes in the parameters that result in large (small) changes in the observable, should be reflected by a large (small) value of the FT.

6.3 Outlook and proposed studies and improvements

The aim of the eEDM project was to extend the $(g-2)_\mu$ study with an analysis on the eEDM while still satisfying all the experimental constraints as implemented in the $(g-2)_\mu$ study. Due to the nature of the data points from the $(g-2)_\mu$ study, we find

that a small variation in the real pMSSM parameters has a profound impact on the DM observables. Collaborators are therefore setting up two new analyses extending the pMSSM parameter set from the $(g-2)_\mu$ study. For the first analysis this include only the parameters that satisfy the upper bound on Δa_μ, while for the second set this requirement is lifted completely. All the other experimental constraints are still satisfied for these sets. These two sets are then expanded to the cpMSSM as explained in Chapter 5.

We propose to study the phenomenology of the regions of cpMSSM parameter space that satisfy the experimental constraint $|d_e^E| < 1.1 \cdot 10^{-29}$ e cm for these two new data sets, similarly to the study in Chapter 4. Due to the close relation between Δa_μ and d_e^E, we expect that these new analyses will allow for spectra with higher sparticle masses, allowing a study on the relationship between sparticle masses and phases in more detail.

Ultimately we aim to study the regions of cpMSSM parameter space that satisfy all experimental constraints. For this purpose we stress the importance of software packages that allow for complex parameters, as not all observables can currently be calculated in the cpMSSM.

Furthermore we propose a study on the effect of the phases in more detail. So far we have only considered the situations where either all the phases have a non-zero value, or only one phase has a non-zero value. From our current results it is obvious that some phases (ϕ_μ, η) have more impact on $|d_e^E|$ than others. It would be interesting to study a scenario where those phases are strictly 0, while all others are allowed to have a non-zero value.

Collaborators are also striving to improve our calculational basis. The code to calculate the FT in the pMSSM part of the parameter space, for which we use Δ_{EW}, will be adapted to take the complex nature of the cpMSSM into account. Compared to the expressions in [124] we expect new contributions and altered expressions for the existing contributions to Σ_d^d and Σ_u^u, which will be determined and added to our in-house code for calculating Δ_{EW}. Additionally, we propose to extend our code by calculating the value of d_e^E including all Barr-Zee type diagrams, also for charged Higgs bosons.

For the long-term future we propose to extend the available software to include the calculation of molecular EDMs in the cpMSSM. This would include a full spectrum generator and an EFT framework to calculate the scalar and tensor contribution to the molecular EDM.

Appendices

APPENDICES

A. Conventions

A.1 General conventions

- We use natural units, in which $\hbar = c = \epsilon_0 = k_{\mathrm{B}} = 1$;
- We define the electron charge as $q_{\mathrm{e}} = Q_e e = -1\, e$;
- We define the spacetime metric as $\eta_{\mu\nu} = \mathrm{diag}(+1, -1, -1, -1)$;
- Repeated indices are assumed to be summed over;
- We use g', g and g_3 for the $U(1)$, $SU(2)$ and $SU(3)$ couplings respectively;
- $\vec{\sigma}$ are the Pauli spin matrices;
- $\sigma^{\mu\nu} = \frac{i}{2}[\gamma^\mu, \gamma^\nu]$;
- The electric dipole moment is given in e cm, which can be converted to $(\mathrm{GeV})^{-1}$ by dividing by $\hbar c = 1.973269788 \cdot 10^{-14}$ GeV cm [45];
- Chiral projection operators are defined as

$$P_L = \frac{1}{2}(1 - \gamma_5) \qquad\qquad P_R = \frac{1}{2}(1 + \gamma_5); \tag{A.1}$$

- Angles are in radians, unless otherwise specified.

We use the Axodraw2 package [233] to draw the Feynman diagrams in this thesis.

A.2 The phase η

As we have already mentioned in Section 2.4, there are different conventions possible with respect to the phase η. At tree level this is straightforward, as the tadpole equations (2.16) relate η directly to ϕ_b and we have seen that we can choose $\phi_b = \eta = 0$. However, at higher orders this is more complicated.

Using the Peccei-Quin and R-type chiral $U(1)_A$ and $U(1)_B$ symmetries we have some freedom in our conventions. If we adopt the convention of (2.6) to ensure real vev's, we will have in general $\eta \neq 0$. However, we can always use a rotation of the kind

$$e^{i\eta(-Y/2+(Q_A+Q_B)/4)} \tag{A.2}$$

to rotate a non-zero η away. Here Q_A and Q_B are the charges corresponding to the $U(1)_A$ and $U(1)_B$ transformations, which are listed in Table 2.3. The corresponding phases are then $\omega_A = \omega_B = \eta/4$. As a result, the parameters μ and b and several fields will be redefined. For the fields, this has no net effect as one can always absorb a phase in the field.

For the parameters however, this rotation results (assuming $\eta \neq 0$) in

$$\eta \to \eta' = 0; \tag{A.3}$$

$$\mu \to \mu' = \mu e^{i\eta} \notin \mathbb{R}; \tag{A.4}$$

$$b \to b' = b e^{i\eta} \notin \mathbb{R}. \tag{A.5}$$

Starting with a non-zero general phase η, we can rotate this to $\phi_{\mu'}, \phi_{b'} \neq 0$. Consequently, beyond tree-level it is not possible to have $\phi_b = 0$ and $\eta = 0$ as a general convention! It is therefore important to be clear which convention is chosen, $\eta = 0$ or $b \in \mathbb{R}$.

A.3 Mixing matrices

There are several different conventions possible when defining the mixing matrices for (s)particles. Unless otherwise specified, the expressions are based on [40]. We do, however, use a different notation. Additionally we implement couplings from [55] for the cpMSSM. In this Section we cover the main differences between [40, 55] and our conventions. An overview of the different labels is given in Table A.1.

Mixing matrix	Name in Sparticles	Name in Ellis' papers	Name in thesis
Slepton	$W^{\tilde{f}}$ (6x6)	$U_{\tilde{f}}$ (2x2)	$X^{\tilde{l}}$ (2x2)
Sneutrino	U	-	$\mathbb{1}$
Chargino	$\mathcal{U}, \mathcal{V}$	C_L, C_R	U, V
Neutralino	Z	N	N

Table A.1 Conventions for the mixing matrices in this thesis compared to Sparticles [40] and Ellis' papers [55].

Chargino mixing

To compare the conventions for the chargino mixing matrices, we first rotate the factor $e^{-i\eta}$ in (2.47) away as described above in Section A.2. This allows for a clean comparison. One way to define the chargino mixing is as follows [55]

$$C_R M_C C_L^\dagger = \text{diag}\{m_{\tilde{\chi}_1^\pm}, m_{\tilde{\chi}_2^\pm}\}, \tag{A.6}$$

with

$$M_C = \begin{pmatrix} M_2 & \sqrt{2}M_W \cos\beta \\ \sqrt{2}M_W \sin\beta & \mu \end{pmatrix} \tag{A.7}$$

Whereas we use [40]

$$U^* M_{\tilde{\chi}^\pm} V^\dagger = \text{diag}\{m_{\tilde{\chi}_1^\pm}, m_{\tilde{\chi}_2^\pm}\} \tag{A.8}$$

(or V^{-1} instead of $V^\dagger$ as this matrix is unitary) where

$$M_{\tilde{\chi}^\pm} = \begin{pmatrix} M_2 & \sqrt{2}M_W \sin\beta \\ \sqrt{2}M_W \cos\beta & \mu \end{pmatrix} \tag{A.9}$$

so we see that $M_C = M_{\tilde{\chi}^\pm}^T$. We can use this to relate the matrices to each other by taking the transpose of the entire diagonalisation expression. We then obtain $C_L = U$ and $C_R = V^*$.

Neutral Higgs boson mixing

In the case of CP violation, the neutral Higgs bosons mix. As a result, we can no longer differentiate between the CP eigenstates h^0, H^0 and A^0 beyond tree-level. Instead, we use a mass ordering and label the three mass eigenstates accordingly. See Section 2.4 for more details.

As described in Section 2.4, there are four gauge eigenstates of which we can identify one as a Goldstone boson. The other three mix into mass eigenstates. Several conventions exist to describe this mixing, using a mixing matrix S, $\mathcal{R}$ or $\mathcal{O}$. Note that the matrix $\mathcal{O}$ as defined in Section 2.4 and [54] is actually O^T in [55]! We use the convention of $\mathcal{O}$, as we feel this makes comparison with the expressions for the neutral Higgs boson couplings in [55] easier than for $\mathcal{R}$ or S. However, keep in mind that the indices are switched compared to the reference.

Sfermion mixing

First, note that we assume that there is no flavour mixing in the (c)pMSSM. As a result, the 6×6 mixing matrix for the charged sleptons $W^{\tilde{f}}$ can be split in 3 blocks of 2×2 mixing matrices, one for each flavour. For the sleptons we label these 2×2 matrices $X^{\tilde{l}}$ for a lepton $l = (e, \mu, \tau)$. The matrices $X^{\tilde{l}}$ are based on the mass ordered mass eigenstates and mix the left- and right-handed components of the sleptons. Similarly we can split the mixing matrices $W^{\tilde{f}}$ of the squarks in 2×2 blocks. See Section 2.4.1 for more details.

The diagonalisation procedure for the 2×2 and 6×6 sfermion mixing per sector can both be defined (in terms of their respective 2-dimensional and 6-dimentional vectors $\tilde{f}$ and mass matrices $M^2_{\tilde{f}}$) in different ways. We compare the different conventions

for a 2-dimensional case, where we take the relevant 2×2 block from the full 6×6 dimensional matrix W.

We can now define [40]

$$(M_{\tilde{f}}^{\text{diag}})^2 = W^{\tilde{f}\dagger} M_{\tilde{f}}^2 W^{\tilde{f}}, \tag{A.10}$$

where $(M_{\tilde{f}}^{\text{diag}})^2$ is the diagonal matrix and $M_{\tilde{f}}^2$ the general form. The 2-dimensional mass eigenstate vector for the sfermions is then given by

$$\tilde{f}^m = W^{\tilde{f}\dagger} f. \tag{A.11}$$

However, one can also define

$$(M_{\tilde{f}}^{\text{diag}})^2 = X^{\tilde{f}} M_{\tilde{f}}^2 X^{\tilde{f}\dagger}, \tag{A.12}$$

as is done in e.g. [101]. The mass eigenstates are then given by

$$\begin{pmatrix} \tilde{f}_1 \\ \tilde{f}_2 \end{pmatrix} = X^{\tilde{f}} \begin{pmatrix} \tilde{f}_L \\ \tilde{f}_R \end{pmatrix}. \tag{A.13}$$

We will adopt the second convention, which accounts for the differences in the expressions compared to [40] in the lepton-neutralino-slepton couplings.

A.4 Feynman rules

A.4.1 Couplings for the one-loop diagrams and related conventions

With our conventions we find the following couplings. Note that $X_{mn}^{\tilde{l}}$ is of course different for the electron and muon; the corresponding slepton mixing matrices have to be used. Definitions for $X^{\tilde{l}}$ and the other mixing matrices can be found in Section 2.4.1.

At first order both a_μ and d_e^E receive contributions from a neutralino and a chargino diagram. The couplings of the lepton to the neutralino (chargino) and slepton (sneutrino) are as follows [101]. Labelling is according to Table A.1.

Neutralino – lepton – charged slepton interactions

We define the interaction between a charged lepton l, neutralino $\widetilde{\chi}_i^0$ and a charged slepton $\tilde{l}_m$ as follows

$$\mathcal{L}_{l\tilde{l}\tilde{\chi}^0} = \bar{\widetilde{\chi}}_i^0 \left[n_{iml}^L P_L + n_{iml}^R P_R \right] \tilde{l}_m^* l + \text{h.c.}, \tag{A.14}$$

where we have assumed the lepton and slepton have the same flavour. The couplings n^L_{iml} and n^R_{iml} can be defined in different ways, according to the chosen convention.

In [40] the neutralino couplings are defined as follows

$$G^L_{iml} = \frac{1}{\sqrt{2}}\left(gN^*_{i2} + g'N^*_{i1}\right)W^*_{1m} - y_l N^*_{i3} W^*_{2m}, \tag{A.15}$$

$$G^R_{iml} = -\sqrt{2}g'N_{i1}W^*_{2m} - y_l N_{i3} W^*_{1m}, \tag{A.16}$$

whereas in [101] we find the following expressions

$$n^L_{iml} = \frac{1}{\sqrt{2}}\left(gN_{i2} + g'N_{i1}\right)(X^{\tilde{l}})^*_{m1} - y_l N_{i3}(X^{\tilde{l}})^*_{m2}, \tag{A.17}$$

$$n^R_{iml} = \sqrt{2}g'N_{i1}(X^{\tilde{l}})_{m2} + y_l N_{i3}(X^{\tilde{l}})_{m1}. \tag{A.18}$$

Here we denote the down-type lepton Yukawa coupling by $y_l = gm_l/(\sqrt{2}M_W\cos\beta)$, where we use the lepton pole mass. To avoid mixing up scales, we implement this as $y_l = \sqrt{2}m_l/(v\cos\beta)$.

Using $W^\dagger = X^{\tilde{l}}$ (if we only consider the 2x2 part of W belonging to $\tilde{l}$), we can write

$$n^L_{iml} = \frac{1}{\sqrt{2}}\left(gN_{i2} + g'N_{i1}\right)W_{1m} - y_l N_{i3} W_{2m}, \tag{A.19}$$

$$n^R_{iml} = \sqrt{2}g'N_{i1}W^*_{2m} + y_l N_{i3} W^*_{1m}. \tag{A.20}$$

Now we can compare the definitions and find that

$$\begin{aligned} G^L_{iml} &= \left(n^L_{iml}\right)^*, \\ G^R_{iml} &= -n^R_{iml}. \end{aligned} \tag{A.21}$$

This implies the following identities that are relevant for $(g-2)_\mu$ or eEDM

$$\begin{aligned} \mathrm{Im}\left[(G^R_{iml})^* G^L_{iml}\right] &= \mathrm{Im}\left[-(n^R_{iml})^*(n^L_{iml})^*\right] = \mathrm{Im}\left[n^R_{iml}n^L_{iml}\right], \\ \mathrm{Re}\left[(G^R_{iml})^* G^L_{iml}\right] &= -\,\mathrm{Re}\left[n^R_{iml}n^L_{iml}\right]. \end{aligned} \tag{A.22}$$

We are interested in the real and imaginary part of $[(G^R)^* G^L]$ for the calculation of the $(g-2)_\mu$ and eEDM contributions respectively. We will stick to the conventions in [40], with the note that we only use the 2×2 flavour specific part of the full 6×6 slepton matrices. The resulting expressions can be found in (3.12) and (3.15) for Δa_μ and the eEDM. Note the minus sign due to our different definition of the couplings with respect to [101] in the first expression. For the latter we have confirmed that our result agrees with the combination of (2.13) and (2.14) in [57].

Note also the factor y_l in our expressions compared to h_l^* in [57]. We think this is due to the $\tan(\beta)$ resummation that we do not take into account at one loop. The resummed Yukawa coupling includes CP violating phases and can therefore be a complex object. Since we consider the electron EDM, we do not take the small EW threshold corrections into account for y_e.

Chargino – lepton – sneutrino interactions

The interaction between a chargino, lepton and a sneutrino is given by the following Lagrangian

$$\mathcal{L}_{l\tilde{\nu}_l\tilde{\chi}^\pm} = c_k^L\ \bar{l}\ P_R(\widetilde{\chi}_k^+)^C\widetilde{\nu}_l + c_{kl}^R\overline{(\widetilde{\chi}_k^+)^C}\ P_R l\ \widetilde{\nu}_l^* + \text{h.c.}, \tag{A.23}$$

where the C represents charge conjugation. Note that we have assumed that the sneutrino and lepton are of the same flavour, in accordance with the (c)pMSSM convention. The couplings c_k^L and c_{kl}^R are defined as

$$c_k^L = -gV_{k1}, \tag{A.24}$$

$$c_{kl}^R = y_l U_{k2}. \tag{A.25}$$

With this definition we get $\text{Re}[c^R c^L]$ and $-\text{Im}[c^R c^L]$ for the 1-loop chargino contribution to $(g-2)_\mu$ and the eEDM, respectively. Note the lack of the complex conjugate for the right-handed couplings compared to [57].

A.4.2 Couplings for the two loop diagrams

Not all higher order contributions are relevant for our work: we only take the Barr-Zee diagrams into account. For these we need to define the neutral Higgs couplings. Note the differences with the conventions in [40] due to the explicit CP violation assumed throughout this work. For the neutral Higgs bosons H_i^0 we use the couplings to fermions, sfermions and charginos as given in Table A.2, equation A.29 and equation A.26, respectively.

Higgs – chargino interactions

Based on [55] we define the following Lagrangian and couplings for the interaction between a neutral Higgs boson and two charginos. We find in our conventions, with $C_L = U$ and $C_R = V^*$, that the interaction is as follows

$$\begin{aligned}
\mathcal{L}_{H^0\tilde{\chi}^+\tilde{\chi}^-} &= -\frac{g}{\sqrt{2}} \sum_{i,j,k} H_i^0 \bar{\tilde{\chi}}_j^- \left(g^S_{H_i\tilde{\chi}_j^+\tilde{\chi}_k^-} + i\gamma_5 g^P_{H_i\tilde{\chi}_j^+\tilde{\chi}_k^-} \right) \tilde{\chi}_k^- \,, \\
g^S_{H_i\tilde{\chi}_j^+\tilde{\chi}_k^-} &= \frac{1}{2} \left\{ [V_{j1}^* U_{k2}^* G_i^{\phi_1} + e^{-i\eta} V_{j2}^* U_{k1}^* G_i^{\phi_2}] + [j \leftrightarrow k]^* \right\} , \\
g^P_{H_i\tilde{\chi}_j^+\tilde{\chi}_k^-} &= \frac{i}{2} \left\{ [V_{j1}^* U_{k2}^* G_i^{\phi_1} + e^{-i\eta} V_{j2}^* U_{k1}^* G_i^{\phi_2}] - [j \leftrightarrow k]^* \right\} ,
\end{aligned} \tag{A.26}$$

where $G_i^{\phi_1} = (\mathcal{O}_{i\phi_1} - is_\beta \mathcal{O}_{ia})$, $G_i^{\phi_2} = (\mathcal{O}_{i\phi_2} - ic_\beta \mathcal{O}_{ia})$. The index $i = 1, 2, 3$ denotes the neutral Higgs boson mass eigenstates H_i^0 and the index $\phi = \phi_1, \phi_2$ and a denotes the three gauge eigenstates $\left(\sqrt{2}\mathrm{Re}\{H_d^0 - v_d/\sqrt{2}\}, \sqrt{2}\mathrm{Re}\{H_u^0 - v_u/\sqrt{2}\}, A_{\text{tree}^0}\right)^T$, where the Goldstone boson is already projected out (see also Section 2.4).

Higgs – fermion interactions

The coupling between a neutral Higgs boson H_i^0, a charged lepton or quark f and its anti-particle $\bar{f}$ is defined by the following Lagrangian

$$\mathcal{L}_{H^0 f\bar{f}} = -\frac{g m_f}{2M_W} \sum_{i=1}^{3} H_i^0 \bar{f} (g^S_{H_i f\bar{f}} + i g^P_{H_i f\bar{f}} \gamma^5) f, \tag{A.27}$$

where $g^S_{H_i f\bar{f}}$ and $g^P_{H_i f\bar{f}}$ are the scalar and pseudoscalar couplings. At tree level, they are given by the expressions in Table A.2. We also include loop-corrections for the third generation fermions by implementing a leading-order resummation of $\tan\beta$, as described in [55]. We present the expressions for this resummation in Appendix A.5.

	$f = u$	$f = d, l$
$g^S_{H_i f\bar{f}}$	$O_{i\phi_2}/\sin\beta$	$O_{i\phi_1}/\cos\beta$
$g^P_{H_i f\bar{f}}$	$-O_{ia}\cot\beta$	$-O_{ia}\tan\beta$

Table A.2 Neutral Higgs couplings to fermions

APPENDIX A. CONVENTIONS

Higgs – sfermion interactions

Based on [55], the Lagrangian that describes the interaction between a neutral Higgs boson H_i^0, an anti-sfermion $\widetilde{f}_j^*$ and a sfermion $\widetilde{f}_k$ is

$$\mathcal{L}_{H^0\tilde{f}_j\tilde{f}_k} = v\sum_{i=1}^{3}\sum_{f=u,d} g_{H_i\tilde{f}_j^*\tilde{f}_k}(H_i^0\tilde{f}_j^*\tilde{f}_k), \tag{A.28}$$

where

$$v g_{H_i\tilde{f}_j^*\tilde{f}_k} = \left(\Gamma^{\alpha\tilde{f}^*\tilde{f}}\right)_{\beta\gamma} O_{i\alpha} X^{\tilde{f}_*}_{\beta j} X^{\tilde{f}}_{\gamma k}. \tag{A.29}$$

We only take the contributions from the third-generation sfermions into account for the Barr-Zee diagrams, as the contributions from the first and second generation are much smaller.

In the $(\widetilde{f}_L, \widetilde{f}_R)$ basis, the effective couplings $\Gamma^{\alpha\widetilde{f}^*\widetilde{f}}$ are given by

$$\Gamma^{a\tilde{b}^*\tilde{b}} = \frac{1}{\sqrt{2}}\begin{pmatrix} 0 & i\,y_b^*(s_\beta A_b^* + e^{i\eta}c_\beta\mu) \\ -i\,y_b(s_\beta A_b + e^{-i\eta}c_\beta\mu^*) & 0 \end{pmatrix},$$

$$\Gamma^{\phi_1\tilde{b}^*\tilde{b}} = \begin{pmatrix} -|y_b|^2 v c_\beta + \frac{1}{4}\left(g^2+\frac{1}{3}g'^2\right)v c_\beta & -\frac{1}{\sqrt{2}}y_b^* A_b^* \\ -\frac{1}{\sqrt{2}}y_b A_b & -|y_b|^2 v c_\beta + \frac{1}{6}g'^2 v c_\beta \end{pmatrix},$$

$$\Gamma^{\phi_2\tilde{b}^*\tilde{b}} = \begin{pmatrix} -\frac{1}{4}\left(g^2+\frac{1}{3}g'^2\right)v s_\beta & \frac{1}{\sqrt{2}}y_b^*\mu e^{i\eta} \\ \frac{1}{\sqrt{2}}y_b\mu^* e^{-i\eta} & -\frac{1}{6}g'^2 v s_\beta \end{pmatrix},$$

$$\Gamma^{a\tilde{t}^*\tilde{t}} = \frac{1}{\sqrt{2}}\begin{pmatrix} 0 & i\,y_t^*(e^{-i\eta}c_\beta A_t^* + s_\beta\mu) \\ -i\,y_t(e^{i\eta}c_\beta A_t + s_\beta\mu^*) & 0 \end{pmatrix},$$

$$\Gamma^{\phi_1\tilde{t}^*\tilde{t}} = \begin{pmatrix} -\frac{1}{4}\left(g^2-\frac{1}{3}g'^2\right)v c_\beta & \frac{1}{\sqrt{2}}y_t^*\mu \\ \frac{1}{\sqrt{2}}y_t\mu^* & -\frac{1}{3}g'^2 v c_\beta \end{pmatrix},$$

$$\Gamma^{\phi_2\tilde{t}^*\tilde{t}} = \begin{pmatrix} -|y_t|^2 v s_\beta + \frac{1}{4}\left(g^2-\frac{1}{3}g'^2\right)v s_\beta & -\frac{1}{\sqrt{2}}y_t^* A_t^* e^{-i\eta} \\ -\frac{1}{\sqrt{2}}y_t A_t e^{i\eta} & -|y_t|^2 v s_\beta + \frac{1}{3}g'^2 v s_\beta \end{pmatrix},$$

$$\Gamma^{a\tilde{\tau}^*\tilde{\tau}} = \frac{1}{\sqrt{2}} \begin{pmatrix} 0 & i\, y_\tau^*(s_\beta A_\tau^* + e^{i\eta} c_\beta \mu) \\ -i\, y_\tau(s_\beta A_\tau + e^{-i\eta} c_\beta \mu^*) & 0 \end{pmatrix},$$

$$\Gamma^{\phi_1\tilde{\tau}^*\tilde{\tau}} = \begin{pmatrix} -|y_\tau|^2 v c_\beta + \frac{1}{4}\left(g^2 - g'^2\right) v c_\beta & -\frac{1}{\sqrt{2}} y_\tau^* A_\tau^* \\ -\frac{1}{\sqrt{2}} y_\tau A_\tau & -|y_\tau|^2 v c_\beta + \frac{1}{2} g'^2 v c_\beta \end{pmatrix},$$

$$\Gamma^{\phi_2\tilde{\tau}^*\tilde{\tau}} = \begin{pmatrix} -\frac{1}{4}\left(g^2 - g'^2\right) v s_\beta & \frac{1}{\sqrt{2}} y_\tau^* \mu e^{i\eta} \\ \frac{1}{\sqrt{2}} y_\tau \mu^* e^{-i\eta} & -\frac{1}{2} g'^2 v s_\beta \end{pmatrix}$$

$$\Gamma^{a\tilde{\nu}_\tau^*\tilde{\nu}_\tau} = 0, \qquad \Gamma^{\phi_1\tilde{\nu}_\tau^*\tilde{\nu}_\tau} = -\frac{1}{4}(g^2 + g'^2) v c_\beta, \qquad \Gamma^{\phi_2\tilde{\nu}_\tau^*\tilde{\nu}_\tau} = \frac{1}{4}(g^2 + g'^2) v s_\beta. \quad \text{(A.30)}$$

A.5 tan(β) resummation

The exchanges of gluinos and charginos give finite loop-induced threshold corrections to the Yukawa couplings $y_{u,d}$ [55], with the structure

$$y_d = \frac{\sqrt{2} m_d}{v \cos\beta} \frac{1}{1 + (\delta y_d / y_d) + (\Delta y_d / y_d) \tan\beta},$$
$$y_u = \frac{\sqrt{2} m_u}{v \sin\beta} \frac{1}{1 + (\delta y_u / y_u) + (\Delta y_u / y_u) \cot\beta}. \quad \text{(A.31)}$$

This modifies the couplings of the neutral Higgs H_i to quarks, for both the scalar and pseudoscalar coupling. We implement this for the top and bottom quarks only, as these are heavy and therefore receive larger corrections that have to be taken into account.

$$g^S_{H_i\bar{d}d} = \mathrm{Re}\left(\frac{1}{1 + \kappa_d \tan\beta}\right) \frac{O_{i\phi_1}}{\cos\beta} + \mathrm{Re}\left(\frac{\kappa_d}{1 + \kappa_d \tan\beta}\right) \frac{O_{i\phi_2}}{\cos\beta} + \mathrm{Im}\left[\frac{\kappa_d (\tan^2\beta + 1)}{1 + \kappa_d \tan\beta}\right] O_{ia},$$

$$g^P_{H_i\bar{d}d} = -\mathrm{Re}\left(\frac{\tan\beta - \kappa_d}{1 + \kappa_d \tan\beta}\right) O_{ia} + \mathrm{Im}\left(\frac{\kappa_d \tan\beta}{1 + \kappa_d \tan\beta}\right) \frac{O_{i\phi_1}}{\cos\beta} - \mathrm{Im}\left(\frac{\kappa_d}{1 + \kappa_d \tan\beta}\right) \frac{O_{i\phi_2}}{\cos\beta}, \quad \text{(A.32)}$$

(A.33)

APPENDIX A. CONVENTIONS

$$
\begin{aligned}
g^{S}_{H_i\bar{u}u} &= \mathrm{Re}\left(\frac{1}{1\,+\,\kappa_u\,\cot\beta}\right)\frac{O_{i\phi_2}}{\sin\beta}\;+\;\mathrm{Re}\left(\frac{\kappa_u}{1\,+\,\kappa_u\,\cot\beta}\right)\frac{O_{i\phi_1}}{\sin\beta} \\
&\quad+\;\mathrm{Im}\left[\frac{\kappa_u\,(\cot^2\beta\,+\,1)}{1\,+\,\kappa_u\,\cot\beta}\right]O_{ia}\,, \\
g^{P}_{H_i\bar{u}u} &= -\,\mathrm{Re}\left(\frac{\cot\beta\,-\,\kappa_u}{1\,+\,\kappa_u\,\cot\beta}\right)O_{ia}\;+\;\mathrm{Im}\left(\frac{\kappa_u\,\cot\beta}{1\,+\,\kappa_u\,\cot\beta}\right)\frac{O_{i\phi_2}}{\sin\beta} \\
&\quad-\;\mathrm{Im}\left(\frac{\kappa_u}{1\,+\,\kappa_u\,\cot\beta}\right)\frac{O_{i\phi_1}}{\sin\beta}\,. \qquad \text{(A.34)}
\end{aligned}
$$

In the above equations, we have used the abbreviation

$$
\kappa_q \;=\; \frac{(\Delta y_q/y_q)}{1\,+\,(\delta y_q/y_q)}\,, \qquad \text{(A.35)}
$$

for $q = u, d$. Detailed expressions for the threshold contributions $(\delta y_q/y_q)$ and $(\Delta y_q/y_q)$ are given by [234]:

$$
\frac{\delta y_d}{y_d} = -\frac{2\alpha_s}{3\pi}\,m^*_{\tilde{g}}A_d\,I(m^2_{\tilde{d}_1},m^2_{\tilde{d}_2},|m_{\tilde{g}}|^2)\;-\;\frac{|y_u|^2}{16\pi^2}\,|\mu|^2\,I(m^2_{\tilde{u}_1},m^2_{\tilde{u}_2},|\mu|^2)\,, \qquad \text{(A.36)}
$$

$$
\frac{\Delta y_d}{y_d} = \frac{2\alpha_s}{3\pi}\,m^*_{\tilde{g}}\,\mu^*\,I(m^2_{\tilde{d}_1},m^2_{\tilde{d}_2},|m_{\tilde{g}}|^2)\;+\;\frac{|y_u|^2}{16\pi^2}\,A^*_u\mu^*\,I(m^2_{\tilde{u}_1},m^2_{\tilde{u}_2},|\mu|^2)\,, \qquad \text{(A.37)}
$$

$$
\frac{\Delta y_u}{y_u} = \frac{2\alpha_s}{3\pi}\,m^*_{\tilde{g}}\mu^*\,I(m^2_{\tilde{u}_1},m^2_{\tilde{u}_2},|m_{\tilde{g}}|^2)\;+\;\frac{|y_d|^2}{16\pi^2}\,A^*_d\mu^*\,I(m^2_{\tilde{d}_1},m^2_{\tilde{d}_2},|\mu|^2)\,, \qquad \text{(A.38)}
$$

$$
\frac{\delta y_u}{y_u} = -\frac{2\alpha_s}{3\pi}\,m^*_{\tilde{g}}A_u\,I(m^2_{\tilde{u}_1},m^2_{\tilde{u}_2},|m_{\tilde{g}}|^2)\;-\;\frac{|y_d|^2}{16\pi^2}\,|\mu|^2\,I(m^2_{\tilde{d}_1},m^2_{\tilde{d}_2},|\mu|^2)\,. \qquad \text{(A.39)}
$$

where $I(a,b,c)$ is the defined as the function

$$
I(a,b,c) \;\equiv\; \frac{ab\ln(a/b)+bc\ln(b/c)+ac\ln(c/a)}{(a-b)(b-c)(a-c)}\,. \qquad \text{(A.40)}
$$

A.6 Conventions in software

The software packages that are used throughout this thesis have different conventions. Especially in the cpMSSM, it is of utmost importance to keep track of these conventions to avoid calculational errors. We describe the conventions here, for as far as they are known.

A.6.1 CPsuperH

The conventions for CPsuperH are relevant for us, even though we do not use the software directly. The package in MicrOMEGAs that implements the CPV violating MSSM is based on CPsuperH. Although we have adapted MicrOMEGAs to override the spectrum from CPsuperH with our own inputfile, we still have to match the conventions. These are:

- At all orders of renormalisation $\eta = 0$;
- Hence b can be a complex parameter beyond loop-level;
- Tadpole equations are solved for sign(μ), $m^2_{H_u}$ and $m^2_{H_d}$
- The neutral Higgs mixing matrix is $\mathcal{O}^T$;
- The SLHA block 'CHVMIX' is the 3x4 mixing matrix accoring to [54].

A.6.2 FeynHiggs

The relevant conventions for FeynHiggs are:

- Im(b) = 0 at all orders;
- The neutral Higgs mixing matrix is $\mathcal{R}$, which is given in the SLHA block 'CHVMIX' (3x3)
- The PDG numbering for the sparticles is according to their flavour composition;
- The mixing matrices for the third generation squarks and charged slepton are presented separately in 2x2 blocks.

We use a rotation as described in (2.36) to switch between the FeynHiggs convention and the SPheno convention for the phases. We transform the trilinear couplings (3x3) T_u, T_d and T_e as calculated by SPheno, together with the input parameters for SPheno. This gives consistent results at tree level.

A.6.3 Low Energy calculation

For our own in-house code, we use the output from both SPheno and FeynHiggs. As we only use FeynHiggs to improve the calculation of the Higgs boson masses, we use the SPheno output for everything beside the Higgs boson masses and the Higgs boson mixing matrices. We do however adopt the FeynHiggs convention to order the sfermions according to their flavour content, i.e. not ordered according to their masses.

A.6.4 MicrOMEGAs

Note that we have adapted MicrOMEGAs to accept an SLHA input file, to avoid using the spectrum as calculated by CPsuperH. As a result, we need the following input that is typically calculated by CPsuperH:

- The input requires the block 'THRESHOLD', containing the components of $\frac{\kappa_q \tan(\beta)}{1+\kappa_q \tan(\beta)}$ for $q = t, b$ (see Table 6 of [109]);
- The input requires the blocks 'HCOUPLINGS' and 'IMHCOUPLINGS', containing the real and imaginary parts of the 7 λ_i as given in (2.8);
- The input requires the block 'CVHMIX', containing the values of the 3x4 neutral Higgs mixing matrix according to the conventions of [54].

We explicitly assume that the conventions for HiggsBounds, HiggsSignals and Lilith are such that this is internally consistent, as MicrOMEGAs offers the option to use an integrated version of these software packages.

A.6.5 SPheno

- We assume both $\mathrm{Im}(b) \neq 0$ and $\eta \neq 0$
- The tadpole equations are solved for $\mathrm{Re}(b), \mathrm{Im}(b)$ and $\mathrm{sign}(\mu)$;
- The mixing matrices for sparticles are based on mass ordering;
- The mixing matrices for the squarks and charged sleptons are presented as 6x6 matrices;
- The PDG numbering for the sparticles is based on mass ordering.

The first convention means we have explicitly not used the freedom as described in Section 2.4 to rotate away any phase, which allows us to solve the tadpole equations as described. As a result, some of the parameters are redundant, but this is not unphysical. Without this convention, we cannot be sure that the results from SPheno are correct.

At tree level, we find that the spectrum as calculated by SPheno is now the same for a set of input parameters, and a set that is rotated according to the transformations in (2.36). For higher orders we find minor differences. Since SPheno does not implement the full one-loop or two-loop calculation, these differences are to be expected.

Note that due to the mass ordering, it can happen that a sparticle with e.g. PDG number 100011 can be (mostly) smuon or stau, if the concerning sparticle is the lightest charged slepton.

We observe that the switch between mass ordering and particle content is not always consistently implemented in SPheno, so we urge a careful treatment when several software packages are used together.

B. Loop Functions

The loop functions for the 1-loop diagrams in 3.1.1 and 3.1.2 read [101]

$$F_1^N(x) = \frac{2}{(1-x)^4}\left[1 - 6x + 3x^2 + 2x^3 - 6x^2\log(x)\right], \tag{B.1}$$

$$F_2^N(x) = \frac{3}{(1-x)^3}\left[1 - x^2 + 2x\log(x)\right], \tag{B.2}$$

$$F_1^C(x) = \frac{2}{(1-x)^4}\left[2 + 3x - 6x^2 + x^3 + 6x\log(x)\right], \tag{B.3}$$

$$F_2^C(x) = \frac{3}{2(1-x)^3}\left[-3 + 4x - x^2 - 2\log(x)\right]. \tag{B.4}$$

We can identify the following relations with [57], where slightly different conventions are used

$$F_2^N(x) = 6B(x), \qquad F_2^C(x) = -3A(x). \tag{B.5}$$

For the 2-loop Barr-Zee diagrams we have the following loop functions [57]

$$F(\tau) = \int_0^1 dx \frac{x(1-x)}{\tau - x(1-x)}\log\left[\frac{x(1-x)}{\tau}\right], \tag{B.6}$$

$$f(\tau) = \frac{\tau}{2}\int_0^1 dx \frac{1-2x(1-x)}{x(1-x)-\tau}\log\left[\frac{x(1-x)}{\tau}\right], \tag{B.7}$$

$$g(\tau) = \frac{\tau}{2}\int_0^1 dx \frac{1}{x(1-x)-\tau}\log\left[\frac{x(1-x)}{\tau}\right]. \tag{B.8}$$

To implement these loop functions in a piece of software, it is not convenient to rely on numerical integration, as this can be very time consuming. Instead, we express the loop functions in terms of dilogarithms as follows. We define the dilogarithm according to

$$\mathrm{Li}_2(\mathrm{z}) = -\int_0^1 \mathrm{dt}\frac{\ln(1-\mathrm{tz})}{\mathrm{t}} = -\int_0^{\mathrm{z}} \mathrm{du}\frac{\ln(1-\mathrm{u})}{\mathrm{u}}. \tag{B.9}$$

We use it to write

$$\int_0^1 dx \frac{\ln(x/a)}{x-a} = -\left[\mathrm{Li}_2(1-\frac{\mathrm{x}}{\mathrm{a}})\right]_{x=0}^{x=1}, \tag{B.10}$$

which we can evaluate as

$$\mathrm{Li}_2(1) - \mathrm{Li}_2(1-\frac{1}{\mathrm{a}}) = \frac{\pi^2}{6} - \mathrm{Li}_2(1-\frac{1}{\mathrm{a}}). \tag{B.11}$$

With these identities we can now write

$$\begin{aligned} g(\tau) &= \frac{\tau}{2}\int_0^1 dx \frac{\ln(x(1-x)/\tau)}{x(1-x)-\tau} \\ &= \frac{\tau}{2}\frac{1}{\sqrt{1-4\tau}}\int_0^1 dx \left(\frac{1}{x_+ - x} + \frac{1}{x-x_-}\right)\ln(\frac{x(1-x)}{x_+ x_-}) \\ &= \frac{\tau}{\sqrt{1-4\tau}}\int_0^1 dx \frac{1}{x_+-x}\left[\ln(\frac{x}{x_+}) + \ln(\frac{1-x}{x_-})\right] \\ &= \frac{\tau}{\sqrt{1-4\tau}}\int_0^1 dx \left[\frac{\ln(x/x_+)}{x_+-x} + \frac{\ln(x/x_-)}{x-x_-}\right], \end{aligned} \tag{B.12}$$

where we have defined $x_\pm = \frac{1}{2}(1 \pm \sqrt{1-4\tau})$. Putting this together we find for the loop function $g(\tau)$ the following expression

$$\begin{aligned} g(\tau) &= \frac{\tau}{\sqrt{1-4\tau}}\left[\mathrm{Li}_2(\frac{-\mathrm{x}_-}{\mathrm{x}_+}) - \mathrm{Li}_2(\frac{-\mathrm{x}_+}{\mathrm{x}_-})\right] \\ &= \frac{\tau}{\sqrt{1-4\tau}}\left[\mathrm{Li}_2(\frac{\sqrt{1-4\tau}-1}{\sqrt{1-4\tau}+1}) - \mathrm{Li}_2(\frac{\sqrt{1-4\tau}+1}{\sqrt{1-4\tau}-1})\right] \end{aligned} \tag{B.13}$$

We implement the last line of this expression in our script to calculate the eEDM. We also implement

$$F(\tau) = -2g(\tau) + 2 + \ln(\tau) \tag{B.14}$$

$$f(\tau) = (1-2\tau)g(\tau) + 2\tau + \tau\ln(\tau). \tag{B.15}$$

In the limit $\tau \to 1/4$ we implement $g(\tau) \to \log(2)$. Note that the Python package scipy.special includes the Spence function, which is defined using a different convention as

$$\mathrm{Spence}(z) = \int_1^z dt \frac{\ln(t)}{1-t} \tag{B.16}$$

$$= \mathrm{Li}_2(1-\mathrm{z}). \tag{B.17}$$

C. Projection operators: a calculational tool

In this appendix we give the expressions for the projection operators that are used to project on the observable of interest and extract the contribution to it originating from a general Feynman diagram, as is necessary to arrive at the expressions given in Chapter 3.

Consider a general diagram as in Figure C.1. At tree level this is simply the interaction between a photon and an electron, determined by the charge of the electron. However, at higher orders there are more structures that can be identified, including the magnetic moment and electric dipole moment. To calculate the contribution of a certain diagram to an observable it is therefore important to identify the relevant part of the diagram. We project on the required observable(s) with specific operators as defined below.

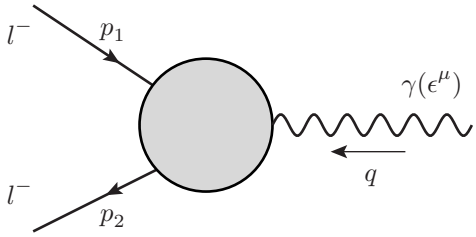

Figure C.1 *General vertex structure of the interaction between a lepton and a photon.*

We can write the general matrix element of Figure C.1 for any lepton as

$$i\mathcal{M} = -ie\ \bar{u}(p_2)\ \Gamma^\mu\ u(p_1)\ \epsilon_\mu(q), \tag{C.1}$$

where we have defined the vertex structure Γ^μ, which reduces at tree level to

APPENDIX C. PROJECTION OPERATORS: A CALCULATIONAL TOOL

$\Gamma^\mu = Q_e\gamma^\mu = -\gamma^\mu$. Beyond tree level we can construct the general structure of Γ^μ, since we know that $\bar{u}(p_2)\,\Gamma^\mu\,u(p_1)$ is a Lorentz-vector. The possible ingredients are the independent momenta of the particles and general Dirac structures like γ^μ, γ_5 and $\sigma^{\mu\nu} = \frac{i}{2}[\gamma^\mu, \gamma^\nu]$. Defining $P^\mu = p_1^\mu + p_2^\mu$ and $q^\mu = p_2^\mu - p_1^\mu$, we can write Γ^μ for a lepton of mass m in terms of the form factors A_i as

$$\Gamma^\mu = \gamma^\mu A_1 + \frac{P^\mu}{2m}A_2 + \frac{q^\mu}{2m}A_3 + \gamma^\mu\gamma_5 A_4 + \frac{q^\mu}{2m}\gamma_5 A_5 + i\frac{P^\mu}{2m}\gamma_5 A_6. \tag{C.2}$$

Using the Gordon identities for $\bar{u}(p_2)\,\Gamma^\mu\,u(p_1)$ we find

$$\bar{u}(p_2)\frac{P^\mu}{2m}u(p_1) = \bar{u}(p_2)\left(\gamma^\mu - i\frac{\sigma^{\mu\nu}q_\nu}{2m}\right)u(p_1) \;\text{ and }\; \bar{u}(p_2)iP^\mu\gamma_5 u(p_1) = \bar{u}(p_2)\sigma^{\mu\nu}q_\nu\gamma_5 u(p_1), \tag{C.3}$$

allowing us to rewrite the vertex structure as

$$\Gamma^\mu = \gamma^\mu(A_1 + A_2) - i\frac{\sigma^{\mu\nu}q_\nu}{2m}A_2 + \frac{q^\mu}{2m}A_3 + \gamma^\mu\gamma_5 A_4 + \frac{q^\mu}{2m}\gamma_5 A_5 + \frac{\sigma^{\mu\nu}q_\nu}{2m}\gamma_5 A_6. \tag{C.4}$$

By imposing current conservation and using the Ward identity we find $A_3 = 0$ and $A_5 = -\frac{4m^2}{q^2}A_4$. Hence

$$\Gamma^\mu = \gamma^\mu(A_1 + A_2) + \left(\gamma^\mu - \frac{2m\,q^\mu}{q^2}\right)\gamma_5 A_4 - i\frac{\sigma^{\mu\nu}q_\nu}{2m}A_2 + \frac{\sigma^{\mu\nu}q_\nu}{2m}\gamma_5 A_6, \tag{C.5}$$

which is usually written as

$$\Gamma^\mu = \gamma^\mu F_E(q^2) + \left(\gamma^\mu - \frac{2m\,q^\mu}{q^2}\right)\gamma_5 F_A(q^2) + i\frac{\sigma^{\mu\nu}q_\nu}{2m}F_M(q^2) + \frac{\sigma^{\mu\nu}q_\nu}{2m}\gamma_5 F_D(q^2). \tag{C.6}$$

We can now identify the physical form factors, which are all defined in the limit $q \to 0$, as follows. The corresponding observables in units of e can be extracted from these form factors.

$F_E = A_1 + A_2$	electromagnetic charge
$F_A = A_4$	anapole moment
$F_M = -A_2$	anomalous magnetic moment
$F_D = A_6$	electric dipole moment

We can rewrite the last lines to the following definitions of the anomalous magnetic moment of the muon a_μ and the electric dipole moment of the electron d_e^E:

$$a_\mu = -F_M(q^2)\Big|_{q^2\to 0} \tag{C.7}$$

$$\frac{d_e^E}{e} = -\frac{F_D(q^2)}{2m_e}\Big|_{q^2\to 0}. \tag{C.8}$$

This allows us to identify the part of a Feynman diagram that contributes to a physical quantity, by splitting the matrix element in the different structures that we recognize as form factors. This is typically done by projecting on the relevant structure. In general, we can design a projection operator O^μ such that a form factor A_i is given by

$$A_i = \mathrm{Tr}\left\{O_{i\mu}\Gamma^\mu\right\}. \tag{C.9}$$

For a lepton of mass m this results in

$$O^\mu = (\not{p}_1 + m)\left(\gamma^\mu c_1 + \frac{P^\mu}{2m}c_2 + \frac{q^\mu}{2m}c_3 + \gamma^\mu\gamma_5 c_4 + \frac{q^\mu}{2m}\gamma_5 c_5 - i\frac{P^\mu}{2m}\gamma_5 c_6\right)(\not{p}_2 + m_e) \tag{C.10}$$

$$\equiv (\not{p}_1 + m_e)\Lambda^\mu(\not{p}_2 + m). \tag{C.11}$$

In D spacetime dimensions we find

$$\begin{aligned}
\mathrm{Tr}\left\{O_\mu\Gamma^\mu\right\} = \sum_{i=1}^{6} A_i g_i \quad &= \quad A_1[c_1(2(D-2)s + 8m^2) + c_2(-2s + 8m^2)] \\
&+ \quad A_2[c_1(-2s + 8m^2) + c_2(-4s + \frac{s^2}{2m^2} + 8m^2)] \\
&+ \quad A_3[c_3(2s - \frac{s^2}{2m^2})] \\
&+ \quad A_4[c_4(2(D-2)s - 8(D-1)m^2) + c_5(2s)] \\
&+ \quad A_5[c_4(-2s) + c_5(\frac{s^2}{2m^2})] \\
&+ \quad A_6[c_6(2s - \frac{s^2}{2m^2})],
\end{aligned}$$

where we have defined $s = q^2$. Requiring $g_i = 1$ and $g_j = 0$ for all $j \neq i$ results in the coefficients c_k as shown in Table C.1 for all $O_i^\mu = (\not{p}_1 + m)\Lambda_i^\mu(\not{p}_2 + m)$. Any unspecified c_k is understood to be zero.

APPENDIX C. PROJECTION OPERATORS: A CALCULATIONAL TOOL

Operator	Coefficients	Expression for Λ^μ
O_1	$c_1 = \frac{s-4m^2}{4m^2}c_2$ $c_2 = \frac{2m^2}{(D-2)s(s-4m^2)}$	$\Lambda_1^\mu = \frac{1}{2s(D-2)}\left\{\gamma^\mu + \frac{4m^2}{s-4m^2}\frac{P^\mu}{2m}\right\}$
O_2	$c_1 = \frac{2m^2}{(D-2)s(s-4m^2)}$ $c_2 = \frac{(D-2)s+4m^2}{s-4m^2}c_1$	$\Lambda_2^\mu = \frac{2m^2}{s(D-2)(s-4m^2)}\left\{\gamma^\mu + \frac{(D-2)s+4m^2}{s-4m^2}\frac{P^\mu}{2m}\right\}$
O_3	$c_3 = \frac{-2m^2}{s(s-4m^2)}$	$\Lambda_3^\mu = \frac{-2m^2}{s(s-4m^2)}\frac{q^\mu}{2m}$
O_4	$c_4 = \frac{s}{4m^2}c_5$ $c_5 = \frac{2m^2}{(D-2)s(s-4m^2)}$	$\Lambda_4^\mu = \frac{1}{2(D-2)(s-4m^2)}\left\{\gamma^\mu + \frac{4m^2}{s}\frac{q^\mu}{2m}\right\}\gamma_5$
O_5	$c_4 = \frac{2m^2}{(D-2)s(s-4m^2)}$ $c_5 = \frac{2s-4m^2-D(s-4m^2)}{s}c_4$	$\Lambda_5^\mu = \frac{2m^2}{s(D-2)(s-4m^2)}\left\{\gamma^\mu + \frac{4(D-1)m^2-(D-2)s}{s}\frac{q^\mu}{2m}\right\}\gamma_5$
O_6	$c_6 = \frac{-2m^2}{s(s-4m^2)}$	$\Lambda_6^\mu = \frac{2im^2}{s(s-4m^2)}\frac{P^\mu}{2m}\gamma_5$

Table C.1 Projection operators in D spacetime dimensions

With these definitions we can obtain the projection operators for a_μ and d_e^E/e specifically. We use $D = 4$ for O_6. The projection operator for a_μ is given by

$$O_2 = (\not{p}_1 + m_l)\frac{2m_l^2}{s(D-2)(s-4m_l^2)}\left\{\gamma^\mu + \left(\frac{s(D-2)/2 + 2m_l^2}{s-4m_l^2}\right)\frac{P^\mu}{m_l}\right\}(\not{p}_2 + m_l), \tag{C.12}$$

where for the muon we have $m_l = m_\mu$. The projection operator for d_e^E/e is given by

$$-O_6/2m_e = (\not{p}_1 + m_e)\frac{-iP^\mu}{2s(s-4m_e^2)}\gamma_5(\not{p}_2 + m_e). \tag{C.13}$$

With these operators one can, in principle, extract the contribution of any Feynman diagram to the relevant observables.

D. Comparison of spectrum generators

We give a comparison of the spectrum generators CPsuperH and SPheno for two example sets of input parameters: one random set of pMSSM input parameters that does produce a non-excluded spectrum with SPheno, and a set where we have adjusted the input to minimize the differences between CPsuperH and SPheno. Note that the second set gives results that would be excluded (e.g. the lack of a SM-like Higgs boson for the SPheno output).

The SM input is set to the latest experimental values [45] for both sets. For the first input set, the SUSY parameters are chosen as in Table D.1, where we assume the masses of the first and second generations are the same.

The output for the first set of parameters is shown in Table D.2, for both CPsuperH and SPheno. We observe that the differences between the two spectra are significant in almost every aspect: only the lightest Higgs, charged Higgs, both bottom squarks and the third and fourth neutralino are similar.

Note that the trilinear couplings and μ obtain imaginary parts in CPsuperH, shown in Table D.3, even though they are defined to be completely real in the input. Apparently, the parameters can still obtain a different value than the given input.

SUSY parameter	CPsuperH	SPheno
$\tan(\beta)$	18.7881	18.7881
$m_H^{\pm}$	1452.2 GeV	solved in tadpoles
$m^2_{H_d}$	solved in tadpoles	2080330.79 GeV^2
$m^2_{H_u}$	solved in tadpoles	-61371.4582 GeV^2
$\lvert\mu\rvert$	252.362768 GeV	solved in tadpoles
$\lvert M_1\rvert$	1454.226 GeV	1454.226 GeV
$\lvert M_2\rvert$	1147.779 GeV	1147.779 GeV
$\lvert M_3\rvert$	1091.982 GeV	1091.982 GeV
$\lvert A_t\rvert$	1736.005 GeV	1736.005 GeV
$\lvert A_b\rvert$	2779.689 GeV	2779.689 GeV
$\lvert A_\tau\rvert$	2263.821 GeV	2263.821 GeV
ϕ_μ	0.0	0 by definition
ϕ_{M_1}	0.0	0 by definition
ϕ_{M_2}	0.0	0 by definition
ϕ_{M_3}	0.0	0 by definition
ϕ_{A_t}	0.0	0 by definition
ϕ_{A_b}	0.0	0 by definition
ϕ_{A_τ}	0.0	0 by definition
m_{Q_3}	1307.134 GeV	1307.134 GeV
m_{U_3}	2490.581 GeV	2490.581 GeV
m_{D_3}	9389.581 GeV	9389.581 GeV
m_{L_3}	1392.465 GeV	1392.465 GeV
m_{E_3}	1175.462 GeV	1175.462 GeV
m_{Q_1}	1589.634 GeV	1589.634 GeV
m_{U_1}	1244.327 GeV	1244.327 GeV
m_{D_1}	1032.191 GeV	1032.191 GeV
m_{L_1}	142.2132 GeV	142.2132 GeV
m_{E_1}	124.4694 GeV	124.4694 GeV

Table D.1 Input parameters for CPsuperH and SPheno, where we expect significant differences in the output. Note that CPsuperH does not take the parameters of the first and second generation directly as input, but rather uses a hierarchy factor, e.g. $\rho_Q = m_{Q_1}/m_{Q_3}$.

PDG code	Particle	CPsuperH mass (GeV)	SPheno mass (GeV)
24	W boson	79.2062590	80.3562659
25	H_1^0	123.123702	125.111301
35	H_2^0	947.796889	1447.53877
36	H_3^0	947.823768	1447.43888
37	$H^{\pm}$	1452.26470	1449.76005
1000005	$\tilde{b_1}$	939.138592	960.950354
2000005	$\tilde{b_2}$	1308.59007	1317.56173
1000006	$\tilde{t_1}$	1299.88299	255.137213
2000006	$\tilde{t_2}$	2500.74286	1341.33913
1000015	$\tilde{\tau_1}$	63.5574611	108.880629
2000015	$\tilde{\tau_2}$	182.514632	130.175652
1000016	$\tilde{\nu_{\tau,L}}$	123.499756	93.9105368
1000022	$\tilde{\chi_1^0}$	262.931125	52.5701692
1000023	$\tilde{\chi_2^0}$	270.375739	-56.8182496
1000025	$\tilde{\chi_3^0}$	1153.80926	1169.45606
1000035	$\tilde{\chi_4^0}$	1455.64069	1457.25828
1000024	$\tilde{\chi_1^{\pm}}$	250.757990	54.5186855
1000037	$\tilde{\chi_2^{\pm}}$	444.024060	1169.74874

Table D.2 The output from CPsuperH and SPheno for the set of input parameters as given in Table D.1

Parameter	Value
A_t	-1295.91650 GeV
A_b	-0.240800634 GeV
A_τ	-0.775613844 GeV
μ	1.08164108 GeV

Table D.3 The imaginary parts of the parameters as given by CPsuperH.

APPENDIX D. COMPARISON OF SPECTRUM GENERATORS

We have also done a run for the input set that is shown in Table D.4, which keeps the sparticles of the same kind (e.g. $\tilde{t}_1$ and $\tilde{t}_2$) close in mass for the SPheno output. This is done to minimize the differences that arise from the approaches taken (running RGEs versus effective potential).

However, the output for this set of parameters that is shown in Table D.5 still has significant differences. Mainly the Higgs sector is clearly treated completely different in the two programs, resulting in a sharp contrast between the resulting masses. For this set also the mass of the SM-like Higgs boson varies more between the two programs. The results in the squark and slepton sector are more similar, especially with respect to the results from the first set, although a $\mathcal{O}(10\%)$ difference still exists.

Again we also obtain imaginary parts in the CPsuperH output, as shown in Table D.6. Interestingly, these imaginary parts are the same as for the first input set. We do not know why this happens.

SUSY parameter	CPsuperH	SPheno
$\tan(\beta)$	18.7881	18.7881
$m_H^{\pm}$	1452.2 GeV	solved in tadpoles
$m^2_{H_d}$	solved in tadpoles	2080330.79 GeV^2
$m^2_{H_u}$	solved in tadpoles	-61371.4582 GeV^2
$\lvert\mu\rvert$	252.362768 GeV	solved in tadpoles
$\lvert M_1\rvert$	1454.226 GeV	1454.226 GeV
$\lvert M_2\rvert$	1147.779 GeV	1147.779 GeV
$\lvert M_3\rvert$	1091.982 GeV	1091.982 GeV
$\lvert A_t\rvert$	17.36005 GeV	17.36005 GeV
$\lvert A_b\rvert$	2779.689 GeV	2779.689 GeV
$\lvert A_\tau\rvert$	22.63821 GeV	22.63821 GeV
ϕ_μ	0.0	0 by definition
ϕ_{M_1}	0.0	0 by definition
ϕ_{M_1}	0.0	0 by definition
ϕ_{M_1}	0.0	0 by definition
ϕ_{A_t}	0.0	0 by definition
ϕ_{A_b}	0.0	0 by definition
ϕ_{A_τ}	0.0	0 by definition
m_{Q_3}	1307.134 GeV	1307.134 GeV
m_{U_3}	1307.134 GeV	1307.134 GeV
m_{D_3}	1307.134 GeV	1307.134 GeV
m_{L_3}	599.246 GeV	599.246 GeV
m_{E_3}	1175.462 GeV	1175.462 GeV
m_{Q_1}	1589.634 GeV	1589.634 GeV
m_{U_1}	1244.327 GeV	1244.327 GeV
m_{D_1}	1032.191 GeV	1032.191 GeV
m_{L_1}	142.2132 GeV	142.2132 GeV
m_{E_1}	124.4694 GeV	124.4694 GeV

Table D.4 Input parameters for CPsuperH and SPheno, where we expect the outputs to be closer together than for the first set. Note that CPsuperH does not take the parameters of the first and second generation directly as input, but rather uses a hierarchy factor, e.g. $\rho_Q = m_{Q_1}/m_{Q_3}$.

PDG code	Particle	CPsuperH mass (GeV)	SPheno mass (GeV)
24	W boson	79.2062590	80.3600340
25	H_1^0	123.123702	116.180397
35	H_2^0	947.796889	1459.53044
36	H_3^0	947.823768	1459.50863
37	$H^{\pm}$	1452.26470	1461.97128
1000005	$\tilde{b_1}$	1301.43596	1323.04887
2000005	$\tilde{b_2}$	1314.38645	1323.95370
1000006	$\tilde{t_1}$	1144.94966	1328.43680
2000006	$\tilde{t_2}$	1463.68888	1332.17120
1000015	$\tilde{\tau_1}$	124.353822	99.1441508
2000015	$\tilde{\tau_2}$	601.325950	598.996568
1000016	$\tilde{\nu_{\tau,L}}$	595.784317	593.322979
1000022	$\tilde{\chi_1^0}$	262.931125	167.046494
1000023	$\tilde{\chi_2^0}$	270.375739	-173.851237
1000025	$\tilde{\chi_3^0}$	1153.80926	1169.22699
1000035	$\tilde{\chi_4^0}$	1455.64069	1458.63705
1000024	$\tilde{\chi_1^{\pm}}$	250.757990	170.079699
1000037	$\tilde{\chi_2^{\pm}}$	444.024060	1169.50377

Table D.5 The output from CPsuperH and SPheno for the set of input parameters as given in Table D.4

Parameter	Value
A_t	-1295.91650 GeV
A_b	-0.240800634 GeV
A_τ	-0.775613844 GeV
μ	1.08164108 GeV

Table D.6 The imaginary parts of the parameters as given by CPsuperH for the second set of input parameters.

E. SARAH model files

To generate a new source code for SPheno that can deal with the complex MSSM, we have used the Mathematica package SARAH 4.0 [184]. We have used the following definitions for our complex MSSM model, which is based on the standard MSSM-CPV files that are included in the installation of SARAH. First, the model file itself:

```
Off[General::spell]

Model`Name = "MSSMCPV";
Model`NameLaTeX ="MSSM-CPV";
Model`Authors = "M. vanBeekveld,M. Schutten,F. Staub";
Model`Date = "2022-02-21";

(*-------------------------------------------------------------------*)
(*    Particle Content*)
(*-------------------------------------------------------------------*)

(* Global symmetries *)

Global[[1]] = {Z[2],RParity};
RpM = {-1,-1,1};
RpP = {1,1,-1};

(* Vector Superfields *)

Gauge[[1]]={B,    U[1], hypercharge, g1, False, RpM};
Gauge[[2]]={WB,  SU[2], left,        g2, True,  RpM};
Gauge[[3]]={G,   SU[3], color,       g3, False, RpM};
```

```
(* Chiral Superfields *)

SuperFields[[1]] = {q,  3, {uL,  dL},    1/6, 2, 3, RpM};
SuperFields[[2]] = {l,  3, {vL,  eL},   -1/2, 2, 1, RpM};
SuperFields[[3]] = {Hd, 1, {Hd0, Hdm},  -1/2, 2, 1, RpP};
SuperFields[[4]] = {Hu, 1, {Hup, Hu0},   1/2, 2, 1, RpP};

SuperFields[[5]] = {d, 3, conj[dR],  1/3, 1, -3, RpM};
SuperFields[[6]] = {u, 3, conj[uR], -2/3, 1, -3, RpM};
SuperFields[[7]] = {e, 3, conj[eR],    1, 1,  1, RpM};

(*-------------------------------------------------------------*)
(* Superpotential *)
(*-------------------------------------------------------------*)

SuperPotential = Yu u.q.Hu - Yd d.q.Hd - Ye e.l.Hd
+ \[Mu] Hu.Hd;


(*-------------------------------------------------------------*)
(*    DEFINITION    *)
(*-------------------------------------------------------------*)

NameOfStates={GaugeES,EWSB};


(* Gauge Sector *)

DEFINITION[EWSB][GaugeSector] =
{
  {{VB,VWB[3]},{VP,VZ},ZZ},
  {{VWB[1],VWB[2]},{VWm,conj[VWm]},ZW},
  {{fWB[1],fWB[2],fWB[3]},{fWm,fWp,fW0},ZfW}
};
```

```
DEFINITION[GaugeES][DiracSpinors]={
  Bino ->{fB, conj[fB]},
  Wino -> {fWB, conj[fWB]},
  Glu -> {fG, conj[fG]},
  H0 -> {FHd0, conj[FHu0]},
  HC -> {FHdm, conj[FHup]},
  Fd1 -> {FdL, 0},
  Fd2 -> {0, FdR},
  Fu1 -> {FuL, 0},
  Fu2 -> {0, FuR},
  Fe1 -> {FeL, 0},
  Fe2 -> {0, FeR},
  Fv -> {FvL,0}
};


DEFINITION[GaugeES][Phases]=
{     {SHup, Exp[I eta]},
      {SHu0, Exp[I eta]}
     };


(* ------ VEVs ------ *)

DEFINITION[EWSB][VEVs]=
  {{SHd0, {vd, 1/Sqrt[2]}, {sigmad, I/Sqrt[2]}, {phid,1/Sqrt[2]}},
   {SHu0, {vu, 1/Sqrt[2]}, {sigmau, I/Sqrt[2]}, {phiu,1/Sqrt[2]}}};

(* ------ Mixings ------ *)

DEFINITION[EWSB][MatterSector]=
{     {{SdL, SdR}, {Sd, ZD}},
      {{SuL, SuR}, {Su, ZU}},
      {{SeL, SeR}, {Se, ZE}},
      {{SvL}, {Sv, ZV}},
      {{phid, phiu, sigmad, sigmau}, {hh, ZH}},
      {{SHdm,conj[SHup]},{Hpm,ZP}},
      {{fB, fW0, FHd0, FHu0}, {L0, ZN}},
      {{{fWm, FHdm}, {fWp, FHup}}, {{Lm,UM}, {Lp,UP}}},
      {{{FeL},{conj[FeR]}},{{FEL,ZEL},{FER,ZER}}},
      {{{FdL},{conj[FdR]}},{{FDL,ZDL},{FDR,ZDR}}},
      {{{FuL},{conj[FuR]}},{{FUL,ZUL},{FUR,ZUR}}}
        };
```

```
DEFINITION[EWSB][Phases]=
{     {fG, PhaseGlu}
    };


DEFINITION[EWSB][DiracSpinors]={
 Fd ->{  FDL, conj[FDR]},
 Fe ->{  FEL, conj[FER]},
 Fu ->{  FUL, conj[FUR]},
 Fv ->{  FvL, 0},
 Chi ->{ L0, conj[L0]},
 Cha ->{ Lm, conj[Lp]},
 Glu ->{ fG, conj[fG]}
};


(* Model not supported by CalcHep *)
SetOptions[MakeAll, IncludeCalcHep->True];
```

The following particles are defined:

```
(* ::Package:: *)

ParticleDefinitions[GaugeES] = {
      {SdL,   {  Description -> "Left Down-Squarks"}},
      {SdR,   { Description -> "Right Down-Squarks"}},
      {SuL,   { Description -> "Left Up-Squarks"}},
      {SuR,   { Description -> "Right Up-Squarks"  }},
      {SeL,   { Description -> "Left Selectron"}},
      {SeR,   { Description -> "Right Selectron"}},
      {SvL,   { Description -> "Left Sneutrino"}},
      {SHd0,  { Description -> "Neutral Down-Higgs"}},
      {SHdm,  { Description -> "Charged Down-Higgs"}},
      {SHu0,  { Description -> "Neutral Up-Higgs"}},
      {SHup,  { Description -> "Charged Up-Higgs"}},
      {VB,    { Description -> "B-Boson"}},
      {VG,    { Description -> "Gluon"}},
      {VWB,   { Description -> "W-Bosons"}},
      {gB,    { Description -> "B-Boson Ghost"}},
      {gG,    { Description -> "Gluon Ghost"  }},
      {gWB,   { Description -> "W-Boson Ghost"}},
      {Glu,   { Description -> "Gluino"}},
      {Wino,  { Description -> "Wino"}},
      {Bino,  { Description -> "Bino"}},
      {H0,    { Description -> "Neutral Higgsinos"}},
      {HC,    { Description -> "Charged Higgsinos"}},
      {Fd1,   { Description -> "Dirac Left Down-Quark"}},
      {Fd2,   { Description -> "Dirac Right Down-Quark"}},
      {Fu1,   { Description -> "Dirac Left Up-Quark"}},
      {Fu2,   { Description -> "Dirac Right Up-Quark"}},
      {Fe1,   { Description -> "Dirac Left Electron"}},
      {Fe2,   { Description -> "Dirac Right Electron"}},
      {Fv,    { Description -> "Neutrinos"  }}
      };
```


```
ParticleDefinitions[EWSB] = {
    {Sd  ,  { Description -> "Down-Squarks"}},
    {Su  ,  { Description -> "Up-Squarks"}},
    {Se  ,  { Description -> "Sleptons"}},
    {Sv  ,  { Description -> "Sneutrinos"}},
    {hh  ,  { Description -> "Higgs",
              PDG -> {0,25, 35,36},
              PDG.IX->{0,100000001,100000002,100000003}    }},
    {Hpm,   { Description -> "Charged Higgs"}},
    {VP,    { Description -> "Photon"}},
    {VZ,    { Description -> "Z-Boson",
               Goldstone -> hh[{1}]}},
    {VG,    { Description -> "Gluon" }},
    {VWm,   { Description -> "W-Boson" }},
    {gP,    { Description -> "Photon Ghost"}},
    {gWm,   { Description -> "Negative W-Boson Ghost"}},
    {gWmC,  { Description -> "Positive W-Boson Ghost" }},
    {gZ,    { Description -> "Z-Boson Ghost" }},
    {gG,    { Description -> "Gluon Ghost" }},
    {Fd,    { Description -> "Down-Quarks"}},
    {Fu,    { Description -> "Up-Quarks"}},
    {Fe,    { Description -> "Leptons" }},
    {Fv,    { Description -> "Neutrinos" }},
    {Glu,   { Description -> "Gluino" }},
    {Chi,   { Description -> "Neutralinos"}},
    {Cha,   { Description -> "Charginos"}}
      };


WeylFermionAndIndermediate = {
      {FHd0, { Description -> "Neutral Down-Higgsino"}},
      {FHu0, { Description -> "Neutral Up-Higgsino" }},
      {FHdm, { Description -> "Charged Down-Higgsino"}},
      {FHup, { Description -> "Charged Up-Higgsino"}},
      {L0,   { Description -> "Neutralino Weyl-Spinor"}},
      {Lm,   { Description -> "Negative Chargino Weyl-Spinor"}},
      {Lp,   { Description -> "Positive Chargino Weyl-Spinor"}},
      {fG,   { Description ->"Gluino Weyl-Spinor"}},
      {fWB,  { Description ->"Wino Weyl-Spinor"}},
      {fW0,  { Description ->"Neutral Wino" }},
      {fWm,  { Description ->"Negative Wino"}},
      {fWp,  { Description ->"Positive Wino"}},
      {fB,   { Description ->"Bino Weyl-Spinor"}},
```

```
    {phid, { Description -> "Scalar Down"}},
    {phiu, { Description -> "Scalar Up"}},
    {sigmad,   { Description -> "Pseudo Scalar Down"}},
    {sigmau,   { Description -> "Pseudo Scalar Up" }},
    {SHd,  { Description -> "Down-Higgs"}},
    {SHu,  { Description -> "Up-Higgs"}},
    {Sl,   { Description -> "Left Slepton" }},
    {Sq,   { Description -> "Left Squark" }},
    {FeL,  { Description -> "Left Electron" }},
    {FeR,  { Description -> "Right Electron" }} ,
    {FdL,  { Description -> "Left Down-Quark" }},
    {FdR,  { Description -> "Right Down-Quark" }},
    {FuL,  { Description -> "Left Up-Quark" }},
    {FuR,  { Description -> "Right Up-Quark" }},
    {FEL,  { Description -> "Rotated Left Electron" }},
    {FER,  { Description -> "Rotated Right Electron" }} ,
    {FDL,  { Description -> "Rotated Left Up-Quark" }},
    {FDR,  { Description -> "Rotated Right Up-Quark" }},
    {FUL,  { Description -> "Rotated Left Down-Quark"}},
    {FUR,  { Description -> "Rotated Right Down-Quark" }},
    {FHd,  { Description -> "Down-Higgsino" }},
    {FHu,  { Description -> "Up-Higgsino" }},
    {Fl,   { Description -> "Left Leptons"}},
    {Fq,   { Description -> "Left Quarks"}},
    {FvL,  { Description -> "Left Neutrino"}},

    {e,    { Description -> "Right Electron Superfield" }},
    {d,    { Description -> "Right Down-Quark Superfield" }},
    {q,    { Description -> "Left Quark Superfield" }},
    {u,    { Description -> "Right Up-Quark Superfield" }},
    {l,    { Description -> "left Lepton Superfield" }},
    {Hd,   { Description -> "Down-Higgs Superfield"}},
    {Hu,   { Description -> "Up-Higgs Superfield" }},
    {G,    { Description -> "Gluon Superfield" }},
    {B,    { Description -> "B Superfield" }},
    {WB,   { Description -> "W Superfield" }}
};
```

The following parameters are defined:

```
(* ::Package:: *)

ParameterDefinitions = {

{g1,        {Description ->"Hypercharge-Coupling"}},
{g2,        {Description ->"Left-Coupling"}},
{g3,        {Description ->"Strong-Coupling"}},

{AlphaS,    {Description ->"Alpha Strong"}},
{e,         {Description ->"electric charge"}},
{Gf,        {Description ->"Fermi's constant"}},
{aEWinv,    {Description ->"inverse weak coupling constant at mZ"}},


{Yu,        {Description ->"Up-Yukawa-Coupling"    }},
{Yd,        {Description ->"Down-Yukawa-Coupling"}},
{Ye,        {Description ->"Lepton-Yukawa-Coupling"}},

{T[Ye],     {Description ->"Trilinear-Lepton-Coupling"}},
{T[Yd],     {Description ->"Trilinear-Down-Coupling"}},
{T[Yu],     {Description ->"Trilinear-Up-Coupling"}},


{eta,       {Description->"Angle for Higgs phases",
                          Real -> True,
             OutputName ->eta,
             LaTeX -> "\\eta",
             LesHouches->{HMIX,500}  }},
{\[Mu],     {Description ->"Mu-parameter"}},
{B[\[Mu]],{Description ->"Bmu-parameter"}},

{mq2,       {Description ->"Softbreaking left Squark Mass"}},
{me2,       {Description ->"Softbreaking right Slepton Mass"}},
{ml2,       {Description ->"Softbreaking left Slepton Mass"}},
{mu2,       {Description ->"Softbreaking right Up-Squark Mass"}},
{md2,       {Description ->"Softbreaking right Down-Squark Mass"}},
{mHd2,      {Description ->"Softbreaking Down-Higgs Mass"}},
{mHu2,      {Description ->"Softbreaking Up-Higgs Mass"}},
```

```
{MassB,       { Description -> "Bino Mass parameter"}},
{MassWB,      { Description -> "Wino Mass parameter"}},
{MassG,       { Description -> "Gluino Mass parameter"}},

{vd,          { Description -> "Down-VEV",
                DependenceNum -> v Cos[ArcTan[TanBeta]]}},
{vu,          { Description -> "Up-VEV",
                DependenceNum -> v Sin[ArcTan[TanBeta]]}},
{v,           { Description -> "EW-VEV"}},
{TanBeta,     { Description -> "Tan Beta", OutputName ->TanBeta}},

{ZD,          { Description -> "Down-Squark-Mixing-Matrix" }},
{ZU,          { Description -> "Up-Squark-Mixing-Matrix"}},
{ZE,          { Description -> "Slepton-Mixing-Matrix"}},
{ZV,          { Description ->"Sneutrino Mixing-Matrix"}},
{ZH,          { Description ->"Scalar-Mixing-Matrix",
                Dependence -> None,
                DependenceNum -> None,
                DependenceOptional -> None,
                Real -> True }},

{ZP,          { Description ->"Charged-Mixing-Matrix",
                Real -> False,
                Dependence -> None,
                DependenceOptional -> None,
                DependenceNum -> None}},

{ZN,          { Description ->"Neutralino Mixing-Matrix" }},
{UP,          { Description ->"Chargino-plus Mixing-Matrix"}},
{UM,          { Description ->"Chargino-minus Mixing-Matrix"}},

{ZEL,         { Description ->"Left-Lepton-Mixing-Matrix"}},
{ZER,         { Description ->"Right-Lepton-Mixing-Matrix" }},
{ZDL,         { Description ->"Left-Down-Mixing-Matrix"}},
{ZDR,         { Description ->"Right-Down-Mixing-Matrix"}},
{ZUL,         { Description ->"Left-Up-Mixing-Matrix"}},
{ZUR,         { Description ->"Right-Up-Mixing-Matrix"}},

{ThetaW,      { Description -> "Weinberg-Angle"}},
{PhaseGlu,    { Description -> "Gluino-Phase" }},

{ZZ, {Description ->   "Photon-Z Mixing Matrix"}},
{ZW, {Description -> "W Mixing Matrix" }},
{ZfW, {Description ->     "Wino Mixing Matrix"}}            };
```

Using this model, these particles and these parameters, we have defined the following settings to generate a new version of SPheno:

```
(* ::Package:: *)

EXTPAR={{1,M1input},
        {2,M2input},
        {3,M3input},
        {11,AUinput},
        {12,ADinput},
        {13,AEinput},
        {21,mHd2input},
        {22,mHu2input},
        {31,meLinput},
        {33,mtauLinput},
        {34,meRinput},
        {36,mtauRinput},
        {41,mQ1input},
        {43,mQ3input},
        {44,muRinput},
        {46,mtRinput},
        {47,mdRinput},
        {49,mbRinput}};

MINPAR={{3,TanBeta},
        {4,SignumMu},
        {6,etaInput}};

RealParameters = {TanBeta, etaInput, mHd2input, mHu2input,
mQ1input, mQ3input, meLinput, mtauLinput, meRinput,
mtauRinput, muRinput, mtRinput, mdRinput, mbRinput};
ParametersToSolveTadpoles = {abs[\[Mu]]^2, re[B[\[Mu]]], im[B[\[Mu]]]};
Tad1Loop[4]=Tad1Loop[3]*vd/vu;

(*TanBeta needed in the matching conditions to the SM*)
DEFINITION[MatchingConditions]=Default[THDMII];
```

```
BoundarySUSYScale={
 {MassB, M1input},
 {MassWB, M2input},
 {MassG, M3input},
 {eta,etaInput},
 {T[Ye], AEinput*Ye},
 {T[Yd], ADinput*Yd},
 {T[Yu], AUinput*Yu},
 {mq2[1,1], mQ1input^2},
 {mq2[2,2], mQ1input^2},
 {mq2[3,3], mQ3input^2},
 {ml2[1,1], meLinput^2},
 {ml2[2,2], meLinput^2},
 {ml2[3,3], mtauLinput^2},
 {md2[1,1], mdRinput^2},
 {md2[2,2], mdRinput^2},
 {md2[3,3], mbRinput^2},
 {mu2[1,1], muRinput^2},
 {mu2[2,2], muRinput^2},
 {mu2[3,3], mtRinput^2},
 {me2[1,1], meRinput^2},
 {me2[2,2], meRinput^2},
 {me2[3,3], mtauRinput^2},
 {mHd2, mHd2input},
 {mHu2, mHu2input},
 {vd,Sqrt[4 mz2/(g1^2+g2^2)]*Cos[ArcTan[TanBeta]]},
 {vu,Sqrt[4 mz2/(g1^2+g2^2)]*Sin[ArcTan[TanBeta]]}
};


RenormalizationScaleFirstGuess =Sqrt[mq2[3,3]*mu2[3,3]];
RenormalizationScale = Sqrt[(mq2[3, 3] + (vu^2*conj[Yu[3, 3]]
*Yu[3, 3])/2)*(mu2[3, 3] + (vu^2*conj[Yu[3, 3]]*Yu[3, 3])/2)
-((vd*\[Mu]*conj[Yu[3, 3]] - vu*conj[T[Yu][3, 3]])
*(vd*conj[\[Mu]]*Yu[3, 3] - vu*T[Yu][3, 3]))/2];

ConditionGUTscale = g1 == g2;
```

```
(* loop decays not supported for this model *)
SetOptions[MakeSPheno, IncludeLoopDecays -> False];
SetOptions[PrepareRGEs, ComplexPhases -> True];


ListDecayParticles = Automatic;
ListDecayParticles3B = Automatic;


SA`AddOneLoopDecay = False;
DefaultInputValues = {etaInput->1,mHd2input->500,mHu2input->500,
TanBeta->10,SignumMu->-1,M1input->1500,M2input->1500,M3input->1500,
AUinput->-2000,ADinput->-2000,AEinput->-2000,mQ1input->1500,
mQ3input->1500,meLinput->1500,mtauLinput->1500,meRinput->1500,
mtauRinput->1500,mdRinput->1500,mbRinput->1500,muRinput->1500,
mtRinput->1500};
```

We then obtain the source code for SPheno as explained in the SARAH manual.

F. Data management

The research in this thesis was carried out under the RUG data management policy, as documented in
www.rug.nl/digital-competence-centre/ug-research-data-policy-2021.pdf.
Accordingly, we explain how to obtain the relevant data in this Appendix.

F.1 Software

We have used several software packages. These can be obtained from the following places:

- CPsuperH – https://www.hep.manchester.ac.uk/u/jslee/CPsuperH.html
- DDCalc – https://ddcalc.hepforge.org/
- FeynHiggs – https://wwwth.mpp.mpg.de/members/heinemey/feynhiggs/index.html
- GM2Calc – https://gm2calc.hepforge.org/
- MicrOMEGAS (including HiggsBounds, HiggsSignals and Lilith) – https://lapth.cnrs.fr/micromegas/
- Prospino – https://www.thphys.uni-heidelberg.de/~plehn/index.php?show=prospino
- SARAH – https://sarah.hepforge.org/
- SPheno – https://spheno.hepforge.org/
- SUSY-AI – https://amia.nikhef.nl/
- SUSYHIT – https://www.itp.kit.edu/~maggie/SUSY-HIT/
- SoftSUSY – https://softsusy.hepforge.org/
- SuperIso –http://superiso.in2p3.fr/
- Vevacious – https://vevacious.hepforge.org/

To obtain the version of SPheno that we have used in our study of the cpMSSM, see Appendix E for the SARAH model files that we have used.

F.2 Datasets

We have generated large sets of data. In Chapters 4 and 5 we describe how the data for the $(g-2)_\mu$ and eEDM projects was generated, respectively. The full datasets, including all input and output files, contain all the input and output files for the various software packages.

- For the $(g-2)_\mu$ study in Chapter 4, the relevant files can be found at [157] under the name 'gm2_data.tar'. A description of the specific files in each map can be found here as well.
  The files are organized in iterations, according to the iteration they were produced in. The map name within one iteration is labeled by "[Barbieri-Giudice fine-tuning measure]_[Electroweak fine-tuning measure]_[time stamp]". It is not straightforward to extract all the necessary data from each of these files. Instead, we have stored the output of the project in a separate file,
  'datagm2_right_omegah2_only.csv', that is also made publicly available. This contains the data from all the files that have the right $\Omega_{\rm DM}h^2$. In the .csv file the data is organised in columns, as described in [157].
- For the eEDM study in Chapter 5, the full set of input output files can be found at [235]. The input files are stored per iteration as 'input_iter[n].csv' and the output files are gathered under the name 'eEDMdata.tar'. The code to obtain the output from the input has been uploaded in the directory 'SPheno_to_eEDM'. The name of the directory ('dir_name') in the output file corresponds to the index of the line in the input file. One directory with the input and output files for each software package is created for each data point. The output in de csv file contains the masses, couplings, mixing matrices, observables and fine-tuning for each data point, which is organised in columns.

G. Phases

This is the full background of the discussion in Section 5.2. For completeness we show all the figures and give the full parameter sets on which these figures are based.

We have done two different sets of studies: in the first, the phases are varied between 0 and 2π. The second study varies the phases between 10^{-8} and 10^{-2}, to gain a better understanding of the behaviour of d_e^E for very small values of the phases.

The value 10^{-8} is chosen because of numerical stability. In several cases we see that the limit of this numerical stability is reached (e.g. in the left panels of the second, third and fourth row in Figure G.2).

M_1 (GeV)	M_2 (GeV)	M_3 (GeV)	A_t (GeV)	A_b (GeV)
-62.3624	236.72669	-4738.12+23.85823j	-5840.988	-1994.2731
A_τ (GeV)	μ (GeV)	$m^2_{H_u}$ (GeV^2)	$m^2_{H_d}$ (GeV^2)	Q_{susy} (GeV)
-792.70011	257.89983	-59954.133	708281.4	3594.556
$\tan\beta$	η	m_{t_L} (GeV)	m_{t_R} (GeV)	m_{b_R}(GeV)
24.58265	0.0	-62.3624	2219.176	1651.646
m_{u_L} (GeV)	m_{u_R} (GeV)	m_{d_R} (GeV)	m_{e_L} (GeV)	m_{e_R} (GeV)
1534.244	1752.216	1975.511	545.7135	4830.292
m_{τ_L} (GeV)	m_{τ_R} (GeV)	ϕ_μ	ϕ_{M_1}	ϕ_{M_2}
4121.306	3642.808	0.0	3.141593	0.0
ϕ_{M_3}	ϕ_{A_t}	ϕ_{A_b}	ϕ_{A_τ}	
3.136557	3.141593	3.141593	3.141593	

Table G.1 The parameters of the first data point. Each of these has been kept constant, except the phase we were studying. The original value of the eEDM was $|d_e^E| = 9.0054 \cdot 10^{-33}$ e cm.

The two original data points have the parameter values as shown in Tables G.1 and G.2.

M_1 (GeV)	M_2 (GeV)	M_3(GeV)	A_t (GeV)	A_b (GeV)
-47.17723	160.3648	4924.345	-4826.255	-2877.530-0.7186789j
A_τ (GeV)	μ (GeV)	$m^2_{H_u}$ (GeV^2)	$m^2_{H_d}$ (GeV^2)	Q_{susy} (GeV)
-2380.637	265.54159	-42278.92	633588.6	2638.648
$\tan\beta$	η	m_{t_L} (GeV)	m_{t_R} (GeV)	m_{b_R} (GeV)
24.7834	0.0	3973.995	1753.604	3418.491
m_{u_L} (GeV)	m_{u_R} (GeV)	m_{d_R} (GeV)	m_{e_L} (GeV)	m_{e_R} (GeV)
1600.814	4429.666	1872.030	708.21701	2052.146
m_{τ_L} (GeV)	m_{τ_R} (GeV)	ϕ_μ	ϕ_{M_1}	ϕ_{M_2}
4154.055	3968.693	0.0	3.141593	0.0
ϕ_{M_3}	ϕ_{A_t}	ϕ_{A_b}	ϕ_{A_τ}	
0.0	3.141593	3.141343	3.141593	

Table G.2 The parameters of the second data point. Each of these has been kept constant, except the phase we were studying. The original value of the eEDM was $|d_e^E| = 6.2557 \cdot 10^{-34}$ e cm.

For each phase we have created two data sets where all the parameters are the same as in Table G.1 and G.2, except the phase we are studying. The results of these studies for different values of the phases are shown in the figures below, starting with the results for general phases.

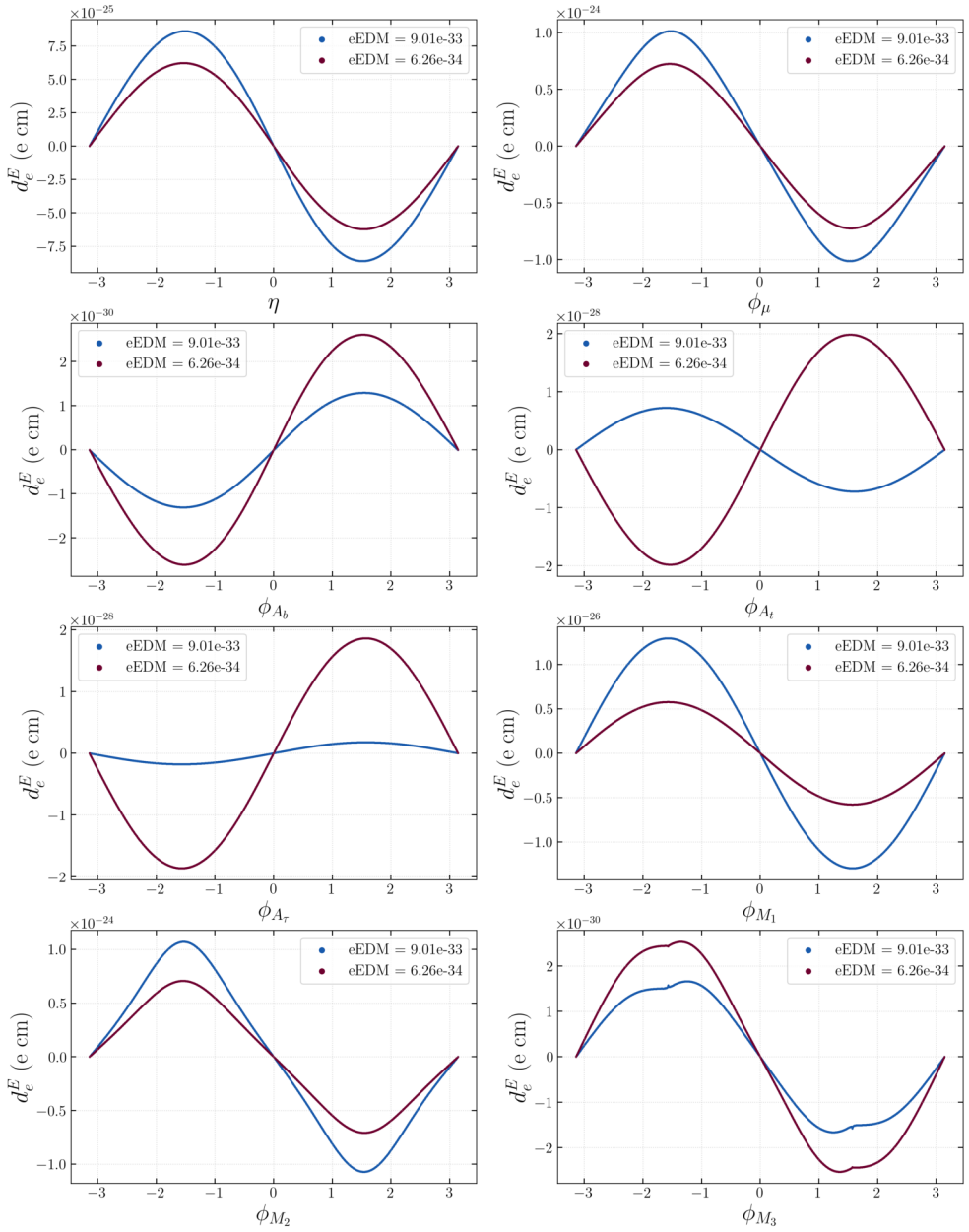

Figure G.1 The dependence of the eEDM d_e^E on the phases, where for each plot all parameters other than that phase have been kept constant.

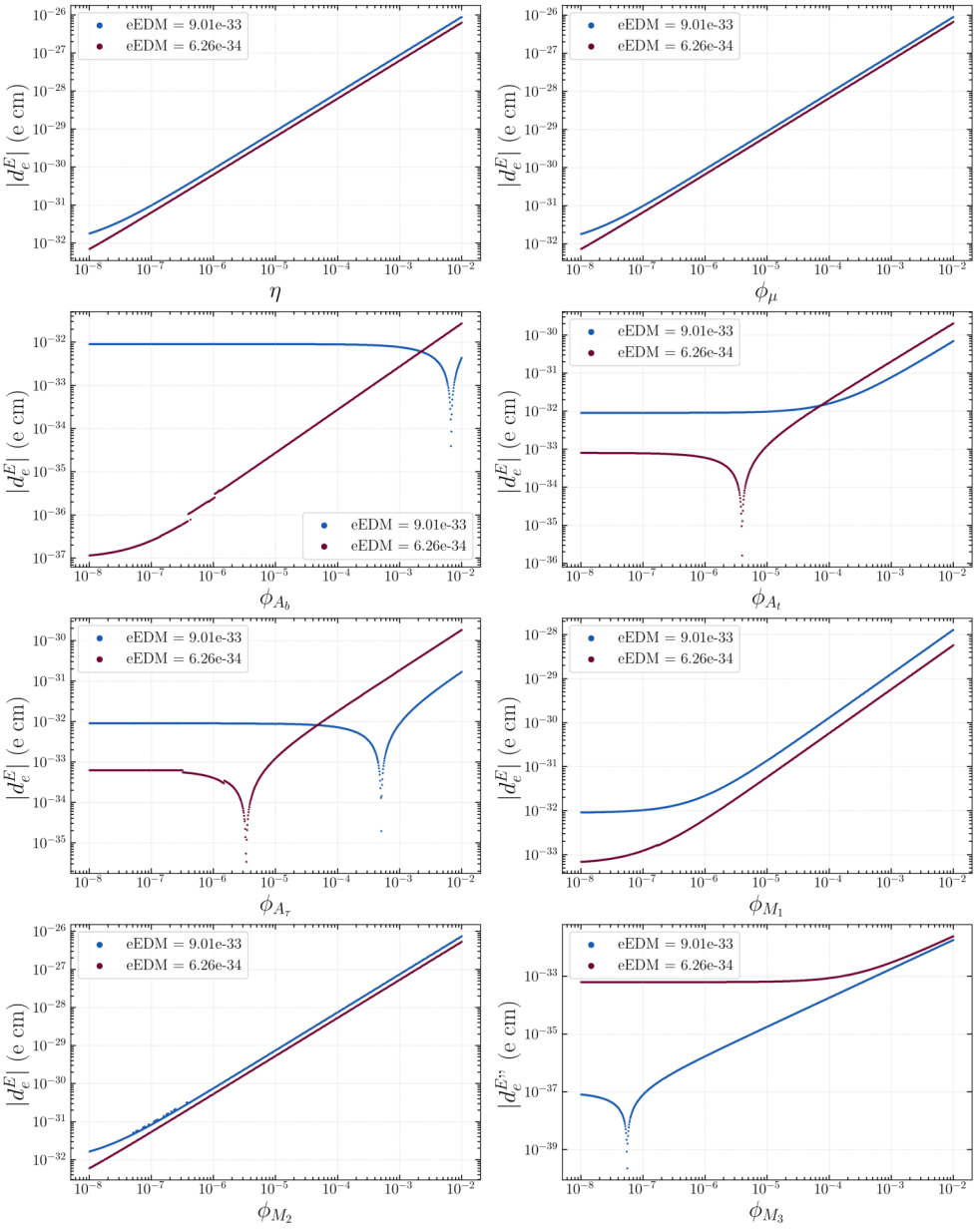

Figure G.2 The dependence of the eEDM d_e^E on the phases, where for each plot all parameters other than that phase have been kept constant; this time for small values of the phases.

Samenvatting

SAMENVATTING

Deze samenvatting is bedoeld voor alle mensen die nog *niet* thuis zijn in de natuurkunde. Aangezien dat een ontzettend brede doelgroep is, heb ik geprobeerd voor ieder wat wils te bieden. Laat je dus niet ontmoedigen door een stuk tekst dat net iets te ver gaat voor je begrip, of als het juist wat langzaam wordt uitgelegd naar jouw smaak.

Uiteindelijk hoop ik dat ik hiermee iedereen een beeld geef van mijn vakgebied. De titel van het proefschrift bevat natuurlijk veel jargon: de meeste mensen zullen niet weten wat observabelen zijn (of meetbare grootheden in beter Nederlands) en een ander idee hebben dan ik bij 'lage energie', laat staan dat ze weten wat ik bedoel met finetuning en het MSSM. Ik hoop dat je aan het eind van deze samenvatting in elk geval weet wat ik met dit jargon bedoel en waarom het interessant is om over dit onderwerp na te denken.

Ik vind het zelf wonderbaarlijk hoe veel we weten over de wereld en ik zou graag een stukje van dat enthousiasme aan je overdragen. De wereld is ingewikkeld en zit vol schijnbare toevalligheden. Wij fysici proberen die toevalligheden te begrijpen en te beschrijven in onze wiskundige modellen. Soms is het daarom juist heel leuk om een stapje terug te doen en je opnieuw te verwonderen. Ik had veel lol in het schrijven van deze samenvatting, dus ik wens je ook veel plezier in het lezen!

Het standaardmodel der deeltjesfysica

Het werk in dit proefschrift speelt zich af in een vakgebied dat we hoge-energiefysica noemen: de natuurkunde die probeert fenomenen te beschrijven, verklaren en voorspellen die zich afspelen als er (extreem) hoge energie in het spel is. Paradoxaal genoeg gaat het ook over heel erg kleine dingen. Dat komt omdat je de kleinste dingen alleen kunt maken als je er heel veel energie in stopt. De kleinste bouwstenen noemen we ook wel fundamentele of elementaire deeltjes en daarom heet het vakgebied soms ook deeltjesfysica.

De elementaire deeltjes kun je zien als een soort Lego blokjes: je kunt ze niet zomaar in tweeën hakken, zonder ze kapot te maken. Tegelijkertijd kun je met deze Lego bouwstenen nieuwe dingen maken, door ze op de juiste manier in elkaar te klikken. Op dezelfde manier vormen bepaalde elementaire deeltjes samen de materie om ons heen door eerst samen te klikken tot protonen en neutronen. Daarna vormen deze samen met elektronen, die ook elementaire deeltjes zijn, grotere blokken, die we atomen noemen. Atomen vormen daarna weer moleculen en daaruit is onze wereld opgebouwd. Een molecuul is het kleinste deeltje dat nog alle eigenschappen van een stof bevat, voor atomen is dat al niet meer waar.

Afhankelijk van de schaal waarop je naar de wereld kijkt, wil je ook een model dat past bij die schaal. Het is bijvoorbeeld helemaal niet handig om de tijd in seconden te meten als je met iemand een afspraak maakt die volgende maand plaatsvindt, of wanneer je van Nijmegen naar Groningen reist. Er bestaan niet voor niets ook minuten, uren, dagen en maanden. Op dezelfde manier beschrijven we een appel die van de boom valt in termen van de boom, de appel en de grond. Het is onnodig

ingewikkeld om na te denken over de moleculen in die appel, laat staan om over nog kleinere deeltjes te praten.

Toch kan het handig zijn om over een model te beschikken dat de allerkleinste deeltjes en hun interacties beschrijft. Allereerst is het gewoon leuk om op elk niveau te weten hoe dingen in elkaar steken en te begrijpen hoe de verschillende niveaus in elkaar overgaan. Daarnaast is het ook praktisch: tegenwoordig kunnen we experimenten doen waarbij we op de kleinste schaal moeten begrijpen hoe de wereld werkt. Om echt te begrijpen hoe atomen en moleculen de wereld om ons heen vormen, is het ook nodig om te weten hoe elementaire deeltjes de atomen vormen. Hiervoor willen we dus graag een model.

Het standaardmodel der deeltjesfysica beschrijft de elementaire deeltjes zoals we die nu kennen. Het model legt ook uit hoe de verschillende deeltjes interageren of met elkaar 'praten'. Er bestaan namelijk verschillende soorten deeltjes: de deeltjes die we materie noemen en zogenaamde krachtdragers. Door een krachtdrager uit te wisselen, praten materiedeeltjes met elkaar: ze gaan een interactie aan. Het is gebruikelijk om dit heel schematisch weer te geven in de vorm van diagrammen, zoals je kunt zien in Figuur 6.3. Zulk soort diagrammen zie je dan ook vaak terugkomen in dit proefschrift als we willen beschrijven wat voor proces er plaatsvindt.

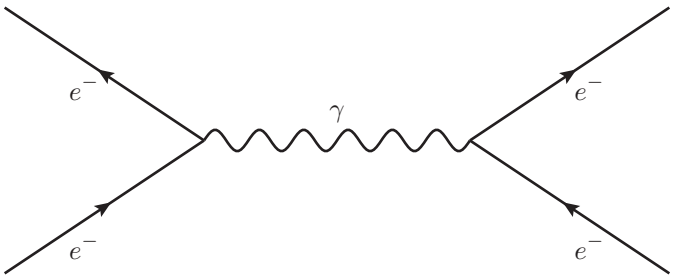

Figuur 6.3 Voorbeeld van een Feynman diagram. Een elektron (links, e^-) zendt een foton (midden, γ) uit dat wordt ontvangen door een ander elektron (rechts, e^-). Een andere manier om dit te zien is dat de twee elektronen elkaar afstoten, omdat ze dezelfde elektrische lading hebben.

Je kunt dit soort processen op twee manieren bekijken. Tot nu toe beschrijf ik dit in termen van deeltjes en interacties. In het voorbeeld zie je twee elektronen die een foton uitwisselen. Een andere manier om ernaar te kijken is dat de elektrisch geladen elektronen elkaar afstoten, omdat de elektromagnetische kracht ze uit elkaar duwt. Beide manieren om hiernaar te kijken zijn even goed en correct. In het dagelijks leven praten we vaker over krachten en net als de fundamentele deeltjes kennen we ook

een paar fundamentele krachten: de elektromagnetische kracht, de sterke kernkracht, de zwakke kernkracht en de zwaartekracht. Met elke kracht kunnen we een deeltje associëren, zodat we een proces ook kunnen beschrijven in termen van elementaire deeltjes en hun interacties.

Het standaardmodel beschrijft al deze deeltjes, zowel voor materie als voor kracht, op een wiskundige manier. In Figuur 6.4 staat een overzicht van alle deeltjes die we nu kennen. Links zien we de 'dagelijkse' deeltjes: de materie om ons heen is hieruit opgebouwd. Protonen en neutronen bestaan namelijk allebei uit een mix van up- en downquarks, die bij elkaar worden gehouden door de uitwisseling van gluonen (of door de sterke kernkracht). Samen met elektronen vormen de protonen en neutronen dan atomen. De middelste en rechterrij van de materiedeeltjes lijken qua eigenschappen op de eerste, maar de deeltjes zijn zwaarder. Rechts daarnaast staan de krachtdragers: het gluon voor de sterke kernkracht, het foton voor de elektromagnetische kracht en de W- en Z-bosonen voor de zwakke kernkracht. Het Higgsdeeltje is een buitenbeetje en beschrijft geen kracht zoals de anderen, maar is verantwoordelijk voor de massa's van de andere deeltjes.

Door het standaardmodel op een wiskundige manier op te schrijven, kunnen we ook regels afleiden waar de deeltjes zich volgens het model aan moeten houden. Hierbij is het heel belangrijk om op te merken dat we zeggen 'volgens het model'. Elke theorie moet namelijk altijd getest worden in experimenten. Het liefst stel je een theorie op die verklaart wat we tot nu toe hebben gezien in experimenten én iets nieuws voorspelt. Daarmee heb je ook meteen iets dat je in een ander experiment kunt controleren. Het vakgebied waarin vooral wordt gekeken naar het samenspel tussen theorie en experiment heet ook wel fenomenologie. Dit is de focus van mijn proefschrift.

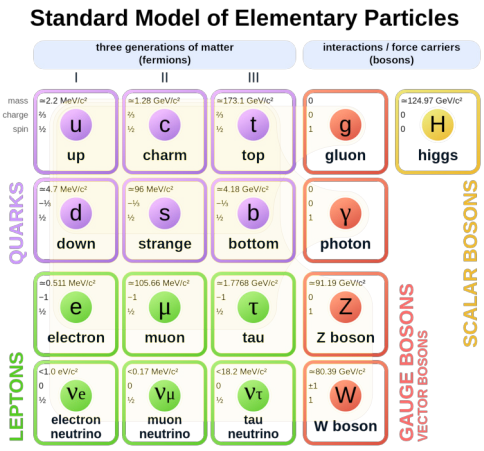

Figuur 6.4 Het standaardmodel met alle deeltjes die we nu kennen [1].

Het standaardmodel testen

Het standaardmodel is in de loop der jaren uitvoerig getest. De allereerste vormen van het model bestaan al sinds de jaren '70, toen het bestaan van quarks werd bevestigd. Sindsdien is het model uitgebreid tot zijn huidige vorm en worden alle onderdelen van het model tot op steeds grotere precisie getest. Dit gebeurt onder andere bij de Large Hadron Collider (LHC) in Cern. Daar laten we protonen met grote snelheden op elkaar botsen, waarbij dan andere (elementaire) deeltjes kunnen ontstaan. Door de botsingen te bestuderen leren we meer over het standaardmodel en kunnen we de voorspellingen die het model doet over processen testen.

Tot nu toe zijn er bij de LHC nog geen echte afwijkingen gevonden. Desondanks weten we vrij zeker dat het model niet compleet is. Geen van de deeltjes uit het standaardmodel biedt namelijk een verklaring voor het fenomeen 'donkere materie'. Dit is een onbekende stof die voorkomt in het universum en daarmee de astrofysische waarnemingen van bijvoorbeeld sterrenstelsels beïnvloedt. Zonder donkere materie begrijpen we niet goed hoe het heelal zich zo heeft ontwikkeld tot de huidige vorm. We begrijpen alleen ook nog niet goed wat donkere materie nou precies is, aangezien geen van de deeltjes in het standaardmodel de juiste eigenschappen heeft om deze stof te kunnen zijn.

Aan de andere kant zijn er waarnemingen bij lage energieën. Hiermee bedoelen we experimenten die niet, zoals bij de LHC of in het heelal, met enorme energieën gepaard gaan. Het verschil is enorm en daardoor bijna niet te bevatten: de typische energy bij de LHC is 10^{-6} joule, terwijl er ook experimenten bestaan die een verschil van 10^{-42} joule kunnen waarnemen. Ter vergelijking: ons melkwegstelsel is 10^{18} kilometer groot, terwijl het verschil tussen deze experimenten 10^{36} is. Het verschil is dus echt enorm.

Het voordeel is dat experimenten bij lage energie is dat ze veel kleinschaliger kunnen zijn en daarmee ook goedkoper dan deeltjesversnellers zoals de LHC. Het nadeel is dat ze veel specifieker kijken naar één meetbare grootheid (observabele) en dus minder algemeen zijn. Wij proberen de bevindingen van beide type experimenten te combineren en daardoor zo veel mogelijk te leren over het model.

Elektrische en magnetische momenten

Er zijn twee observabelen waar we naar kijken: het afwijkend magnetische moment van het muon[1] en het elektrisch dipoolmoment van het elektron. Deze twee hebben we uitgekozen omdat ze nauw verbonden zijn en er in Groningen een experiment wordt gemaakt om het elektrisch dipoolmoment te meten. Dit is nogal een mondvol en om te begrijpen wat deze observabelen zijn moeten we eerst kijken naar een andere eigenschap van deeltjes: spin. Elementaire deeltjes hebben een aantal eigenschappen die vastliggen voor elk deeltje van dezelfde soort. Zo hebben alle elektronen dezelfde massa en elektrische lading. Ze hebben ook dezelfde spin.

[1] Dit is het zwaardere broertje van het elektron.

Als we kijken naar een grote bol, dan kan deze om zijn eigen as draaien. Dat beschrijven we met iets dat we impulsmoment noemen. Dit is een maat voor de hoeveelheid draaiïng in verhouding tot de bol en zijn massa. De vergelijking gaat niet helemaal goed op, maar spin is voor elementaire deeltjes een beetje wat impulsmoment is voor bollen.[2] Daarna kan er een wisselwerking ontstaan tussen de spin van een deeltje en het elektrisch of magnetisch veld. De sterkte van die wisselwerking heeft een eigen naam en is ook weer een eigenschap van het elementaire deeltje. Voor het elektrisch veld noemen we dat het elektrisch dipoolmoment en voor het magnetisch veld heet dit het magnetisch moment.

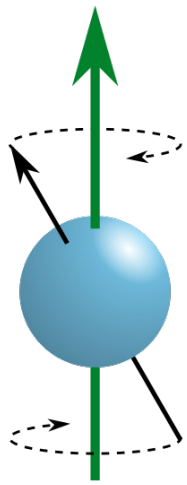

Figuur 6.5 Het tollen van een bol, die ook al om zijn eigen as draait [236].

Opnieuw kunnen we proberen dit beter te begrijpen door te kijken naar bollen in plaats van deeltjes. Stel je voor, we maken een bol die bestaat uit allemaal verschillende stukjes. Elk stukje geven we dan een elektrische lading en een magnetische lading.[3] De totale bol heeft nu ook een lading. Daarna geven we een flinke zwiep aan de bol, zodat hij om zijn eigen as gaat tollen. Vervolgens kijken we dan hoe de draaiende bol zich gedraagt in een magnetisch veld en in een elektrisch veld. In Figuur 6.5 staat een schematische weergave hiervan.

Wat we zien is het volgende: de draaiende bol gaat een tollende beweging maken, ofwel precessie. Helaas kan ik hier geen filmpje laten zien, maar bijvoorbeeld `https://nl.wikipedia.org/wiki/Precessie#/media/Bestand:Gyroscope_precession.gif` is heel duidelijk. Je kunt denken aan een tol die niet netjes rechtop staat. Behalve dat hij om zijn eigen as tolt, maakt hij ook nog een extra draaibeweging. Iets dergelijks gebeurt als de as van onze draaiende bol niet dezelfde richting heeft het als magneetveld. De bol gaat dan een precessiebeweging maken. De snelheid van deze precessiebeweging hangt af van het magnetisch moment van de bol.

Dit werkt alleen als de bol een lading heeft en die lading niet helemaal uniform is verdeeld over de bol. Je kunt het magnetisch moment daarom zien als een maat voor de verdeling van de magnetische lading en het elektrisch dipoolmoment als een maat voor de verdeling van de elektrische lading.

Elementaire deeltjes hebben een intrinsieke eigenschap die hier direct vergelijkbaar mee is. Het magnetisch moment beschrijft de sterkte van de interactie tussen de spin van het deeltje en een magneetveld, het elektrisch dipoolmoment beschrijft de sterkte van de interactie tussen de spin van het deeltje en een elektrisch veld. Door heel precies

[2] Een elementair deeltje is eigenlijk een punt, geen bol, en draait ook niet daadwerkelijk... Volg je het nog?

[3] We maken ons even niet druk over hoe die bol dan één geheel blijft en niet uit elkaar valt omdat de verschillende ladingen elkaar afstoten. De bol bestaat gewoon.

te meten hoe de elementaire deeltjes zich gedragen als je ze in een magneetveld en elektrisch veld laat bewegen, kun je ook meten wat het intrinsieke magnetisch moment en elektrisch dipoolmoment is.

Het standaardmodel voorspelt ook een waarde voor het magnetisch moment en elektrisch dipoolmoment van elk elementair deeltje. Door die te meten, kun je dus testen of het standaardmodel klopt. Voor het elektrisch dipoolmoment is de voorspelde waarde helaas te klein om te meten door de huidige experimenten: er zitten nog ongeveer 8 ordes van grootte tussen de voorspelling en de gevoeligheid van het beste experiment. Dat kun je zien als een voorspelling over de vorm van een cafeïne molecuul, terwijl wij op het moment alleen nog in staat zijn om een koffiekop te zien. Om dit echt goed te testen, moeten we dus nog veel preciezer zien te meten en daarvoor hebben we nu nog niet de benodigde technieken. Voor het magnetisch moment is er al wel een experimentele waarneming mogelijk en het lijkt er voorlopig op dat het standaardmodel er net even naast zit bij het muon. Het verschil is nog niet groot genoeg om officieel het stempel 'ontdekking' te krijgen, maar het is wel interessant om te bestuderen.

Uitbreidingen van het standaardmodel

Om de afwijkende waarnemingen te verklaren, moet het standaardmodel aangepast worden. Een mogelijkheid is om extra deeltjes toe te voegen en het model uit te breiden. Dit wordt bijvoorbeeld gedaan in supersymmetrie, waar elk bekend elementair deeltje een zogenaamde superpartner krijgt. Alle kwantumgetallen van de superpartners zijn hetzelfde als die van het standaardmodeldeeltje, behalve de spin. Hierdoor bestaat er ook een deeltje dat, met de juiste aanvullende eigenschappen, donkere materie zou kunnen zijn. Daarnaast zou dit nieuwe model kunnen verklaren wat de experimentele waarneming is voor het magnetisch moment van het muon. Tot slot kunnen we aan de hand van het nog niet waargenomen elektrisch dipoolmoment van het elektron ook controleren of het model nog niet is uitgesloten.[4]

Een uitdaging van werken met supersymmetrie is dat het model komt met heel veel vrije parameters. De symmetrie is namelijk niet helemaal kloppend, hij is gebroken. Je kunt dit vergelijken met je spiegelbeeld. Een volledige symmetrie betekent dat jij en je spiegelbeeld precies hetzelfde zijn. Een gebroken symmetrie leidt tot verschillen: je spiegelbeeld heeft bijvoorbeeld net even een andere kleur shirt aan, of gedraagt zich net niet helemaal hetzelfde als jij. Op dezelfde manier zijn de supersymmetrische deeltjes die we zouden kunnen zien, als ze bestaan, ook net even anders dan we gedacht hadden. De precieze manier waarop ze verschillen, hangt af van de parameters van het model.

[4] Een model is uitgesloten als het een voorspelling doet die wordt weerlegd door een experimenteel resultaat.

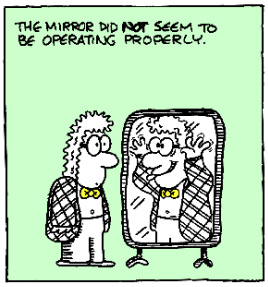

Figuur 6.6 Spiegelsymmetrie [237].

Spiegelsymmetrie kennen we in de deeltjesfysica ook, namelijk onder de naam CPT symmetrie. Dit staat voor Charge conjugation, Parity en Time reversal. De volledige CPT symmetrie maakt van een deeltje een anti-deeltje dat zich in tegenovergestelde richting beweegt en tegen de tijd ingaat. Aangezien we de tijd niet om kunnen draaien, kunnen we niet direct testen of deze symmetrie klopt (behouden is). We gaan hier wel altijd vanuit in onze modellen, omdat er anders grote problemen ontstaan. Indirect kunnen we wel controleren of eigenschappen die heel nauw verbonden zijn aan CPT symmetrie kloppen. Een voorbeeld is bijvoorbeeld dat we aannemen dat fysica zich overal in het Heelal hetzelfde gedraagt, volgens dezelfde natuurwetten. Dit is wel te testen.

Wat we ook kunnen doen, is kijken naar losse stukken. Wanneer het elektrisch dipoolmoment niet precies 0 is, dan betekent dit automatisch dat de CP symmetrie gebroken is. Op de omslag zie je een voorbeeld van de implicaties: het elektron zou er dan net even anders uitzien in spiegelbeeld.

Mijn werk

Wat ik in dit proefschrift beschrijf, is hoe we voorspellingen kunnen doen over het muon magnetisch moment en het elektrisch dipoolmoment van het elektron in een bepaald supersymmetrisch model, namelijk het minimale supersymmetrische standaardmodel (MSSM). Daarvoor moet je eerst een keuze maken voor alle vrije parameters van het model. Vergelijk het met een radio die ontzettend veel knoppen heeft om aan te draaien. Voor elke knop maak je een keuze en daarna kijk je of je een radiozender te pakken hebt gekregen.

Ik bekijk eerst een model waar 19 knoppen zijn. Je kunt je voorstellen dat als je willekeurig aan deze knoppen gaat draaien, de kans erg klein is dat je een radiozender tegenkomt met goede muziek. Daarom maken we gebruik van optimalisatiemodellen die op een slimme manier aan de knoppen draaien. Wat we verstaan onder goede muziek is een model waar de juiste waarde van het muon magnetisch moment uitkomt en waarbij het model een deeltje heeft dat donkere materie kan verklaren. Daarnaast mag het model op geen enkele manier botsen met de experimentele resultaten die we hebben, bijvoorbeeld de metingen bij de LHC. Tot slot stellen we een grens aan de zogenaamde finetuning van het model.

Met finetuning bedoelen we dat de uitkomsten van het model niet te sterk afhankelijk mogen zijn van de input. Dit kan komen door twee verschillende dingen. De eerste vorm van finetuning is als je een totaal andere uitkomst had gekregen door maar een heel klein beetje aan een knop te draaien. Stel dat je een parameter met 1% verandert, maar je daardoor je magnetisch moment 100% verandert. Dan moeten de

parameters wel erg goed afgestemd zijn om de juiste waarde eruit te krijgen. Men is het niet helemaal eens over de geaccepteerde hoeveelheid finetuning, maar wij gaan uit van 1%.

Wat ook kan gebeuren, is dat een meetbare grootheid afhankelijk is van andere getallen. Bijvoorbeeld als het een som is van verschillende waarden, zoals het geval is bij de massa van het Higgs deeltje. De getallen in de som zijn dan weer afhankelijk van de parameters in het model. Als de verschillende onderdelen dan heel precies op elkaar afgestemd moeten zijn om de juiste massa te krijgen, spreken we ook van finetuning. Denk bijvoorbeeld aan de som $125 = 38210429431 - 38210429306$. Die twee getallen moeten dan erg nauwkeurig kloppen om op 125 uit te komen en een relatief kleine verandering in een van de twee getallen kan al snel een grote verandering betekenen voor de uitkomst. Daarom staan we niet te veel finetuning toe in een model.

Voor het magnetisch moment van het muon hebben we bestudeerd wat de fenomenologie is van de oplossingen die de juiste waarde voorspellen voor het magnetisch moment, maar ook een passend deeltje hebben voor donkere materie en geen enkel experiment tegenspreken. Hier blijken allerlei mogelijkheden te bestaan waarbij de finetuning onder de 1% blijft. Wel zien we dat in de nabije toekomst onze oplossingen allemaal getest kunnen worden in een categorie experimenten waarbij donkere materie gezocht wordt. Daarmee zouden de oplossingen dus uitgesloten kunnen worden.

Voor het elektrisch dipoolmoment van het elektron neemt men vaak aan dat een supersymmetrisch model alleen onder de experimentele limiet kan blijven, als het model veel finetuning heeft. Ook wordt vaak gezegd dat bepaalde parameters heel klein moeten zijn, of de massa's van de supersymmetrische deeltjes heel groot. In mijn werk laat ik zien dat dit niet zo zwart-wit te zien is. Ik heb oplossingen gevonden voor niet al te zware deeltjes, waarbij de betreffende parameters ook niet ontzettend klein hoeven te zijn. In vervolgonderzoek zullen anderen deze oplossingen nog verder uitwerken.

Daarnaast bestudeer ik de finetuning van de gevonden oplossingen. Het blijkt lastig te zijn om een goede definitie te vinden die de finetuning zoals hierboven beschreven weergeeft. Daarom bekijken we twee verschillende definities, die we met elkaar vergelijken. De resultaten daarvan laten zien dat er nog verbetering mogelijk is in de definitie, om echt goed te vangen wat we met finetuning bedoelen. Hiervoor stellen we dus ook vervolgonderzoek voor.

Al met al blijkt dat de metingen aan het elektrisch dipoolmoment nog veel ruimte laten voor interessante supersymmetrische modellen, ook met een kleine finetuning of met kleine massa's. Dit was tegen de voorspellingen in, dus dat is een leuke conclusie!

Dankwoord

DANKWOORD

DANKWOORD

Het laatste onderdeel van de thesis, maar wel het stuk dat iedereen als eerste wil lezen: het dankwoord! Want zoals geldt voor elke PhD thesis, had ook dit werk er niet zo uit gezien zonder de hulp van mijn begeleiders, vrienden en familie. Als het goed is horen jullie dat niet nu voor het eerst, maar het is fijn om het hier nog eens te kunnen benadrukken. Het is een flinke uitdaging geweest om het hele traject af te ronden en ik ben blij dat ik er nu op kan terugblikken en iedereen nog eens kan bedanken voor zijn bijdrage.

Allereerst wil ik mijn begeleiders bedanken, want zonder jullie, Rob en Wim, zou dit project überhaupt nooit hebben bestaan. Ik ben dankbaar dat ik aan zo'n inspirerend onderwerp heb mogen werken, waar allerlei verschillende onderdelen in samenkomen. Dat zou zonder de uitgebreide input van jullie beiden niet mogelijk zijn geweest.

Daarnaast ben ik heel dankbaar voor de vrijheid die ik heb gekregen door de jaren heen. Het zal niet altijd makkelijk geweest zijn om mij en het project te begeleiden. Ondanks alle ups en downs hebben jullie met me mee gedacht hoe we het project het beste vorm konden geven, waarbij ik zelfs naar de andere kant van het land (terug) ben verhuisd. Achteraf gezien was dat, zeker met de coronacrisis, de enige manier om het project voort te zetten. Ik ben dan ook ontzettend dankbaar dat jullie deze verhuizing mogelijk hebben gemaakt en als een mogelijkheid hebben gezien, in plaats van een probleem.

Zelfs naast alle managementtaken is het jullie altijd gelukt om tijd voor me te maken. Door de jaren heen heb ik veel van jullie geleerd en ik kijk met veel plezier terug op onze samenwerking. Bedankt!

Naast mijn begeleiders zijn ook de leden van de manuscriptcommissie onmisbaar geweest voor dit boekje. Bedankt voor jullie tijd om dit werk van voor tot achter te lezen en voor alle nuttige feedback die daaruit volgde. Jullie onafhankelijke oordeel en frisse blik heeft geholpen om het resultaat nog weer beter te maken.

Verder hebben ook allerlei anderen dit proefschrift gevormd met hun feedback, door het als bètalezer te testen en te helpen zo veel mogelijk fouten eruit te halen. Iedereen die de tijd heeft genomen een stuk aandachtig te lezen, weet hoe waardevol jullie bijdrages voor me zijn geweest.

Ook mijn collega's verdienen een plekje hier, want jullie hebben de fijne werkplek mogelijk gemaakt waar ik al die jaren naar dit resultaat heb toegewerkt. Aan alle collega's in Groningen, Nijmegen en Amsterdam: het was altijd gezellig en ik heb er veel aan gehad om mijn ups en downs met jullie te kunnen delen, zowel inhoudelijk als persoonlijk. Dankzij de discussies bij de koffie-automaat voelt het toch als een gezamelijke project en ik ben dankbaar voor alle hulp, oplossingen en suggesties die ik door de jaren heen van jullie gekregen heb.

Een speciaal plekje daarin verdienen de mensen met wie ik een kantoor gedeeld heb: eerst Femke en Pi, ook al was dat niet zo lang als we hadden gedacht. Later Bart, Bob, David, Jesse, Jochem, Inge en Zhongyi: hopelijk kunnen jullie de planten die ik heb achter gelaten een beetje in leven houden. Het was fijn om er niet alleen

voor te staan en van elkaar te kunnen leren.

Melissa, zonder jou had dit proefschrift er niet gelegen. Inhoudelijk heb je van tijd tot tijd het project helemaal uit het slop weten te trekken met je nieuwe idee/ën en kennis van zaken. Daarnaast heb je ook mij regelmatig uit de dip weten te trekken, zelfs vanuit Oxford. Een stukje tekst hier is veel te weinig om het goed te kunnen zeggen, maar je weet gelukkig ook al hoe dankbaar ik voor alles ben.

Sandra en Nicole, ondanks de afstand lukt het nog altijd om onze vriendschappen te onderhouden en ik ben ontzettend blij dat jullie er altijd voor me zijn. Als paranimf is het nog een laatste keertje in de contekst van mijn PhD, maar ook daarna hoop ik dat we er voor elkaar kunnen zijn. Ik voel me een gelukkig mens om jullie tot mijn vrienden te kunnen rekenen.

Bob, ik ben je heel dankbaar voor het eindeloze geduld waarmee je naar mijn programmeerproblemen hebt geluisterd en hebt meedacht over oplossingen. Ik heb ontzettend veel van je geleerd en zonder jou was de code die er nu ligt lang niet zo succesvol. Laten we in de toekomst zo min mogelijk met andermans code bezig gaan.

Chris, het stukje structuur dat we elkaar konden geven door bij jou thuis te werken was echt een reddingsboei destijds. Marion, ik ben heel blij dat we ondanks alles nog steeds goed bevriend zijn en tijd voor elkaar blijven maken. Lennert en Corneel, soms zit geluk in de kleine dingen, zoals elke week eventjes alle natuurkunde achter je laten door je een viking of dwerg te wanen.

Ik wil ook alle teamgenoten bedanken die me door de jaren heen hebben gesteund en begrip hebben getoond als ik weer eens gestresst of overspannen aankwam bij het volleybal. Het heeft altijd veel voor me betekend om ondanks alles wat er overdag gebeurde, ik het 's avonds even achter me kon laten om te gaan volleyballen. Die constante factor heeft me door moeilijke tijden heen gesleept.

Jochem, jij bent het lichtpuntje van een PhD doen tijdens de coronacrisis. Zonder de gesprekken die we opeens samen voerden toen er niemand anders op de afdeling was, hadden we elkaar nooit zo goed kunnen leren kennen. Wat ben ik blij dat we elkaar hebben ontmoet. Ooit word ik vast (bijna) net zo goed als jij in dingen okken.

Lia en Geert, Hanneke en Bas Jan, Martin en Silke, bedankt voor het warme welkom in de familie.

Pap, mam, Jeroen, jullie zijn er altijd voor me geweest en het is een geruststellende gedachte dat ik altijd bij jullie terecht kan voor afleiding of advies. Jullie zijn de basis waar alles op gebouwd is. Bedankt voor alle jaren onvoorwaardelijke steun en hulp.

Bibliography

BIBLIOGRAPHY

[1] Wikipedia. Standard model, 2023. https://en.wikipedia.org/wiki/Standard_Model Accessed 28-03-2023.

[2] M.E. Peskin and D.V. Schroeder. *An Introduction To Quantum Field Theory*. Frontiers in Physics. Avalon Publishing, 1995.

[3] K. Ottnad, B. Kubis, U. G. Meissner, and F. K. Guo. New insights into the neutron electric dipole moment. *Phys. Lett. B*, 687:42–47, 2010.

[4] C. Abel et al. Measurement of the Permanent Electric Dipole Moment of the Neutron. *Phys. Rev. Lett.*, 124(8):081803, 2020.

[5] C. S. Wu, E. Ambler, R. W. Hayward, et al. Experimental Test of Parity Conservation in β Decay. *Phys. Rev.*, 105:1413–1414, 1957.

[6] J. H. Christenson, J. W. Cronin, V. L. Fitch, and R. Turlay. Evidence for the 2π decay of the k_2^0 meson. *Phys. Rev. Lett.*, 13:138–140, Jul 1964.

[7] C. Jarlskog. Commutator of the Quark Mass Matrices in the Standard Electroweak Model and a Measure of Maximal CP Nonconservation. *Phys. Rev. Lett.*, 55:1039, 1985.

[8] A. D. Sakharov. Violation of CP Invariance, C asymmetry, and baryon asymmetry of the universe. *Pisma Zh. Eksp. Teor. Fiz.*, 5:32–35, 1967.

[9] F. Zwicky. Die Rotverschiebung von extragalaktischen Nebeln. *Helv. Phys. Acta*, 6:110–127, 1933.

[10] F. Zwicky. On the masses of nebulae and of clusters of nebulae. *The Astrophysical Journal*, 86:217, October 1937.

[11] A.G. Doroshkevich, Vladimir N. Lukash, and E.V. Mikheeva. A solution to the problems of cusps and rotation curves in dark matter halos in the cosmological standard model. *Uspekhi Fizicheskih Nauk*, 182(1):3, 2012.

[12] Vera C. Rubin and Jr. Ford W. Kent. Rotation of the andromeda nebula from a spectroscopic survey of emission regions. *The Astrophysical Journal*, 159:379, February 1970.

[13] Gianfranco Bertone and Dan Hooper. History of dark matter. *Rev. Mod. Phys.*, 90(4):045002, 2018.

[14] Ruth A. Daly. Cosmological inflation and large-scale structure cosmological inflation and large-scale structure andrew r. liddle and david h. lyth cambridge u. press, new york, 2000. $80.00, $34.95 paper (400 pp.). ISBN 0-521-66022-x, ISBN 0-521-57598-2 paper. *Physics Today*, 54(7):56–58, July 2001.

[15] N. Aghanim et al. Planck 2018 results. VI. Cosmological parameters. *Astron. Astrophys.*, 641:A6, 2020. [Erratum: Astron.Astrophys. 652, C4 (2021)].

[16] James S. Bullock and Michael Boylan-Kolchin. Small-Scale Challenges to the ΛCDM Paradigm. *Ann. Rev. Astron. Astrophys.*, 55:343–387, 2017.

[17] Marusa Bradac, Steven W. Allen, Tommaso Treu, et al. Revealing the properties of dark matter in the merging cluster MACSJ0025.4-1222. *Astrophys. J.*, 687:959, 2008.

[18] Shany Danieli, Pieter van Dokkum, Charlie Conroy, et al. Still missing dark matter: KCWI high-resolution stellar kinematics of NGC1052-DF2. *The Astrophysical Journal*, 874(2):L12, March 2019.

[19] Pieter van Dokkum, Shany Danieli, Roberto Abraham, et al. A second galaxy missing dark matter in the NGC 1052 group. *The Astrophysical Journal*, 874(1):L5, March 2019.

[20] R. D. Peccei and Helen R. Quinn. Constraints Imposed by CP Conservation in the Presence of Instantons. *Phys. Rev. D*, 16:1791–1797, 1977.

[21] R. D. Peccei and Helen R. Quinn. CP Conservation in the Presence of Instantons. *Phys. Rev. Lett.*, 38:1440–1443, 1977.

[22] G. W. Bennett et al. Final Report of the Muon E821 Anomalous Magnetic Moment Measurement at BNL. *Phys. Rev. D*, 73:072003, 2006.

[23] **Muon g − 2** Collaboration. Muon (g-2) Technical Design Report. 1 2015.

[24] M. Abe et al. A New Approach for Measuring the Muon Anomalous Magnetic Moment and Electric Dipole Moment. *PTEP*, 2019(5):053C02, 2019.

[25] K. S. Babu, Bhaskar Dutta, and R. N. Mohapatra. Seesaw constrained MSSM, solution to the SUSY CP problem and a supersymmetric explanation of epsilon-prime / epsilon. *Phys. Rev. D*, 61:091701, 2000.

[26] Jonathan L. Feng. Naturalness and the Status of Supersymmetry. *Ann. Rev. Nucl. Part. Sci.*, 63:351–382, 2013.

[27] Iosif B. Khriplovich and Steve K. Lamoreaux. *Theoretical Predictions for Neutron and Electron Dipole Moments*, pages 107–118. Springer Berlin Heidelberg, Berlin, Heidelberg, 1997.

[28] J. J. Hudson, D. M. Kara, I. J. Smallman, et al. Improved measurement of the shape of the electron. *Nature*, 473(7348):493–496, May 2011.

[29] V. Andreev, Daniel Ang, D. DeMille, et al. Improved limit on the electric dipole moment of the electron. *Nature*, 562:355–360, 10 2018.

[30] Tanya S. Roussy et al. A new bound on the electron's electric dipole moment. 12 2022.

[31] Parul Aggarwal, , Hendrick L. Bethlem, et al. Measuring the electric dipole moment of the electron in BaF. *The European Physical Journal D*, 72(11), November 2018.

[32] Gerard 't Hooft. Naturalness, chiral symmetry, and spontaneous chiral symmetry breaking. *NATO Sci. Ser. B*, 59:135–157, 1980.

[33] Marc Schumann. Direct Detection of WIMP Dark Matter: Concepts and Status. *J. Phys. G*, 46(10):103003, 2019.

[34] E. Aprile et al. The XENON1T Dark Matter Experiment. *Eur. Phys. J. C*, 77(12):881, 2017.

[35] D. S. Akerib et al. Results from a search for dark matter in the complete LUX exposure. *Phys. Rev. Lett.*, 118(2):021303, 2017.

[36] Xiangyi Cui et al. Dark Matter Results From 54-Ton-Day Exposure of PandaX-II Experiment. *Phys. Rev. Lett.*, 119(18):181302, 2017.

[37] P. Agnes et al. Low-Mass Dark Matter Search with the DarkSide-50 Experiment. *Phys. Rev. Lett.*, 121(8):081307, 2018.

[38] D. S. Akerib et al. LUX-ZEPLIN (LZ) Conceptual Design Report. 9 2015.

[39] Toward a next-generation dark matter search with the PICO-40L bubble chamber. https://indico.cern.ch/event/606690/contributions/2623446/attachments/1497228/2330240/Fallows_2017_07_24__TAUP__PICO-40L_v1.2.pdf. Accessed: 2021-03-24.

[40] Manuel Drees, Rohini Godbole, and Probir Roy. *Theory and phenomenology of Sparticles: an account of four-dimensional N=1 supersymmetry in high-energy physics*. World Scientific, Singapore, 2004.

[41] Stephen P. Martin. A Supersymmetry primer. *Adv. Ser. Direct. High Energy Phys.*, 18:1–98, 1998.

[42] P. Fayet. Spontaneously broken supersymmetric theories of weak, electromagnetic and strong interactions. *Physics Letters B*, 69(4):489–494, January 1977.

[43] Glennys R. Farrar and Pierre Fayet. Phenomenology of the production, decay, and detection of new hadronic states associated with supersymmetry. *Physics Letters B*, 76(5):575–579, July 1978.

[44] Apostolos Pilaftsis and Carlos E. M. Wagner. Higgs bosons in the minimal supersymmetric standard model with explicit CP violation. *Nucl. Phys. B*, 553:3–42, 1999.

[45] M. Tanabashi, K. Hagiwara, K. Hikasa, et al. Review of particle physics. *Phys. Rev. D*, 98:030001, Aug 2018.

[46] Patrick Draper and Heidi Rzehak. A review of higgs mass calculations in supersymmetric models. *Physics Reports*, 619:1–24, Mar 2016.

[47] Particle Data Group, P A Zyla, R M Barnett, et al. Review of Particle Physics. *Progress of Theoretical and Experimental Physics*, 2020(8), 08 2020. 083C01.

[48] Amit Chakraborty, Biswaranjan Das, J. Lorenzo Diaz-Cruz, et al. 125 GeV Higgs signal at the LHC in the CP-violating MSSM. *Phys. Rev. D*, 90(5):055005, 2014.

[49] M. Carena, J. Ellis, J. S. Lee, et al. CP Violation in Heavy MSSM Higgs Scenarios. *JHEP*, 02:123, 2016.

[50] **MSSM Working Group**. The minimal supersymmetric standard model: group summary report. In *GDR (Groupement De Recherche) - Supersymetrie Montpellier, France, April 15-17, 1998*, 1998.

[51] F. Gabbiani, E. Gabrielli, A. Masiero, and L. Silvestrini. A Complete analysis of FCNC and CP constraints in general SUSY extensions of the standard model. *Nucl. Phys. B*, 477:321–352, 1996.

[52] Savas Dimopoulos and Scott D. Thomas. Dynamical relaxation of the supersymmetric CP violating phases. *Nucl. Phys. B*, 465:23–33, 1996.

[53] Bing Li and Carlos E. M. Wagner. CP-odd component of the lightest neutral Higgs boson in the MSSM. *Phys. Rev. D*, 91:095019, 2015.

[54] B. C. Allanach et al. SUSY Les Houches Accord 2. *Comput. Phys. Commun.*, 180:8–25, 2009.

[55] J. S. Lee, A. Pilaftsis, Marcela Carena, et al. CPsuperH: A Computational tool for Higgs phenomenology in the minimal supersymmetric standard model with explicit CP violation. *Comput. Phys. Commun.*, 156:283–317, 2004.

[56] Steven Weinberg. *The quantum theory of fields. Vol. 3: Supersymmetry.* Cambridge University Press, 6 2013.

[57] John R. Ellis, Jae Sik Lee, and Apostolos Pilaftsis. Electric Dipole Moments in the MSSM Reloaded. *JHEP*, 10:049, 2008.

[58] Chengcheng Han. Muon g-2 and CP violation in MSSM. 4 2021.

[59] Tanya S. Roussy et al. Experimental Constraint on Axionlike Particles over Seven Orders of Magnitude in Mass. *Phys. Rev. Lett.*, 126(17):171301, 2021.

[60] Julian S. Schwinger. On Quantum electrodynamics and the magnetic moment of the electron. *Phys. Rev.*, 73:416–417, 1948.

[61] Gilberto Colangelo, Martin Hoferichter, and Peter Stoffer. Two-pion contribution to hadronic vacuum polarization. *JHEP*, 02:006, 2019.

[62] Michel Davier, Andreas Hoecker, Bogdan Malaescu, and Zhiqing Zhang. Reevaluation of the hadronic vacuum polarisation contributions to the Standard Model predictions of the muon $g-2$ and $\alpha(m_Z^2)$ using newest hadronic cross-section data. *Eur. Phys. J.*, C77(12):827, 2017.

[63] Alexander Keshavarzi, Daisuke Nomura, and Thomas Teubner. Muon $g-2$ and $\alpha(M_Z^2)$: a new data-based analysis. *Phys. Rev.*, D97(11):114025, 2018.

[64] Martin Hoferichter, Bai-Long Hoid, and Bastian Kubis. Three-pion contribution to hadronic vacuum polarization. *JHEP*, 08:137, 2019.

[65] Alexander Kurz, Tao Liu, Peter Marquard, and Matthias Steinhauser. Hadronic contribution to the muon anomalous magnetic moment to next-to-next-to-leading order. *Phys. Lett.*, B734:144–147, 2014.

[66] Kirill Melnikov and Arkady Vainshtein. Hadronic light-by-light scattering contribution to the muon anomalous magnetic moment revisited. *Phys. Rev.*, D70:113006, 2004.

[67] Gilberto Colangelo, Martin Hoferichter, Massimiliano Procura, and Peter Stoffer. Dispersion relation for hadronic light-by-light scattering: two-pion contributions. *JHEP*, 04:161, 2017.

[68] Martin Hoferichter, Bai-Long Hoid, Bastian Kubis, et al. Dispersion relation for hadronic light-by-light scattering: pion pole. *JHEP*, 10:141, 2018.

[69] Antoine Gérardin, Harvey B. Meyer, and Andreas Nyffeler. Lattice calculation of the pion transition form factor with $N_f = 2 + 1$ Wilson quarks. *Phys. Rev.*, D100(3):034520, 2019.

[70] Gilberto Colangelo, Franziska Hagelstein, Martin Hoferichter, et al. Longitudinal short-distance constraints for the hadronic light-by-light contribution to $(g-2)_\mu$ with large-N_c Regge models. *JHEP*, 03:101, 2020.

[71] Gilberto Colangelo, Martin Hoferichter, Andreas Nyffeler, et al. Remarks on higher-order hadronic corrections to the muon $g-2$. *Phys. Lett.*, B735:90–91, 2014.

[72] Pere Masjuan and Pablo Sánchez-Puertas. Pseudoscalar-pole contribution to the $(g_\mu - 2)$: a rational approach. *Phys. Rev.*, D95(5):054026, 2017.

[73] Thomas Blum, Norman Christ, Masashi Hayakawa, et al. The hadronic light-by-light scattering contribution to the muon anomalous magnetic moment from lattice QCD. *Phys. Rev. Lett.*, 124(13):132002, 2020.

[74] Joaquim Prades, Eduardo de Rafael, and Arkady Vainshtein. The Hadronic Light-by-Light Scattering Contribution to the Muon and Electron Anomalous Magnetic Moments. *Adv. Ser. Direct. High Energy Phys.*, 20:303–317, 2009.

[75] M. Davier, A. Hoecker, B. Malaescu, and Z. Zhang. A new evaluation of the hadronic vacuum polarisation contributions to the muon anomalous magnetic moment and to $\boldsymbol{\alpha(m_Z^2)}$. *Eur. Phys. J.*, C80(3):241, 2020. [Erratum: Eur. Phys. J. **C80**, 410 (2020)].

[76] Alexander Keshavarzi, Daisuke Nomura, and Thomas Teubner. The $g-2$ of charged leptons, $\alpha(M_Z^2)$ and the hyperfine splitting of muonium. *Phys. Rev.*, D101:014029, 2020.

[77] C. Gnendiger, D. Stöckinger, and H. Stöckinger-Kim. The electroweak contributions to $(g-2)_\mu$ after the Higgs boson mass measurement. *Phys. Rev.*, D88:053005, 2013.

[78] Andrzej Czarnecki, William J. Marciano, and Arkady Vainshtein. Refinements in electroweak contributions to the muon anomalous magnetic moment. *Phys. Rev.*, D67:073006, 2003. [Erratum: Phys. Rev. **D73**, 119901 (2006)].

[79] Marc Knecht, Santiago Peris, Michel Perrottet, and Eduardo De Rafael. Electroweak hadronic contributions to the muon (g-2). *JHEP*, 11:003, 2002.

[80] Tatsumi Aoyama, Toichiro Kinoshita, and Makiko Nio. Revised and Improved Value of the QED Tenth-Order Electron Anomalous Magnetic Moment. *Phys. Rev. D*, 97(3):036001, 2018.

[81] Tatsumi Aoyama, Masashi Hayakawa, Toichiro Kinoshita, and Makiko Nio. Complete Tenth-Order QED Contribution to the Muon $g-2$. *Phys. Rev. Lett.*, 109:111808, 2012.

[82] T. Aoyama et al. The anomalous magnetic moment of the muon in the Standard Model. *Phys. Rept.*, 887:1–166, 2020.

[83] G. W. Bennett et al. Measurement of the negative muon anomalous magnetic moment to 0.7 ppm. *Phys. Rev. Lett.*, 92:161802, 2004.

[84] G. W. Bennett et al. Measurement of the positive muon anomalous magnetic moment to 0.7 ppm. *Phys. Rev. Lett.*, 89:101804, 2002. [Erratum: Phys.Rev.Lett. 89, 129903 (2002)].

[85] Sz. Borsanyi, Z. Fodor, J. N. Guenther, et al. Leading hadronic contribution to the muon magnetic moment from lattice QCD. *Nature*, 593(7857):51–55, April 2021.

[86] Marco Cè et al. Window observable for the hadronic vacuum polarization contribution to the muon $g-2$ from lattice QCD. 6 2022.

[87] G. Colangelo, A. X. El-Khadra, M. Hoferichter, et al. Data-driven evaluations of Euclidean windows to scrutinize hadronic vacuum polarization. 5 2022.

[88] **Muon g − 2** Collaboration. Measurement of the positive muon anomalous magnetic moment to 0.46 ppm. *Phys. Rev. Lett.*, 126:141801, Apr 2021.

[89] **Muon g − 2** Collaboration. Magnetic-field measurement and analysis for the muon $g-2$ experiment at fermilab. *Phys. Rev. A*, 103:042208, Apr 2021.

[90] **Muon g − 2** Collaboration. Measurement of the anomalous precession frequency of the muon in the fermilab muon $g-2$ experiment. *Phys. Rev. D*, 103:072002, Apr 2021.

[91] Tsutomu Mibe. Measurement of muon g-2 and edm with an ultra-cold muon beam at j-parc. *Nuclear Physics B - Proceedings Supplements*, 218(1):242–246, 2011. Proceedings of the Eleventh International Workshop on Tau Lepton Physics.

[92] Marcin Badziak and Kazuki Sakurai. Explanation of electron and muon g − 2 anomalies in the MSSM. *JHEP*, 10:024, 2019.

[93] M. E. Pospelov and I. B. Khriplovich. Electric dipole moment of the W boson and the electron in the Kobayashi-Maskawa model. *Sov. J. Nucl. Phys.*, 53:638–640, 1991.

[94] Maxim Pospelov and Adam Ritz. Electric dipole moments as probes of new physics. *Annals Phys.*, 318:119–169, 2005.

[95] Daniel Ng and John N. Ng. A Note on Majorana neutrinos, leptonic CKM and electron electric dipole moment. *Mod. Phys. Lett. A*, 11:211–216, 1996.

[96] Jonathan Engel, Michael J. Ramsey-Musolf, and U. van Kolck. Electric Dipole Moments of Nucleons, Nuclei, and Atoms: The Standard Model and Beyond. *Prog. Part. Nucl. Phys.*, 71:21–74, 2013.

[97] Ivan Kozyryev and Nicholas R. Hutzler. Precision Measurement of Time-Reversal Symmetry Violation with Laser-Cooled Polyatomic Molecules. *Phys. Rev. Lett.*, 119(13):133002, 2017.

[98] Peter Athron, Markus Bach, Helvecio G. Fargnoli, et al. GM2Calc: Precise MSSM prediction for $(g-2)$ of the muon. *Eur. Phys. J. C*, 76(2):62, 2016.

[99] Peter Athron, Csaba Balazs, Adriano Cherchiglia, et al. Two-loop prediction of the anomalous magnetic moment of the muon in the Two-Higgs Doublet Model with GM2Calc 2. *Eur. Phys. J. C*, 82(3):229, 2022.

[100] Takeo Moroi. The Muon anomalous magnetic dipole moment in the minimal supersymmetric standard model. *Phys. Rev. D*, 53:6565–6575, 1996. [Erratum: Phys.Rev.D 56, 4424 (1997)].

[101] Stephen P. Martin and James D. Wells. Muon Anomalous Magnetic Dipole Moment in Supersymmetric Theories. *Phys. Rev. D*, 64:035003, 2001.

[102] Dominik Stockinger. The Muon Magnetic Moment and Supersymmetry. *J. Phys. G*, 34:R45–R92, 2007.

[103] Helvecio Fargnoli, Christoph Gnendiger, Sebastian Paßehr, et al. Two-loop corrections to the muon magnetic moment from fermion/sfermion loops in the MSSM: detailed results. *JHEP*, 02:070, 2014.

[104] H. G. Fargnoli, C. Gnendiger, S. Paßehr, et al. Non-decoupling two-loop corrections to $(g-2)_\mu$ from fermion/sfermion loops in the MSSM. *Phys. Lett. B*, 726:717–724, 2013.

[105] Kingman Cheung, Otto C. W. Kong, and Jae Sik Lee. Electric and anomalous magnetic dipole moments of the muon in the MSSM. *JHEP*, 06:020, 2009.

[106] Adriano Cherchiglia, Patrick Kneschke, Dominik Stöckinger, and Hyejung Stöckinger-Kim. The muon magnetic moment in the 2HDM: complete two-loop result. *JHEP*, 01:007, 2017. [Erratum: JHEP 10, 242 (2021)].

[107] Adriano Cherchiglia, Dominik Stöckinger, and Hyejung Stöckinger-Kim. Muon g-2 in the 2HDM: maximum results and detailed phenomenology. *Phys. Rev. D*, 98:035001, 2018.

[108] Apostolos Pilaftsis. Higgs boson two loop contributions to electric dipole moments in the MSSM. *Phys. Lett. B*, 471:174–181, 1999.

[109] J. S. Lee, M. Carena, J. Ellis, et al. CPsuperH2.3: an Updated Tool for Phenomenology in the MSSM with Explicit CP Violation. *Comput. Phys. Commun.*, 184:1220–1233, 2013.

[110] Apostolos Pilaftsis. Higgs mediated electric dipole moments in the MSSM: An application to baryogenesis and Higgs searches. *Nucl. Phys. B*, 644:263–289, 2002.

[111] Paolo Gondolo and Graciela Gelmini. Cosmic abundances of stable particles: Improved analysis. *Nucl. Phys. B*, 360:145–179, 1991.

[112] M. Tanabashi, K. Hagiwara, K. Hikasa, et al. Review of particle physics. *Physical Review D*, 98(3), August 2018.

[113] Joakim Edsjo and Paolo Gondolo. Neutralino relic density including coannihilations. *Phys. Rev. D*, 56:1879–1894, 1997.

[114] Yong Du. *Searching for new physics at colliders and from precision measurements*. PhD thesis, Massachusetts U., Amherst, 2020.

[115] Melissa van Beekveld. *Myth busting precision physics*, chapter 6 The fine-tuning problem. Number ISBN 9789464023879. 2020.

[116] Eldad Gildener. Gauge Symmetry Hierarchies. *Phys. Rev. D*, 14:1667, 1976.

[117] Leonard Susskind. Dynamics of Spontaneous Symmetry Breaking in the Weinberg-Salam Theory. *Phys. Rev. D*, 20:2619–2625, 1979.

[118] Steven Weinberg. Gauge hierarchies. *Physics Letters B*, 82(3-4):387–391, April 1979.

[119] M. J. G. Veltman. The Infrared - Ultraviolet Connection. *Acta Phys. Polon. B*, 12:437, 1981.

[120] Melissa van Beekveld, Wim Beenakker, Sascha Caron, et al. Supersymmetry with Dark Matter is still natural. *Phys. Rev. D*, 96(3):035015, 2017.

[121] Melissa van Beekveld, Sascha Caron, and Roberto Ruiz de Austri. The current status of fine-tuning in supersymmetry. *JHEP*, 01:147, 2020.

[122] Riccardo Barbieri and G. F. Giudice. Upper Bounds on Supersymmetric Particle Masses. *Nucl. Phys. B*, 306:63–76, 1988.

[123] Howard Baer, Vernon Barger, Peisi Huang, et al. Radiative natural SUSY with a 125 GeV Higgs boson. *Phys. Rev. Lett.*, 109:161802, 2012.

[124] Howard Baer, Vernon Barger, Peisi Huang, et al. Radiative natural supersymmetry: Reconciling electroweak fine-tuning and the higgs boson mass. *Physical Review D*, 87(11), June 2013.

[125] María Eugenia Cabrera, J. Alberto Casas, Antonio Delgado, et al. Naturalness of MSSM dark matter. *JHEP*, 08:058, 2016.

[126] Melissa Van Beekveld, Wim Beenakker, Marrit Schutten, and Jeremy De Wit. Dark matter, fine-tuning and $(g-2)_\mu$ in the pMSSM. *SciPost Phys.*, 11(3):049, 2021.

[127] E. Aprile et al. Dark matter search results from a one ton-year exposure of XENON1T. *Phys. Rev. Lett.*, 121(11):111302, 2018.

[128] E. Aprile et al. Constraining the spin-dependent WIMP-nucleon cross sections with XENON1T. *Phys. Rev. Lett.*, 122(14):141301, 2019.

[129] Andi Tan et al. Dark matter results from first 98.7 days of data from the PandaX-II experiment. *Phys. Rev. Lett.*, 117(12):121303, 2016.

[130] Jingkai Xia et al. PandaX-II constraints on spin-dependent WIMP-nucleon effective interactions. *Phys. Lett.*, B792:193–198, 2019.

[131] C. Amole et al. Improved dark matter search results from PICO-2L Run 2. *Phys. Rev.*, D93(6):061101, 2016.

[132] C. Amole et al. Dark Matter Search Results from the PICO-60 C_3F_8 Bubble Chamber. *Phys. Rev. Lett.*, 118(25):251301, 2017.

[133] C. Amole et al. Dark Matter Search Results from the Complete Exposure of the PICO-60 C_3F_8 Bubble Chamber. 2019.

[134] Kamila Kowalska, Leszek Roszkowski, Enrico Maria Sessolo, and Andrew J. Williams. GUT-inspired SUSY and the muon g − 2 anomaly: prospects for LHC 14 TeV. *JHEP*, 06:020, 2015.

[135] M. Adeel Ajaib, Bhaskar Dutta, Tathagata Ghosh, et al. Neutralinos and sleptons at the LHC in light of muon $(g-2)_\mu$. *Phys. Rev. D*, 92(7):075033, 2015.

[136] Siba Prasad Das, Monoranjan Guchait, and D. P. Roy. Testing SUSY models for the muon g-2 anomaly via chargino-neutralino pair production at the LHC. *Phys. Rev. D*, 90(5):055011, 2014.

[137] Motoi Endo, Koichi Hamaguchi, Sho Iwamoto, and Teppei Kitahara. Muon $g-2$ vs LHC Run 2 in supersymmetric models. *JHEP*, 04:165, 2020.

[138] Kaoru Hagiwara, Kai Ma, and Satyanarayan Mukhopadhyay. Closing in on the chargino contribution to the muon g-2 in the MSSM: current LHC constraints. *Phys. Rev. D*, 97(5):055035, 2018.

[139] Hieu Minh Tran and Huong Thu Nguyen. GUT-inspired MSSM in light of muon $g-2$ and LHC results at $\sqrt{s} = 13$ TeV. *Phys. Rev. D*, 99(3):035040, 2019.

[140] Murat Abdughani, Ken-Ichi Hikasa, Lei Wu, et al. Testing electroweak SUSY for muon $g-2$ and dark matter at the LHC and beyond. *JHEP*, 11:095, 2019.

[141] Archil Kobakhidze, Matthew Talia, and Lei Wu. Probing the MSSM explanation of the muon g-2 anomaly in dark matter experiments and at a 100 TeV pp collider. *Phys. Rev. D*, 95(5):055023, 2017.

[142] Motoi Endo, Koichi Hamaguchi, Sho Iwamoto, and Keisuke Yanagi. Probing minimal SUSY scenarios in the light of muon $g-2$ and dark matter. *JHEP*, 06:031, 2017.

[143] Manimala Chakraborti, Sven Heinemeyer, and Ipsita Saha. Improved $(g-2)_\mu$ Measurements and Supersymmetry. *Eur. Phys. J. C*, 80(10):984, 2020.

[144] Peter Cox, Chengcheng Han, and Tsutomu T. Yanagida. Muon $g-2$ and dark matter in the minimal supersymmetric standard model. *Phys. Rev. D*, 98(5):055015, 2018.

[145] Manimala Chakraborti, Sven Heinemeyer, and Ipsita Saha. Improved $(g-2)_\mu$ Measurements and Wino/Higgsino Dark Matter. 3 2021.

[146] E. A. Bagnaschi et al. Supersymmetric Dark Matter after LHC Run 1. *Eur. Phys. J. C*, 75:500, 2015.

[147] Gianfranco Bertone, Francesca Calore, Sascha Caron, et al. Global analysis of the pMSSM in light of the Fermi GeV excess: prospects for the LHC Run-II and astroparticle experiments. *JCAP*, 04:037, 2016.

[148] C. Strege, G. Bertone, G. J. Besjes, et al. Profile likelihood maps of a 15-dimensional MSSM. *JHEP*, 09:081, 2014.

[149] Andrew Fowlie, Kamila Kowalska, Leszek Roszkowski, et al. Dark matter and collider signatures of the MSSM. *Phys. Rev. D*, 88:055012, 2013.

[150] E. Bagnaschi et al. Likelihood Analysis of the pMSSM11 in Light of LHC 13-TeV Data. *Eur. Phys. J. C*, 78(3):256, 2018.

[151] Peter Athron et al. A global fit of the MSSM with GAMBIT. *Eur. Phys. J. C*, 77(12):879, 2017.

[152] Tianjun Li and Shabbar Raza. Electroweak supersymmetry from the generalized minimal supergravity model in the MSSM. *Phys. Rev. D*, 91(5):055016, 2015.

[153] Tianjun Li, Shabbar Raza, and Kechen Wang. Constraining Natural SUSY via the Higgs Coupling and the Muon Anomalous Magnetic Moment Measurements. *Phys. Rev. D*, 93(5):055040, 2016.

[154] Manuel Drees and Ghazaal Ghaffari. Impact of the Bounds on the Direct Search for Neutralino Dark Matter on Naturalness. 3 2021.

[155] Murat Abdughani, Lei Wu, and Jin Min Yang. Status and prospects of light bino–higgsino dark matter in natural SUSY. *Eur. Phys. J. C*, 78(1):4, 2018.

[156] Howard Baer, Vernon Barger, Dibyashree Sengupta, and Xerxes Tata. Is natural higgsino-only dark matter excluded? *Eur. Phys. J.*, C78(10):838, 2018.

[157] Melissa van Beekveld. Supplementary Data: "Dark matter, fine-tuning and mu(g-2) in the pMSSM", June 2021. https://doi.org/10.5281/zenodo.4934398.

[158] B. C. Allanach. SUSY Predictions and SUSY Tools at the LHC. *Eur. Phys. J. C*, 59:427–443, 2009.

[159] Marcela Carena, John R. Ellis, A. Pilaftsis, and C. E. M. Wagner. Renormalization group improved effective potential for the MSSM Higgs sector with explicit CP violation. *Nucl. Phys. B*, 586:92–140, 2000.

[160] J. S. Lee, M. Carena, J. Ellis, et al. CPsuperH2.0: an Improved Computational Tool for Higgs Phenomenology in the MSSM with Explicit CP Violation. *Comput. Phys. Commun.*, 180:312–331, 2009.

[161] Torsten Bringmann et al. DarkBit: A GAMBIT module for computing dark matter observables and likelihoods. *Eur. Phys. J. C*, 77(12):831, 2017.

[162] Peter Athron et al. Global analyses of Higgs portal singlet dark matter models using GAMBIT. *Eur. Phys. J. C*, 79(1):38, 2019.

[163] S. Heinemeyer, W. Hollik, and G. Weiglein. FeynHiggs: A Program for the calculation of the masses of the neutral CP even Higgs bosons in the MSSM. *Comput. Phys. Commun.*, 124:76–89, 2000.

[164] H. Bahl, T. Hahn, S. Heinemeyer, et al. Precision calculations in the MSSM Higgs-boson sector with FeynHiggs 2.14. *Comput. Phys. Commun.*, 249:107099, 2020.

[165] Philip Bechtle, Sven Heinemeyer, Oscar Stål, et al. Applying exclusion likelihoods from LHC searches to extended Higgs sectors. *Eur. Phys. J.*, C75(9):421, 2015.

[166] Philip Bechtle, Oliver Brein, Sven Heinemeyer, et al. HiggsBounds−4: Improved tests of extended Higgs sectors against exclusion bounds from LEP, the Tevatron and the LHC. *Eur. Phys. J.*, C74(3):2693, 2014.

[167] Philip Bechtle, Oliver Brein, Sven Heinemeyer, et al. Recent developments in HiggsBounds and a preview of HiggsSignals. *PoS*, 2012:024, 2012.

[168] Philip Bechtle, Oliver Brein, Sven Heinemeyer, et al. HiggsBounds 2.0.0: Confronting neutral and charged Higgs sector predictions with exclusion bounds from LEP and the Tevatron. *Comput. Phys. Commun.*, 182:2605–2631, 2011.

[169] Philip Bechtle, Oliver Brein, Sven Heinemeyer, et al. HiggsBounds: confronting arbitrary Higgs sectors with exclusion bounds from LEP and the Tevatron. *Comput. Phys. Commun.*, 181:138–167, 2010.

[170] Oscar Stål and Tim Stefaniak. Constraining extended Higgs sectors with HiggsSignals. *PoS*, 2013:314, 2013.

[171] Philip Bechtle, Sven Heinemeyer, Oscar Stål, et al. Probing the Standard Model with Higgs signal rates from the Tevatron, the LHC and a future ILC. *JHEP*, 1411:039, 2014.

[172] Philip Bechtle, Sven Heinemeyer, Oscar Stål, et al. *HiggsSignals*: Confronting arbitrary Higgs sectors with measurements at the Tevatron and the LHC. *Eur. Phys. J. C*, 74(2):2711, 2014.

[173] Philip Bechtle, Sven Heinemeyer, Tobias Klingl, et al. HiggsSignals-2: Probing new physics with precision Higgs measurements in the LHC 13 TeV era. *Eur. Phys. J. C*, 81(2):145, 2021.

[174] Jeremy Bernon and Beranger Dumont. Lilith: a tool for constraining new physics from Higgs measurements. *Eur. Phys. J. C*, 75(9):440, 2015.

[175] Sabine Kraml, Tran Quang Loc, Dao Thi Nhung, and Le Duc Ninh. Constraining new physics from Higgs measurements with Lilith: update to LHC Run 2 results. *SciPost Phys.*, 7(4):052, 2019.

[176] G. Belanger, F. Boudjema, A. Pukhov, and A. Semenov. micrOMEGAs: Version 1.3. *Comput. Phys. Commun.*, 174:577–604, 2006.

[177] G. Belanger, F. Boudjema, A. Pukhov, and A. Semenov. MicrOMEGAs 2.0: A Program to calculate the relic density of dark matter in a generic model. *Comput. Phys. Commun.*, 176:367–382, 2007.

[178] G. Belanger, F. Boudjema, A. Pukhov, and A. Semenov. Dark matter direct detection rate in a generic model with micrOMEGAs 2.2. *Comput. Phys. Commun.*, 180:747–767, 2009.

[179] G. Belanger, F. Boudjema, P. Brun, et al. Indirect search for dark matter with micrOMEGAs2.4. *Comput. Phys. Commun.*, 182:842–856, 2011.

[180] G. Belanger, F. Boudjema, A. Pukhov, and A. Semenov. micrOMEGAs_3: A program for calculating dark matter observables. *Comput. Phys. Commun.*, 185:960–985, 2014.

[181] Genevieve Belanger, Ali Mjallal, and Alexander Pukhov. Recasting direct detection limits within micrOMEGAs and implication for non-standard Dark Matter scenarios. *Eur. Phys. J. C*, 81(3):239, 2021.

[182] G. Belanger, F. Boudjema, S. Kraml, et al. Relic density of neutralino dark matter in the MSSM with CP violation. *Phys. Rev. D*, 73:115007, 2006.

[183] W. Beenakker, R. Hopker, and M. Spira. PROSPINO: A Program for the production of supersymmetric particles in next-to-leading order QCD. 11 1996.

[184] Florian Staub. SARAH 4 : A tool for (not only SUSY) model builders. *Comput. Phys. Commun.*, 185:1773–1790, 2014.

[185] Federico Ambrogi et al. SModelS v1.2: long-lived particles, combination of signal regions, and other novelties. 2018.

[186] Jan Heisig, Sabine Kraml, and Andre Lessa. Constraining new physics with searches for long-lived particles: implementation into SModelS. *Phys. Lett.*, B788:87–95, 2019.

[187] Juhi Dutta, Sabine Kraml, Andre Lessa, and Wolfgang Waltenberger. SModelS extension with the CMS supersymmetry search results from Run 2. *LHEP*, 1(1):5–12, 2018.

[188] Federico Ambrogi, Sabine Kraml, Suchita Kulkarni, et al. SModelS v1.1 user manual: Improving simplified model constraints with efficiency maps. *Comput. Phys. Commun.*, 227:72–98, 2018.

[189] Sabine Kraml, Suchita Kulkarni, Ursula Laa, et al. SModelS: a tool for interpreting simplified-model results from the LHC and its application to supersymmetry. *Eur. Phys. J.*, C74:2868, 2014.

[190] Werner Porod. SPheno, a program for calculating supersymmetric spectra, SUSY particle decays and SUSY particle production at e+ e- colliders. *Comput. Phys. Commun.*, 153:275–315, 2003.

[191] W. Porod and F. Staub. SPheno 3.1: Extensions including flavour, CP-phases and models beyond the MSSM. *Comput. Phys. Commun.*, 183:2458–2469, 2012.

[192] Sascha Caron, Jong Soo Kim, Krzysztof Rolbiecki, et al. The BSM-AI project: SUSY-AI–generalizing LHC limits on supersymmetry with machine learning. *Eur. Phys. J.*, C77(4):257, 2017.

[193] A. Djouadi, M. M. Muhlleitner, and M. Spira. Decays of supersymmetric particles: the program SUSY-HIT (SUspect-SdecaY-Hdecay-InTerface). *Acta Phys. Polon.*, B38:635–644, 2007.

[194] B. C. Allanach. SOFTSUSY: a program for calculating supersymmetric spectra. *Comput. Phys. Commun.*, 143:305–331, 2002.

[195] F. Mahmoudi. SuperIso: A Program for calculating the isospin asymmetry of B —> K* gamma in the MSSM. *Comput. Phys. Commun.*, 178:745–754, 2008.

[196] F. Mahmoudi. SuperIso v2.3: A Program for calculating flavor physics observables in Supersymmetry. *Comput. Phys. Commun.*, 180:1579–1613, 2009.

[197] J. E. Camargo-Molina, B. O'Leary, W. Porod, and F. Staub. **Vevacious**: A tool for finding the global minima of one-loop effective potentials with many scalars. *Eur. Phys. J.*, C73(10):2588, 2013.

[198] T. L. Lee, T. Y. Li, and C. H. Tsai. Hom4ps-2.0: a software package for solving polynomial systems by the polyhedral homotopy continuation method. *Computing*, 83(2):109, 2008.

[199] Carroll L. Wainwright. CosmoTransitions: Computing cosmological phase transition temperatures and bubble profiles with multiple fields. *Comput. Phys. Commun.*, 183:2006–2013, 2012.

[200] J. H. Kotecha and P. M. Djuric. Gaussian particle filtering. *IEEE Transactions on Signal Processing*, 51(10):2592–2601, Oct 2003.

[201] Motoi Endo, Koichi Hamaguchi, Teppei Kitahara, and Takahiro Yoshinaga. Probing Bino contribution to muon $g-2$. *JHEP*, 11:013, 2013.

[202] M. Ackermann et al. Searching for Dark Matter Annihilation from Milky Way Dwarf Spheroidal Galaxies with Six Years of Fermi Large Area Telescope Data. *Phys. Rev. Lett.*, 115(23):231301, 2015.

[203] Howard Baer, Vernon Barger, Peisi Huang, et al. Radiative natural supersymmetry with a 125 GeV higgs boson. *Physical Review Letters*, 109(16), October 2012.

[204] Howard Baer, Vernon Barger, and Maren Padeffke-Kirkland. Electroweak versus high scale finetuning in the 19-parameter SUGRA model. *Phys. Rev.*, D88:055026, 2013.

[205] Howard Baer, Vernon Barger, Dan Mickelson, and Maren Padeffke-Kirkland. SUSY models under siege: LHC constraints and electroweak fine-tuning. *Phys. Rev.*, D89(11):115019, 2014.

[206] M. Drees and Jong Soo Kim. Minimal natural supersymmetry after the LHC8. *Phys. Rev.*, D93(9):095005, 2016.

[207] Howard Baer, Vernon Barger, James S. Gainer, et al. Reach of the high-energy LHC for gluinos and top squarks in SUSY models with light Higgsinos. *Phys. Rev.*, D96(11):115008, 2017.

[208] Azar Mustafayev and Xerxes Tata. Supersymmetry, Naturalness, and Light Higgsinos. *Indian J. Phys.*, 88:991–1004, 2014.

[209] Howard Baer, Vernon Barger, Peisi Huang, et al. Radiative natural supersymmetry: Reconciling electroweak fine-tuning and the higgs boson mass. *Phys. Rev. D*, 87:115028, Jun 2013.

[210] Howard Baer, Vernon Barger, and Michael Savoy. Upper bounds on sparticle masses from naturalness or how to disprove weak scale supersymmetry. *Phys. Rev. D*, 93:035016, Feb 2016.

[211] LEP2 SUSY Working Group, ALEPH, DELPHI, L3 and OPAL experiments.

[212] A. Heister et al. Absolute lower limits on the masses of selectrons and sneutrinos in the MSSM. *Phys. Lett. B*, 544:73–88, 2002.

[213] Marcela Carena, Andre de Gouvea, Ayres Freitas, and Michael Schmitt. Invisible Z boson decays at e^+e^- colliders. *Phys. Rev.*, D68:113007, 2003.

[214] Tao Han, Zhen Liu, and Aravind Natarajan. Dark matter and Higgs bosons in the MSSM. *JHEP*, 11:008, 2013.

[215] G. Belanger, F. Boudjema, A. Cottrant, et al. The MSSM invisible Higgs in the light of dark matter and g-2. *Phys. Lett. B*, 519:93–102, 2001.

[216] Takeshi Nihei, Leszek Roszkowski, and Roberto Ruiz de Austri. Exact cross-sections for the neutralino slepton coannihilation. *JHEP*, 07:024, 2002.

[217] Morad Aaboud et al. Search for chargino-neutralino production using recursive jigsaw reconstruction in final states with two or three charged leptons in proton-proton collisions at $\sqrt{s} = 13$ TeV with the ATLAS detector. *Phys. Rev. D*, 98(9):092012, 2018.

[218] A. M. Sirunyan et al. Combined search for electroweak production of charginos and neutralinos in proton-proton collisions at $\sqrt{s} = 13$ TeV. *JHEP*, 03:160, 2018.

[219] Albert M Sirunyan et al. Search for supersymmetry in final states with two oppositely charged same-flavor leptons and missing transverse momentum in proton-proton collisions at $\sqrt{s} = 13$ TeV. 12 2020.

[220] Albert M Sirunyan et al. Search for supersymmetry with a compressed mass spectrum in the vector boson fusion topology with 1-lepton and 0-lepton final states in proton-proton collisions at $\sqrt{s} = 13$ TeV. *JHEP*, 08:150, 2019.

[221] Search for electroweak production of charginos and neutralinos in proton-proton collisions at sqrt(s)=13 TeV. Technical Report CMS-PAS-SUS-19-012, CERN, Geneva, 2021.

[222] Morad Aaboud et al. Search for the direct production of charginos and neutralinos in final states with tau leptons in $\sqrt{s} = 13$ TeV pp collisions with the ATLAS detector. *Eur. Phys. J. C*, 78(2):154, 2018.

[223] Albert M Sirunyan et al. Search for direct pair production of supersymmetric partners to the τ lepton in proton-proton collisions at $\sqrt{s} = 13$ TeV. *Eur. Phys. J. C*, 80(3):189, 2020.

[224] Albert M Sirunyan et al. Search for Supersymmetry with a Compressed Mass Spectrum in Events with a Soft τ Lepton, a Highly Energetic Jet, and Large Missing Transverse Momentum in Proton-Proton Collisions at $\sqrt{s} =$ TeV. *Phys. Rev. Lett.*, 124(4):041803, 2020.

[225] Georges Aad et al. Search for direct stau production in events with two hadronic τ-leptons in $\sqrt{s} = 13$ TeV pp collisions with the ATLAS detector. *Phys. Rev. D*, 101(3):032009, 2020.

[226] Georges Aad et al. Searches for electroweak production of supersymmetric particles with compressed mass spectra in $\sqrt{s} = 13$ TeV pp collisions with the ATLAS detector. *Phys. Rev. D*, 101(5):052005, 2020.

[227] Georges Aad et al. Search for electroweak production of charginos and sleptons decaying into final states with two leptons and missing transverse momentum in $\sqrt{s} = 13$ TeV pp collisions using the ATLAS detector. *Eur. Phys. J. C*, 80(2):123, 2020.

[228] Jason Kumar and Danny Marfatia. Matrix element analyses of dark matter scattering and annihilation. *Phys. Rev.*, D88(1):014035, 2013.

[229] J. Aalbers et al. First Dark Matter Search Results from the LUX-ZEPLIN (LZ) Experiment. 7 2022.

[230] Florian Staub, Thorsten Ohl, Werner Porod, and Christian Speckner. A Tool Box for Implementing Supersymmetric Models. *Comput. Phys. Commun.*, 183:2165–2206, 2012.

[231] Mark D. Goodsell, Kilian Nickel, and Florian Staub. Two-Loop Higgs mass calculations in supersymmetric models beyond the MSSM with SARAH and SPheno. *Eur. Phys. J. C*, 75(1):32, 2015.

[232] Mark D. Goodsell and Florian Staub. The Higgs mass in the CP violating MSSM, NMSSM, and beyond. *Eur. Phys. J. C*, 77(1):46, 2017.

[233] John C. Collins and J. A. M. Vermaseren. Axodraw Version 2. 5 2016.

[234] Marcela Carena, John R. Ellis, S. Mrenna, et al. Collider Probes of the MSSM Higgs Sector with Explicit CP Violation. *Nucl. Phys. B*, 659:145–178, 2003.

[235] Marrit Schutten. Supplementary data for eEDM study in thesis 'Low energy observables and fine-tuning in the MSSM', March 2023.

[236] Wikipedia. Larmor precession, 2023. https://en.wikipedia.org/wiki/Larmor_precession Accessed 28-03-2023.

[237] Syracuse University. Lhcb experiment, 2023. https://hep.syr.edu/quark-flavor-physics/outreach/hep-tour/lhcb-experiment/ Accessed 28-03-2023.